A STUDY ON AMPHIPHILIC SIDEROPHORE DETECTION, STRUCTURE ELUCIDATION AND THEIR IRON-MEDIATED VESICLE SELF-ASSEMBLY

by

Luis O'mar Serrano Figueroa

A dissertation submitted in partial fulfillment
of the requirements for the degree

of

Doctor of Philosophy

in

Microbiology

MONTANA STATE UNIVERSITY
Bozeman, MT

April 2015

ProQuest LLC.
789 East Eisenhower Parkway
P.O. Box 1346
Ann Arbor, MI 48106 - 1346

DEDICATION

To the love of Mamita, my husband Jospeh,
family and friends.
To God, for creating Nature and the Universe
and allowing us to understanding it through Science.

ACKNOWLEDGEMENTS

After six years of enduring research, some difficulties and being far from family and friends back in Puerto Rico I want to give thanks to God for allowing me finishing this degree. Another step in life is completed with enthusiasm and with the support from different persons here in Montana, back home, and absent. First, to my beloved Mamita for your support, messages of positiveness and counseling during this process. Papi Pedro, in his absence, I always thought of him, and I know he was guiding me in my studies all these years. Joseph, my love, in difficult times he never let me down and provided his care, kindness and patience so I could say I am done and I finish this important step. Love you! Titi, for your emotional support as well and I love you lots. To all my friends here and back home for never doubting me. To the Camper Lab: Gem, Mark, Andy, Justin and Stephen; thanks for everything. Thanks to the CBE grad students, staff and faculty for guidance and assistance. Thanks to Betsey Pitts, Jonathan Hilmer, Benjamin Schwartz and Masaki Uchida for their collaboration efforts and their input in different laboratory techniques. Special thanks for my committee, Drs. Abigail Richards, Anne Camper, Michael Franklin and Ross Carlson, for their constant ideas, support and guidance during this process.

TABLE OF CONTENTS

TABLE OF CONTENTS – CONTINUED

TABLE OF CONTENTS – CONTINUED

LIST OF TABLES

LIST OF TABLES – CONTINUED

LIST OF TABLES – CONTINUED

LIST OF FIGURES

LIST OF FIGURES – CONTINUED

LIST OF FIGURES – CONTINUED

LIST OF FIGURES – CONTINUED

LIST OF FIGURES – CONTINUED

LIST OF FIGURES – CONTINUED

Figure Page

LIST OF FIGURES – CONTINUED

LIST OF FIGURES – CONTINUED

Figure Page

LIST OF FIGURES – CONTINUED

LIST OF FIGURES – CONTINUED

LIST OF FIGURES – CONTINUED

LIST OF IMAGES

LIST OF IMAGES – CONTINUED

LIST OF IMAGES – CONTINUED

ABSTRACT

Soap Lake, located in Washington State, was the subject of an NSF funded Microbial Observatory and is a naturally occurring saline and alkaline lake. Several organisms inhabiting this lake have been identified as producers of siderophores that are unique in structure. Two isolates SL01 & SL28 were the focus of this study of siderophore production, structure elucidation and vesicle self-assembly. Bacterial isolates, enriched from Soap Lake sediment and water samples, were screened for siderophore production. Siderophore production was confirmed through the chrome azurol S (CAS) agar plate method. Isolates SL01 and SL28 were found to produce relatively high concentrations of siderophores in liquid medium. Extraction was performed by the methanol/water protocol in Varian cartridges and siderophore purification was done on HPLC with a 0-70% acetonitrile gradient. Lyophilization or *in vacuo* evaporation followed in order to store siderophores. Siderophore structure was determined using liquid chromatography and tandem mass spectrometry (LC/MS/MS) with fatty acid methyl ester (FAME) analysis. Vesicle self-assembly studies were performed using dynamic light scattering (DLS) and epifluorescence microscopy (employing cryoembedding and cryosectioning). Three new amphiphilic siderophore families (two from SL01 and one from SL28) were produced by the bacterial isolates, found to be most closely related to *Halomonas variablis* and *Halomonas pantelleriensis*, respectively. These siderophores resemble the amphiphilic aquachelin siderophores produced by *Halomonas aquamarina* strain DS40M3, a marine bacterium. Addition of ferric iron (Fe^{+3}) at different equivalents demonstrated vesicle formation and this was confirmed by both DLS and epifluorescence microscopy. Bacteria thriving under saline and alkaline conditions are capable of producing unique siderophores resembling those produced by microbes inhabiting marine environments. Vesicle self-assembly was confirmed quantitatively and qualitatively. Amphiphilic siderophores may have different applications in medical and environmental fields.

CHAPTER ONE

SIDEROPHORES FOR IRON ACQUISITION IN MICROORGANISMS: CLASSIFICATION AND THEIR APPLICATIONS

Introduction

Almost all microorganisms require iron for their cellular processes. It is involved in amino acid synthesis, oxygen transport, respiration, nitrogen fixation, methanogenesis, citric acid cycle, photosynthesis and DNA biosynthesis. However its concentration in the extracellular environment is very low (10^{-18} M) and limited by the insolubility of $Fe(OH)_3$. Iron can be present in its ferric (Fe^{+3}) or ferrous (Fe^{+2}) forms. The redox potential of the latter is suitable as a protein catalytic center. For pathogenic microorganisms like *S. aureus* and *P. aeruginosa*, iron availability is even lower due to mammalian host proteins (heme, lactoferrin, transferrin and ferritin) that sequester iron from the plasma (Krewulak & Vogel 2008). Microorganisms require micromolar concentrations of iron, but ocean surface water has concentrations ranging from 0.01 – 2 nM (Luther & Wu 1997). In order to obtain ferric iron organisms have developed different mechanisms: siderophores, hemophores, ferric binding proteins and transferrin/lactoferrin receptors (Sandy & Butler 2009).

In this chapter, several topics will be considered including, iron acquisition, the different types of siderophores discovered so far and the potential applications they may have. Iron acquisition could be mediated by siderophores, heme or transferrin/lactoferrin, as previously mentioned. The types, or classification, of siderophores focus on three different functional groups: catecholates, hydroxamates and α-hydroxycarboxylates. Also, two environments account for most of the siderophores discovered so far: marine

and terrestrial. In subsequent chapters, a third new environmental niche, soda lakes, accounts for the presence of more siderophores. Finally, applications of siderophores ranging throughout different science areas of medicine, bioremediation, biosensors, agricultural biotechnology etc. will be discussed.

Acquisition and Transport of Ferric Iron

Siderophore-Mediated Iron Acquisition

The transport of ferric iron across the cell is active (Figure 1.1 (Crosa 2004)), due to the use of porins for the high molecular weight ferric-siderophore complex. This requires different transport proteins and receptors. There are outer membrane receptors in charge of recognizing iron-bound siderophores outside the cell. Some of these receptors are FhuA, FecA and FepA found in *E. coli* (Ferguson et al. 1998, Ferguson et al. 2000, Ferguson et al. 2001, Ferguson et al. 2002, Yue et al. 2003), and BtuB, FpvA and FptA found in *P. aeruginosa* (Cobessi et al. 2005a, Cobessi et al. 2005b, Cornelis et al. 2009). In general, their structure is composed of β-barrel and cork domains (Krewulak & Vogel 2008). The β-barrels are transmembrane domains that help to form a hollow space where the iron-sidrophore complex passes through to the periplasm. The N-terminal domain is also referred as the cork domain. Its function is to bind the iron-siderophore complex and bring it in to the β-barrel.

How energy is obtained in order to transport the ferric siderophore from the extracellular space into the periplasm? The outer membrane of Gram-negative cells does not have a proton motive force that will provide the energy required for active transport. That role is performed by the TonB, ExbB and ExbD proteins; they provide the proton motive force required for transport. TonB has an amino-terminal domain that acts as a cytoplasmic membrane signal anchor. It comprises amino acids 1 to 32, and has a

transmembrane section from amino acids 12 to 32. The second domain is a central region that goes from amino acids 33 to 100. No essential role in signal or energy transduction has been described. The third and last domain is the carboxy-terminal (amino acids 103 to 239). It is required for the interaction with the outer membrane and outer membrane transporters. Both the amino- and carboxy-terminal domains are required for full function of TonB in order to provide the energy required to transport ferri-siderophores across the outer membrane. Mutations on this domain cause the lack of activity in TonB, therefore affecting the energy transduction and eventually siderophore transport. The other proteins, ExbB and ExbD, assist TonB in energy transduction, too. Both proteins are transmembrane proteins in nature, like TonB, and are expressed in an operon at different levels of expression. ExbB is present at higher concentrations to that of ExbD. Both proteins interact with TonB and help it shuttle to the outer membrane and transduce the required energy for siderophore-iron transport.

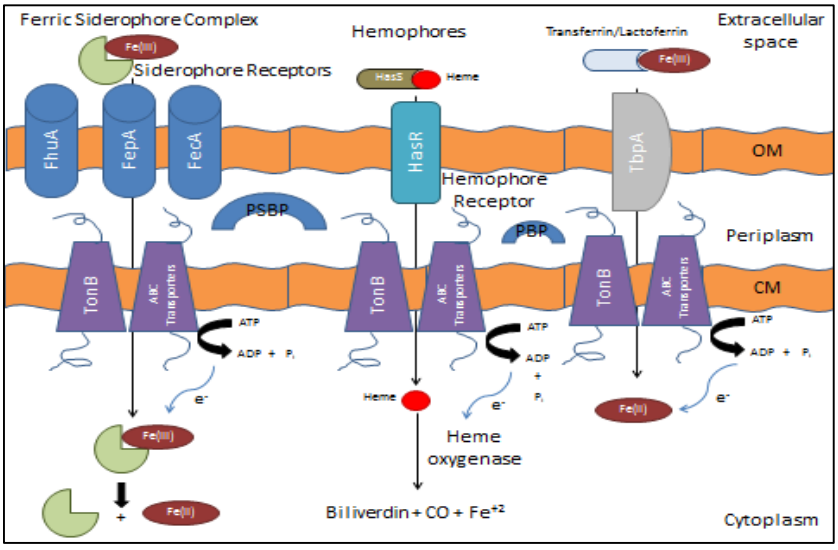

Figure 1.1. Iron acquisition in a Gram-negative bacterial cell. OM: outer membrane; CM: cytoplasmic membrane; PSBP: periplasmic siderophore binding protein; PBP: periplasmic binding protein. ABC transporter includes proteins ExbB and ExbD and help in ATP hydrolysis to obtain energy for active transport. Adapted from Krewulak and Vogel (2008).

In the periplasm there are periplasmic siderophore binding proteins (PSBP) to transport ferric siderophores across the cytoplasmic membrane. The word siderophore is included in this term because there are about eight different clusters of periplasmic binding proteins (Crosa 2004, Krewulak & Vogel 2008) that bind oligosaccharides, sugars, phosphate, amino acids (polar and non-polar), organic polyanions, peptides, iron complexes and other metals. FhuD, FbpA and BtuF are the most studied PSBPs today and they are associated with iron uptake metabolism and transport. They consist of bilobes joined by two or three β strands or by backbone helixes. This structure similarity contrasts well even though there is poor sequence identity of less than 10%. Specific group-coordinating PSBPs will shuttle their corresponding siderophore through the periplasm until the PSBP-siderophore-iron complex reaches transporters on the cytoplasm.

The transporters are a class of ATP-binding cassettes (ABC transporter proteins). The best example known today is the FhuBDC. As previously discussed, FhuD is the PSBP for hydroxamate siderophores, and well-studied due to its complete structure elucidation. FhuB and FhuC are known as the ABC transporter proteins. The complex couples ATP hydrolysis to transport the iron-siderophore thorugh the cytoplasmic membrane into the cytoplasm. FhuBC forms channels due to their transmembrane domains where the siderophore-iron complex passes through. It also has two nucleotide binding domains that hydrolyze ATP. In brief, FhuD transfers the siderophore-iron complex to FhuB, the complex is translocated to the channel; in the meantime FhuC hydrolyses ATP. Finally the siderophore-iron complex is dissociated by an electron transfer to ferric iron (Fe^{+3}), converting it to ferrous iron (Fe^{+2}).

Iron Uptake by Heme, Transferrin & Lactoferrin

The importance of iron to the cell has been previously established. In the host of a pathogenic bacterium iron is in the form of heme. The bacterial cell has developed a system that helps in its uptake from the host (Tong & Guo 2009). They express outer membrane receptors and transport proteins specific to heme. Also hemophore synthesis is part of the uptake process and they bring heme to their specific receptor. One of the most studied hemophores is HasA, and belongs to *Serratia marcescens* (Krieg et al. 2009). The mechanism of heme transport into the cell is similar to that of siderophore-iron acquisition. A proton motive force is required for the active transport provided by the ABC transporters associated with TonB. The hemophore-heme interacts with its receptors (HasR), then the complex passes to the periplasm and finally to the cytoplasm where heme oxygenase acts on the tetrapyrrole ring and degrades it (Zhu et al. 2000).

The host also expresses several iron transport proteins that will reduce iron concentration or bioavailability. Those proteins are transferrin and lactoferrin. To overcome this, bacteria express the production of receptor proteins on the outer membrane that will help in transferrin/lactoferrin uptake (Morgenthau et al. 2013). Iron is removed from the transporter protein by interaction with the appropriate receptor. This interaction is species specific; *Neisseria* sp. receptors will recognize human lactoferrin only, meanwhile *Actinobacillus pleuropneumoniae* is able to bind the pig transferrin (Williams & Griffiths 1992, GrayOwen & Schryvers 1996, Noinaj et al. 2013). The receptors involved in transferring acquisition are TbpA and TbpB.

Ferrous Iron Uptake

The mechanism of ferrous iron intake, contrary to ferric iron acquisition, is not well understood. Ferrous iron solubility is higher at neutral pH compared to ferric iron

and this facilitates transport across the membrane. Ferrous iron concentration is higher only under anaerobic or reducing conditions. Two different systems for ferrous iron uptake have been described: Feo and Sit (Weaver et al. 2013, Carpenter & Payne 2014). The Feo system in *E. coli* is composed of an operon of three genes, *feoABC*, that code for their respective proteins, FeoA, FeoB and FeoC (Kammler et al. 1993). A regulatory region is found upstream the gene, where Fur and iron (II) function as co-repressors. FeoB is the larger protein (~70 kDa) and it is located on the cytoplasmic membrane. There are sequence homologs to ATPases and this may be a signal that the system requires active transport. FeoA is a smaller cytoplasmic protein with a SH3-like domain. FeoC is a small protein that functions as a [Fe-S]-dependent translational receptor and it is located in the cytoplasm as well.

The second system for ferrous iron transport mentioned above was Sit, comprised by the operon *sitABCD* (Carpenter & Payne 2014). It is generally absent from non-pathogenic microorganisms but it is found in *S. enterica* Typhimurium (Boyer et al. 2002), *Shigella* (Payne & Mey 2010), and some pathogenic *E. coli* (Payne & Mey 2010). As these previous reports suggests this system could overlap with manganese transport as well.

Both ferrous uptake systems described are required for pathogenicity. As examples, *S. enterica feoB* mutants were not able to colonize mouse intestines like the wild type did (Tsolis et al. 1996) and no virulence in susceptible mice strain was reported (Boyer et al. 2002). Also, the *sit* operon is needed for the pathogenicity of *S. flexneri* (Fisher et al. 2009).

Iron Storage

Extracellular iron is not the only available source of iron for bacteria. Iron is stored in reserves of iron storage proteins (Andrews et al. 2003). Three types of iron storage proteins are found in bacteria: the ferritins (found also in eukaryotes), the bacterioferritins (which contains heme) and Dps proteins (present only in prokaryotes). Although their primary function is iron storage they are evolutionarily distant but have retained similar structural characteristics. The molecular architecture of ferritins and bacterioferritins is 24 identical subunits (Dps has 12 subunits) that assemble to form a spherical protein shell and a hollow that serves as the iron reservoir. Ferritins/bacterioferritins accumulate more iron than Dps proteins.

Storage proteins take up iron in its soluble ferrous ion (Fe^{+2}) and store it in the central cavitiy in its oxidized form (Fe^{+3}). This requires a ferroxidation step which is catalyzed by specific sites (ferroxidase center) within the iron storage protein. The site is highly conserved among ferritins and bacterioferritins and they bind two ferrous ions and used O_2 in the redox reaction. The ferric ion migrates to the center of the protein where ferrihydrite may form or, in the presence of phosphates, amorphous ferric phosphate. In contrast, the ferroxidase sites are not conserved in Dps proteins, binding the ferrous ion at a different site (at the two-fold interface between subunits) (Ilari et al. 2000). Therefore, the 12-meric and 24-meric iron storage proteins oxidize iron in different ways. Also Dps proteins utilize H_2O_2 as the oxidant indicating that the principal role for this protein is DNA protection andti-redox agents. The function of ferritin A in *E. coli* is to storage iron during post exponential growth and eventually use the reserve at iron-limiting conditions (Abdul-Tehrani et al. 1999). Ferritins and bacterioferritins can also detoxify the cell from some heavy metals and hydroxy radicals (Bou-Abdallah et al.

2002, Zhang et al. 2013). Heme-containing bacterioferritins are more common in bacteria than ferritins. The heme is normally in the form of protoporphyrin IX and 12 heme groups are present per 24-mer located at the two-fold interfaces between subunits.

Regulatory Characteristics of Siderophore Production

Fur-Mediated Regulation of Siderophore Production

Bacteria, as noted before, require iron for their survival and they use siderophores to obtain it. However, iron toxicity should be avoided and here lies the importance of iron regulation. The siderophore production is regulated by the *fur* (for ferric uptake regulation) gene and it has been described for the past 30 years as being the main player in iron regulation in microorganisms (Crosa 2004). The gene encodes the regulatory protein Fur. When iron levels (in the form of ferrous iron) are high in the bacterial cell, Fe^{+2} binds to Fur and then the complex binds to sequences on the DNA called Fur boxes (also known as iron boxes) located between the TATA box and -35 region of the siderophore promoter. This represses transcription of siderophore synthesis and siderophore transport proteins genes. But when iron levels are high, ferrous iron bound to Fur makes the protein unable to bind to its correspondent Fur boxes. At this point the RNA polymerase can bind to the siderophore producing genes and transcription happens. Siderophores are synthesized and transported to the extracellular space for iron scavenging. Figure 1.2 presents a general description of the regulation system described previously.

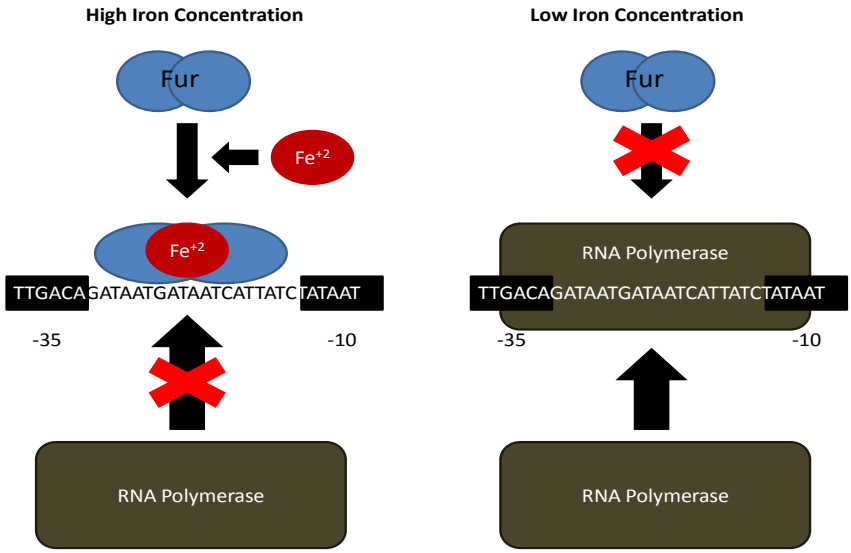

Figure 1.2. Siderophore-mediated iron acquisition system regulated by the Fur protein. Adapted from Crosa et al. (2004).

Siderophore Regulation by Quorum Sensing

Some bacteria regulate siderophore production by means of quorum sensing. The phenomenon happens in a cell density-dependent manner and helps regulate different tasks in the cell. In many organisms it is based on the production of small molecules called acyl homoserine lactones (HSLs). The more bacterial cells are found, the more HSLs are produced and interact with cells. The HSLs freely diffuse into cells and when concentrations are high they bind to receptor proteins, interacting eventually with DNA sequences and triggering the corresponding phenotype response. Different physiological conditions are affected by quorum sensing, including: biofilm formation (Christiaen et al. 2014, Kadirvel et al. 2014), swarming motility (Vasavi et al. 2014), bioluminescence (Packiavathy et al. 2013), antibiotic production and resistance (Fineran et al. 2005), production of pharmaceuticals (Raina et al. 2012) and toxins (Tal-Gan et al. 2013).

Siderophore production is well affected by quorum sensing in some bacteria, especially pathogens. Stintzi and co-workers (1998) described that *lasR* mutants were affected in siderophore production, specifically pyoverdine in *P. aeruginosa*. The pyoverdine gene (*pvd*) expression was not affected by the mutation on the quorum sensing system. Another siderophore produced by *P. aeruginosa* is pyochelin and it was not affected by the deficiency in the autoinducer production. In contrast, *Burkholderia cepacia* quorum sensing mutants tend to overproduce the siderophore ornibactin (Lewenza et al. 1999). Complementation restores siderophore to original levels. More studies should be done in terms of siderophore production and the relationship with quorum sensing to see how iron acquisition mechanisms are regulated.

Siderophore Coordination Groups

Siderophore classification is based on certain functional groups that are involved in ferric iron coordination. Those groups include catechols, as in enterobactins; hydroxamates, as in desferrioxamines; and α-hydroxycarboxilates, as in achromobactins (Figure 1.3). These functional groups are donors of three OO' in order that six oxygen atoms are coordinating the ferric iron. Mixed functional group siderophores are also observed in nature. An example of this is the siderophore aerobactin that has two hydroxamates and one hydroxycarboxilic acid group.

Tris-Catecholate Siderophores

The main examples of this type of siderophores are enterobactin, bacillibactin and salmochelin. They are framed on a cyclic tri-ester scaffold form by L-serine or L-threonine. Enterobactin is a cyclic trimer of 2,3-dihydroxybenzoyl-L-serine produced by *E. coli* and other enteric pathogens (Gehring et al. 1997). This siderophore was

investigated and found that it inhibits the anthrax toxin lethal factor from *B. anthracis* (Thomas & Castignetti 2009). Salmochelin is the glucosylated form of enterobactin. It is produced by *Salmonella enterica* and uropathogenic *E. coli*; two of its catechols contain glucose at the C-5 position (Bister et al. 2004). Very important in bacterial pathogenesis, this siderophore protects *Salmonella* from reactive oxygen species (Achard et al. 2013). *Bacillus subtilis* and other *Bacillus* species produce bacillibactin which incorporates a cyclic trimester scaffold of L-threonine (Dertz et al. 2006). The threonine amines are elongated by glycine ligated to 2,3-dihydroxybenzoic acid. Bacillibactin and its producer, *B. subtilis*, have been found to inhibit *Fusarium* growth and *Phytophthora* blight disease, being candidates for biocontrol strategies (Woo & Kim 2008, Yu et al. 2011). Recently, Han and co-workers (2013) discovered another siderophore that falls in this classification called turnerbactin, produced by an endosymbiont of a shipworm (Han et al. 2013). It is a trimer of N-(2, 3-DHB)-L-Orn-L-Ser linked to three monomeric units of serine esters. Cyclic trichrysobactins were also discovered by another group of researchers (Sandy & Butler 2011). The structural characterisitic is a tris-catecholate siderophore, but the plant pathogen that produces it (*Dickeya chrysamthemi*) also modifies it in dimer and linear forms. The cyclic counterpart is a trimer of the linear chrysobactin, made of L-Serine, D-Lysine and 2,3-DHBA. Structural detail of some selected catecholate siderophores is presented in Figure 1.4.

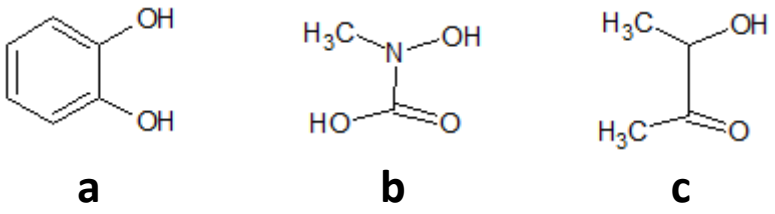

Figure 1.3. Siderophore functional groups: catechols (a), hydroxamates (b) and α-hydroxycarboxylates (c). Note the OO' groups provided by the hydroxyl and carbonyl moieties. Adapted from Krewulak and Vogel (2008).

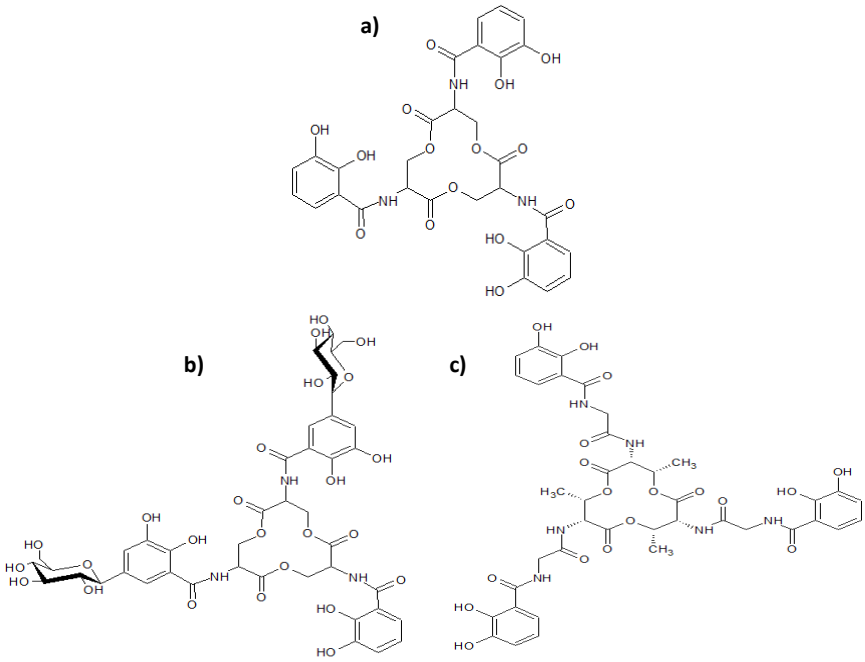

Figure 1.4. Enterobactin (a), salmochelin S4 (b) and bacillibactin (c) structures. Adapted from Sandy and Butler (2009).

Tris Hydroxamate Siderophores

The best known example of hydroxamate siderophores are the ferrioxamines (or desferrioxamines when no ferric iron is coordinated). Their structural composition is alternating units of succinic acid and monohydroxylated diamine, either N-hydroxycadaverine or N-hydroxyputrescine. Figure 1.5 presents the structure for some desferrioxamines. Some of them are in cyclic form like desferrioxamine E (Konetschnyrapp et al. 1992, Ejje et al. 2013), or linear like desferrioxamines B (Martinez et al. 2001, Ejje et al. 2013) and G (Bergeron et al. 1992, Ejje et al. 2013). Desferrioxamine B has been used in iron chelation therapy in cases of iron overload disease (Payne et al. 2008). Some applications of hydroxamates like deferrioxamine B is their use to improve phytoremediation activities in heavy metal-contaminated sites (Dimkpa et al. 2008). They found that *Streptomyces* sp. siderophores will not only bind

ferric iron (Fe^{+3}) but Al^{+3}, Cd^{+2}, Cu^{+2} and Ni^{+2} as well. An increase in auxins was observed when siderophores were in the presence of these cations, increasing the growth and remediation potential of plants. *Streptomyces coelicolor* produced another hydroxamic acid siderophore called coelichelin (Challis & Ravel 2000, Dimkpa et al. 2008). Another siderophore that falls in this category is amychelin, produced by *Amycolaptosis sp*., an actinomycete (Seyedsayamdost et al. 2011). More recently, di-hydroxamic acid siderophores (putrebactins) have been characterized from *Shewanella putrefaciens* (Soe & Codd 2014). This type of siderophore was produced by precursor-directed biosynthesis and it is composed of cyclic hydroxamate dimers. Two other siderophores, scabichelins and turgichelins, were produced by *Streptomyces antibioticus, Streptomyces scabies* and *S. turgidiscabies* (Kodani et al. 2013). These siderophores not only chelate iron but also Ga(III). A fungus, *Scedosporium apiospermum* is responsible for the production of two other hydroxamic acid siderophores: dimemuric acid and N-methyl coprogen B (Bertrand et al. 2009). Like desferrioxamine B and G, both siderophores are linear (Figure 1.5). Another siderophore that falls in this category is produced by *Saccharopolyspora erythraea*, erythrochelin (Robbel et al. 2010, Robbel et al. 2011). In this study the researchers revealed the tetrapeptide sequence of the molecule: D-α-acetyl-δ-N-acetyl-δ-N-hydroxyornithine-D-serine-cyclo(L-δ-N-hydroxyornithine-L-δ-N-acetyl-δ-N-hydroxyornithine).

Hydroxycarboxilates, Carboxylates and Mixed Functional Group Siderophores

There are several examples of this group of siderophores. Achromobactin is a siderophore produced by *Pseudomonas syringae* pv. *syringae* (Berti & Thomas 2009). It is a tris-α-hydroxycarboxylate siderophore and the two coordinating groups are donated by α-ketoglutarate and the third comes from citric acid. A second siderophore that falls in

this group is vibrioferrin. It is categorized as a bis-α-hydroxycarboxilic siderophore: one group coming from α-ketoglutarate and a second from citrate (Harris et al. 2007, Amin et al. 2009). Rhizoferrin's two coordinating groups are donated from two citrates as well as those from staphyloferrin A (Meiwes et al. 1990, Drechsel et al. 1991, Harris et al. 2007, Cotton et al. 2009). Both rhizoferrin and staphyloferrin A share common structure and the only difference is an extra carboxylic acid for staphyloferrin A (see Figure 1.6). Also staphyloferrin B has been characterized as part of the *S. aureus* iron acquisition system (Cheung et al. 2009). Citric acid is also an iron chelator and considered a siderophore (Guerinot et al. 1990). It forms the bis-ferri-citrato complex that is recognized by the outer membrane receptor FecA and is produced by *B. japonicum*, a nitrogen-fixing soybean symbiont. Structures are presented in Figure 1.6.

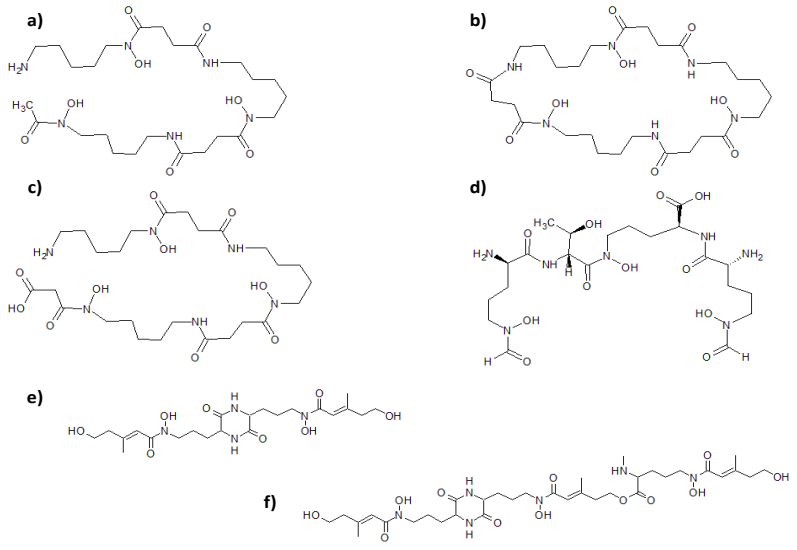

Figure 1.5. Example of hydroxamic acid-containing siderophores: desferrioxamines B (a), E (b), G (c) and coelichelin (d). Adapted from Sandy and Butler (2009).

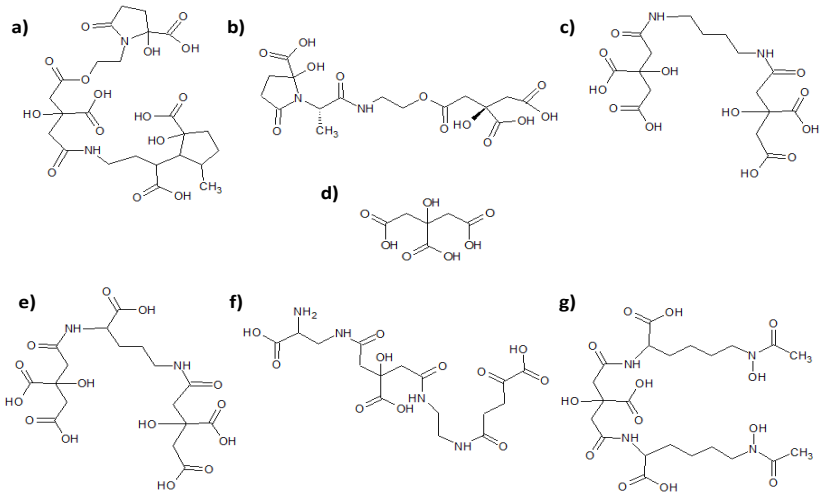

Figure 1.6. Selected hydroxycarboxylic acid siderophores: achromobactin (a), vibrioferrin (b), rhizoferrin (c), citric acid (d), staphyloferrin A (e), staphyloferrin B (f) and aerobactin (g). Aerobactin is part of the mixed functional groups siderophores. Adapted from Sandy and Butler (2009).

There are many of siderophores that contain mixed coordinating functional groups. This group of siderophores is composed by bidentate ligand and also amphiphilic siderophores. Aerobactin contains hydroxamates and α-hydroxycarboxylates (Figure 1.7 (Neilands 1995)). Examples are amphibactins, ochrobactins, marinobactins, aquachelins among others that will be discussed on next section. Lystabactins are another type of siderophores produced by *Pseudoalteromonas* sp. (Zane & Butler 2013). The microbe was isolated from the Deep Water Horizon spill site and the three different siderophores were characterized by mass spectrometry and NMR. Dhungana and co-workers also discovered another mixed ligand siderophore called rhodobactin (Dhungana et al. 2007). The siderophore was produced by a soil bacterium called *Rhodococcus rhodochrous*. It is composed of two catechol and one hydroxamic acid moieties that are involved in ferric iron chelation. Amychelin, a siderophore, is produced by *Amycolaptosis* sp. (Seyedsayamdost et al. 2011). The moieties responsible for ferric

iron coordination were: 2-hydroxybenzoyl-oxazoline (N-terminus), N-OH-N-formyl-ornithine and a cyclic N-OH-ornithine (C-terminus). As described previously, these types of siderophores' functional groups are mostly composed of two hydroxamic acids and one catechol.

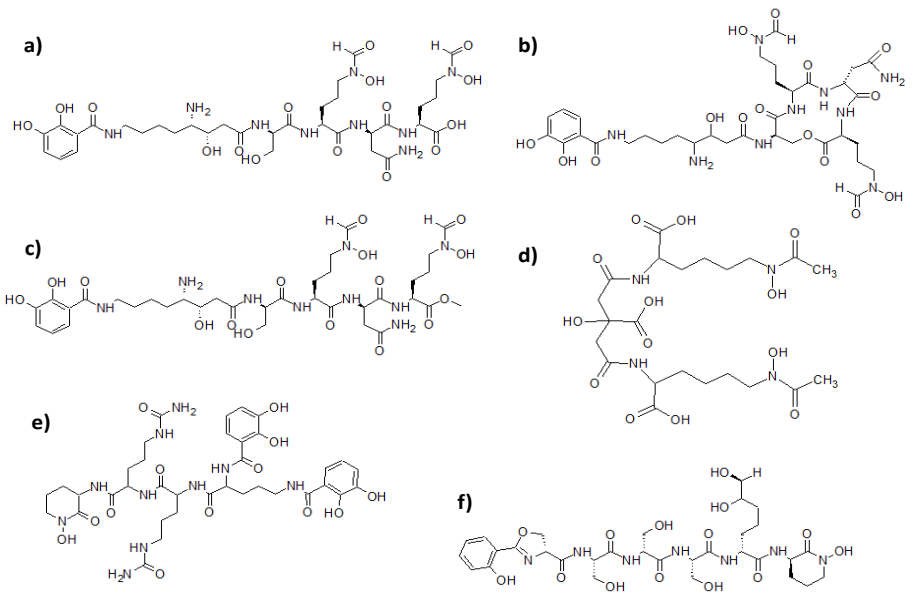

Figure 1.7. Some mixed functional groups siderophores: lystabactins A-C (a-c), aerobactin (d), rhodobactin (e) and amychelin (f). Adapted from Sandy and Butler (2009), Seyedsayamdost et al. (2011) and Dhungana et al. (2007).

Siderophores Produced by Microorganisms from the Sea

Microorganisms thrive in different environments like soil (Tara et al. 2014), freshwater (Manczak & Szuflicka 1974, Duckworth et al. 2009), seawater (Bonde 1967, Basu et al. 2013), drinking water (Reilly et al. 2000, Smith et al. 2000), hydrothermal vents (Yanagawa et al. 2013), salterns/soap lakes (Norton & Grant 1988, Aston & Peyton 2007), and ice/permafrost (De Souza et al. 2007, Carr et al. 2013); characterized by different pH, salinity, humidity and temperatures gradients. Most of the siderophores

described are produced by terrestrial microorganisms. Marine siderophores, in contrast, are not as abundant, but every year more are characterized by different groups. Most of them are amphiphiles, meaning that the same molecule will have polar and non-polar components. The polar headgroup is the iron binding site and it is attached to one or two of a series of fatty acids (Martinez et al. 2000, Martinez et al. 2003, Ito & Butler 2005, Owen et al. 2005, Martin et al. 2006, Gauglitz et al. 2012). Figure 1.8 shows selected amphiphilic siderophore structures. Another structural feature is the presence of α-hydroxycarboxylic acid moiety, usually in the form of β-hydroxyaspartic acid or citric acid. This structural characteristic confers photochemical reactivity to the molecule as demonstrated previously (Butler et al. 2001, Barbeau et al. 2002, Barbeau et al. 2003, Butler & Theisen 2010b). In brief, the ferric amphiphilic siderophore exposed to light yields a fatty acid and ferric-headgroup complex as photoproducts. This implies that amphiphilic siderophores play an important role in maintaining the ferrous iron pool in open oceans.

Amphiphilic Siderophores

From the previous figure it is possible to observe the similarity in structure discussed before: a polar headgroup and a fatty acid tail, or tails, and the differences in polar headgroup size and fatty acid length. This confers to the molecule a certain level of hydrophilicity or hydrophobicity. A clear example of this is the hydrophobicity of amphibactins (Gledhill et al. 2004, Vraspir et al. 2011), moanachelins (Gauglitz & Butler 2013a) and ochrobactins (Gauglitz et al. 2012) contrasting to the hydrophilic lohichelins (Homann et al. 2009b). The former have smaller polar headgroups and longer fatty acids (C16-C18), meanwhile the loihichelins posses a bigger polar headgroup and short fatty acid moieties. This also affects their extraction: amphibactins, moanachelins and

ochrobactins are mainly obtained from cell pellet extracts, contrasting to the supernatant extracts that contain loihichelins.

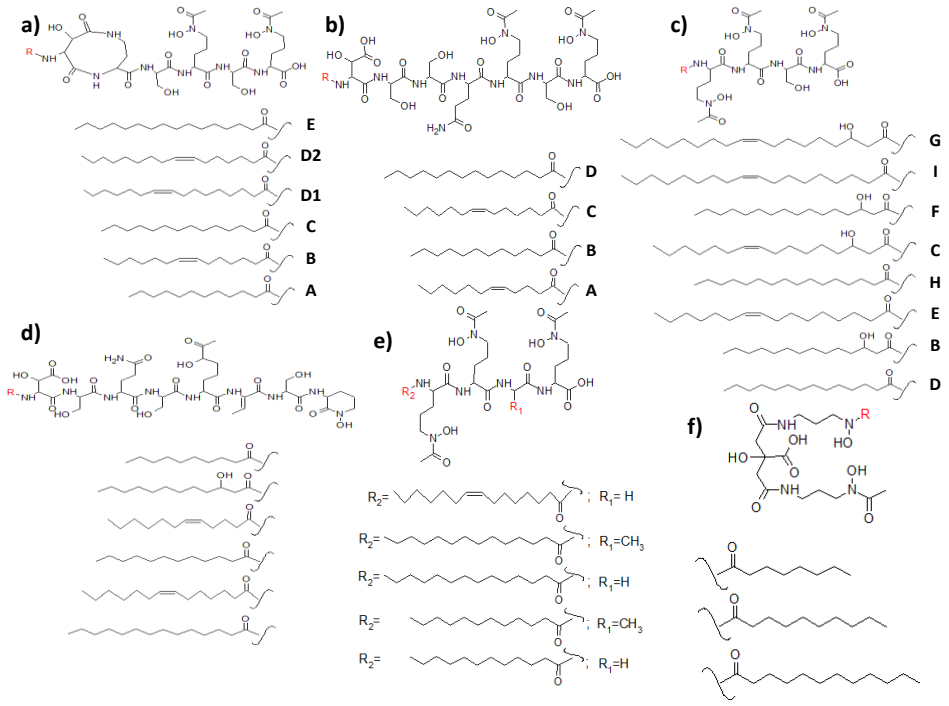

Figure 1.8. Some suites of marine amphiphilic siderophores structures characterized: marinobactins (a), aquachelins (b), amphibactins (c), loihichelins (d), moanachelins (e) and synechobactins (f). Adapted from Sandy and Butler (2009).

Marinobactins have been the most studied of the amphiphiles (Xu et al. 2002, Martinez & Butler 2007). Their amphiphilicity varies within the family as a result of the differences in fatty acid length. Marinobactins D and E are in the middle of the amphiphilic spectrum due to their six amino acid head group and fatty acid tails of C16. However, Marinobactin F has been isolated from bacterial cell pellet extracts due to its C18 long fatty acid. The most hydrophilic are the marinobactins. Xu and co-workers (2002) validated this by studying membrane affinities using synthetic liposomes. The membrane studies were also done on the ochrobactins giving similar results to those of the marinobactins (Martin et al. 2006). The partitioning coefficients for these

siderophores decreased when ferric iron was bound to them. Aquachelins are quite hydrophilic especially aquachelins I and J isolated from *Halomonas meridiana* (Vraspir et al. 2011). *Synechococcus* sp. produces synechobactins that appear on Figure 1.8 and they are related to schizokinen (Ito & Butler 2005). This type of siderophores is the first one discovered from a marine cyanobacterium and they are composed of a citrate backbone and two 1, 3-diaminopropane units. Other siderophores can be taken up by another type of microorganism and then undergo changes in their structure. Amphi-enterobactin is a recently new classic example of this (Zane et al. 2014). This siderophore is used by *Vibrio harveyi* and in the cell it undergoes a chemical modification to transform it into an amphiphile by adding fatty acids ranging in different lengths (C10-C14), saturation levels and hydroxylation.

Another property of amphiphilic siderophores is the capacity of the molecules to self-assemble in micelles and vesicles upon iron coordination (Martinez et al. 2000, Luo et al. 2002, Owen et al. 2005, Owen et al. 2007, Bednarova et al. 2008, Owen et al. 2008). The science behind this phenomenon is based on the critical micelle concentration (cmc) of the amphiphile molecule. When the concentration of the amphiphilic siderophore is over the cmc and the siderophore is not bound to iron, micelle formation occurs. Adding ferric iron (~1 Eq.) to the solution causes micelle size reduction, but if the iron concentration increases (>1 Eq.) a micelle-to-vesicle transition happens (Owen et al. 2005). A brief description of this process appears in Figure 1.9.

For marinobactins, their cmc ranges from 50 to 150 μM and they tend to form micelles with diameters of about 50 to 200 nm (Martinez et al. 2000). Diameter sizes for apo-marinobactin E and ferri-marinobactin E micelles are 4 and 2.8 nm, respectively (Owen et al. 2005). This group showed that when excess iron (2-3 Eq.) is added to the

solution, multilamellar vesicles or stacks of lamellae could form. Some groups have worked with synthetic amphiphilic siderophores with catechol functional groups (Bednarova et al. 2008). Here, micelle formation was accomplished for both synthetic molecules and aggregation was confirmed by cryo-transmission electron microscopy (cryo-TEM). They reported that micelle-to-vesicle formation was slow, but it increased when 1% octanol was added to the solution. Micelle and vesicle diameters were about 4 and 50 nm, respectively. Also other cations could induce micelle or vesicle formation on amphiphilic siderophores. Owen and co-workers (2008) reported that cadmium (Cd^{+2}) and zinc (Zn^{+2}) multilamellar vesicle formation was detected by means of X-ray absorption spectroscopy(Owen et al. 2008)(Owen et al. 2008)(Owen et al. 2008)(Owen et al. 2008)(Owen et al. 2008)(Owen et al. 2008)(Owen et al. 2008)(Owen et al. 2008). Cd^{+2} and Zn^{+2} vesicles showed diameters of 282 and 110 nm, respectively.

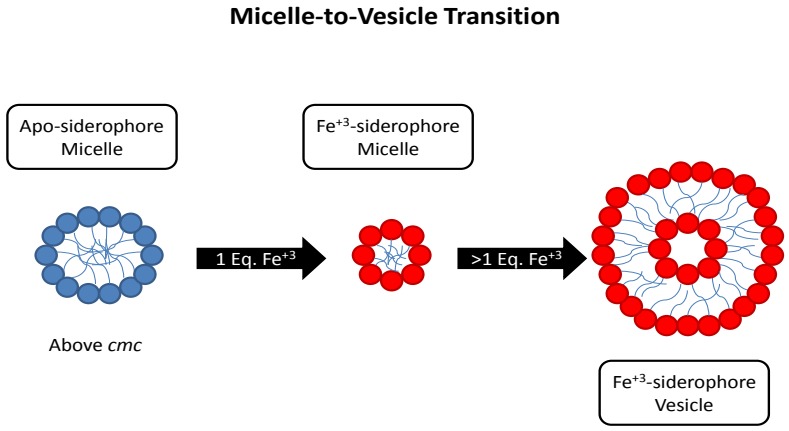

Figure 1.9. Micelle and vesicle formation on amphiphilic siderophores due to critical micelle concentration (cmc) and ferric iron chelation. Adapted from Owen et al. (2005).

Non-Amphiphilic Marine Siderophores

Apart from amphiphilic siderophores described above, oceans have a diverse siderophore pool. Aerobactin and vibrioferrin, produced by *Vibrio* sp., are examples of non-amphiphilic marine siderophores (Haygood et al. 1993, Amin et al. 2009). As mentioned before, aerobactin is a mixed functional group siderophore with two hydroxamic acid moieties and a citric acid. Vibrioferrin is a carboxilate type siderophore. Other bacteria such as *Marinobacter hydrocarbonoclasticus* and *M. aquaeoli* produce petrobactin and its sulfonated forms as shown in Figure 1.10 (Homann et al. 2009a). Petrobactins have 3,4-dihydroxybenzoyl (3,4-DHB) as its OO' donor, replacing the most common 2,3-dihydroxybenzoate. Due to the sulfonate groups this molecules shows a certain degree of hydrophilicity. Other sulfonated siderophores include the pseudoalterobactins (Figure 1.10) that *Pseudoalteromonas* sp. produces (Kanoh et al. 2003). This may suggest that catechol sulfonation is an important and emergent structural modification. Amonabactins are produced by *Aeromonas hydrophila* and the four molecules of this group contains two catechols as the OO' donors and a hydrophobic amino acid: phenylalanine (Telford & Raymond 1997). Sandy and co-workers (2010) described the structure of two siderophores produced by *Vibrio anguillarum*: anguibactin and vanchrobactin (structure on Figure 1.10)(Sandy et al. 2010). Both are mixed functional group siderophores. *Alteromonas luteoviolacea* produces alterobactins A and B (Holt et al. 2005).

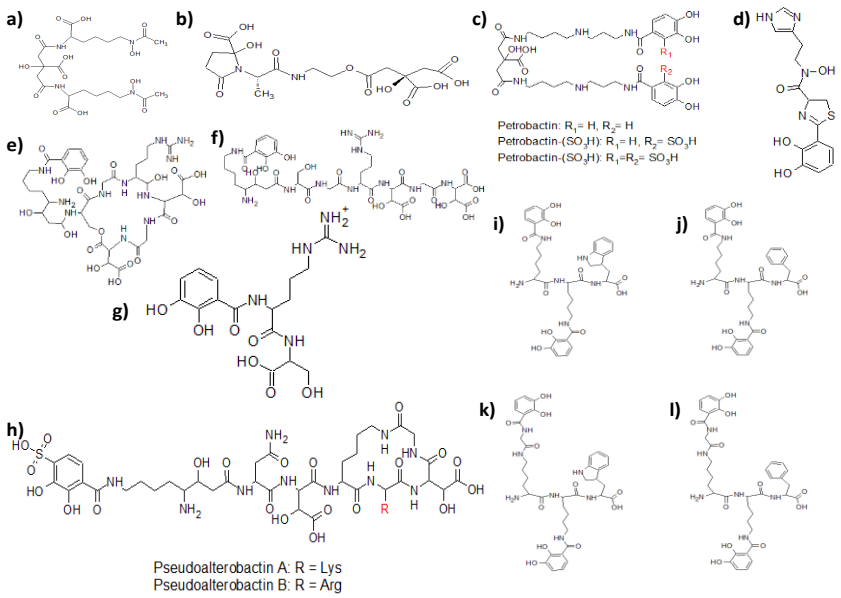

Figure 1.10. Non-amphiphilic marine siderophores: aerobactin (a), vibrioferrin (b), petrobactins (c), anguibactin (d), alterobactin A (e), alterobactin B (f), vanchrobactin (g), pseudoalterobactins (h) and amonabactins (i-l). Adapted from Sandy and Butler (2009), Amin et al. (2009) and Crosa et al. (2004).

Siderophores Isolated from other Environmental and Clinical Settings

Microorganisms can be found in different environments and can survive different stresses and conditions. The previous section was focused on siderophores produced from microorganisms found in the sea, or marine siderophores. This will focus on other environmental and clinical settings (siderophores produced by pathogens).

Siderophores Produced by Plant and Human Pathogens

An example of a mixed functional coordinating group siderophore, isolated from the plant pathogen and thermophilic actinomycete *Thermobifida fusca*, are the three fuscachelins A, B and C (Dimise et al. 2008). As Figure 1.11 shows, all of them possess two catechol and one hydroxamic acid moieties that help in ferric iron coordination. Pathogenic *Yersinia* species produce a clinically important siderophore yersiniabactin

which is composed of different rings and its precursor is cysteine (Gehring et al. 1998, Suo et al. 1999). This siderophore can also be produced by *Klebsiella pneumoniae* and has beneficial effects on the pathogenicity of the microorganism by improving lung infection (Lawlor et al. 2007). Another cysteine-containing siderophore is pyochelin (Cobessi et al. 2005a). It is a very common virulence factor of several *Pseudomonas* species and *Burkholderia cepacia*. Pyoverdine is a non-amphiphilic peptide siderophore produced by *P. aeruginosa, P. chlororaphis, P. syringae* and *P. fluorescens* (Barelmann et al. 2003, Owen & Ackerley 2011, Hannauer et al. 2012). This siderophore may play an important role in the rhizosphere of tomato plants, increasing iron acquisition and improving plant health and growth (Nagata et al. 2013). Chrysobactins are siderophores produced by a plant pathogen, *Dickeya chrysanthemy* (Sandy & Butler 2011). As previously discussed, they can be cyclic but also linear (linear trichrysocabtin and dichrysobactin) and they contain catechol, lysine, serine and DHB, and are therefore refer to as a catecholamide siderophores.

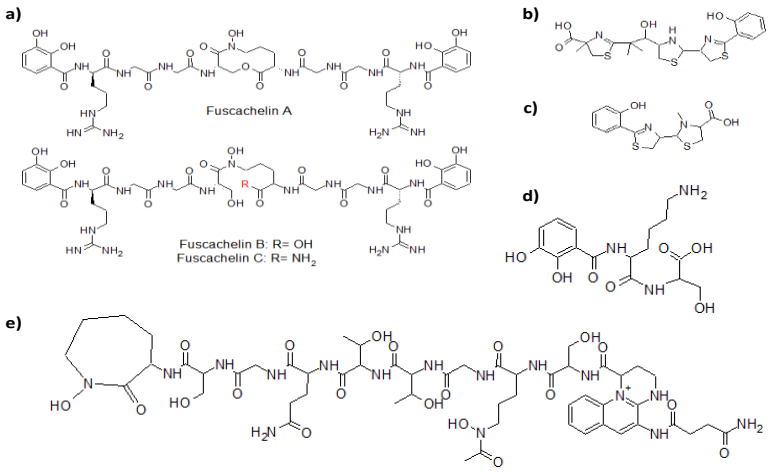

Figure 1.11. Siderophores produced by pathogenic bacteria: fuscachelins A-C (a), yersiniabactin (b), pyochelin (c), chrysobactin (d) and pyoverdine (e). Adapted from Sandy and Butler (2009) and Crosa et al. (2004).

Siderophores Found in Freshwater

Anabaena cylindrica is a freshwater cyanobacterium that produces anachelins (Figure 1.12) as siderophores (Ito et al. 2004). They are composed of amino acids and modified catechols. Another aquatic bacterium, *Alcaligenes xylosoxidans*, produces a siderophore called alcaligin (Nishio et al. 1988, Nishio & Ishida 1990). The siderophore is a cyclic hydroxamate type and it has been also found in some human pathogenic bacteria like *Bordetella pertussis* (Nishio & Ishida 1990, Moore et al. 1995). There have been other studies on freshwater siderophores that have shown the presence of siderophore-dependent iron acquisition systems but further work to elucidate their structures should be done (Naito et al. 2004, Wang et al. 2010, Silva-Stenico et al. 2011, Guan et al. 2013).

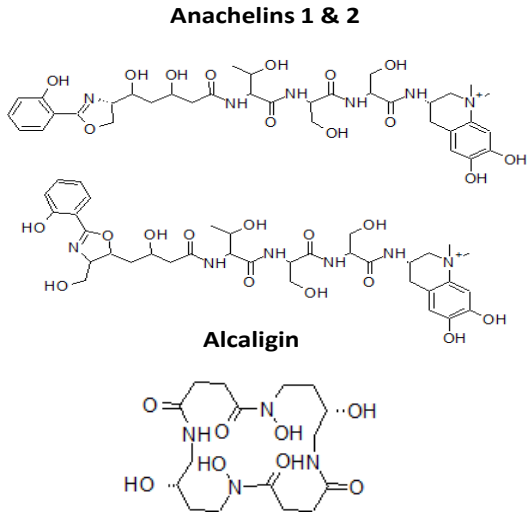

Figure 1.12. Siderophores produced by freshwater cyanobacteria. Adapted form Crosa et al. (2004) and Ito et al. (2004).

Amphiphilic Siderophores
Produced by other Microorganisms

Several amphiphilic siderophores are produced by non-marine microorganisms. *Herbaspirillum seropedicae*, which is an endophyte of wheat, rice, corn and sorghum, produces serobactins (Rosconi et al. 2013). Serobactins (Figure 1.13) are amphiphilic siderophores with three molecules that differ in the length of the fatty acid moieties (C10-C14) and their polar head group is composed of 6 amino acids. Other groups have identified cupriachelins (Figure 1.13) as iron-chelating amphiphiles (Kreutzer et al. 2012). This siderophore is produced by the bioplastic producer *Cupriavidus necator* and, as with some of its marine counterparts, it is photoreactive. The molecular structure is mainly composed of five amino acids and a C-10 fatty acid tail. Another environmental bacterium, the nitrogen-fixing *Cupriavidu taiwanensis*, produces taiwachelin (Kreutzer & Nett 2012). It has a C12 fatty acid moiety attached to the N-terminus of a hexapeptide and its structure was elucidated by genome mining and spectroscopic studies.

Some amphiphilic siderophores from pathogens have been characterized. Mycobactins are siderophores produced by *Mycobacterium tuberculosis* (White & Snow 1969). The siderophore suite is composed of 4 mycobactins differing in their fatty acid length (C14 to C20). They have been found to efficiently extract intracellular macrophage iron playing an integral part of *M. tuberculosis* pathogenesis (Luo et al. 2005). In addition, other mycobacteria produce amphiphilic siderophores similar to the mycobactins. This are called carboxymycobactins and are produced by *M. smegmatis* (Ratledge & Ewing 1996). Its major structural change is a shorter fatty acid moiety (C8) capped with a carboxy group at the end. Some common siderophores precursors, like acyl-pyoverdine, are amphiphilic in nature (Hannauer et al. 2012). The acyl chains of this precursor in *P. aeruginosa* are myristic or myrystoleic fatty acids. Other siderophores

with amphiphilic characteristics are the ornibactins (Stephan et al. 1993). Their basic structure is composed mainly of a tetrapeptide (L-Orn-D-Asp-L-Ser-L-Orn) attached to a fatty acids varying in lengths (C4, C6 and C8). They were first discovered in *Pseudomonas cepacia* (known now as *Burkholderia cepacia*) which is involved in cystic fibrosis microbiome (Lewenza et al. 1999). Other Burkholderiales produces ornibactins as well, like *B. vietnamiensis*, but this one in particular was isolated from the rice plant rhizosphere (Meyer et al. 1995). Also *Pseudomonas aeruginosa* is a producer of ornibactins when is iron starved (Stephan et al. 1993). Please refer to Figure 1.13 for several structures of previous siderophores discussed here.

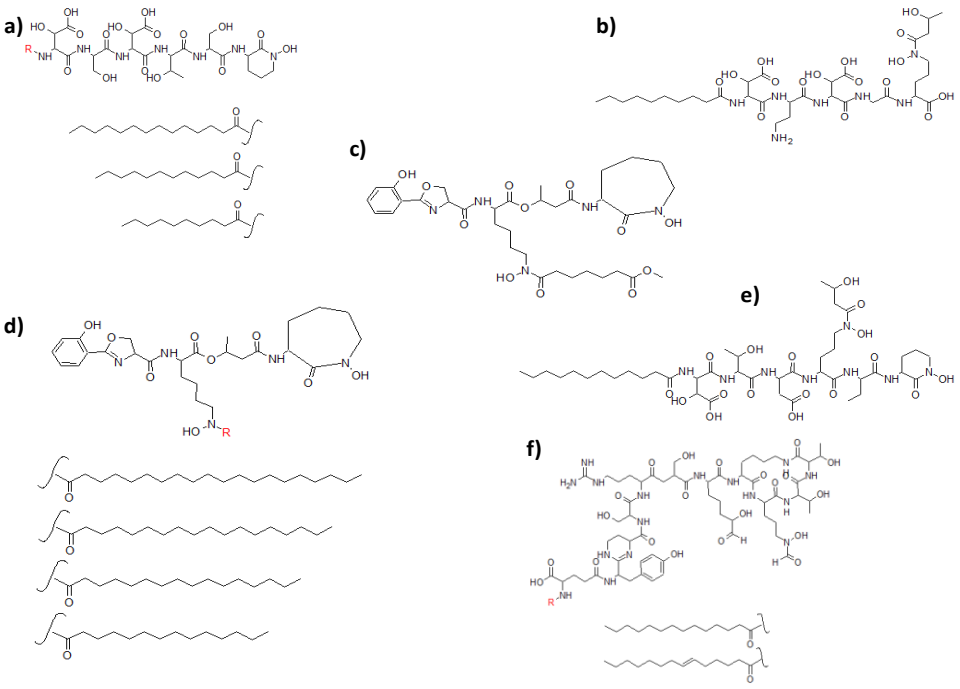

Figure 1.13. Amphiphilic siderophore isolated from environmental samples other than marine: serobactins (a), cupriachelin (b), carboxymycobactin (c), mycobactins (d), taiwachelin (e) and acyl pyoverdine precursors (f). Adapted from Sandy and Butler (2009), Kreutzer et. al. (2012) and Kreutzer and Nett (2012).

Biotechnology of Siderophores

As discussed previously, iron plays an important function in different cellular processes. It is involved in DNA metabolism, protein function, fatty acid synthesis and other chemical reactions. This is observed at all levels of the tree of life (from prokaryotes to eukaryotes). In humans, iron at higher concentrations than normal could become toxic by increasing oxidative stress, causing myocardial malfunction and inflammation responses to the pancreas (Sampaio et al. 2014). Other studies have suggested damages to adipose tissue and liver of obese persons (Fernandez-Real & Manco 2014). Different treatments for iron overload have been studied and they include the use of insulin, ferritin, transferrin and hepcidin. Also iron is well known to be required for plant nutrition, development and health (Geetha & Joshi 2013, Mishra et al. 2014, Rastogi et al. 2014). Photosynthesis and chlorophyll biosynthesis are affected at low iron concentrations hindering plant growth (Schurmann 1966, Machold 1971). Because of the important effects of iron at the medical, environmental and agricultural levels, scientists have studied the role of siderophores for biotechnology purposes. Agricultural, environmental, bioremediation and medical aspects of siderophore biotechnology will be discussed below.

Plant Growth and Biocontrol of Pathogens

Scientists have researched different aspects of iron and siderophore applications for agricultural purposes. The main focus is on the natural potential of using siderophores to help concentrate the natural iron source found in soil. For example, endophytes use siderophores as a key component to improve plant iron uptake from soil and also help in the production of indole-3-acetic acid, which is a plant growth hormone (Rout et al. 2013). Bacterial endophytes from invasive *Sorghum* sp. changed the

rhizobial population of native plants allowing the former to improve its survival rate. Also it was noticed that horizontal transfer of the rhizome population occurred. Simple plants, as bryophytes (moss) from the species *Racomitrium japonicum*, benefited from their rhizobia due to inhibition of pathogenic fungi and plant growth enhancement (Tani et al. 2011). Researchers in this study identified three major species that were involved in moss rhizobia composition: *Pseudomonas*, *Rhodococcus* and *Duganella*. Rhizobia siderophore production was confirmed in the study. The potential use of rhizobia as biofertilizers was studied, presenting a good way to improve moss growth and create an industry for green roofs.

There are siderophores that, in a clinical manner, can be detrimental to the host in bacterial infections but in other settings could potentially be beneficial. An example of this is the production of pyoverdine by *Pseudomonas fluorescens* (Nagata et al. 2013). In this report, it was found that pyoverdine production enhanced iron nutrition of tomato plants (Strategy I plants, which cannot produce pyoverdine). Strategy I plants use proton extrusion to increase their ferric iron uptake. When researchers compared ferrous iron and pyoverdine supplementation a significant accumulation of ferric iron in roots and leaves was detected. Also, plants showed better growth when supplemented with ferric iron and the siderophore than with just ferric iron alone due to an increase in leaves and plant weight. Molecular biology tests for ferric-chelate reductase and iron-regulated transporter genes showed decreased expression. Pigment (chlorophyll, carotenoids and anthocyanin) production was restored to levels of ferrous iron-treated plants. Thus, *Pseudomonas*-produced pyoverdine could potentially be used as a biofertilizer component. Another report examined siderophore production and its application on wheat harvest (Gull & Hafeez 2012). Several strains (14) of siderophore producers were evaluated for biocontrol purposes against *Rhizoctonia solani*, a plant fungal pathogen

and develops in both cultured and non-cultured soils. It infects mostly seeds and during plant growth causes damping-off and root rot. From the 14 isolates studied, Mst 8.2 showed more inhibition of the fungal pathogen radial growth by two different assays (round circle and spot inoculation assays), reducing it by 41 and 71 %, respectively. The strain also produced several antibiotics, chitinase and protease, essential metabolites that play a role in its antifungal properties. Wheat plants seeds treated with Mst 8.2 bacterial suspensions showed root rot lesion reduction and enhanced plant growth. After 16S rRNA sequencing, strain Mst 8.2 was found to be related to *Pseudomonas fluorescens*. Another rhizobacterium, *Alcaligenes faecalis*, associated with the groundnut rhizosphere was found to produce siderophores (Sayyed et al. 2010). Inoculation of this microorganism enhanced several plant growth characteristics, like seed germination, root length, shoot length and chlorophyll content.

Nabti and co-workers (2014) studied the beneficial rhizobacterium *Cellulosimicrobium* sp. and its barley growth-promoting traits. This bacterium produced several antibiotics, siderophores and enzymes necessary for soil colonization. It inhibited growth of several fungal pathogens of barley: *Botrytis*, *Fusarium* and *Verticillium*. Therefore it has potential as an inoculant and biocontrol agent. Also some *Bacillus* species are found to be plant growth promoting bacteria (Ravari & Heidarzadeh 2014). Root and plant weight improved in bacilli-treated wheat plants and siderophore-producing bacilli were the best performers. However, no siderophore mutants were prepared to confirm that siderophore production is linked with plant growth and health.

Bacillibactin has been also studied as a siderophore with potential uses in agriculture as a biocontrol agent (Woo & Kim 2008, Yu et al. 2011). In the Yu and co-workers study, siderophore-producing *Bacillus subtilis* inhibited *Fusarium* wilt disease and enhanced plant growth in peppers. However, iron supplementation helped the

fungal pathogen in colonizing the plant even if the beneficial, siderophore-producing microbe was present. Also Woo and Kim showed that this siderophore can be a good biocontrol agent of the red pepper blight pathogen *Phytophthora capsici*. This demonstrates the potential use of bacillibactin as a biocontrol agent and an enhancer of plant growth. Siderophores enhance iron solubilization and this was confirmed by a study with *Acinetobacter calcoaceticus* (Zhao et al. 2014). The bacterium degrades the phosphate pesticide chlorpyriphos, helping in phosphorus solubilization to the plant, and produces siderophores that enhance plant growth. Another example of biocontrol by siderophore production and iron availability and sequestration was studied on a strain isolated from the plant *Arisaema erubescens* (Lin et al. 2013b). The strain was identified as *Bacillus atrophaeus* by molecular techniques and produced siderophores. Siderophore extracts prevented the growth of the cotton wilt pathogen *Fusarium oxysporum*. As the literature shows, several siderophores or siderophore producing microorganisms could be implemented in biofertilizers uses, rhizobial inoculations, sprays and biocontrol agents to benefit important crops for human consumption.

Potential Bioremediation Uses

Bioremediation is the utilization of organisms to clean-up contaminated sites, like soil, water, oceans etc. Several heavy metal contaminants can be found in soil and bodies of water sediments, including lead, nickel, copper, cadmium, zinc and chromium (Gao et al. 2014). Other heavy metals include arsenic, strontium, and titanium (Baceva et al. 2014, Gbadebo & Ekwue 2014). Most of these heavy metals are detrimental to living organisms but bacterial community analysis has shown that microorganisms can grow in the presence of these contaminants (De Souza et al. 2007, Zhu et al. 2013). Other bacterial species tend to grow in environments contaminated with petroleum-

based oils or radionuclides (Gadd 1996, Farkas et al. 2000, Lin et al. 2013a). Some examples of bioremediation of heavy metals and radionuclide mobilization by siderophore and siderophore-producing microorganisms will be discussed below.

The ideal sites to isolate strains that will have the potential of metal transformations are mines. An example is the study of copper mines and how the extracted ore could be used as the sole energy source for isolate growth (Matlakowska & Sklodowska 2009). The Lubin copper mine was studied and isolates from different genera (*Microbacterium*, *Acinetobacter*, *Bacillus* and *Pseudomonas*) were obtained. Multi-resistance to copper, arsenic, nickel and zinc was confirmed in the study. In another study, Nair and co-workers found a direct role of siderophores in arsenic soil decontamination (Nair et al. 2007). The siderophore was produced by *Pseudomonas azotoformans* and FTIR studies revealed hydrogen bonding formation between the siderophore and arsenic. Arsenic removal by the molecule was 92.8 % compared to citric acid and EDTA (70 and 77.3 %, respectively). The study didn't check for concentration-wise removal characteristics that will reveal more information about the process and the potential of siderophores as bioremediation agents. However bioremediation by siderophores, or siderophore-producing microorganisms, may be more complex. A study using siderophore producing *Pseudomonas aeruginosa*, *Pseudomonas fluorescens* and *Ralstonia metallidurans* showed that rhizobial inoculation with these species to maize plants increased the phytoremediation of chromium (Cr) and lead (Pb) (Braud et al. 2009). Siderophore production and cell growth increased with the use of skim milk and calcium alginate beads. Another microorganism, *Staphylococcus arlettae*, also is responsible for chromium (VI) reduction and its bioremediation from industrial effluent samples (Sagar et al. 2012). Chromium removal was at the 98 % in

120 h and plant growth effects were tested on common wheat plants showing shoot and root length improvement.

Radionuclides present a contamination problem especially with industrial, mining, weapons testing and nuclear energy demand and related accidents (like Chernobyl and Fukushima). There is evidence of radionuclide immobilization by microorganisms (Gadd 1996, Farkas et al. 2000, Edberg et al. 2010). As demonstrated in the literature and previous research siderophores can be used as bioremediation agents to immobilize radionuclide and heavy metals. The results may vary due to concentration of the siderophore, solubility, bioavailability of the metal or radionuclide and several environmental conditions like pH, electron potential and ionic strength (Gadd 1996). In brief, a radionuclide phase (water soluble or insoluble) is changed by microbial metabolism (biotransformation) avoiding further contamination of the ecosystem. Uranium removal from mine ore was assessed in a study published by Edberg and co-workers (Edberg et al. 2010). They noticed that pyoverdine from *P. fluorescens* has the potential to reduce uranium and decrease its water solubility. Iron solubility was also reduced but this could be also done abiotically by the formation of iron oxides ($Fe(OH)_3$). Farkas and colleagues (2000) determined that some bacterial isolates from a mine to be considered for a nuclear waste repository were siderophore producers and radiotolerant. Polonium (Po) and protactinium (Pa) have been found to be chelated by hydroxamic siderophores from marine bacteria (Chuang et al. 2013). Other researchers proposed the use of siderophores for plutonium phytoremediation at the Savannah River Site (Demirkanli et al. 2009). Another radionuclide studied by researchers was uranium and its immobilization by desferrioxamine B, a medically relevant siderophore (Wolff-Boenisch & Traina 2007). In brief, uranyl was desorbed from kaolinite when the

siderophore concentration was about 100 μM. This effect was not only due to desorption capabilities of desferrioxamine B, but also by neutral species formed.

Some evidence of petroleum-degrading bacteria and siderophore production has been published (Barbeau et al. 2002, Yasumoto-Hirose et al. 2006). Barbeau and colleagues isolated the petroleum-degrading bacterium *Marinobacter hydrocarbonoclasticus* and studied petrobactin, a siderophore produced by it. No studies on how siderophore affects oil-degrading capabilities or mechanisms were done but it was inferred that this molecule helps in iron acquisition from the petroleum. Other oil-degrading species like *Vibrio* sp. isolated from the Gulf of Mexico (Deep Water Horizon oil spill) produced siderophores (Gauglitz et al. 2012). The ochrobactins may be involved in the metabolic characteristics of this petroleum-degrading microorganism. Lin and co-workers isolated an oil-degrading bacteria, *Pseudomonas sagittaria*, from contaminated oil and it produced siderophores (Lin et al. 2013a). No structural studies were done to determine of the type of siderophore functional groups present. Also no studies correlated siderophore production with oil-degrading activity. Although there is no direct evidence of petroleum degradation by siderophore-producing bacteria, the potential for this is suggested and more studies should aim to discover this relationship.

Pharmacological and Medical Applications

Metabolites produced by bacteria, or microorganisms, have the potential to serve as pharmacological targets (biomarkers) or have therapeutic effects. In this section the focus will be mainly on how siderophores can be used or applied to solve different diseases or help to develop diagnostic tests to improve human health. The first and most studied aspect of siderophore biotechnology is the treatment of iron overload caused when transfusion happens due to non-hemorrhagic conditions (Moeschlin & Schnider

1963, Norman 1964). Desferrioxamine B, a siderophore produced by the bacteria *Streptomyces pilosus*, has been used in different cases of iron poisoning, confirming its biotechnological potential (Nuesch et al. , Kobayakawa & Kodani 2012). Deferrioxamine does not chelate only ferric (Fe^{+3}) but also ferrous (Fe^{+2}) iron (Goodwin & Whitten 1965). Bergeron and colleagues decided to modify desferrioxamine structure starting from the premise that a low molecular weight molecule could function better as a pharmacophore (Bergeron et al. 1992). The structural modification caused a differentiation in the lipophilicity of the molecule when compared to the parent molecule chelator. Other synthetic heteropodate iron and metal chelators have been developed and eventually could have some medical applications (Cohen et al. 2000).

Siderophore antimicrobial properties have been also previously discovered. One of the first key studies was one in which *Azospirillum lipoferum* was found to produce siderophores (Shah et al. 1992). This microbe associates with different plant rhizospheres and promotes nitrogen fixation. To determine siderophore antmicrobial properties extracts were tested against different bacterial and fungal species. Bactericidal action was on cowpea *Rhizobium* species, *Azotobacter*, *E. coli*, *S. marsecens*, *S. aureus* and *Bacillus*. Fungicidal activity was on *Rhizoctonia*, *Fusarium oxysporium*, *Aspergillus niger*, *A. sydowii*, *A. variecolor* and *Penicillium funiculosum*. In a similar study, isolates (258) from two cenotes environmental samples were studied for interspecies interactions and antimicrobial properties (De la Rosa-Garcia et al. 2007). A representative fraction of the isolates (13%) showed antimicrobial properties due to siderophore production. Most of the antimicrobially active isolates were identified in the genera *Aeromonas, Bacillus, Burkholderia, Photobacterium, Pseudomonas, Serratia, Shewanella and Stenotrophomonas*. Some microorganisms like cyanobacteria from either terrestrial or freshwater environments have been found to produce siderophores

with potential biotechnological applications (Silva-Stenico et al. 2011). The study showed that extracts from cyanobacteria isolates that produced siderophores (aeruginosins) have antimicrobial properties. Also other toxins and antimicrobial agents were produced by them, including microcystin and cyanopeptolin. Antimicrobial properties were found also in a bacterial species, *Stenotrophomonas maltophilia*, and it was also a siderophore-producing bacteria (Minkwitz & Berg 2001). This microorganism has become very important for biotechnological purposes and also for its increasing role in nosocomial infections. Researchers studied 50 environmental and clinical *S. maltophilia* isolates and their inter-species interaction. Antifungal activities against the human pathogen *C. albicans* were detected more on environmental isolates which produced siderophores and antibiotics.

Another application for siderophore biotechnology is antimicrobial conjugates. In this application the siderophore of interest is attached to an antibiotic and used as a "Trojan horse" to serve as a drug delivery agent (Ghosh & Miller 1993, Miller 1995, Mollmann et al. 2009, Miller et al. 2011). This approach facilitates antibiotic transport throughout the membrane using siderophore receptors. Two arthrobactin-carbacephem conjugates were developed and *E. coli* was treated at 10 μM (Ghosh & Miller 1993). Bacterial growth was affected by the siderophore-antibiotic conjugates and the effect was enhanced if an iron chelator (EDDA) was added to the media. Siderophore-β-lactam conjugates have also been of interest (Kline et al. 2000). Cephalosporin conjugated to a siderophore was tested against different pathogenic bacteria including *E. coli*, *P.aeruginosa* and *S. aureus*. Artificial siderophores have been developed and their antimicrobial properties when conjugated with a carbacephalosporin (Lorabid) have been studied (Minnick et al. 1992). Treating simultaneously with hydroxamic and catechol siderophore conjugates decreased bacterial growth. Other molecules of interest

are the sideromycins, linked with either Lorabid or ciprofloxacin (Wencewicz et al. 2013). The first conjugate attacks the periplasm and the later one the cell wall. The sideromycins effectively inhibited growth of *S. aureus*. Another siderophore conjugate complex studied was pyochelin-norfloxacin (Rivault et al. 2007). Analogues of the siderophore were synthesized and linked to norfloxacin (antibiotic). Antimicrobial activities were tested on *Pseudomonas* and two of the four conjugates were effective against the pathogen. Another example of siderophore analogs is the vanchrobactin-norfloxacin conjugate showing antimicrobial activities against *Vibrio anguillarum* and its mutants (Souto et al. 2013). However, there is evidence that some siderophore-antibiotic conjugates improve bacterial growth. Spermexatol-carbacephalosporin conjugates showed no effects on *Mycobacterium smegmatis* (Mollmann et al. 1998). A common situation is when *in vivo* and *in vitro* studies do not correlate to each other, making the solution process cumbersome. An example of this is a siderophore-monobactam compound, MB-1, that was studied for its potential in *P. aeruginosa* growth inhibition (Tomaras et al. 2013). *In vitro* and *in vivo* assays did not correlate and this may be due to native siderophore competitors.

Siderophores may be used to develop vaccines and this has been reviewed extensively (Kingsley et al. 1994, Fernandez et al. 2007, Garenaux et al. 2011). Bergeron and colleagues reported the use of a vibriobactin analogue linked to either ovalbumin (OVA) or bovine serum albumin (BSA) and their ability to promote antibody production in mice (Bergeron et al. 2009). The immune response was detected and IgG antibodies for BSA and OVA were isolated from mice plasma. Other reports showed the use of the iron transport receptors in bacterial pathogens as important components of vaccines. Siderophore receptors and porin proteins from *E. coli* O157:H7 were evaluated on cattle (Fox et al. 2009). Two and 3 mL doses of the vaccine were injected

subcutaneously and prevalence of *E. coli* O157:H7 was reduced in both treatments, but the 3 mL dose obtained fewer days of the cattle being positive for *E. coli*. In another case, the FhuD receptor of *S. aureus* was analyzed as a potential vaccine component (Mariotti et al. 2013). FhuD-ferrichrome was used as the model vaccine antigen and was determined to have potential because of its lack of conformational changes.

There is also the potential to use of siderophores as radiopharmaceutical imaging agents. Petrik and colleagues demonstrated clinical use in imaging pulmonary aspergillosis (Petrik et al. 2012). Mouse and rat infection models were developed and siderophores (triacetylfusarinine and ferrioxamine E) were labeled with gallium 68 (^{68}Ga). In both models with iron-deficient conditions, *A. fumigatus* absorbed both of the siderophore-radionuclide conjugates. There was rapid excretion by the renal system in normal mice. Conjugate accumulation in the lungs was observed in the rat model by positron emission tomography (PET) and increased with the severity of infection (correlating with CT images). An important point that was not discussed in this paper is how fungal growth could be affected by these conjugates.

Concluding Remarks

Iron is ubiquitous in the environment and it is required by most living organisms. It is not bioavailable due to its poor solubility in water, but microorganisms have developed iron acquisition systems to overcome this problem. Siderophore production and respective receptors and transport proteins are part of that system and they help obtain iron from the extracellular environment in iron-limiting conditions. In general, three different functional groups form the siderophore molecule: hydroxamic acids, catechols and α-hydroxycarboxylic acids. These groups help coordinate the ferric iron ion and then the siderophore-iron complex is recognized by receptors on the cell membrane,

internalized and transported by periplasmic binding proteins and active transport proteins into the cytoplasm. Different structures (from linear, to bi-dentate or tri-dentate, to amphiphilic) are found in different environments including marine, terrestrial, freshwater, soda lakes etc. The amphiphilic property in siderophores makes them candidates to form micelles and vesicles upon iron chelation. Siderophores help maintain the equilibrium of iron on the environments.

The different biotechnological uses for siderophores are limitless. It is important to note that these applications vary (clinical, agricultural, and environmental), each one has their own requirements for treatment, and one should be aware of them to pursue the desired applicability. In clinical (medical/pharmacological) applications, more caution needs to be taken due to eventual human uses and the need to avoid recalls of the drug or pharmacophore. Therefore, more studies should be done on how siderophores are absorbed, distributed, metabolized and excreted in humans. Some precautions with siderophore-based biocontrol strategies in human consumption crops, like: avoiding cross-contamination with the bacteria or the siderophore. Bioremediation using microorganisms could be relaxed in terms of its applicability if the contaminated site is not close to subterranean water sources, rivers, lakes or the ocean. Avoiding bacteria or any of their cellular components leaching from the site to sources of water is a key of biosafety measure to be considered. In siderophore and phytoremediation-based treatments particular attention should be paid to the correct disposal of the plants. However, the use of well scientific approaches, experimental designs and taking biosafety into consideration would help develop good siderophore biotechnology for the benefit of human beings and the environment.

CHAPTER TWO

SIDEROPHORE PRODUCTION STUDIES DUE TO DIFFERENT PHYSIOLOGICAL CONDITIONS OF HALOALKALIPHILIC ISOLATES FROM SOAP LAKE, WA

Introduction

The requirement of iron for living cells makes its acquisition a very important process for survival. Iron, especially its ferric form, it is at low concentrations (~10^{-18} M) at neutral pH. This is due to the low solubility and the formation of $Fe(OH)_3$ (Crosa 2004). To overcome the low bioavailability of iron, cells have developed different complex iron uptake systems. Among these systems is the production of siderophores, or iron chelators. Several proteins and receptors play an integral part in siderophore synthesis, transport and up-take. The type of siderophore molecules produced has been discussed in the previous chapter. The main objective of this chapter is to describe and characterize the effects of different environmental variables on *Halomonas* sp. SL01 and SL28 growth and siderophore production.

To detect siderophores in solution the CAS assay is employed. The assay has been a basic, easy to use and fast method described previously by Schwyn and Neilands (Schwyn & Neilands 1987). The solution is composed by the chrome azurol S, ferric iron and HDTMA. Poor coordination of ferric iron by chrome azurol S and HDTMA causes an immediate transfer of this ion to higher affinity molecules (e.g. siderophores) and a change in color (dark blue to orange) in the solution happens. Also, this assay can be employed not only in liquid media but in agar plates as demonstrated in previous work (Schwyn & Neilands 1987); (Oliveira et al. 2006, Martinez & Butler 2007, Bertrand et al. 2009, Rosconi et al. 2013) and in this chapter.

However, other methods of siderophore detection have been employed. Some are chemical assays that require the use of advanced instruments (Thieme et al. 2012, Boiteau et al. 2013) and others are biological-based (Bossier & Verstraete 1986). In the work done by Boiteau and co-workers, they used reverse phase high-performance liquid chromatography coupled with mass spectrometry (RP-HPLC/MS). Sample analysis was done and the detection limit was determined to be as sensitive as 1 pM. The method was sensitive to changes in the mobile phase and sample composition as well. The other group (Thieme and co-workers) presented how near edge X-ray absorption fine structure spectroscopy (NEXAFS) could not only detect siderophore presence in a sample, but also determine its spatial localization. As a model organism they used *Parmelia saxatilis*, a lichen, growing on hematite rocks. Ferrichrome and coprogen were detected by the spectroscopic method and the microscopy technique. A third approach is the bioassay method described by Bossier and Verstraete (1986). They used *Arthrobacter* JG-9 as an indicator of siderophore presence in soil samples. Their hypothesis was founded in that if siderophores were present in soil samples, the model microorganism will grow efficiently and reduce the amount of organic carbon present. Thus, total organic carbon (TOC) and siderophore concentration relationships were measured. Ferrioxamine B was used as a model siderophore for this bioassay.

Some problems can be found with these methods compared to the CAS assay. Although using mass spectrometry and HPLC can be of great help, the intensive training could hinder result discovery. Also, mobile phase composition could be troublesome; separation must be optimized to improve the detection process. Cost could be also an important factor when using PR-HPLC/MS or NEXAFS methods due to equipment prices and maintenance. Using a bioassay method could definitely present a labor intensive learning process as well as false positive results due to sample contamination. In this

chapter, siderophore detection using the CAS assay and physiological conditions experiments will study the effects of NaCl concentration, temperature and media pH on selected soda lake isolates growth performance and siderophore production.

Methods

Soap Lake Media (SLM) Preparation and Environmental Conditions:

The SLM growth media used in all the experiments was an artificial medium, similar in composition to Soap Lake, WA, where the biological strains (*Halomonas* SL01 and SL28) were isolated. For the physiological studies performed, different NaCl (Fisher) concentrations were used for both strains: 10.0, 50.0, and 100.0 g/L (representing in % w/v: 1, 5 and 10, respectively). Sodium pyruvate (Fisher) was the carbon source at 5.0 g/L. The other components of the media were: 1.12 g/L sodium borate, 1.0 g/L ammonium chloride, 0.06 g/L calcium chloride, 0.05 g/L magnesium chloride hexahydrate, 0.85 g/L sodium nitrate, 0.50 g/L potassium phosphate monobasic, 0.01 g/L potassium chloride and 0.25 g/L yeast extract. SL01 and SL28 strains were subjected to different temperatures and pH conditions as well. The temperatures studied were 37° C and ambient temperature (around 25° C). The pH values were adjusted at 8.0, 9.0, 10.0 and 11.0 with 10 N NaOH (Fisher Scientific). The media was treated with Chelex (200 mL bed volume, Sigma Aldrich) resin to eliminate iron traces and other metals that could be present. All media was filtered sterilized with 0.22 µm polyethylene sulfonate (PES, Nalgene) membrane filters.

Chelex Resin Activation:

Chelex resin was used to chelate iron from media. The resin was first activated by adding 2 bed volumes 1 N HCl (Fisher Scientific), then 5 bed volumes nanopure water, following 2 bed volumes 1 N NaOH and finalizing with 5 bed volumes of nanopure water. Then, the resin was mixed for 5 min with the SLM for its treatment.

Siderophore Detection in
Solution & Calibration Curve:

Stock solutions were prepared beforehand: (1) 10 mM HDTMA (Fisher); (2) iron solution: 1 mM $FeCl_3$•6H2O (Acros) in 10 mM HCl; (3) 2 mM aqueous chrome azurol sulfonate (CAS, Sigma) and (4) 0.2 M 5-sulfosalicylic acid (Fisher). Then the CAS assay solution was prepared by adding 6 mL of 10 mM HDTMA in a volumetric flask (100 mL) diluted with a bit of water. In that same flask, 1.5 mL iron solution and 7.5 mL of 2 mM CAS solution were added. Then in a separate flask, 4.307 g anhydrous piperazine (Acros) was dissolved in some water and 6.25 mL 12 M HCl were added. This buffer was rinsed into the volumetric flask with HDTMA, CAS and iron solution and volume completed with nanopure water.

To determine the presence and concentration of siderophores in solution, a 0.5 mL aliquot of siderophore solution or media supernatant (centrifuged at 12,000 g for 5 min, Eppendorf 5417C) plus 0.5 mL CAS assay solution were added to a cuvette. Then 20 µL 5-sulfosalicylic acid (or to a final concentration of 4 mM) were added. Absorbance of the solution at 630 nm was measured after equilibrium was reached (30 min-2 h, but no longer than 6 h). This absorbance value was then used in an equation obtained from the calibration curve using deferrioxamine B (DFB, Sigma) as a model siderophore. A 10 mM DFB solution was prepared and then diluted to 0.1 mM. From the former solution,

dilutions were made to create 50, 25, 20, 18, 15, 12, 10, 8, 5, 2, 1 and 0 μM DFB solutions.

Growth Culture Preparation and Sampling:

To prepare the growth cultures for the physiological studies, a frozen stock of the particular strain was thawed at room temperature. After thawing, the frozen stock volume (approximately 1 mL) was inoculated in 100 mL SLM in a baffled flask (Pyrex). A sterile control was also prepared in a disposable 50 mL tube (Falcon or BD). Then this starter culture and control were placed in the shaker incubator (140 rpm at room temperature or 37 °C; Infors HT Ecotron) and optical densities (OD, at 600 nm) and siderophore assays (CAS, at 630 nm) were done once a day.

Once the CAS absorbance readed about 0.100, 1 mL aliquots were transfered in to 3, 1 L baffled flasks, filled with 400 mL SLM. A sterile control flask was also prepared. Then the flasks were placed in the shaker incubator and OD and CAS readings (UV spectrophotometer, Spectronic Gensys 5) were taken every day until a maximum siderophore production was detected by corresponding dilutions. After this, media was ready for extraction of siderophores by ultracentrifuging (Sorvall Instruments RC5C; GSA rotor) at 6,238 g for 20 min at 4° C and processing the supernatant after that. This was repeated for SLM conditions of 10, 50 and 100 g/L NaCl, at 37° C or ambient temperature.

SLM and CAS Plates:

To check for culture purity, SLM plates were prepared and streaked. For SLM plate preparation, Noble agar (30 g/L, Difco) was dissolved and sterilized by autoclaving for 20 min at 121 °C in 500 mL nanopure water. Then, the agar solution was placed in a water bath at 60 °C. Soap Lake media was prepared as in Table 1, pH was adjusted and

the solution filtered sterilized with 0.22 µm membrane filter and placed in a water bath for 3 hours. When both solutions were at temperature (60 °C), 500 mL of SLM was poured in the Noble agar bottle and allowed to mix by magnetic stirring for 5 minutes. Finally, plates were poured in a laminar flow hood (Nuaire) solidified overnight. When growth culture was in stationary phase and siderophore production was detected, streaks of SLM plates were done.

CAS plates were prepared in a similar way to SLM plates. A CAS/HDTMA mix was prepared by first mixing chrome azurol sulfonate (605 mg), water (500 mL) and 1 mM $FeCL_3$ in 10 mM HCl (100 mL) together (Solution A). HDTMA (729 mg) was dissolved in water (400 mL) to form Solution B. Slowly, Solution A was added to B, providing gentle stirring to avoid foam formation. The resulting mixture was sterilized by autoclaving at 121 °C for 20 min and then placed in a water bath. Noble agar solution (500 mL, 30 g/L) was prepared and sterilized (in autoclave, then placed in water bath) and SLM (400 mL) was filter sterilized and placed in a water bath at 60 °C. SLM and CAS/HDTMA solutions were mixed with the Noble agar solution and plates were poured in a laminar flow hood and solidified overnight. Streak plates were done as a double verification for siderophore production and culture purity.

Siderophore Extraction:

For siderophore extraction, the C2 column (Varian) was first conditioned by treating it with methanol (5 mL, Fisher) and 5 mL nanopure water. After this point, the column was always kept wet and no air flowed through it. Otherwise, a new column was used.

To extract siderophores form the supernatant a 50 mL sample was run through the column (collecting in the waste beaker). Then the column was filled with nanopure water and this phase collected because some siderophores may be present. After this, the column was filled with methanol this phase collected in a second tube. This phase will have the majority of siderophores. For a second time the column was filled with nanopure water and an additional 5 mL collected in the waste beaker. The next 50 mL of sample was processed as previously indicated until no more supernatant (and first collected nanopure water) remained. Extracts were concentrated by evaporation centrifugation (at 50 °C, Labconco) for 2 h, stored at 4 °C and later purified by HPLC (Dionex).

Siderophore Purification and Lyophilization:

To purify the extracts a HPLC method was created. Briefly, two mobile phases were used: (A) water with 0.01% trifluoroacetic acid (TFA, Fisher) and (B) acetonitrile (Fisher) with 0.01% TFA. The mobile phase gradient was 10 to 70% B for 63 min. The injection volume was 500 µL and a C4 reverse phase column (4.6 mm ID X 250 mm, Grace) was used. The UV detection (AD20 absorbance detector) wavelength was set to 220 nm. The pump was an ICS-3000 and the column was placed in a CH-30 Eppendorf column heater. The interface was the UCI-50 Universal Chromatography Interface. Siderophore-containing fractions were collected, lyophilized overnight and stored (4 °C) for future characterization and tests.

Results

Siderophore Production & Growth: Strain SL01

Physiological environmental changes were applied to both strains (SL01 and SL28) to determine the response of growth and siderophore production. *Halomonas* sp. SL01 studies are presented first. At room temperature conditions (25 ºC), lag phases were not detected at 1 or 5 % (w/v) NaCl, showing rapid growth of this microorganism. In all NaCl treatments stationary phase was observed. In contrast, the 10 % (w/v) NaCl treatment showed a lag phase suggesting an adjustment period for isolate SL01. Following the lag, growth absorbance peaked and, as Figure 2.1 presents, was the highest of all salt treatments. Siderophore production was also affected by salt concentration (Figure 2.2). The best production was observed at 5 % (w/v) NaCl, followed by 10 and 1 % (w/v), in descending order. An important characteristic was that siderophore production was not observed after 40 h.

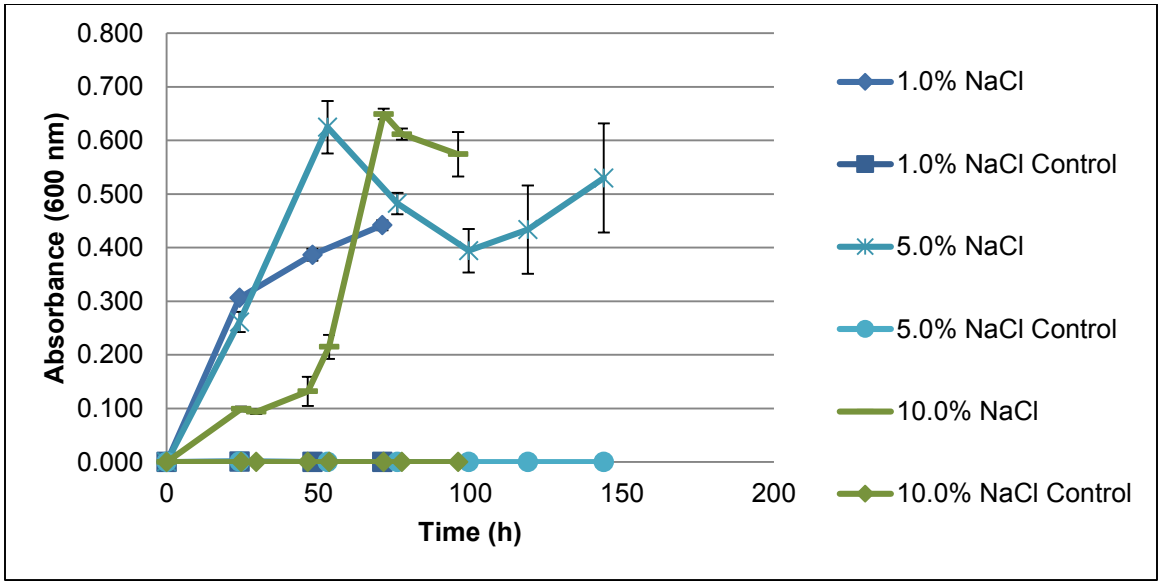

Figure 2.1. Growth of *Halomonas* sp. SL01 dependent on NaCl concentration at room temperature. Average results of triplicates with standard deviations (s. d.) are presented.

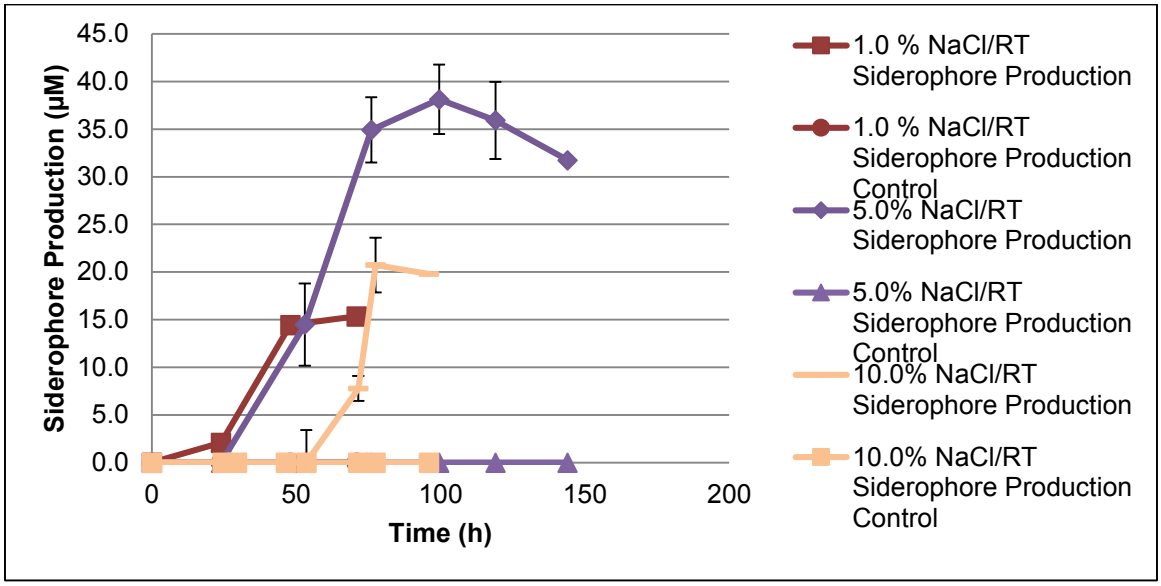

Figure 2.2. Siderophore production of *Halomonas* sp. SL01 dependent on NaCl concentration at room temperature. Average results of triplicates with standard deviations (s. d.) are presented.

At 37 ºC there are similar patterns in siderophore production and growth (Figure 2.3). When NaCl was at 1 % (w/v), the lag phase lasted more than 80 h and no log phase was observed. The 5 % (w/v) treatment shows an improvement in *Halomonas* sp. SL01 growth and there were defined log and stationary phases. The 10 % (w/v) NaCl growth curve also shows well defined log and stationary phases. In brief, at 37 °C and with higher salt concentration, higher growth and a shorter lag phase was observed.

Figure 2.4 shows how siderophore production at 37 ºC was affected by NaCl concentration in Soap Lake media. Siderophores were not produced at 1 % (w/v) salt concentration as per the chrome azurol sulfonate (CAS) assay. Siderophores were detected at the other treatments, with 5 % (w/v) yielding the highest concentration.

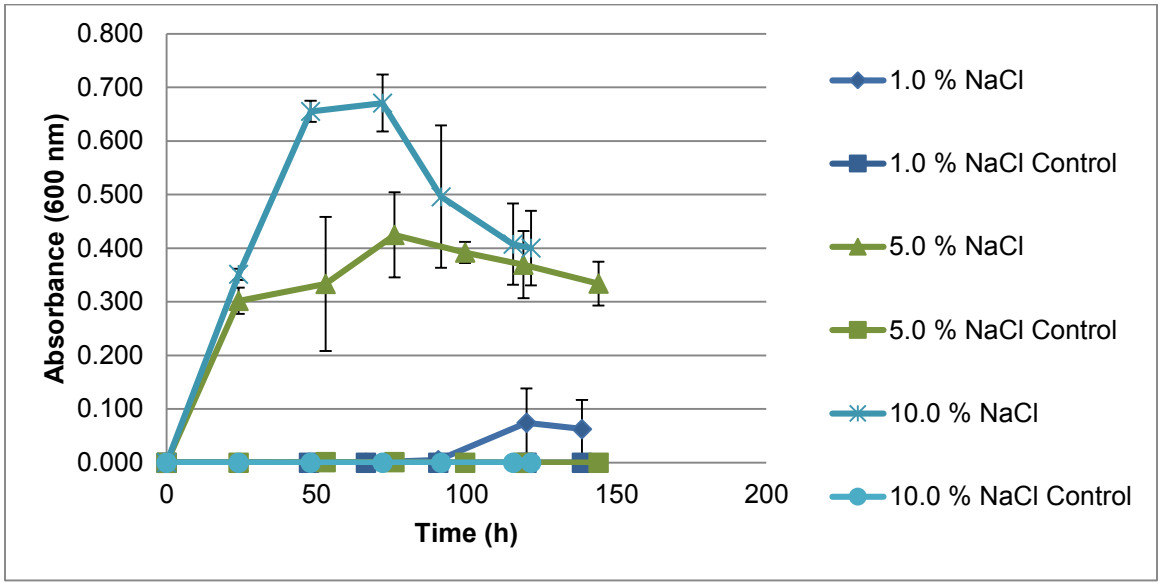

Figure 2.3. Growth of *Halomonas* sp. SL01 dependent on NaCl concentration at 37 ºC. Average results of triplicates with standard deviations (s. d.) are presented.

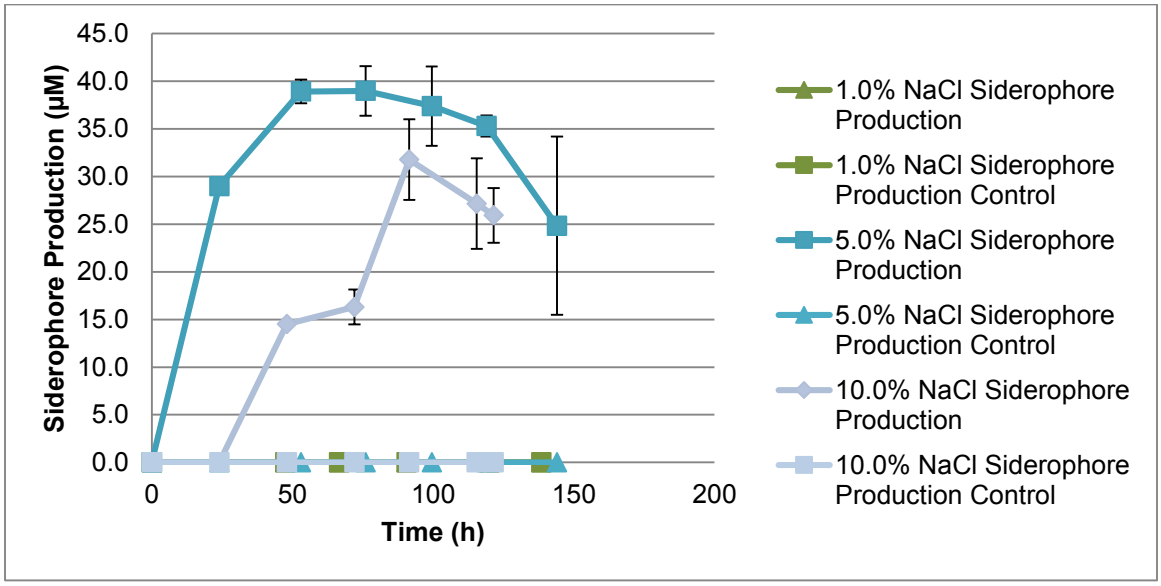

Figure 2.4. Siderophore production of *Halomonas* sp. SL01 dependent on NaCl concentration at 37 ºC. Average results of triplicates with standard deviations (s. d.) are presented.

Another important characteristic that the physiological studies showed was that growth was detected earlier than siderophore production. Figure 2.5 shows the pattern when *Halomonas* sp. SL01 was grown at room temperature and 5 % (w/v) NaCl SLM.

The siderophore curve shows a log phase, stationary phase and finally a decrease in concentration. Two possible scenarios could contribute to siderophore reduction in the media: (1) siderophores are being phagocytized by cells or (2) molecule denaturation is happening affecting its chelating properties. An example of that appears in Figure 2.6 when comparing the growth of the studied microorganism at the same salt concentration (5 % w/v NaCl) but different temperatures (room temperature vs. 37 °C). At 37 °C, *Halomonas* sp. SL01 has a reduction in siderophore concentration in solution when its growth starts to decrease as determined by optical density measurements. Also, at this higher temperature there is no lag phase for produced siderophores contrary to room temperature treatment.

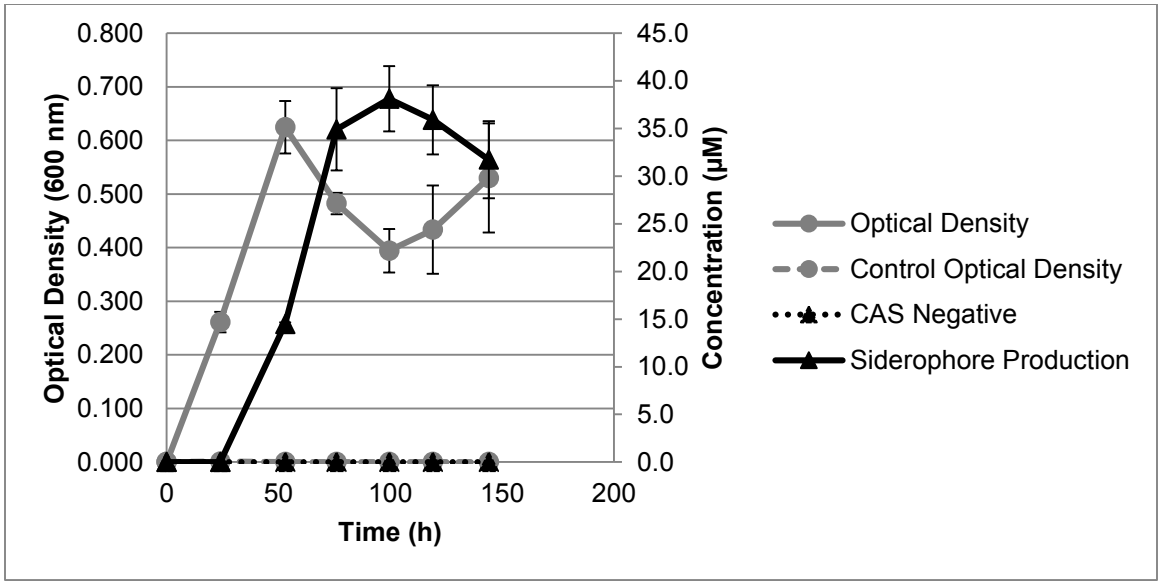

Figure 2.5. Growth and siderophore production of *Halomonas* sp. SL01 grown on 5 % (w/v) NaCl SLM, at room temperature. Average results of triplicates with standard deviations (s. d.) are presented.

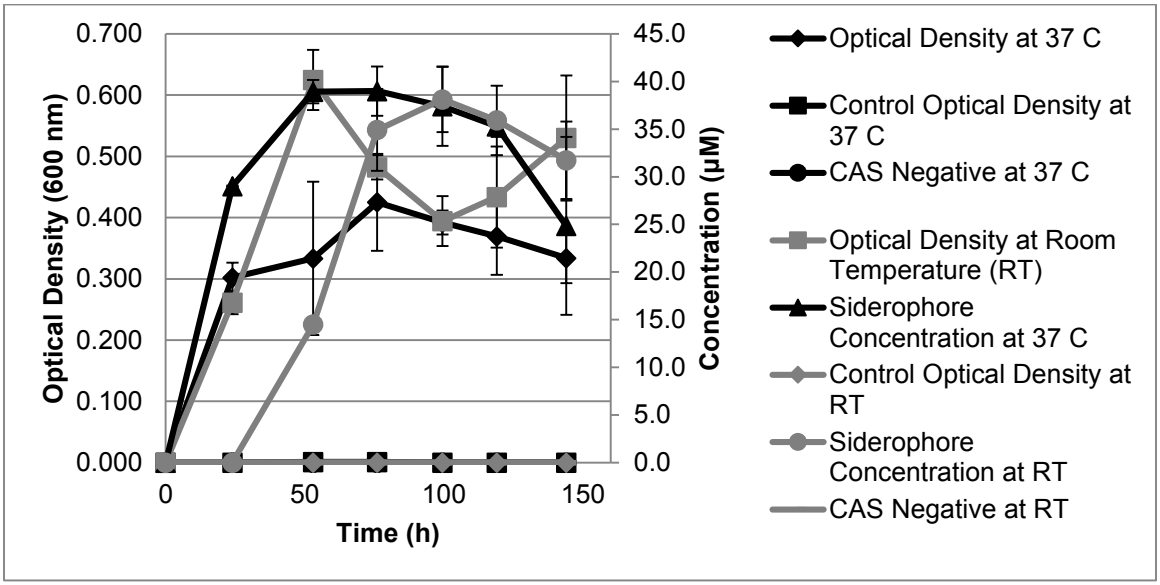

Figure 2.6. *Halomonas* sp. SL01 grown on 5 % (w/v) NaCl SLM, but different temperature. Average results of triplicates with standard deviations (s. d.) are presented.

In general the physiological studies of *Halomonas* sp. SL01 found that temperature may increase siderophore production but only when the right salt concentration is present in the environment. Figure 2.7 presents a histogram pattern for siderophore concentrations for both temperatures. It seems that for 5 % (w/v) NaCl, there is no significant difference in maximum siderophore production standard deviations at either temperature treatments. At 10 % (w/v), the higher temperature helps increase siderophore concentration in solution when compared to room temperature. However, the opposite happens when NaCl is at 1 % (w/v).

Siderophore Production & Growth: Strain SL28

For *Halomonas* sp. SL28 the results were different. Stock growth cultures were prepared to assess siderophore production at 37 °C. As noted on Table 2.1, no siderophore was detected by CAS assay at 1.0 and 5.0 % NaCl concentration. Growth was slow because optical densities were not increasing as fast as for strain SL01. At 5.0

% NaCl treatment, optical densities started at 0.133 after 20 h of growth, but in subsequent days, OD went down. A different pattern was observed at 10.0 % NaCl showing good growth and siderophore production. The concentration was similar to that of *Halomonas* sp. SL28 grown at the same salt concentration at room temperature (>10 µM, see Figure 2.8).

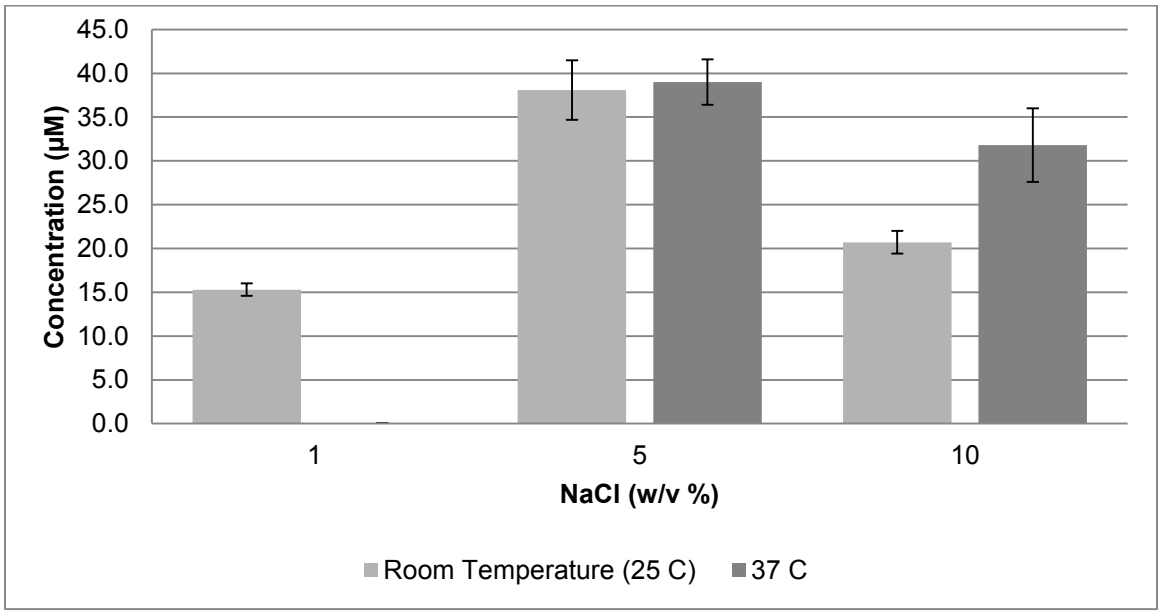

Figure 2.7. *Halomonas* sp. SL01 maximum siderophore production. Average results of triplicates with standard deviations (s. d.) are presented.

Because of lack of sufficient growth and siderophore production at 37 °C, studies at room temperature were performed. Figure 2.8 shows how growth was dependent on NaCl concentration, with the 10% (w/v) treatment the best in optical density (or growth). This pattern was similar to the one found in strain SL01.

Table 2.1. Siderophore production of *Halomonas* sp. SL28 stock growth cultures in SLM at 37 °C.

SL28 Stock Cultive	Time (h)	Optical Density		CAS Assay			
		Stock	Control	Stock	Negative Control	Siderophore Concentration (μM)	Negative Control Concentration (μM)
1.0 % NaCl	23.0	0.001	0.005	1.071	1.002	0.00	0.00
	46.0	0.041	0.001	0.999	0.996	0.00	0.00
	70.0	0.038	0.000	0.954	0.963	0.00	0.00
	94.0	0.042	0.001	0.96	0.976	0.00	0.00
	121.0	0.184	0.000	0.993	0.969	0.00	0.00
5.0 % NaCl	21.5	0.133	0.000	1.120	1.123	0.00	0.00
	29.5	0.043	0.000	1.126	1.126	0.00	0.00
	47.0	0.054	0.000	1.147	1.135	0.00	0.00
	74.0	0.066	0.000	1.151	1.132	0.00	0.00
	93.0	0.065	0.000	1.140	1.123	0.00	0.00
10.0 % NaCl	23.5	0.200	0.000	0.938	0.975	0.00	0.00
	47.5	0.568	0.000	0.812	0.964	3.6	0.00
	71.5	0.676	0.000	0.444	0.996	14.8	0.00
	124.5	0.674	0.000	0.476	0.971	13.9	0.00
	143.5	0.641	0.000	0.505	0.963	13.0	0.00

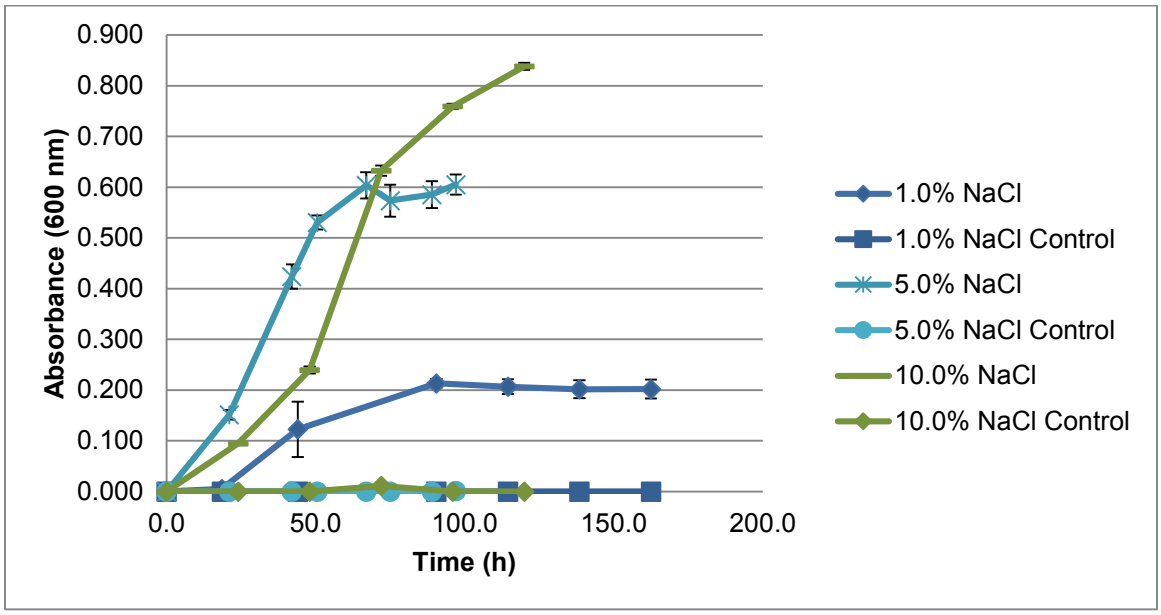

Figure 2.8. Growth of *Halomonas* sp. SL28 dependent on NaCl concentration at room temperature. Average results of triplicates with standard deviation (s. d.) are presented.

When measuring siderophore production at room temperature with the CAS assay, a dependency for salt concentration was found. As more NaCl was found in the media, siderophore concentration increased (Figure 2.9). At 1% (w/v), siderophore production was not noticed until 160 h of growth. When NaCl was increased to 5% (w/v), siderophores were produced (6.7 µM maximum) after 40 h of growth (48 h for 10% w/v NaCl at 12.3 µM). The pattern contrasts with results of *Halomonas* sp. SL01 (Figure 2.2), where the best NaCl concentration for siderophore production was at 5% (w/v). Thus, both strains behave in different ways, strain SL01 preferring less NaCl concentrations than strain SL28.

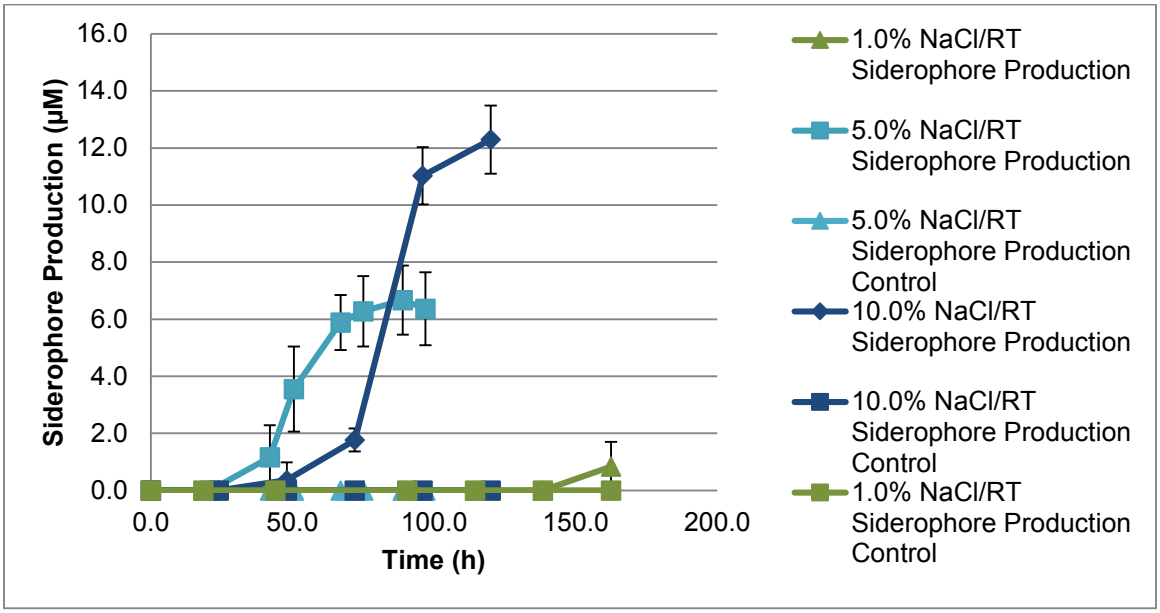

Figure 2.9. Siderophore production of *Halomonas* sp. SL28 dependent on NaCl concentration at room temperature. Average results of triplicates with standard deviations (s. d.) are presented.

Another similar result found for *Halomonas* sp. SL28 when compared to SL01 is the correlation between growth and siderophore production. Comparing growth and siderophore production (Figure 2.10), growth starts immidiately (gray diamonds) and reaches a stationary phase. There is a delay in siderophore concentration curve (black triangles). Concentration starts to increase rapidly after about 40 h of growth and by 70 h it reaches a plateau, few hours later than growth (just about 65 h). The pattern, or correlation, of growth and siderophore production was similar to the one found in *Halomonas* sp. SL01 (Figure 2.18), but strain SL01 produced more siderophore (38.1 µM) than strain SL28 (6.7 µM), at the same conditions.

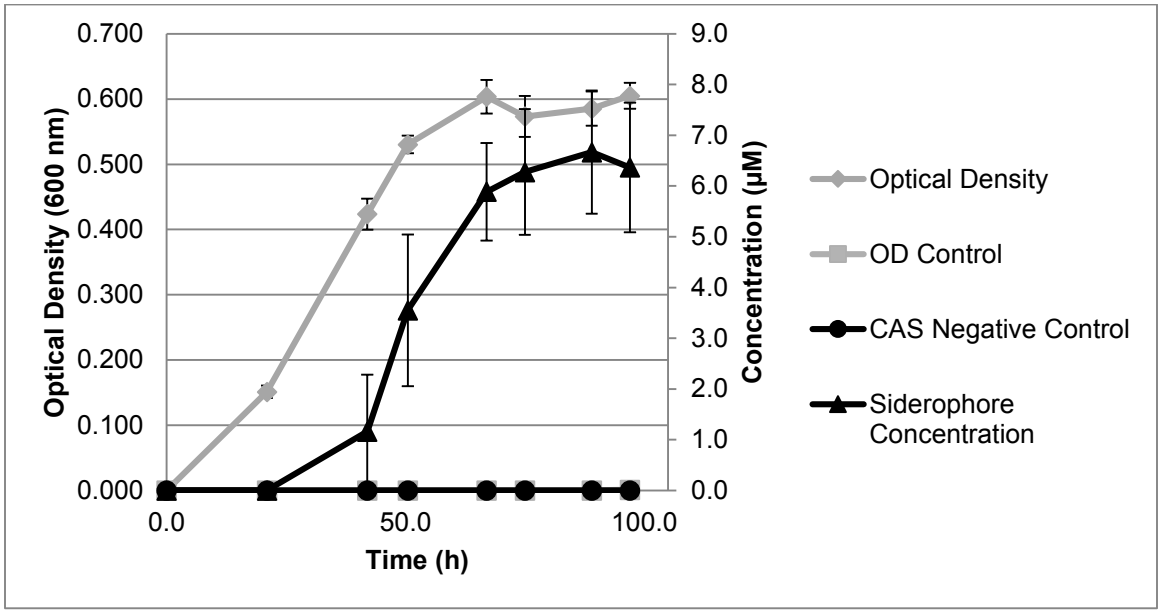

Figure 2.10. Growth and siderophore production of *Halomonas* sp. SL28 grown on 5% (w/v) NaCl SLM, at room temperature. Average results of triplicates with standard deviations (s. d.) are presented.

As in strain SL01, a maximum siderophore concentration was determined (Figure 2.11) a positive correlation between NaCl and siderophore concentration (production) in solution exists. The higher sodium chloride, the higher the siderophore production by strain SL28. As noted in the beginning of this section, at 37 °C no siderophore was detected by CAS assay at NaCl concentrations of 1 and 5% (w/v). However, at 10% NaCl the maximum siderophore production was even higher than at 10%, room temperature. It is important to note that the 14.8 µM value was obtained from a stock solution. No replicates were done and the experiment was terminated to follow experimental treatment at room temperature. At room temperature, *Halomonas* sp. SL28 was more active in siderophore production than at 37°C. At 10% (w/v) NaCl, this strain produced more siderophore as well. This contrasted with results from strain SL01 which produced higher siderophores at lower NaCl concentrations (see Figure 2.7). Refer to

Appendix A for detailed optical densities and CAS assay data collected at the environmental conditions reported in this section (Tables A1 to A8).

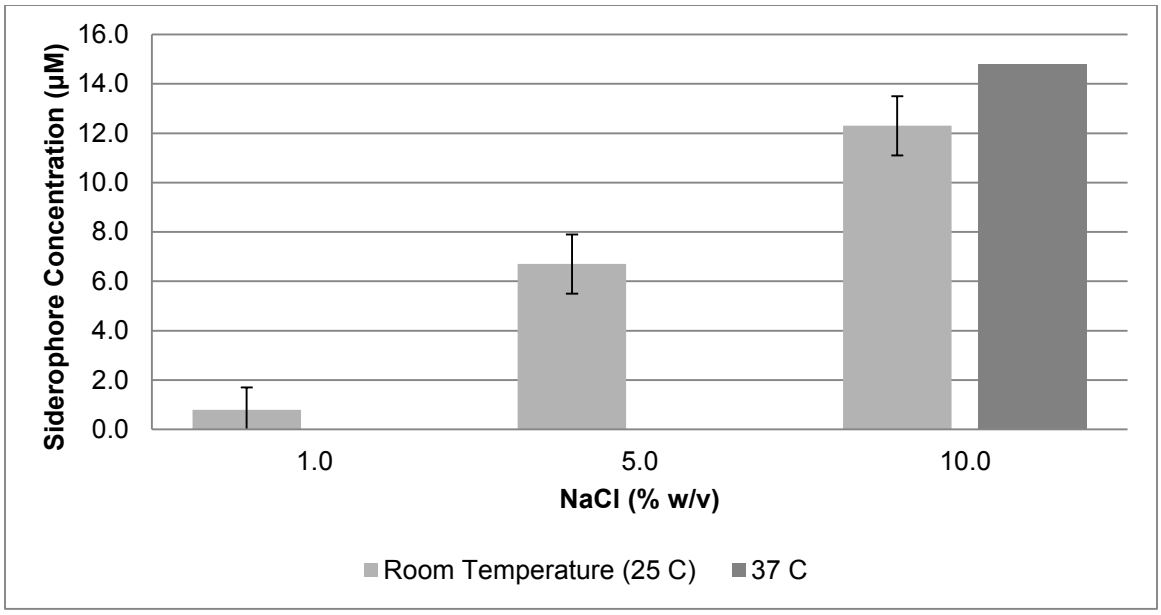

Figure 2.11. *Halomonas* sp. SL28 maximum siderophore production. Average results of triplicates with standard deviations (s. d.) are presented.

SLM pH Effects on Growth &
Siderophore Production of *Halomonas* Strains

After looking for temperature and sodium chloride concentration effects on siderophore production in both bacterial strains, pH was studied. First, strain SL01 was grown at 37 °C and 5% (w/v) NaCl meanwhile SL28 was grown at 10% (w/v) NaCl and room temperature. The pH treatments were at 8, 9 10 and 11. Figure 2.12 presents the pH effect on strain SL01 growth. Growth rates were faster at pH treatments of 8 and 9 during the first 24 h, and no lag phases were measured. In both cases higher optical density values were measured at 50 and 75 h, respectively. When observing the growth curves for pH 10 and 11 treatments, longer lag phases were measured, especially for pH 10 where it took approximately 140 h to start a short exponential phase then transitioned

into stationary phase. It took 30 h of lag phase for the strain to start exponential growth at pH 11. Both treatments did have less optical density values than at lower alkaline pH values, indicating *Halomonas* sp. SL01 prefers to grow at lower alkaline pH.

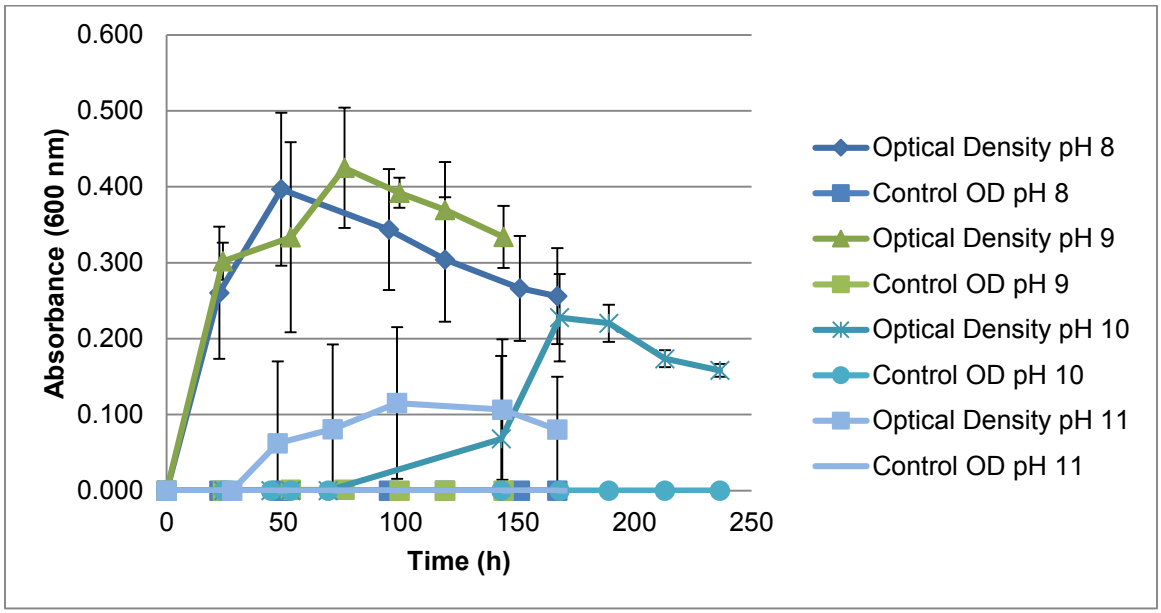

Figure 2.12. Growth of *Halomonas* sp. SL01 dependent on SLM pH at 37 ºC and 5% (w/v) NaCl . Average results of triplicates with standard deviation (s. d.) are presented.

Figure 2.13 shows siderophore production patterns of *Halomonas* sp. SL01 grown at the same. Siderophores were not initially detected for higher pH treatments (10 and 11). A delay period was characteristic and siderophore detection started after the bacteria entered exponential phase growth. The concentration was between 5 and 10 µM for both treatments. At pH 8, siderophore production also had a shorter delay period but at pH 9 the production rate was higher. The maximum siderophore concentration measured for pH 8 was 32.4 µM. In all treatments production of siderophore reached a plateau and as bacterial growth decreased siderophore concentration also decreased. It is understood from the results that *Halomonas* sp. SL01 grows better and produces more siderophores at pH 9, reaching almost 40 µM.

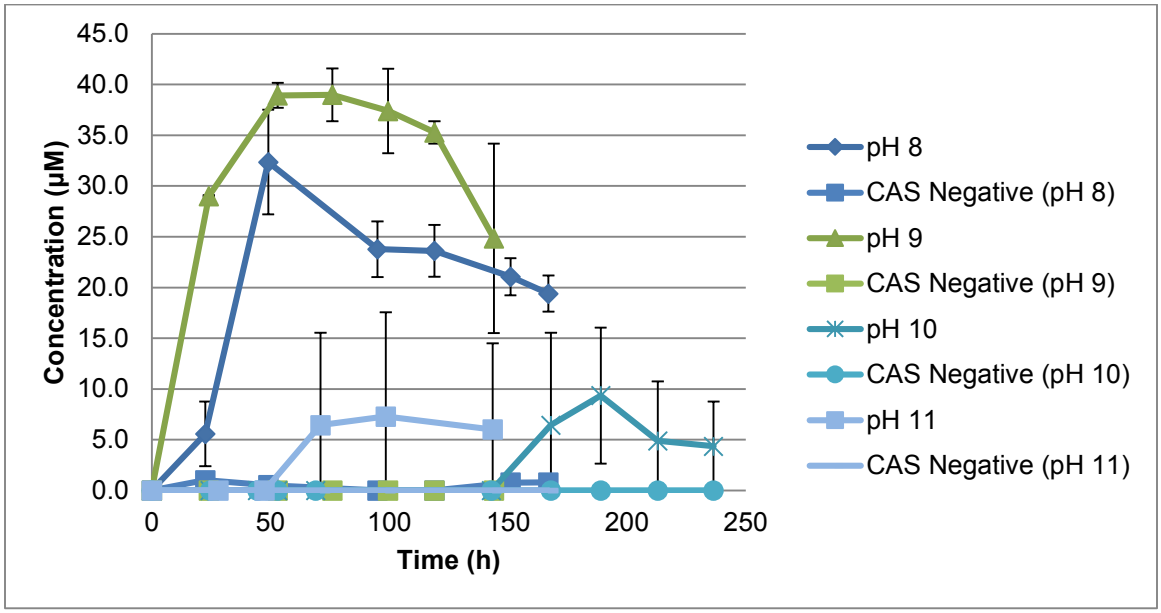

Figure 2.13. Siderophore production of *Halomonas* sp. SL01 dependent on SLM pH at 37 ºC and 5% (w/v) NaCl. Average results of triplicates with standard deviations (s. d.) are presented.

Results for strain SL28 were similar to those of strain SL01. Starting with growth on 10% (w/v) NaCl and room temperature SLM, pH was adjusted to the same values as for *Halomonas* sp. SL01 of: 8, 9, 10 and 11. Figure 2.14 presents the effect of pH on strain SL28 growth measured with optical density. Growth at pH 9 shows is better (OD 0.80) than the other treatments. At pH 8, the exponential phase was similar to that of pH 9, but reached a maximum absorbance of 0.70. The growth was less on the stationary phase for pH 8 than 9. At pH 10 and 11, lag and exponential phases were observed. However the growth rate was better at pH 10 than pH 11. The stationary phase for pH 10 remained at about OD 0.40, meanwhile for pH 11 it was about 0.20. Thus, *Halomonas* sp. SL28 grows better at pH 9, at room temperature and 10% NaCl.

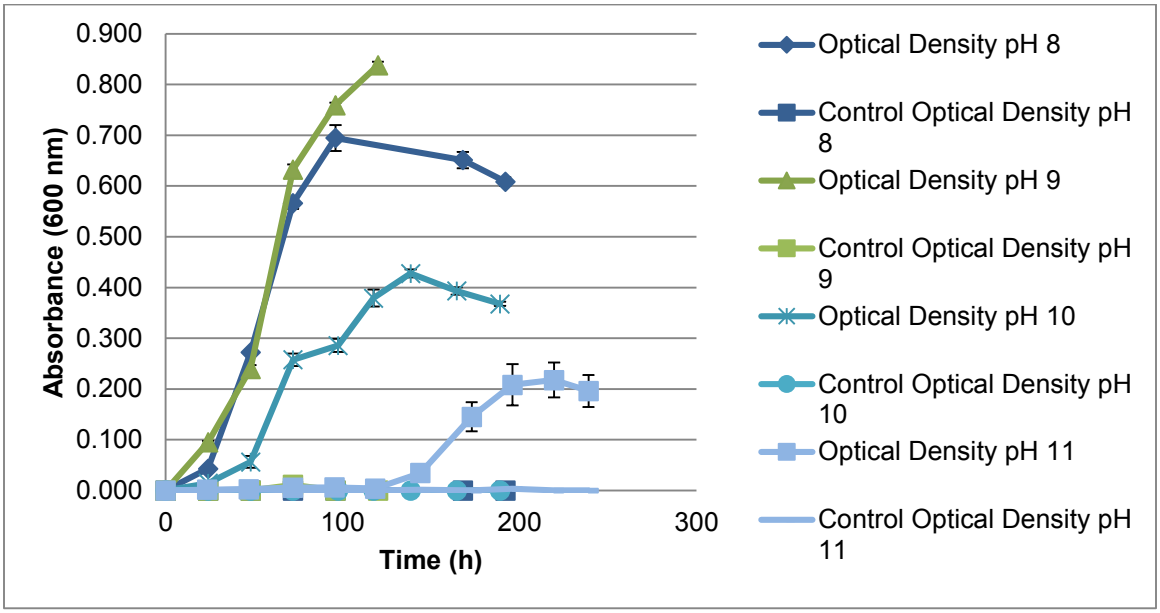

Figure 2.14. Growth of *Halomonas* sp. SL28 dependent on SLM pH at room temperature and 10% (w/v) NaCl. Average results of triplicates with standard deviations (s. d.) are presented.

When observing the siderophore production for strain SL28 by the CAS assay, some changes in the patterns were detected (Figure 2.15). *Halomonas* sp. SL28 produces more siderophore at pH 8 (41.5 μM). This contrasts with siderophore concentration at pH 9, with a value of 12.3 μM (approximately 3 times less than pH 8). Delay periods of siderophore production were detected in all treatments, and pH 11 was the longest (173 h). However, at this pH, siderophore concentration was even higher than at pH 10 (14.1 and 4.6 μM, respectively). In general, growth and siderophore production were correlated to each other, having growth establishment first and then siderophore production. The reason for this could be that bacteria are first sensing their environment and then take action to obtain their nutrients. For specific data acquired for figures presented in this section refer to Appendix A (Tables A9 to A14).

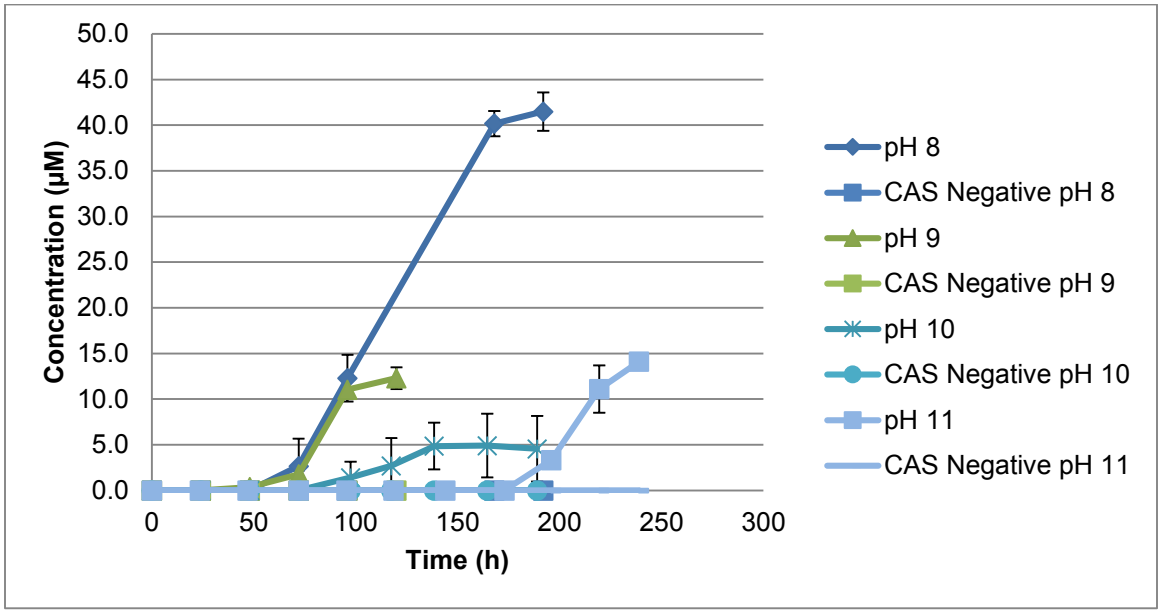

Figure 2.15. Siderophore production of *Halomonas* sp. SL28 dependent on SLM pH at room temperature and 10% (w/v) NaCl. Average results of triplicates with standard deviations (s. d.) are presented.

Discussion

Because of iron requirements for good cellular function (Crosa 2004, Raymond & Dertz 2004), siderophores could be synthesized, excreted and internalized by the cells. Siderophore production affects by certain environmental conditions were studied here on two *Halomonas* strains. Several factors studied were salt concentration, temperature and pH of the media. For strain SL01, growth was affected by salt concentration, with growth decreasing as NaCl % (w/v) decreased. A similar study of another haloalkaliphile, *Halomonas campisalis*, found that it grows better at 2 – 3 % (w/v) NaCl (Aston & Peyton 2007). This microorganism was isolated from Soap Lake, WA the same isolation place as our studied strains SL01 and SL28. This microorganism was found to produce different solutes depending on media salinity and terminal electron acceptor. However the project did not focused on siderophore effects from these conditions. However

strains SL01 and SL28 both performed better at higher salinities than *H. campisalis*. More studies could be done with the studied strains here that may include: (1) effects of anaerobic conditions on siderophore production, (2) electron acceptors and (3) higher salinities (>10 % w/v NaCl) on *Halomonas* sp. SL01 and SL28.

Another research project found in the literature presented the factors that affected *E. coli* strain Nissle 1917 siderophore production (Valdebenito et al. 2006), a probiotic strain. Four siderophores were studied in this research: enterobactin, salmochelin, aerobactin and yersiniabactin. Enterobactin and aerobactin were produced at higher concentrations in more acidic (pH 5.6) media compared to salmochelin and yersiniabactin. Contrary to that, salmochelin and yersiniabactin were produced at higher concentrations when the media was more alkaline (pH 7.0 and 7.6, respectively).

The main objective of this study was to determine siderophore production and structure (discussed ahead in Chapter 3). Due to that, SLM was deferrated with Chelex resin because that iron-starved media promotes maximum siderophore production. As per the research performed by Stintzi and Raymond (2000), amonabactin production from *A. hydrophila* was higher when iron levels were low or when it was not present (Stintzi & Raymond 2000). Also, the study suggested iron uptake by amonabactin from tranferrin or lactoferrin. They developed a kinetic model based on their experiments and found that amonabactin actually removes ferric iron from the N- or C- terminal binding sites, eventually leaving the protein in its apo-form (without iron). Because it has been reported *Halomonas* infections in dyalisis patients and related equipment contamination (Stevens et al. 2009), a future direction for the present research could be to determine the possibility of siderophore-transferrin/lactoferrin interactions and host iron high-jacking by *Halomonas* sp. SL01 and SL28.

Different iron acquisition pathways have been described previously in diverse microorganisms that span the tree of life. As one report shows, the cyanobacteria, *Anabaena flos-aquae,* has a siderophore-dependent and siderophore-independent pathways (Sonier et al. 2012). The other report studied *Leishmania* heme uptake and ferric reductase, both siderophore-independent acquisition systems (Flannery et al. 2013). An example of bacteria, *P. aeruginosa* has diverse pathways for ferric and ferrous iron acquisition. Konings and co-workers determined that this microorganism, when infecting cystic fibrosis patients, has siderophore-mediated and –independent iron acquisition mechanisms (Konings et al. 2013). Another siderophore-independent iron acquisition mechanism present in Pseudomonas *aeruginosa* is ferric iron reduction by phenazine-1-carboxilate. Wang and co-workers found that in the presence of the phenazine, pyochelin and pyoverdine mutants still has the ability to grow and develop biofilms (Wang et al. 2011). Extraction of ferric iron from host and iron-bearing proteins has been studied in the well known pathogen, *S. aureus* (Farrand et al. 2013). Regulatory pathways exist in this pathogen that control iron acquisition and survival. With previous information confirming siderophore production by strains SL01 and SL28, studies on transport, regulatory mechanisms and pathways involved should be investigated. There could be the potential that these strains could produce other molecules that are not necessary linked to siderophore-mediated iron acquisition.

CHAPTER THREE

STRUCTURAL CHARACTERIZATION OF AMPHIPHILIC SIDEROPHORES PRODUCED BY A SODA LAKE ISOLATE, *HALOMONAS* SP. SL01, REVEALS CYSTEINE-, PHENYLALANINE- AND PROLINE-CONTAINING HEAD GROUPS

Contribution of Authors and Co-Authors

Manuscript in Chapter 3

Author: Luis O. Serrano Figueroa

Contributions: Conceived and developed experimental design. Performed experiments and collected and analyzed data. Wrote first draft of the manuscript.

Co-Author: Benjamin Schwarz

Contributions: Performed mass spectrometry experiments. Collected and analyzed data. Commented and reviwed the manuscript draft.

Co-Author: Dr. Abigail M. Richards

Contributions: Conceived and developed experimental design. Advised on data analysis. Commented and reviewed manuscript draft.

Manuscript Information Page

Luis O'mar Serrano Figueroa, Benjamin Schwarz, Abigail M. Richards
Extremophiles
Status of Manuscript:
____ Prepared for submission to a peer-reviewed journal
__x_ Officially submitted to a peer-review journal
____ Accepted by a peer-reviewed journal
____ Published in a peer-reviewed journal

Published by Springer, Inc.

CHAPTER THREE

STRUCTURAL CHARACTERIZATION OF AMPHIPHILIC SIDEROPHORES PRODUCED BY A SODA LAKE ISOLATE, *HALOMONAS* SP. SL01, REVEALS CYSTEINE-, PHENYLALANINE- AND PROLINE-CONTAINING HEAD GROUPS

Introduction

Iron is an important element for different biological processes in most microorganisms, with the exception of some lactobacilli (Crosa 2004). Siderophores are low molecular weight entities with high iron (III) affinity. These molecules help the microbial cell to obtain iron (III) due to its low bioavailability (10^{-18} M) at a nearly neutral pH environment (Raymond & Dertz 2004). As different microorganisms are found in any type of environment, there are different siderophore types as well. Most of them are divided in three categories by functional groups involved in the iron coordination process: hydroxamates, catecholates and carboxylate siderophores. For hydroxamates, acylation of ornithine produces hydroxamic acid groups, meanwhile catechol and its molecular modifications (like 2,3-dihydroxy benzoic acid) are required for the catecholate siderophores to work properly; carboxylate siderophore must have α-hydroxy donor groups (Pattus & Abdallah 2000, Butler & Theisen 2010a). Some of the siderophores will have only one of the coordinating groups but others can have multiple ones. As an example, aerobactin, produced by *E. coli*, contains both hydroxamic and hydroxycarboxylic coordinating groups (Valdebenito et al. 2006, Gauglitz et al. 2012). Another type of siderophore that will have different coordinating groups is amphiphilic siderophores. These molecules have a polar amino acid head group and an aliphatic fatty acid tail attached to the N-terminus of the head group,

leading to amphiphilic characteristics. Like non-amphiphilic siderophores, amphiphilic siderophores may contain catechols, α-hydroxycarboxylic acid and hydroxamic acid coordinating groups. Citrate and hydroxyaspartic acid could be also found as part of amphiphilic siderophores structure (Sandy & Butler 2009). Examples of amphiphilic siderophores variability in functional groups are ochrobactins (Martin et al. 2006), synechobactins (Ito & Butler 2005) and petrobactins (Homann et al. 2009a).

To date, most of the amphiphilic siderophores come from marine microorganisms, such as *Marinobacter* sp. and *Vibrio* sp. (Sandy & Butler 2009, Butler & Theisen 2010b, Sandy et al. 2010, Amin et al. 2012). In this report we describe two distinct families of amphiphilic siderophores produced by an isolate from Soap Lake located in Washington State, *Halomonas* sp. SL01. Soap Lake is a meromictic lake with a pH of 9.8 and a dissolved solids concentration ranging from 140 g/L in the monimolimnion layer to 14 g/L in the mixolimnion layer (Edmondson & Anderson 1965, Sorokin et al. 2007). The microbial population in Soap Lake is diverse and includes phylogenetic groups α-, β-, and γ-Proteobacteria, Acidobacteria, Verrucomicrobia, Synechococcus, Actinobacteria and Thermotogales, among others (Dirnitriu et al. 2008). Also, Fe(III) reduction has been characterized on different isolates including *Bacillus* sp. (Pollock et al. 2007) and our siderophore-producing halophile *Halomonas* sp. SL01 (VanEngelen et al. 2008). It is implied then that this reduction process is due to siderophore production by this microorganism and the purpose of this report is to identify the structure of the siderophores produced by this isolate.

Methods

Soap Lake Media (SLM) Preparation and Environmental Conditions:

The SLM growth media used in all the experiments was an artificial medium, similar in composition can be found in Soap Lake, WA, where *Halomonas* sp. SL01 was isolated. The media was prepared with 50.0 g/L sodium chloride (Fisher), 1.12 g/L sodium borate, 1.0 g/L ammonium chloride, 0.06 g/L calcium chloride, 0.05 g/L magnesium chloride hexahydrate, 0.85 g/L sodium nitrate, 0.50 g/L potassium phosphate monobasic, 0.01 g/L potassium chloride, 0.25 g/L yeast extract and sodium pyruvate (5.0 g/L, Fisher) as the carbon source. The media was treated with Chelex (Sigma Aldrich) resin at 200 mL bed volume to eliminate iron traces and other metals that could be present in the chemicals used and glassware was acid washed. All media were filtered sterilized with 0.22 µm polyethylene sulfonate (PES, Nalgene) membrane filters and pH was adjusted to 9.0 with 10 N NaOH (Fisher).

Chelex Resin Activation:

Chelex resin was used to deferrate the media. The resin was first activated by adding 2 bed volumes 1 N HCl (Fisher Scientific), then 5 bed volumes nanopure water, followed by 2 bed volumes 1 N NaOH and finalizing with 5 bed volumes of nanopure water. Then, the resin was mixed for 5 min with SLM for its treatment.

Siderophore Detection in Solution by CAS Assay:

Stock solutions were prepared in advance: (1) 10 mM HDTMA (Fisher); (2) iron solution: 1 mM $FeCl_3$•6H2O (Acros) in 10 mM HCl; (3) 2 mM aqueous chrome azurol sulfonate (CAS, Sigma) and (4) 0.2 M 5-sulfosalicylic acid (Fisher). Then the CAS assay

solution was prepared by adding 6 mL of 10 mM HDTMA in a volumetric flask (100 mL) diluted with a bit of water. In that same flask, 1.5 mL iron solution and 7.5 mL of 2 mM CAS solution were added. Then in a separate flask, 4.307 g anhydrous piperazine (Acros) was dissolved in some water and 6.25 mL 12 M HCl were added. This buffer was rinsed into the volumetric flask with HDTMA, CAS and iron solution and volume completed with nanopure water.

To determine the presence and concentration of siderophores in solution, a 500 µL aliquot of media supernatant (previously centrifuged at 12,000 xg for 5 min, Eppendorf 5417C) plus 500 µL CAS assay solution were added to a cuvette. Then 20 µL 5-sulfosalicylic acid (or to a final concentration of 4 mM) was added. Absorbance of the solution at 630 nm was measured after equilibrium was reached (30 min-2 h, but no longer than 6 h).

Growth Culture Preparation and Sampling:

To prepare the growth cultures, a frozen stock of *Halomonas* sp. SL01 was thawed at room temperature. After thawing, the frozen stock volume (approximately 1 mL) was inoculated in 100 mL SLM in a baffled flask (Pyrex). A sterile control was also prepared in a disposable 50 mL tube (Falcon or BD). Then this starter culture and control were placed in the shaker incubator (140 rpm at room temperature or 37 °C; Infors HT Ecotron) and optical densities (OD, at 600 nm) and siderophore assays (CAS, at 630 nm) were done once a day withdrawing 1 mL aliquots.

Once the CAS absorbance readed about 0.100, transfers of 1 mL aliquots were done into 3, 1 L baffled flasks, filled with 400 mL SLM. A sterile control flask was also prepared for the study. Then the flasks were placed in the shaker incubator and OD and CAS readings (UV spectrophotometer, Spectronic Gensys 5) were taken every day until

a maximum siderophore production was detected (48 to 72 h) by corresponding dilutions. After this, the media was ready for extraction of siderophores by first ultra-centrifuging (Sorvall Instruments RC5C; GSA rotor) at 5,856 xg for 20 min at 4° C and processing supernatant.

SLM and CAS Plates:

To check for culture purity, SLM plates were prepared and streaked. For SLM plate preparation, Noble agar (30 g/L, Difco) was dissolved and sterilized by autoclaving for 20 min at 121 °C in 500 mL nanopure water. Then, the agar solution was placed in a water bath at 60 °C. Soap Lake media was prepared with salts (50 g/L NaCl, 1.12 g/L $Na_2B_4O_7$, 1.0 g /L NH_4Cl, 0.06 g/L $CaCl_2{\cdot}2H_2O$, 0.05 g/L $MgCl_2{\cdot}6H_2O$, 0.85 g/L $NaNO_3$, 0.50 g/L KH_2PO_4, 0.01 g/L KCl), 0.25 g/L yeast extract and 10 g/L sodium pyruvate as carbon source. The SLM medium pH was adjusted and then filtered sterilized with 0.22 µm membrane filter and placed in a water bath for 3 hours. When both solutions were at temperature (60 °C), 500 mL of SLM was poured in the Noble agar bottle and allowed to mix by magnetic stirring for 5 minutes. Finally, plates were poured in a laminar flow hood (Nuaire) to solidified overnight. When growth culture was in stationary phase and siderophore production was detected, streaks of SLM plates were done.

CAS plates were prepared in a similar way to SLM plates. A CAS/HDTMA mix was prepared by first mixing chrome azurol sulfonate (605 mg), water (500 mL) and 1 mM $FeCl_3$ in 10 mM HCl (100 mL) together (Solution A). HDTMA (729 mg) was dissolved in water (400 mL) to form Solution B. Slowly, Solution A was added to B, providing gentle stirring to avoid foam formation. The resulting mixture was sterilized by autoclaving at 121 °C for 20 min and then placed in a water bath. Noble agar solution (500 mL, 30 g/L) was prepared and sterilized (in autoclave, then placed in water bath)

and SLM (400 mL) was filter sterilized and placed in a water bath at 60 °C. SLM and CAS/HDTMA solutions were mixed with the Noble agar solution and plates were poured in a laminar flow hood and solidified overnight. Streak plates were done as a double verification for siderophore production and culture purity.

Siderophore Extraction from Media:

For siderophore extraction, the C2 column (Varian) was first conditioned by treating it with methanol (5 mL, Fisher) and 5 mL nanopure water. After this point, the column was always kept wet and no air flowed through it. Otherwise, a new column was used. To extract siderophores from the supernatant a 50 mL sample was run through the column (collecting in the waste beaker). Then the column was filled with nanopure water and this phase collected because some siderophores may be present. After this, the column was filled with methanol this phase collected in a second tube. This phase would have the majority of siderophores. For a second time the column was filled with nanopure water and an additional 5 mL collected in the waste beaker. The next 50 mL of sample was processed as previously indicated until no more supernatant (and first collected nanopure water) remained. Extracts were concentrated by evaporation centrifugation (at 50 °C, Labconco) for 2 h, stored at 4 °C and later purified by HPLC (Dionex).

Siderophore Purification and Lyophilization:

To purify the extracts obtained from *Halomonas* sp. SL01, a HPLC method was created. Briefly, two mobile phases were used: (A) water with 0.01% (v/v) trifluoroacetic acid (TFA, Fisher) and (B) acetonitrile (Fisher) with 0.01% (v/v) TFA. The mobile phase gradient was 10 to 70% (v/v) B for 63 min. The injection volume was 500 µL and a C4 reverse phase column (4.6 mm ID X 250 mm, Grace) was used. The UV detection

(AD20 absorbance detector) wavelength was set to 220 nm. The pump was an ICS-3000 and the column was placed in a CH-30 Eppendorf column heater. The interface was the UCI-50 Universal Chromatography Interface. Siderophore fractions were collected, frozen, lyophilized overnight and stored (4 °C) for future tests.

Mass Spectrometry (MS) Analysis:

To confirm siderophore presence, lyophilized samples were dissolved in nanopure water and the CAS assay was performed. Siderophore-positive samples were analyzed on an Agilent 6538 QTOF LC/MS with electro spray ionization (ESI) to determine their chemical structure. Samples were further purified using a 10-100% (v/v) acetonitrile gradient for 10 min on the LC before entering the MS. Acidified water with 0.1% (v/v) formic acid was used as aqueous buffer. Samples were analyzed in positive mode and with a fragmentation voltage of 150 V. MS/MS analysis was done on the same equipment with a constant stream of directly infused sample administered with a syringe pump. A target ion was selected from the MS analysis and fragmentation was ramped in cycle to provide a progression of fragments for each sample (Table 2). Data analysis was done using the Bruker's DataAnalysis software.

Fatty Acid Methyl Ester (FAME):

To determine aliphatic tail structure, fatty acid methyl ester (FAME) analyses were done by MIDI Labs, Inc. Lyophilized siderophore samples were dissolved in nanopure water and analyzed through FAME in a four step reaction process: (1) saponification, (2) methylation, (3) extraction and (4) wash for sample clean up. Four reagents were prepared to help cleaved the tail from the siderophore and they were particularly related to each reaction step in FAME. Reagent 1 (for saponification) was made from 45 g NaOH, 150 mL methanol and 150 mL distilled water. Reagent 2 (for

methylation) was made with 325 mL certified 6.0 N HCl and 275 mL methyl alcohol. The fatty acid was poorly soluble in the aqueous phase at this point. Reagent 3 (for extraction) was made of 200 mL hexane and 200 mL methyl tert-butyl ether. This reagent extracted the fatty acid tails into the organic phase for use with the gas chromatograph (GC). Reagent 4 (for sample clean up) was made of 10.0 g NaOH dissolved in 900 mL distilled water.

Sample processing to prepare GC ready extracts was made following the 4 steps mentioned previously. Briefly, for saponification, 1 mL of reagent 1 was added to the siderophore samples. Tubes were sealed and vortexed (5 to 10 s) and heated in a boiling water bath for 5 min, at which time the tubes were vortexed again and placed in the bath for an additional 25 min. In the methylation reaction step, 2 mL of reagent 2 were added. The tubes were capped and vortexed and tubes were heated for 10 ± 1 min at 80 ± 1 °C and after this samples were cooled at room temperature. For the extraction step, 1.25 mL of reagent 3 were added, tubes recapped and tumbled in a clinical rotator for 10 min. The aqueous phase was discarded. To clean up the sample, about 3 mL of reagent 4 were added to the organic phase, the tubes were tumbled for 5 min. After that, approximately 2/3 of the organic phase was then analyzed in the GC.

Gas Chromatography (GC):

After FAME, samples were analyzed in a gas chromatograph (Agilent Technologies 5890, 6890 and 6850) with Sherlock MIS Software. A 25 mm x 0.2 mm phenyl methyl silicone fused silica capillary column (Ultra 2) was used. The method increased temperature from 170 °C to 270 °C at 5 °C/min. To ensure column cleaning and life span, a 300 °C ballistic temperature increase was held for 2 min after each sample was analyzed. A flame ionization detector was also employed to provide good

sensitivity. Hydrogen was the carrier gas, nitrogen the “make up” gas and air was used to support the flame. GC calibration was done using a standard with mixtures of straight chain saturated fatty acids from 9 to 20 carbons in length (9:0 to 20:0) and 5 hydroxy acids.

Results

Siderophore Production in Soap Lake Media and Purification:

Strain SL01 from the genus *Halomonas* sp. grew very well in Soap Lake media. The conditions to which it was subjected were, as previously mentioned, 5.0 % (w/v) NaCl concentration, room temperature (25 °C) and pH 9.0. As shown in Figure 3.1, a lag phase was absent. In contrast, a delay was detected for siderophore production. Perhaps this occured because of the utilization of ferrous iron reserves (bacterioferritin and ferritin) by the microorganism (Andrews et al. 2003). Production of siderophores detected by the chrome azurol sulfonate (CAS) assay was stable after 76 h of growth and harvesting was done for eventual purification. The maximum siderophore production was detected at 38.1 µM. Optical density reached a maximum of 0.625, decreased and increased again up to 0.530.

In Appendix B, Figure B1 shows the chromatogram with the distinctive fractions (A-H) obtained after siderophore HPLC purification. The iron chelating active fractions were peaks B, C, D, E and F; peaks A and H were not active for iron chelation and peak G was not soluble in water. Table 3.1 presents a summary of the iron-chelating activities of the corresponding peaks revealing siderophore presence in most of them. Fractions active in iron chelation were further analyzed to determine siderophore structure via mass spectrometry and fatty acid methyl ester.

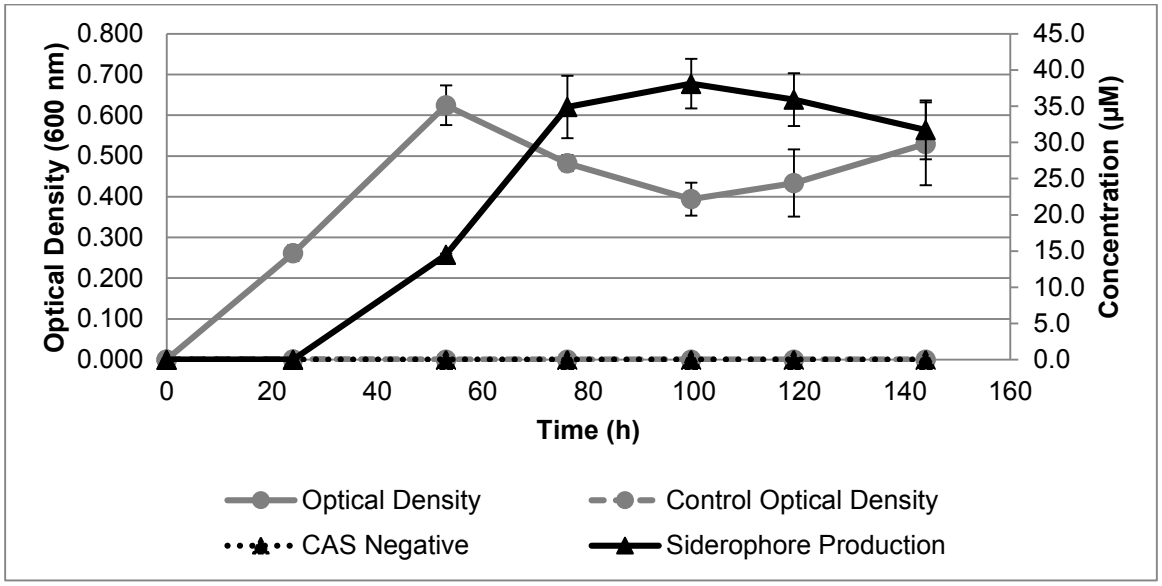

Figure 3.1. Growth and siderophore production of *Halomonas* sp. SL01at 5% NaCl Soap Lake Media and room temperature. Average of triplicates and error bars are ± standard deviation (s.d.).

Table 3.1. HPLC fractions with iron-chelating activities revealing siderophore-containing peaks. CAS assay absorbance at 630 nm. [a]Iron (III) chelation activities are positive for absorbances < 0.800 at 630 nm and blue to orange color change is observable in the aliquot.

Fraction	$Absorbance_{630}$[a] (50x)	Siderophore Concentration (µM)	Apparent Mass (amu)
A	0.912	0	-
B	0.708	213.3	1,052.45
C	0.540	413.1	1,096.45
D	0.346	643.9	989.4
E	0.645	288.2	1,080.48
F	0.662	268.0	1,017.38
G	1.030	0	-
H	1.077	0	-
Control	0.917	0	-

Structural Analysis of Siderophores by Mass Spectrometry and Fatty Acid Methyl Ester (FAME):

To study siderophore structure a QTOF LC/MS tandem MS/MS method was developed. Initial results showed two different siderophore families produced by *Halomonas* sp. SL01 by comparing the mass spectra for each peak. Three siderophore fractions (B, C and E) have similar fragmentation patterns ("y" fragments). This sharing of fragments suggested common amino acid composition in the head group. The siderophore molecules also differed in some fragments giving the idea of differences in aliphatic tail length. Fractions D and F also shared a common fragmentation pattern suggesting common amino acid sequence in the head group. This fragmentation pattern from siderophore fractions D and F differed from those fragments found in fractions corresponding to siderophores B, C & E. This suggests that *Halomonas* sp. SL01 produces two families of amphiphilic siderophores called halochelins.

For Halochelins B, C and E, total *m/z* was 1091.39 atomic mass units (amu), 1135.42 amu and 1,119.43 amu, respectively (Appendix B, Figures B2 through B4, respectively). Parent ions were attached to potassium (M+K) providing the apparent total mass for each molecule (refer to Table 3.1). The common "y" fragments obtained by the *m/z* in the spectra provided information that a polar head group is shared by the three siderophores. The corresponding amino acid residue sequence for the polar head group of these molecules was found to be (N- to C-terminus): phenylalanine (Phe), threonine (Thr), cysteine (Cys), arginine (Arg), glutamine (Gln), threo-β-OH-asp (Thr-β-OH-asp) and D-N-OH-ornithine (D-N-OH-orn). The "b" fragmentation pattern was not common within this siderophore family suggesting differences in the remainder of the molecule (beyond the N-terminus, or Phe). These fragments also confirmed the amino acid

sequence. Table 3.2 shows a summary of fragmentation found with mass spectrometry studies.

Table 3.2**.** Mass spectrometry pattern fragmentation for one of the amphiphilic siderophore families (Halochelins B, C and E) produced by *Halomonas* sp. SL01.

Halochelins			
Fragments (C- to N-terminus)	**B**	**C**	**E**
y (amu)	**b (amu)**		
131	921	965	949
262	790	834	818
390	662	706	690
546	506	550	534
649	403	447	431
750	302	346	330
897	155	199	183

All fragments for each siderophore molecule were compared and mass differences were calculated to provide more information on the chemical composition. Halochelin B total apparent mass was 1,052 amu and Halochelin C mass was 1,096 amu. The mass difference between them was 44 amu, which suggested an additional -(CH_2CH_2OH)- group in Halochelin C. This 44 amu difference between both molecules was also found in the other “b” fragments from the mass spectrometry results. Then, by comparing Halochelins B and E, a 28 amu difference was found. This suggested a -(CH_2CH_2)- group for Halochelin E. A 16 amu difference was found between Halochelins C and E that corresponded to an oxygen atom (-O) for the former one. The structural groups described above were associated with fatty acid tail differences for the respective siderophores. One fragment for each siderophore also suggested the approximate molecular mass for the fatty acid tails: 155 amu for Halochelin B, 199 amu for Halochelin C and 183 amu for Halochelin E (Table 3.2). For more detailed information about

fragments generated please refer to Figures B2 to B4 and Tables B1 to B5 in Appendix B.

To confirm fatty acid tail presence and structure in each siderophore, FAME with gas chromatography (GC) analysis on HPLC siderophore fractions was done. Various fatty acid GC fractions were present in the lyophilized sample for Halochelins B and C (analyzed in the same fraction). At retention times 1.2238 and 2.0545 min GC fractions were identified by the Sherlock MIS Software to be related to Halochelins B and C, respectively. Halochelin B fatty acid fraction (retention time 1.2238 min) revealed a fatty acid with structure 10:0, suggesting that the aliphatic tail was composed of a 10 carbon chain with no double bonds or side groups. Halochelin C showed a fatty acid fraction (retention time 2.0545 min) with a 12:0 3OH structure, which meant a 12 carbon chain, no double bonds and a hydroxyl (-OH) side group on the third carbon position. The difference in atomic mass from FAME revealed an additional 44 amu to Halochelin C that correlated with MS data. Halochelin E HPLC lyophilized fraction was also analyzed and the GC showed several fatty acids fractions. However, at retention time 1.6482 min a fatty acid with structure 12:0 was detected. This suggested a 12-carbon chain, no double bonds or side group substitutions. The atomic mass difference between Halochelins E and B was 28 amu, correlating with the findings of MS data. For gas chromatograms and retention times for fatty acid fractions refer to Appendix B (Figures B5 and B6, Tables B6 and B7). A detailed and complete siderophore structure is presented in Figure 3.2 demonstrating similarities with other marine amphiphilic siderophores (like marinobactins).

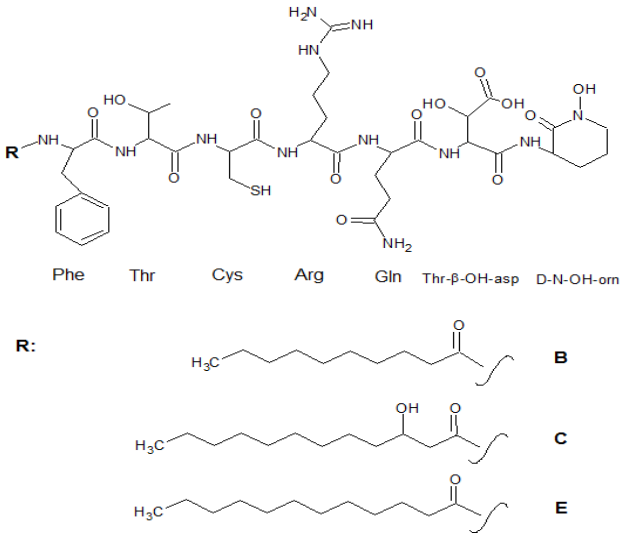

Figure 3.2. Halochelins B, C and E, produced by *Halomonas* sp. SL01.

Halochelin D and F, total *m/z* was 1,079.45 and 1,107.48 amu, respectively. Parent ions detected by mass spectrometry were attached to hydrogen (M+H) and hydrated with 5 molecules of water providing the apparent total mass for each molecule (refer to Table 3.1). The common “y” fragments obtained by the *m/z* in the spectra were provided information that the polar head group is shared with the two halochelins. The corresponding amino acid sequence for the polar head group of these amphiphilic siderophore molecules was determined as: proline (Pro), arginine (Arg), serine (Ser), threo-β-OH-asp (Thr-β-OH-asp), threonine (Thr), serine (Ser) and D-N-OH-ornithine (D-N-OH-orn). The “b” fragmentation pattern was not common within this siderophore family suggesting differences in the remainder of the molecule (beyond the N-terminus, or Pro). These fragments also confirmed the amino acid residue sequence. Table 3.3 shows a summary of fragmentation found with mass spectrometry studies for Halochelin D and F.

Table 3.3**.** Mass spectrometry pattern fragmentation of the Halochelins D and F produced by *Halomonas* sp. SL01.

Halochelins		
Fragments (C- to N-terminus)	**D**	**F**
y (amu)	**b (amu)**	
131	858	886
218	771	799
319	670	698
450	539	567
537	452	480
693	296	324
790	199	227

As was done with the first suite of halochelins (B, C and E), fragments for each siderophore molecule were compared and mass differences were obtained. Halochelin D total apparent mass was 989 amu and Halochelin F mass was 1,017 amu. The mass difference between them was 28 amu, which suggested an additional $–CH_2CH_2-$ group in Halochelin F. This 28 amu difference was also found in the other “b” fragments from the mass spectrometry results. Aliphatic tail fragment mass for Halochelin C and D was the same (199 amu), revealing that even though they belong to different families they share the same fatty acid structure (12:0 3OH). Eventually this was confirmed with FAME studies. Thus, Halochelin F has a fatty acid tail structure of 14:0 3OH, accounting for the additional 28 amu. For more detailed information about fragments generated please refer to Appendix C (Figures C1 and C2, Tables C1 to C7).

To confirm fatty acid tail structure of Halochelin D and F, FAME with gas chromatography (GC) analysis was performed. Different fractions were detected in the sample, but the 1.9840 min GC fraction was identified by the Sherlock MIS Software to be the Halochelin D fatty acid. The fraction analysis revealed a fatty acid with structure 12:0 3OH suggesting that the aliphatic tail was composed of a 12 carbon chain, no double bonds and a hydroxyl (-OH) side group on the third carbon. This also confirmed

that Halochelins C and D share a fatty acid tail. For Halochelin F HPLC lyophilized fraction at retention time 2.663 min a fatty acid with structure 14:0 3OH was detected. That suggested a fatty acid tail with a 14-carbon chain, no double bonds and a hydroxyl (-OH) side group on the third carbon. The atomic mass difference between Halochelins D and F was 28 amu, correlating with the findings of MS data. For gas chromatograms and retention time tables for the fatty acid fractions please refer to Appendix C (Figures C3 and C4, Tables C8 and C9). A detailed and complete siderophore structure is presented in Figure 3.3 demonstrating similar structures to previously reported amphiphilic siderophores.

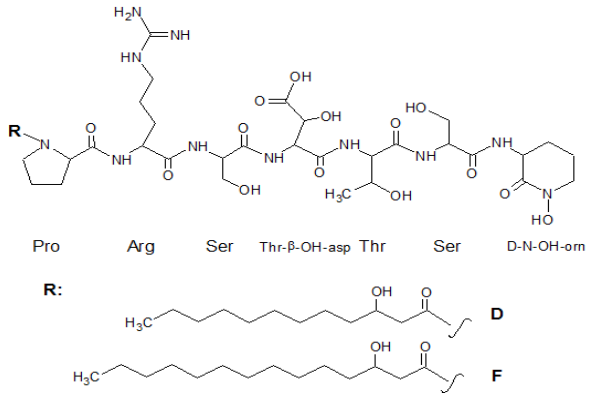

Figure 3.3. Halochelins D and F, produced by *Halomonas* sp. SL01.

Discussion

The siderophores produced by *Halomonas* sp. SL01 were found to be amphiphilic and we propose the names of Halochelins B, C, D, E and F. A slight delay in siderophore production was detected in cultures suggesting siderophore production was enhanced resulting from growth induced iron limitation. Similar results were presented in a report that studied erythrobactin, a hydroxamate-type siderophore produced by the actinomycete *S. erythraea* (Crosa 2004, Oliveira et al. 2006). Siderophore production

was detected after 24 h of growth. This trend in growth was also found in physiological data about *Halomonas* sp. SL01 and SL28, in which the microorganisms start to grow and after a time period (usually 24 h) produce siderophores. Bertrand and co-workers (2009) also presented data that shows similar patterns in siderophore production and microorganism growth at different media pH. The siderophore production delay should be further investigated to determine what cellular processes, at the genetic or molecular levels, controlled it and what ecological or evolutionary importance has. This approach may determine if there are ferritins, bacterioferritins or Dps proteins in *Halomonas* sp SL01 that may serve as iron reservoirs (Andrews et al. 2003) therefore explaining siderophore production delay.

The amphiphilic siderophores produced by *Halomonas* sp. SL01 were found to contain two distinct amino acid head groups. In addition to the ability to chelate iron, the head group has polar properties due to the amino acid composition; contrary to that, the fatty acid tail is non-polar. Fragmentation patterns were common in siderophores within each sub family but different between them as previously presented. The presence of proline, phenylalanine and cysteine were surprising but previous research by other groups demonstrated siderophores that contains these amino acids: amonabactins (Telford & Raymond 1997), pyochelins (LIU & SHOKRANI 1978, COX et al. 1981, Quadri et al. 1999), yersiniabactins (Heesemann et al. 1993, Suo et al. 1999) and thioquinolobactins (Matthijs et al. 2007). The incorporation of serine, arginine, threonine, glutamine, thr-β-OH-asp and cyclized ornithine are common for amphiphilic siderophores (Dhungana et al. 2007, Martinez & Butler 2007, Homann et al. 2009b, Vraspir et al. 2011, Rosconi et al. 2013). In contrast to the aforementioned studies, our present report describes the first cysteine-, phenylalanine- and proline-containing amphiphilic siderophores produced by a halophile isolated from a soda lake.

It is possible that halochelins produced by *Halomonas* sp. SL01 play a role in the bioavailability of iron within Soap Lake. Soap Lake is a meromictic soda lake, containing three layers, the mixolimnion, chemocline and monimolimnion layers, which are permanently stratified and do not physically mix. *Halomonas* sp. SL01 was isolated from the upper layer (mixolimnion) which has more exposure to light and oxygen compared to the lower layers. Also, the mixolimnion has the lower dissolved solid concentration (about 14 g/L) opposite to the monimolimnion (140 g/L), but high when comparing to other lake types that intermix their layers (Edmondson & Anderson 1965, Sorokin et al. 2007). Soda lakes dissolved solids values are higher comparing to hydrochemical studies of freshwater lakes (Karatayev et al. 2008, Conzonno & Ulibarrena 2010). Karatayev and co-workers measured average dissolved solids at 119 mg/L in 550 lake in Belarus and Conzonno and Ulibarrena determined the value at 10 g/L in Lago Grande, Argentina. These high dissolved solutes in soda lakes could provide iron hydroxides that are not soluble in aerobic, alkaline environments (Duckworth et al. 2009) but allowing haloalkaliphilic microorganisms to use siderophores to obtain ferric iron. Evidence of carbon, sulfur and nitrogen biogeochemistry in soda lakes have been described and reviewed (Sorokin et al. 2014), however information on iron cycling is limited (Emmerich et al. 2012). Emmerich and co-workers studied the mineralogy, geochemistry and microbial ecology of Lake Kasin (Southern Russia). Ferric oxides content in lake sediments were reported to be 1.13 % (w/w) and a comparison of ferric reducing microorganisms most probable number (MPN) counts against ferric oxidizing microorganisms values revealed similar numbers. However, the research was done on sediments (no pelagic lake waters) and no information on siderophore-mediated iron acquisition was linked to ferric iron cycling. Bacteria and Archaea isolates (from Lake Kasin sediment samples) sequencing data revealed the presence of potential ferric iron-

reducing microorganisms, but actual siderophore production was not confirmed by CAS assay. The marine amphiphilic siderophores aquachelins are photoreactive and this may play an important role in biotic and abiotic ferric iron cylcling (Barbeau et al. 2001). Photochemical reactivity causes a cleavage on aquachelin, separating it from its fatty acid moiety and reduces ferric iron to ferrous iron. However, the polar head group of aquachelin remains active and continues to facilitate ferric iron chelation. Therefore photochemical reactivity is an abiotic process that contributes in ferric iron cycling in pelagic ocean waters providing reduced iron to organisms. How halochelins in pelagic hypersaline lake waters function or contributes to iron cycling is to be investigated, but photoreactivity may play a significant role.

Another question to address is what relevance, importance or function the fatty acyl moieties serve to amphiphilic siderophores. The main hypothesis is that aliphatic tails may provide siderophores the ability to interact with the cell membrane, allowing exposure of the molecule to the extracellular environment without totally releasing the molecule to the extracellular environment. Different diffusion limitation or prevention mechanisms utilized are: (1) acylated siderophores that anchor in the cell membrane; (2) polysaccharide- or matrix-mediated protection of the siderophore in a sheltered environment, limiting siderophore release; or (3) siderophore piracy and utilization of siderophores from various bacteria (Stintzi et al. 2000, Martinez & Butler 2007). Siderophores with small peptide head groups and longer fatty acid tails (>C15) would be more likely associated with the cell (Martinez & Butler 2007) as shown with the siderophore marinobactin F, which has those characteristics. In the case of marinobactin F, the supernatant siderohpore concentration was low but halos present on inoculated CAS assay plates suggested the possibility that the amphiphile could remain closely associated with the *Marinobacter* sp cells. Another study presented by the same group

shows how marinobactin E in its deferrated form has more affinity for L-α-dimyristoylphosphatidilcholine vesicles than its ferrated counterpart (Xu et al. 2002). It is apparent the importance for the bacterial cell to prevent siderophore diffusion in pelagic ocean waters in order to optimize iron acquisition in such diluted environments. To confirm this importance in hypersaline lakes it would be required to assess halochelins membrane interactions and affinity with the corresponding experiments.

Halomonas sp SL01 and other microorganisms from Bacteria and Archea produce diverse siderophore suites and the reasons for this should be investigated. One way is to grow the microorganism of interest in different environmental conditions. Valdebenito and co-workers (2006) described how neutral or alkaline media affected siderophore type produced by *E. coli* Nissle 1917. Enterobactin and aerobactin were produced at higher concentrations in more acidic media compared to salmochelin and yersiniabactin. *Pseudomonas aeruginosa* produces both pyoverdine and pyochelin siderophores and each one act in different ways that contributes to pathogenicity. Pyoverdine helps in biofilm formation (Banin et al. 2005) meanwhile pyochelin helps in host immune response evasion by not binding to siderocalins (proteins that hi-jack siderophores) in mammals (Abergel et al. 2006). In this case, pyochelin still provides iron to *Pseudomonas aeruginosa* allowing its growth and survival in spite of the host's innate immunity by means of restricting iron. Some bacteria will produce the hydrophilic form of the siderophore but others, due to a change in hydrophilicity, incorporates fatty acids to them (Martin et al. 2006). This will provide an amphiphilicity to the molecule and helps in organism survival. More studies should be done to determine how halochelins from *Halomonas* sp. SL01 are synthesized and if environmental conditions change the amphiphilic siderophore suite.

Previous microbiological data in soda lakes, or hypersaline lakes, have shown a diverse microbial population and examples of these environments are Sambhar Lake in India, Soap Lake in WA, USA and Mierlei Lake in Romania (Dirnitriu et al. 2008, Sahay et al. 2012). Similar hypersaline study sites include salt marshes and salterns (Ghozlan et al. 2006). Bacterial phyla observed in these extreme environments are Proteobacteria, Firmicutes and Actinobacteria and different *Halomonas*-related species (*Halomonas campisalis*, *H. titanicae*, *H. taeanensis* and *H. elongata* among others) have been isolated, sequenced and identified (Sorokin et al. 2014). Halobacteriacea and Methanomicrobia are archaea phyla identified in hypersaline environments and haloarchaeal species (*Haloferax volcanii*, *Halobacterium* sp., *Halogeometricum borinquense*, *Haloarcula* and *Halorubrum alkaliphilum* among others) have been isolated, identified and sequenced (Ghozlan et al. 2006, Anderson et al. 2011, Sorokin et al. 2014). Different studies provided information on siderophore-producing microorganisms. *Halomonas campisalis* is one of the siderophore-producing microorganisms in Sambhar Lake (Sahay et al. 2012) and the presence of siderophore synthesis genes have been described in *H. borinquense* however, the siderophore structural analyses have been performed (Anderson et al. 2011). Another study by Buyer and co-workers (1991) described aerobactin production by a halophilic pseudomonad. Amphiphilic siderophores have been mostly isolated and described from marine environments: marinobactins, aquachelins, ochrobactins, loihichelins, amphibactins and synechobactins (Homann et al. 2009a, Homann et al. 2009b, Vraspir et al. 2011, Gauglitz & Butler 2013b). With the present report it is demonstrated that amphiphilic siderophores are synthesized by microorganisms in other extreme environments, like soda lakes, different form marine waters. Structural resemblance is conserved among marine and hypersaline amphiphilic siderophores.

CHAPTER FOUR

VESICLE SELF-ASSEMBLY OF AMPHIPHILIC SIDEROPHORES PRODUCED BY BACTERIAL ISOLATES FROM SOAP LAKE, WA

Contribution of Authors and Co-Authors

Manuscript in Chapter 4

Author: Luis O. Serrano Figueroa

Contributions: Conceived and developed experimental design. Performed experiments and collected and analyzed data. Wrote first draft of the manuscript.

Co-Author: Betsey Pitts

Contributions: Assisted in epifluorescence microscopy method development. Provided training in light microscope and MetaMorph®. Commented and reviewed the manuscript draft.

Co-Author: Dr. Masaki Uchida

Contributions: Provided training on Brookhaven Zeta Sizer for dynamic light scattering method. Assisted in method development and commented on manuscript draft.

Co-Author: Dr. Abigail M. Richards

Contributions: Conceived and developed experimental design. Advised on data analysis. Commented and reviewed manuscript draft.

Manuscript Information Page

Luis O'mar Serrano Figueroa, Betsey Pitts, Masaki Uchida, Abigail M. Richards
Canadian Journal of Chemistry
Status of Manuscript:
____ Prepared for submission to a peer-reviewed journal
__x_ Officially submitted to a peer-review journal
____ Accepted by a peer-reviewed journal
____ Published in a peer-reviewed journal

Published by NRC Research Press, Inc.

CHAPTER FOUR

VESICLE SELF-ASSEMBLY OF AMPHIPHILIC SIDEROPHORES: A QUANTITATIVE AND QUALITATIVE STUDY

Introduction

Iron is an important mineral for bacteria and they have developed siderophores for its uptake. Metal chelation by different molecules (like cardiolipins and phosphatidylserine) have focused on ferric iron and manganese (Puskin 1977). Other studies have paid attention in siderophores. Examples are studies analyzing the potential chelation of uranium (VI) by deferrioxamine B and pyochelins (Mullen et al. 2007, Wolff-Boenisch & Traina 2007). Other researchers have demonstrated neptunium (V) and boron chelation (Harris et al. 2007, Moll et al. 2010). Amphiphilic siderophores have key vesicle self-assembly and surfactant properties when ferric iron is chelated (Martinez et al. 2000, Owen et al. 2005, Owen et al. 2007). Self-assembly in amphiphilic siderophores was first described by Martinez and co-workers (2000). Those physicochemical properties confer siderophores the potential to form micelles in their deferrated form, when over their critical micelle concentration (cmc), which in marinobactins and aquachelins is about 25 to 150 μM. Trends of higher cmc are expected when siderophores are ferrated.

Quantitative methods have been developed to study this property. Micelle-to-vesicle transitions for marinobactin E have been confirmed, indicating vesicle diameter sizes of 140 to 180 nm by dynamic light scattering (DLS) (Martinez et al. 2000). Due to micelle diameter in the proximity to the limit of detection of DLS, other methods have

been developed to obtain precise data. As an example, researchers have employed small-angle neutron scattering (SANS) with DLS to account for micelle formation (Owen et al. 2005). When deferrated siderophore was in solution over its cmc micelles formed at size about 4 nm. Addition of ferric iron (~1 Eq.) caused micelles to decrease in size (~3 nm) and further addition of the metal increased diameters up to 200 nm. Vesicle self-assembly also occurs in amphiphilic siderophores due to metals other than iron (Owen et al. 2007). Researchers in this report discovered that zinc (II) and cadmium (II) interact in the same fashion with the amphiphiles and micelle-to-vesicle transition was observed with the difference of multilamellar vesicle formation when compared to iron chelation (Owen et al. 2005). At higher iron equivalents, zinc-induced micelle-to-vesicle transition produced three types of vesicles varying in bilayers numbers (6 to 8). With SANS was possible to determine the interbilayer and bilayer thicknesses. In another study, X-ray diffraction (XRD) and X-ray absorption spectroscopy (XAS) were used to determine the distance between bilayers and the mode of coordination, respectively (Owen et al. 2008). In this case, zinc (II) and cadmium (II) were added to ferri-marinobactin E being previously formed in micelles. Amphiphilic siderophores free-carboxilate (COO^-) groups caused divalent cation chelation and micelle-to-vesicle transition occurred.

To study amphiphilic siderophores micelles and vesicles via microscopy, cryogenic transmission electron microscopy (cryo-TEM) has been developed. This qualitative method has provided researchers results similar to those obtained with previous quantitative methods discussed above (Martinez et al. 2000, Owen et al. 2005, Owen et al. 2007). A study used cryo-TEM on synthetic amphiphilic siderophores, sulfonated monocatechols, and their self-assembly properties (Bednarova et al. 2008). Researchers also used UV spectra, pK_a, complexation constants and surface tension for physicochemical characterization properties of these molecules with iron chelation.

Another way vesicles have been studied is by confocal microscopy and staining with fluorophores (Nicola et al. 2009). In this report researchers developed a method to observe cellular vesicles produced by *C. neoformans*. Other studies focused on vesicles derived from cells and they employed similar microscopic techniques as the previous report (Crivellato et al. 1999, Bergeron et al. 2014). One study used lipids to form giant vesicles stained with rhodamine and fluorescein meanwhile another utilized BODIPY lipids as staining agents of the actin-containing dimyristoylphosphatidylcholine (DMPC) vesicles (Limozin et al. 2003, Chemin et al. 2012). Fluoresence microscopy was utilized to observe and characterize the morphology of the structures.

In this chapter, results on particle size analysis of some sodachelins (C and D) and halochelins (D, E and F) produced by strains *Halomonas* sp. SL28 and SL01, respectively, at different ferric iron equivalents are presented. Their micelle-to-vesicle formation could be determined by dynamic light scattering and epifluorescence microscopy. To date, micelle-to-vesicle transition experiments have been performed on marine amphiphilic siderophores. Understanding the micelle-to-vesicle transition of selected halochelins could prove to be relevant for physiological aspects of iron uptake and future applications as drug delivery systems or other biotechnological applications.

Methods

Bacterial Strains Growth, Siderophore Production and Purification:

To produce and harvest amphiphilic siderophores (halochelins and sodachelins), *Halomonas* sp. SL01 and SL28 were grown in SLM at 5 % (w/v) NaCl and room temperature. To monitored growth and amphiphilic siderophore concentration optical density and CAS assay readings were taken twice a day, respectively. Siderophore

extraction from media supernatant (previously centrifuged and filtered) with methanol and water mobile phases on C18 Varian cartridge columns was performed when maximum siderophore production was reached. Extract concentration was done by overnight lyophilization or *in-vacuo* evaporation (40 °C, 4 – 6 h). Siderophore purification by HPLC was achieved with water (A)/acetonitrile (B) mobile phases (10 to 70 % gradient of B) in a C4 reverse column. Purified siderophore-containing fractions were pooled and lyophilized for further iron-mediated vesicle self assembly. Detailed methodology is found in Chapter 2.

Siderophore/Iron Solution Preparation:

First, purified, lyophilized siderophores were dissolved in 1 to 2 mL nanopure water. To check that CAS assay absorbance values were above 0.100, corresponding dilutions were made (1/5, 1/10, 1/25, 1/50 and 1/100) and CAS assays were performed as previously shown (Chapter 2). The dilution that gave the absorbance value between 0.100 and 0.200 was the one chosen for further studies.

Second, iron solutions were prepared from $FeCl_3 \cdot 6H_2O$ (Fisher) at different molar equivalents so that when mixed with the siderophore solution their final concentrations are: 0.5, 1.0, 1.5, 2.0, 3.0 and 4.0 Eq. After that, filtration with 0.22 µm PES filter was done. In a microcentrifuge tube (Fisher), 50 µL iron solutions were added to an equal volume of siderophore solutions and then tapped a few times to enhance mixing. In a disposable Uvette cuvette (Eppendorf), 80 µL were discharged, and the cuvette was sealed. At this point samples were ready for particle size analysis by dynamic light scattering (DLS).

Particle Size Analysis by
Dynamic Light Scattering (DLS):

To check for the micelle to vesicle transition as iron is added to the siderophore solution, dynamic light scattering was employed. The instrument used was a 90Plus Brookhaven Zeta Sizer. Samples were tapped a few times to ensure re-suspension of particles, placed in the cuvette chamber and analyzed at a 90° angle from the detector. The measuring time was set to 5 min at 25 °C and all samples were done in triplicate. Mean diameter and particle size distribution were recorded. Data analysis was performed using Microsoft® Excel.

Siderophore/Iron Solution Staining:

To verify vesicle formation in a qualitative manner, epifluorescence microscopy was employed. A study by a research group used different lipophilic dyes for *C. neoformans* vesicle staining (Nicola et al. 2009). Among those dyes the best performer in dyeing the vesicles was DiI (1,1'-dioctadecyl-3,3,3',3'-tetramethylindocarbocyanine perchlorate; Vibrant DiI cell labeling solution) from Molecular Probes® life technologies™. The dyeing protocol was done as follows. In brief, 1 µL of DiI was added to 100 µL siderophore and iron (0, 1.0 and 4.0 Eq.) solution. Ferric iron controls from $FeCl_3$ were prepared at the corresponding equivalents: 1 or 4 Eq. The mixtures were then incubated for 20 min at 37 ºC and then centrifugation was applied at 2,100 x g for 5 min to start the washing steps. Accumulation of stained vesicles was observed at the bottom of the microcentrifuge tubes and the supernatant was removed carefully. Vesicles were re-suspended in 100 µL of nanopure water at 37 ºC, and centrifuged at the same conditions. The wash step was repeated two more times and a regeneration period of 10 min followed.

Epifluorescence Microscopy by
Cryoembedding and Cryosectioning:

After staining with DiI, samples were ready for cryoembedding by applying a layer of Tissue-Tek® OCT compound into the mold containing 80 µL of previously stained siderophore/iron solution, and allowing freezing over dry ice. A second layer of OCT was applied and frozen (about 5 min). Samples were cryosectioned in 5 µm slabs in a Leica CM 1850 Cryostat and placed on Fisherbrand® Superfrost® Plus glass slides. Images were taken on dry mounts with a Nikon Eclipse E800 microscope equipped with a photometrics® CoolSNAP MYO camera. Objectives used were a 10X Nikon Plan Apo DICL ∞/0.17 WD 4.0, 20X Nikon Plan Apo DICM ∞/0.17 WD 1.0 and 60X Nikon Plan Apo DICM ∞/0.11-0.23 WD 0.15. Fluorescence of fluorophore dye was achieved by using a PhotoFluor® LM 75 89 North UV lamp and a TRITC filter for absorption (549 nm) and emission (565 nm) maxima. Image preparation and analysis (particle size count) was performed using MetaMorph® software. Statistical analysis of particle size data was done with Minitab 16 and 17®.

Results

Particle Size Analysis by DLS: Halochelins

To determine self-assembly in micelle or vesicle form of amphiphilic siderophores DLS was used as a quantitative method. Halochelins from *Halomonas* sp. SL01 and sodachelins from *Halomonas* were analyzed. It has been found in previous literature the hability of amphiphilic siderophores to form vesicles in their ferri form (meaning that they are chelating ferric iron). As equivalents of iron are added, a micelle-to-vesicle transition occurs and size tends to increase (Martinez et al. 2000, Owen et al. 2005). Halochelin E from the first family and Halochelin F from the second family showed similar patterns. At

no iron equivalents their mean diameter was 1.08 ± 0.17 and 6.03 ± 0.94 nm, respectively. When 1 Eq. Fe^{+3} was added to the solution the diameter increased to 105.2 ± 109.3 and 611.4 ± 297.6 nm, respectively. At the higher 4 Eq. Fe^{+3} the mean diameter increased for both to 419.8 ± 257.0 and 848.8 ± 478.2 nm, respectively. Note that Halochelin F has consistently a bigger mean diameter than Halochelin E. This may be due to a longer fatty acid tail from the former (C14 vs. C12).

Particle size distribution analysis was done for Halochelin E. At 4 Eq. of ferric iron there was greater distribution of vesicle sizes compared to the other treatments (Figure 4.1). Four different population sizes can be observed at 4 equivalents iron treatment: (1) les than 250 nm; (2) between 250 and 500 nm; (3) 600 to 1000 nm and (4) greater than 1000 nm. Decreasing iron content in the solution brings the distribution closer and less polydisperse (two populations are detected). At no iron added the distribution was monodisperse demonstrating more controlled micelle formation. There is a direct proportionality effect of ferric iron equivalents and vesicle population numbers (N).

However, for Halochelin F the 1 Eq. Fe^{+3} treatments showed higher vesicle population numbers than for 4 and 0 equivalents (Figure 4.2). The particle size distribution shows a polydisperse population, even more so than with Halochelin E. At 1 Eq. Fe^{+3} three populations are distinguished: (1) 0 to 150 nm; (2) 600 to 1200 nm sand (3) > 1500 nm. Similar distribution was found at 4 equivalents of ferric iron. At no iron added the distribution was monodisperse as in Halochelin E. Statistical analysis showed that ferric iron treatments were significantly different for both siderophores (Appendix E, Figures E4 and E5).

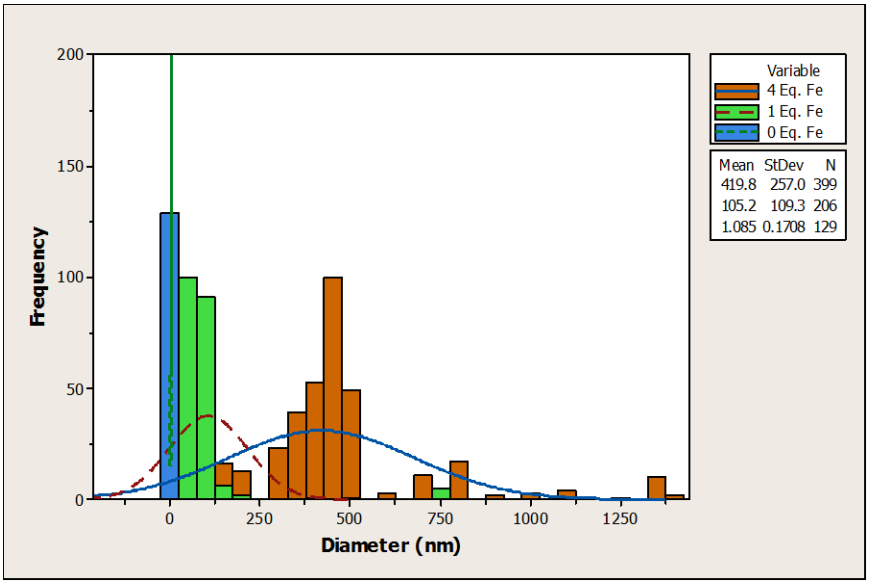

Figure 4.1. Particle size distribution for Halochelin E at different ferric iron equivalents. Means and standard deviations are presented for each treatment. N stands for the treatment population size.

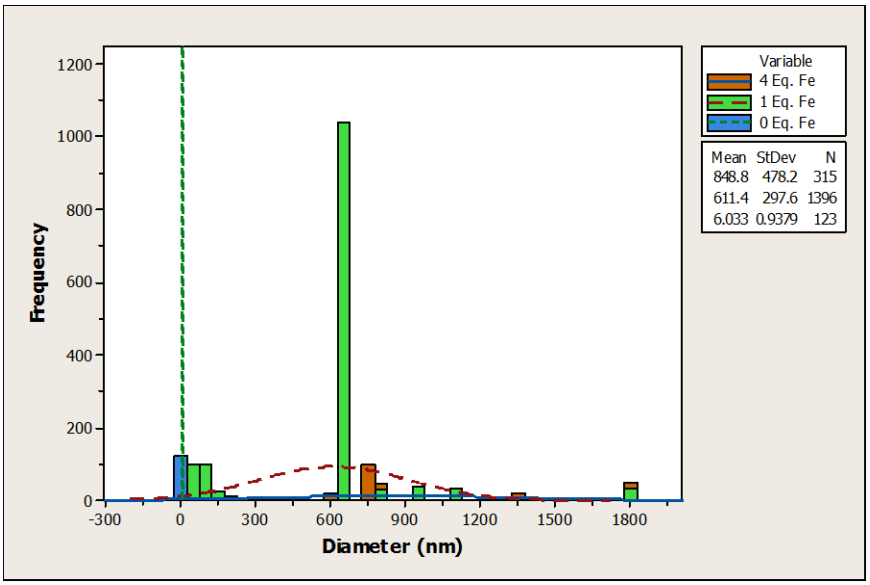

Figure 4.2. Particle size distribution for Halochelin F at different ferric iron equivalents. Means and standard deviations are presented for each treatment. N stands for the treatment population size.

Apparently not all amphiphilic siderophores followed the pattern of increasing vesicle mean diameter as iron was added. As an example, Halochelins B and C presented micelles sizes of about 1.03 ± 0.08 and 8.46 ± 1.84 nm, respectively. Their sizes at 1 equivalent of ferric iron were higher than those at 4 equivalents. A summary in Table 4.1 shows that for Halochelin B the 1 Eq. Fe^{+3} solution mean diameter was at 817.6 ± 610.3 nm and for 4 Eq. Fe^{+3} was 269.1 ± 410.4 nm. However, analysis showed statistical differences between 1 and 4 Eq. Fe^{+3} and their respective controls (see Figures E1 and E2, in Appendix E). A different case was observed for Halochelin D in which no statistical difference was observed (Figure E3, Appendix E). This also is observed in Table 4.1 where the 1 and 4 equivalents treatment mean diameters were not different from each other (430.3 ± 618.4 and 446.8 ± 371.9 nm, respectively).

Table 4.1. Mean diameters at different ferric iron equivalents for selected *Halomonas* sp. SL01 halochelins.

Halochelins	Equivalents of Fe^{+3}	DLS	
		Mean Diameter (nm)	Std. Dev. (nm)
B	0	1.03	0.08
	1	817.6	610.3
	4	269.1	410.4
C	0	8.46	1.84
	1	939.5	636.2
	4	724.7	569.2
D	0	1.08	0.13
	1	430.3	618.4
	4	446.8	371.9
E	0	1.08	0.17
	1	105.2	109.3
	4	419.8	257.0
F	0	6.03	0.94
	1	611.4	297.6
	4	848.8	478.2

Particle Size Analysis by DLS: Sodachelins

Particle size studies were also performed on sodachelins from *Halomonas* sp. SL28, also called sodachelins. Sodachelin D exhibited the behavior of micelle-to-vesicle transition that was reported in previous literature. At 0 Eq. Fe^{+3}, its micelle mean diameter was 2.1 ± 0.98 nm. That increased to 258.8 ± 340.3 nm at 1 equivalent of ferric iron and 297.1 ± 334.6 nm for the 4 equivalents treatment. Statistical analysis showed differences between the treatments and their respective controls. Particle size distribution was performed on the siderophore with the ferric iron treatments and showed polydisperse distribution at 4 Eq. Fe^{+3} than at 1 Eq. Fe^{+3} (Figure 4.3). The treatment of 4 equivalents of iron added showed two population sizes: (1) < 450 nm; (2) > 1000 nm. At 1 Eq. Fe^{+3} the population was more polydisperse showing three population sizes: (1) 0 to 450 nm; (2) 575 to 1000 nm and (3) 1700 to 2000 nm. When no iron was added the population was monodisperse as in previous particle size analyses. Statistical analysis of this siderophore at different ferric iron equivalent treatments showed that they are different from each other and their controls (see Figure E7, in Appendix E).

Sodachelin F did not followed the typical micelle-to-vesicle transition because its 1 Eq. ferric iron treatment showed higher mean diameter (434.3 ± 210.7 nm) compared to 4 Eq. Fe^{+3} (402.6 ± 333.8 nm). Also when iron was not added in the siderophore solution no micelle formation was detected. However, despite the two iron treatments having different means, no statistical differences were found (Figure E9, Appendix E). Sodachelin F particle size distribution revealed size differences at 4 equivalents of ferric iron added compared to 1 equivalent. At 4 equivalents smaller vesicles (less than 275 nm) were found (Figure 4.4). As more iron was added the vesicle population size (N) increased. For controls and other data regarding additional sodachelin particle size analysis, refer to Appendixes D and E.

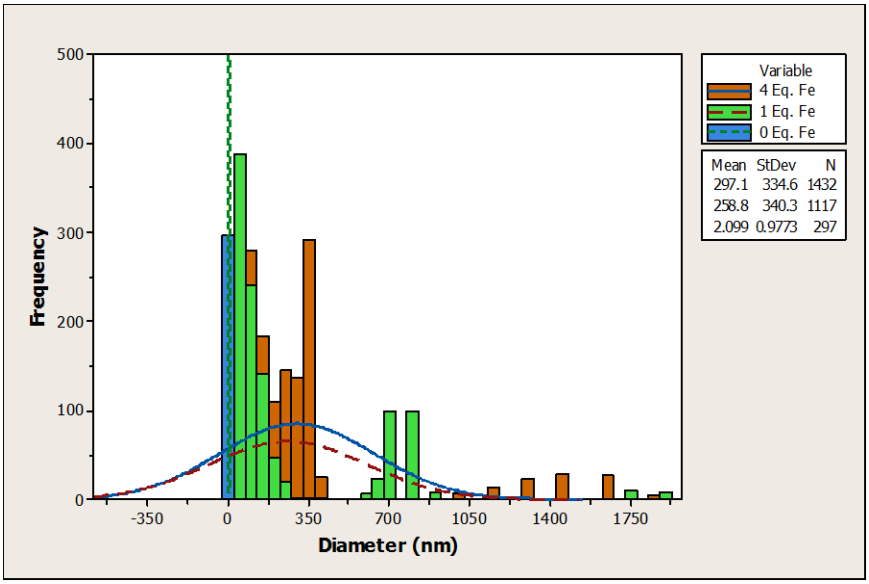

Figure 4.3. Particle size distribution for Sodachelin D at different ferric iron equivalents. Means and standard deviations are presented for each treatment. N stands for the treatment population size.

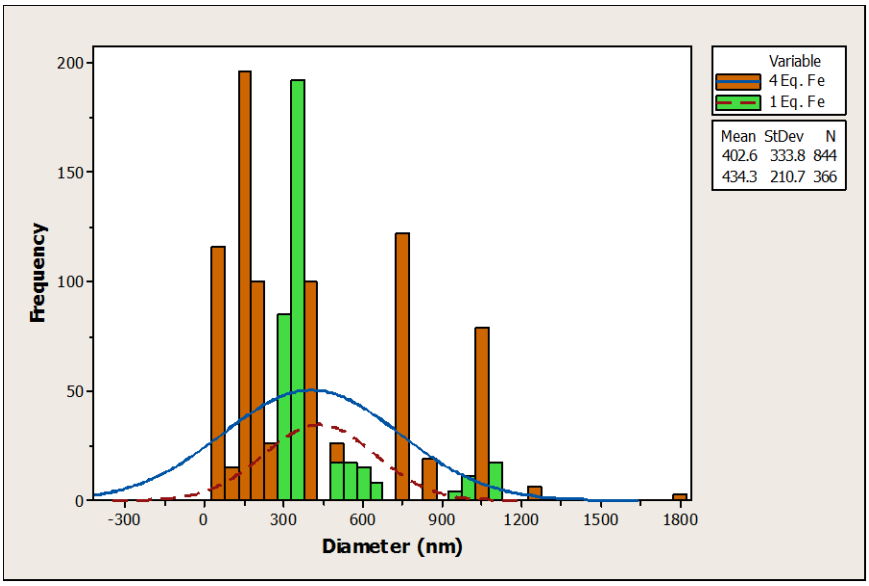

Figure 4.4. Particle size distribution for Sodachelin F at different ferric iron equivalents. Means and standard deviations are presented for each treatment. N stands for the treatment population size.

Table 4.2 shows that Sodachelins C and E did not follow the typical micelle-to-vesicle transition. Their 1 equivalent of ferric iron added treatment had higher mean

diameters than at 4 equivalents but high standard deviations suggested less size control in vesicle formation. No micelles were detected for Sodachelins E and F at 0 equivalent perhaps due to the limit of detection of the instrument (> 1 nm); thus, micelles for these sodachelins must be less than 1 nm in diameter.

Table 4.2. Mean diameters at different ferric iron equivalents for selected *Halomonas* sp. SL28 sodachelins.

Sodachelins	Equivalents of Fe^{+3}	DLS	
		Mean Diameter (nm)	Std. Dev. (nm)
C	0	1.06	0.15
	1	707.7	636.8
	4	561.7	565.1
D	0	2.1	0.98
	1	258.8	340.3
	4	297.1	334.6
E	0	Not detected	
	1	669.3	580.2
	4	423.2	446.9
F	0	Not detected	
	1	434.3	210.7
	4	402.6	333.8

Epifluorescence Microscopy for Halochelins

To confirm the micelle-to-vesicle transition in a qualitative way, epifluorescence microscopy was performed. A summary of vesicle and micelle sizes is presented in Table 4.3. Note the size difference at 0 Eq. Fe^{+3} of these microscopic studies with values obtained with dynamic light scattering. At this ferric iron treatment the mean diameters were between 400 to 700 nm, contrasting to no detection in some cases to 9 nm in size (using DLS). The size variability (by the standard deviation) was less than with the DLS. Fluoresecence was observed at no iron added for all halochelins. There was a

proportional relationship between mean diameter size and ferric iron added to Halochelin D, but statistical analysis showed that Halochelin D at 1 Eq. Fe^{+3} was not significantly different from 0 Eq. Fe^{+3} (Appendix E, Figure E10). This suggests that the size change was not necessarily related to ferric iron addition. In contrast, Halochelins E and F did not show direct proportionality and their statistically their sizes remained about the same (Figures E11 and E12 in Appendix E).

Table 4.3. Epifluorescence mean diameters for selected halochelins.

Halochelin	Equivalents of Fe^{+3}	Epifluorescence	
		Mean Diameter (nm)	Std. Dev. (nm)
D	0	562.3	318.4
	1	714.6	484.2
	4	904.8	655.9
E	0	437.2	152.0
	1	448.2	284.7
	4	563.6	320.2
F	0	405.7	159.6
	1	458.4	248.2
	4	465.8	203.7

Images showed an increase in fluorescence for Halochelin D as more iron was added confirming micelle-to-vesicle formation (Image 4.1). Agglomeration occured in this system due to their amphiphilic properties and this may be an effect of the cryoembedding technique. At the 4 Eq. Fe^{+3} treatment there were some large stained particles and those were assumed to be ferric iron crystals. Similar results were obtained for Halochelins E and F (Image 4.2 and 4.3). Fluorescence increased as ferric iron increased and agglomeration occurred at the highest ferric iron equivalent treatment. In all cases vesicle population size increased as ferric iron increased in solution. Less fluorescence was observed at 0 equivalents for both Halochelins E and F and the

particle sizes were smaller than that for Halochelin D. Also, both treatments of no iron added and 1 equivalent were very similar in fluorescence and this was confirmed by the statistical analysis previously mentioned. See Appendix F for more images of these siderophores.

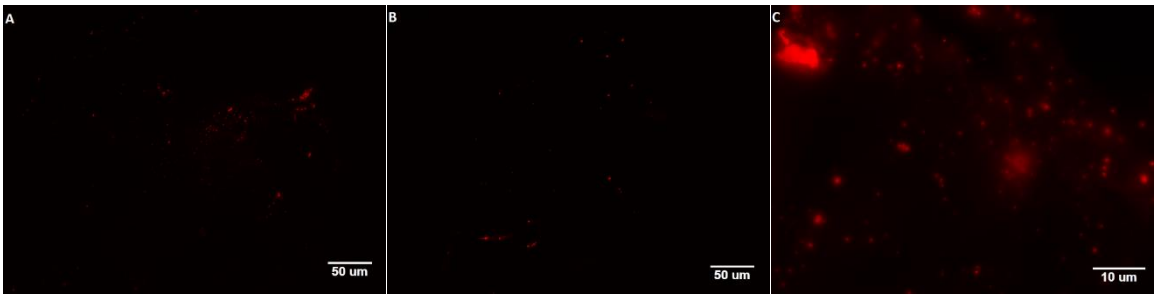

Image 4.1. Halochelin D epifluorescence images at different ferric iron equivalents: 0 (A), 1 (B) and 4 (C). Magnifications were at 10X (A and B) and 60X (C).

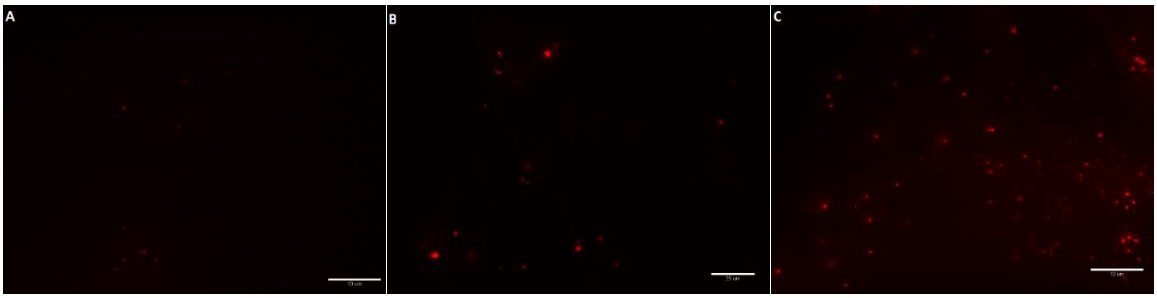

Image 4.2. Halochelin E epifluorescence images at different ferric iron equivalents: 0 (A), 1 (B) and 4 (C). Magnifications were at 20X (B) and 60X (A and C). Scale bars are at 10 (A and C) and 25 µm (B).

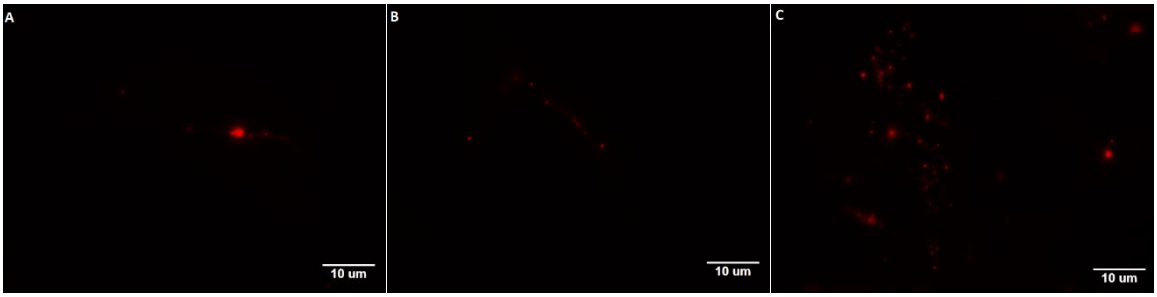

Image 4.3. Halochelin F epifluorescence images at different ferric iron equivalents: 0 (A), 1 (B) and 4 (C). Magnifications was at 60X.

Five images per treatment were analyzed to determine particle size distribution. In general, all had a normal distribution. In Figure 4.5, Halochelin D mean diameter increased but the vesicle population size (N) decreased from 0 to 1 Eq. Fe^{+3}. That number increased again at 4 equivalents of ferric iron added. The majority of the vesicle population was found in diameter sizes between 0 and 2000 nm. At 4 equivalents, polydispersity was observed confirming what DLS results previously showed and suggesting micelle-to-vesicle formation.

Particle size distribution for Halochelin E in Figure 4.6 showed normal distributions of vesicle size and more polydispersivity. The mean diameter for 0 and 1 Eq. Fe^{+3} of ferric iron remained unchanged as well as the vesicle population size (66 vs. 97 particles counted, respectively). However this number increases to 695 particles at 4 Eq. Fe^{+3} confirming the pattern of micelle-to-vesicle formation. For lower iron equivalents the size range was smaller (0 to 1000 nm) contrasting to a more disperse range at 4 equivalents (0 to 2000 nm).

When looking at Halochelin F, there was a normal particle size distribution analysis for all the ferric iron treatments (Figure 4.7). Mean diameters increased but due to high standard deviations no statistical significant difference was found. However the population size tends to be directly proportional to ferric iron added.

For halochelins D, E and F, fluorescence microscopy results correlated with micelle-to-vesicle transition due to an increase in vesicle population numbers (N). Particle size distributions for ferric iron equivalents controls were performed and they can be found on Appendix D.

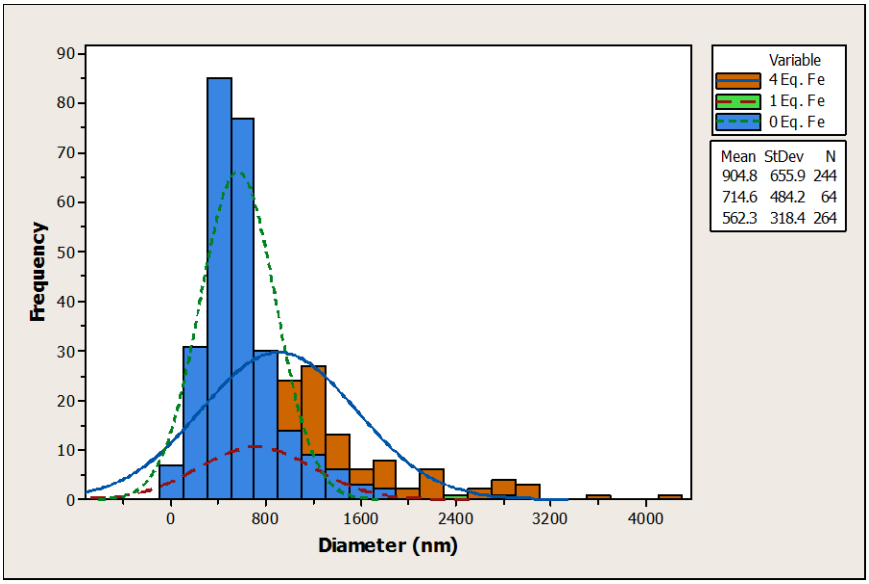

Figure 4.5. Particle size distribution for Halochelin D at different ferric iron equivalents. Means and standard deviations are presented for each treatment. N stands for the treatment vesicle population size.

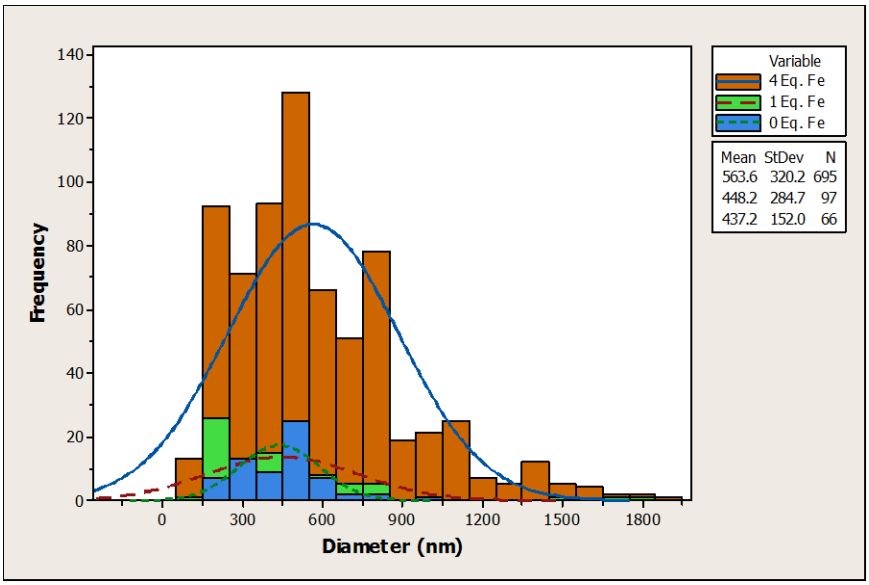

Figure 4.6. Particle size distribution for Halochelin E at different ferric iron equivalents. Means and standard deviations are presented for each treatment. N stands for the treatment vesicle population size.

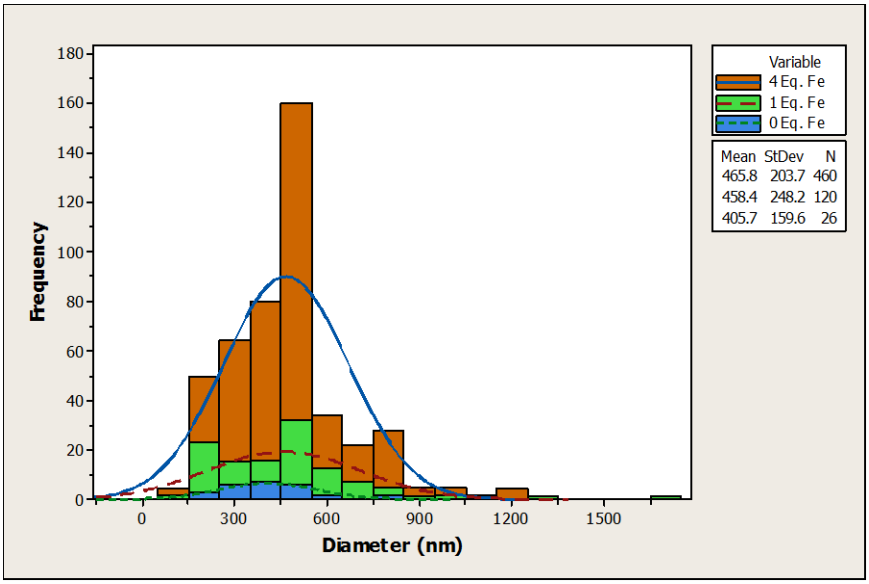

Figure 4.7. Particle size distribution for Halochelin F at different ferric iron equivalents. Means and standard deviations are presented for each treatment. N stands for the treatment vesicle population size.

Epifluorescence Microscopy for Sodachelins:

Sodachelins C and D were also analyzed by microscopy using epifluorescence. In Table 4.4 Sodachelin C at 0 Eq. Fe^{+3} showed a mean diameter of 489.7 ± 224.7 nm but when ferric iron was added at 1 equivalent level, the diameter size decreased to 420.8 ± 159.1 nm. Addition of more iron (4 Eq.) created an increase of the mean diameter size to 490.0 ± 353.4 nm. In all treatments the standard deviations were very high and statistical analysis demonstrated that only at 1 Eq. of ferric iron was there a statistical significance in size (Figure E13, Appendix E). Sodachelin D also showed no statistically significant difference among all the treatments suggesting a different micelle-to-vesicle formation from other siderophores. The mean diameter pattern was similar to that of Sodachelin C, decreasing in size at 1 Eq. of ferric iron and increasing when iron levels increased to 4 equivalents.

Table 4.4. Epifluorescence mean diameters for selected sodachelins.

Sodachelin	Equivalents of Fe^{+3}	Epifluorescence	
		Mean Diameter (nm)	Std. Dev. (nm)
C	0	489.7	224.7
	1	420.8	159.1
	4	490.0	353.4
D	0	673.6	562.0
	1	500.4	248.2
	4	588.5	406.8

Images for Sodachelin C showed little difference in fluorescence (Image 4.4) for all treatments. This suggests immediate vesicle self-assembly and perhaps a micelle-to-vesicle transition as in other amphiphilic siderophores. In contrast, Sodachelin D epifluorescence at 4 Eq. Fe^{+3} treatment was different from the 1 and 0 equivalents (see Image 4.5). However, no statistically significant difference was found (Figure E14, Appendix E). It seems that at 0 Eq. Fe^{+3} there was micelle formation in comparison to the 1 Eq. (which has less particles visible). See Appendix F for more images of these siderophores.

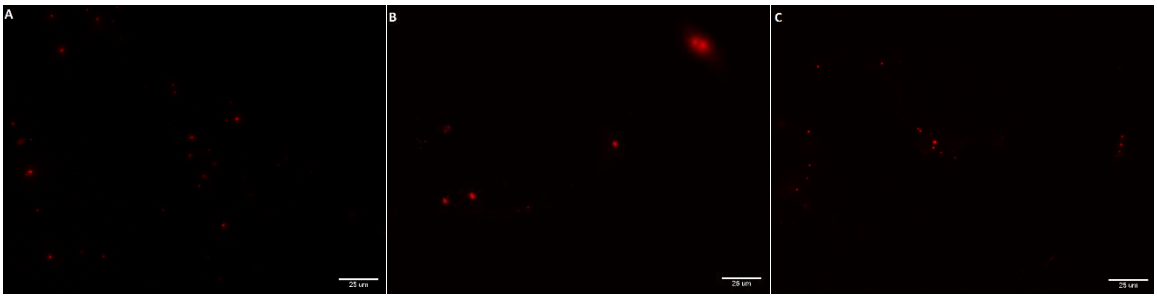

Image 4.4. Sodachelin C epifluorescence images at different ferric iron equivalents: 0 (A), 1 (B) and 4 (C). Magnifications were at 20X and scale bars are 25 µm.

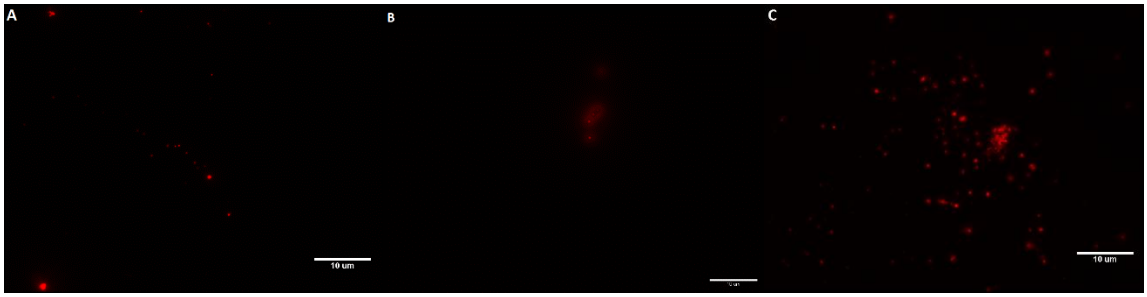

Image 4.5. Sodachelin D epifluorescence images at different ferric iron equivalents: 0 (A), 1 (B) and 4 (C). Magnifications were at 60X and scale bars are 10 μm.

Images were analyzed for particle size distribution as was done for the halochelins in the previous section. Normal distributions were found for each treatment and siderophore. In Figure 4.8, Sodachelin C presented bigger sizes of particles (>1200 nm) at 4 equivalents ferric iron. This may suggest the formation of iron oxides in the siderophore-iron solution as happened for the halochelins at the same treatment. Mean diameter at 0 equivalents was 489.7 ± 224.7 nm and that contrasts to the DLS value of about 1 nm. This may have happened due to agglomeration causing the size of the micelles to increase and making them difficult to detect individually. Adding 1 equivalent of ferric iron decreased the mean diameter (420.8 ± 159.1 nm) and adding 4 equivalents restored sizes to the no-iron treatment value (490.0 ± 353.4 nm). Population polydispersity was found at high iron equivalent treatment and not at the low-iron or no-iron ones. The population sizes did not change for other siderophores (like Halochelin F). Statistical analysis by one-way ANOVA revealed a significant difference at the 1 Eq. Fe^{+3} treatment suggesting vesicle formation due to ferric iron addition.

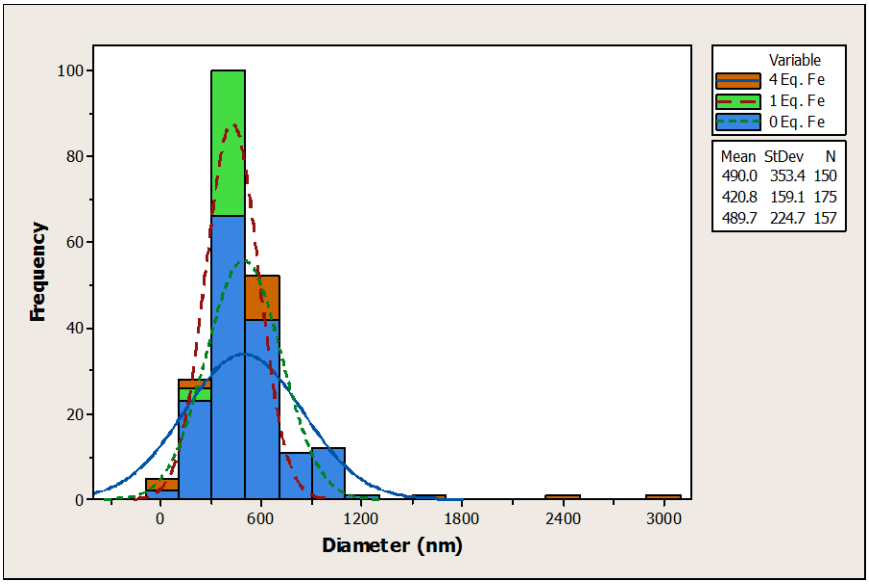

Figure 4.8. Particle size distribution for Sodachelin C at different ferric iron equivalents. Means and standard deviations are presented for each treatment. N stands for the treatment vesicle population size.

The experiment of Sodachelin D is a very particular one and results similar to Halochelin D. Higher vesicle population size were expected to be at high-iron and low-iron equivalents, but experimental results did not confirmed this. At 4 Eq. Fe^{+3} vesicle population was N = 405 and at low iron (1 Eq. Fe^{+3}) was N = 14 (Figure 4.9). The no-iron treatment reported a vesicle population size of 110. However, the mean diameter at no-iron was the highest at 673.6 ± 562.0 nm suggesting, as in Sodachelin C, some agglomeration of micelles. The mean diameter decreased to 500 nm when 1 Eq. Fe^{+3} was added and more iron again increased the mean diameter. One-way ANOVA statistical analysis revealed no difference among the treatments suggesting that vesicle formation may be due to other physical or chemical variables not accounted for in this experiment.

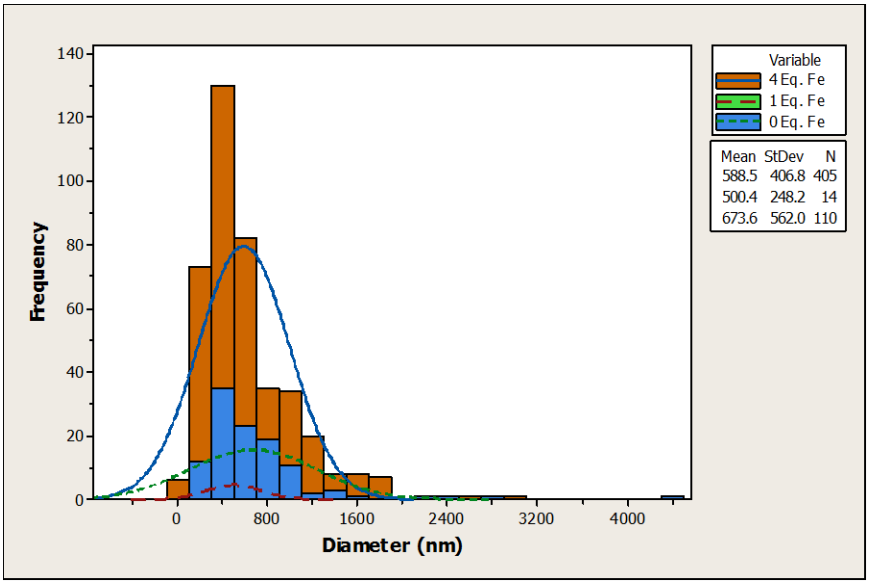

Figure 4.9. Particle size distribution for Sodachelin D at different ferric iron equivalents. Means and standard deviations are presented for each treatment. N stands for the treatment vesicle population size.

Discussion

Previous research has presented vesicle and micelle formation of amphiphilic siderophores (Martinez et al. 2000, Martinez & Butler 2007). This physicochemical phenomenon is in part due to the molecule's own nature and is enhanced via metal chelation with: zinc, cadmium or ferric iron (Owen et al. 2005, Owen et al. 2007). The results obtained during this experiment showed the metal-dependency of micelle-to-vesicle formation of halochelins and sodachelins produced from *Halomonas* sp. SL01 and SL28, respectively. Most of the siderophores studied formed micelles when over their *cmc* in aqueous solution. In theory, it is believed that the micelle-to-vesicle transition occurrs due to amphiphilic siderophore conformational change from the conical to cylindrical form when chelation of ferric iron takes place (Israelachvili et al. 1980).

A dynamic light scattering method was implemented to determine, in a quantitative way, vesicle and micelle diameters. Some halochelins (D, E and F) and

sodachelins (D and F) were similar to previous models discussed. Ferric addition and its subsequent chelation mediated micelle and vesicle formation in a concentration-dependent fashion. As more equivalents of iron were added more vesicles were formed and their diameter size increased. Halochelins D, E and F created relatively small micelles (1 to 6 nm) and their vesicle sizes increased at 1 or 4 equivalents of ferric iron. It is important to note that the molecule structure may play a role in the different sizes that were obtained by DLS. Halochelin F presented the bigger diameter size (848 nm) contrasting to medium-sized diameters of Halochelins D and E (446.8 and 419 nm, respectively). This may be due to Halochelin F having a longer fatty acid moiety (C14:0) versus a C12:0 for both Halochelin D and E fatty acids moieties (Figure 4.10). In contrast, Halochelin B was the siderophore with smaller vesicle diameter size at 4 equivalents. This may be due to its shorter fatty acid moiety (C10 compared to the remaining halochelins (C12 or C14).

For the sodachelins the structure of the molecule may be playing a similar role as for the halochelins. Both Sodachelins E and F had larger mean diameters and this may be due to their longer C14 fatty acid moieties. Also the double bond in the fatty acid may play a role in vesicle size because Sodachelin C (C12:1 ω7c) has a bigger diameter than Sodachelin D (C12:0). The hydroxyl (-OH) group on the fatty acid may also play a role on vesicle size due to repulsive interactions of the fatty acid moieties. Using this example we can find Halochelin E (with no –OH group at its fatty acid) with a smaller mean diameter size compared to Halochelin C (with –OH grpup on the third carbon position of its fatty acid). Even across families (Halochelin E vs. Halochelin D or F) the group seems to be relevant. Previous research has been done on different marinobactins with different fatty acid lengths, but no difference in sizes for micelles or vesicles were found (Owen et al. 2007).

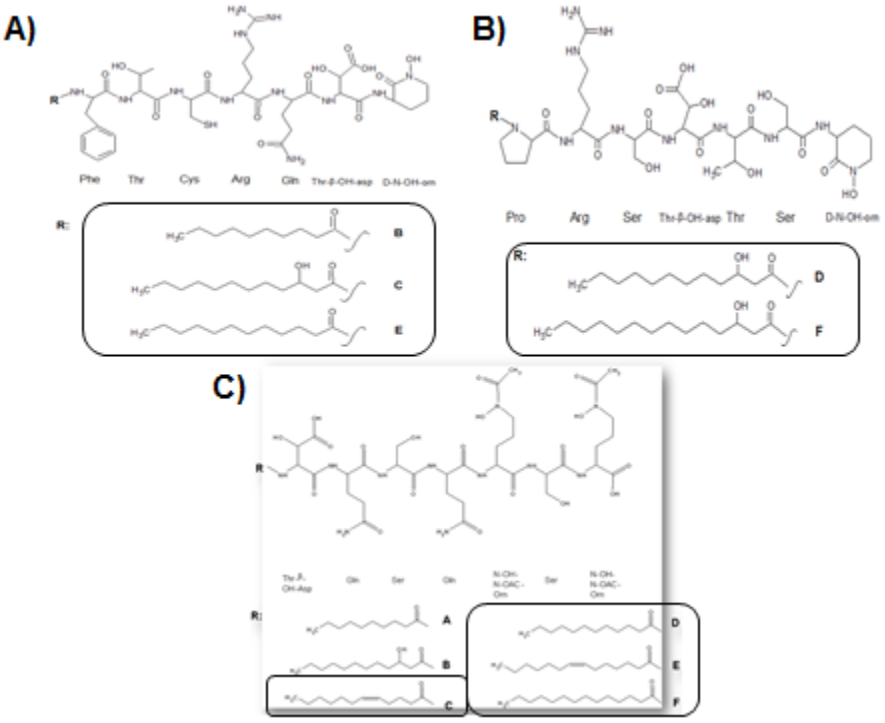

Figure 4.10. Halochelins and sodachelins selected for micelle-to-vesicle studies. Shown are first halochelin family (A), second halochelin family (B) and sodachelins (C). Circled fatty acids correspond to studied amphiphilic siderophores.

One important observation during microscopic studies was the high size particles in the no-iron treatments had. Previous researchers have found agglomeration of micelles from synthetic amphiphilic siderophore-like ligands (Bednarova et al. 2008) and this might be the reason for such results. Also polydispersity of diameter size was found to be more common at high ferric iron equivalents for the amphiphilic siderophores studied. This phenomena was found in a report by Owen and co-workers when 3 Eq. of Zn^{+2} were added to a ferric iron-marinobactin E complex (Owen et al. 2007). The group confirmed, via cryo-TEM and small angle neutron scattering (SANS), that the vesicles were multilamellar in nature, something that could not be seen in this study with the fluorescence technique. The variability in mean diameter between samples (see Appendix D, Figures D1 – D70) has also been described in previous research (Owen et

al. 2005, Owen et al. 2007). Future studies for the amphiphiles analyzed here should include cryo-TEM and SANS to confirm what DLS and epifluorescence microscopy revealed.

The significance or importance of micelle or vesicle formation in amphiphilic siderophores could rest on maintaining the integrity of the molecule avoiding denaturation. Protection of decapeptides was described previously (Lee et al. 1999). Where a decapeptide attached to two C14 fatty acids was developed. The lipopeptide self-assembled in tubular or helical forms and when trypsin was added no hydrolysis occurred. Solubilization of the lipopeptide with detergent caused micelle formation and easy access of trypsin to the head group and subsequent hydrolysis. Hydrolysis has been reported, specifically fatty acid hydrolysis from the polar head group, when ferric iron is chelated in the presence of natural sunlight in a phenomenon called photoreactivity (Barbeau et al. 2001, Barbeau et al. 2003, Butler & Theisen 2010a). The research studied amphiphilic siderophores (aquachelins) produced by *Halomonas aquamarina* DS40M3. The photoproduct was composed of ferrous iron (Fe^{+2}) and the cleaved fatty acid and head group. The head group lost its β-OH-asp moiety and this caused less ferric iron affinity by a decrease of the conditional stability constant. It is very important to note that iron-aquachelin complexes were not over their critical micelle concentration and thus, future studies of halochelin and sodachelin micelle-to-vesicle formation may investigate the possible protection from photoreactivity of these physical structures.

Studying micelle-to-vesicle formation will help us undertand how this structural conformations could be applied in other fields of science or biomedicine. Previous applied research on siderophore ligands and conjugates have been reported (Ghosh & Miller 1993, Miller 1995, Ghosh et al. 1996). The science behind these studies relies in

conjugating an antibiotic, or antimicrobial, to a ferri-siderophore complex and employed as a “Trojan horse” delivery system. The antibiotic-ligand-siderophore complex is internalized by the pathogenic bacteria iron uptake transport system. Release of the antibiotic occurs as the complex is recycled by the cell metabolism. The disadvantage is that the complex is not protected from enzymes that may degrade the antimicrobial or the complex. In contrast, utilizing vesicles or micelles could hinder this degradation effect. Lipid-based (liposomes) delivery systems have been studied as therapeutics for bacterial infections (Alhariri et al. 2013, He et al. 2013) or tumors (Kontogiannopoulos et al. 2014, Qin et al. 2014). He and co-workers (2013) studied the effects of polymyxin B liposomes on *P. aeruginosa*’s mice lung infection models. Bacterial burden was reduced and prolonged survival of animals was observed. In tumor biology research, *in vitro* and *in vivo* experiments were performed utilizing chlorotoxin-loaded liposomes as therapeutic agents for breast cancer (Qin et al. 2014). Toxicity assays revealed drug-loaded liposome binding to tumors. BALB/c mice were treated and size reduction of metastatic tumor was observed. Iron-mediated vesicle formation could also lead to the utilization of these structures as magnetic-responsive biomaterials. Iron response to magnetic fields makes the element a prime candidate for medical and biomedical imaging applications (Quarta et al. 2008, Liu et al. 2012). Further studies on amphiphilic properties of halochelin and sodachelin should be done to determine the potential as drug carriers (antibiotics, antimycotics, and antitumorals) and imaging agents. The studies could look at the vesicle incorporation of the drug and describe the system at pharcokinetical and pharmacological levels. Vesicle-microbe and vesicle-tumor interactions could be studied to help determine how the internalization process occurs.

CHAPTER FIVE

GENERAL CONCLUSION AND FUTURE APPROACHES

We have described the biological importance of iron: every living organism requires it for several cellular and metabolic functions and microorganisms are not the exception. Several ferric iron uptake systems have evolved over time and microorganisms have been in this evolutionary race in order to make iron more bioavailable. Siderophore-mediated iron acquisition is the most important iron uptake system for them and they depend on not only their own produced siderophores but also on other microorganisms' siderophores. This helps them to be competitive and in their eventual success as species in overcoming environmental constraints or challenges. Another example is the ability to obtain iron from other sources like heme or transferrin/lactoferrin systems from higher organisms (like pathogens infecting humans). The variability in siderophore molecules is very diverse; catecholates, hydroxamates and carboxylates are just some of the molecular features present in siderophores.

The ubiquituosness of ferric iron in the planet also contributes to the competition to obtain it. No matter the environment in which the organism lives, an iron acquisition system must be developed to help in its survival. We presented the physiological aspects of two haloalkaliphiles (*Halomonas* sp. SL01 and SL28, isolated from Soap Lake, WA) and how their siderophore production was affected by certain environmental conditions. Sodium chloride concentration, temperature and pH of the medium demonstrated to affect both bacterial isolates growth and siderophore production. The information obtained helped optimize for siderophore production and eventual molecular structure studies. Amphiphilic siderophores were identified, purified and characterized by mass spectrometry and two halochelin families were discovered to be produced by

Halomonas sp. SL01. Studies on iron-mediated vesicle-self assembly were performed quantitatively and qualitatively. A micelle-to-vesicle transition was directly proportional to ferric iron concentration. The transition was observed and confirmed qualitatively by epifluorescence microscopy for selected halochelins and sodachelins.

Future Projects and Approaches

Future considerations in amphiphilic siderophore and physiological characteristics of the bacterial isolates studied here could be on how the presence of other metals affects siderophore production. Heavy metals are present in diverse environments like: fresh water, mine drainage and soils (Baceva et al. 2014, Gao et al. 2014, Gbadebo & Ekwue 2014). Bacterial composition of these contaminated environments could change as per phylogentic analyses that demonstrated the presence of β- and γ-Proteobacteria and Firmicutes (Zhu et al. 2013). Previous hypersaline lake *Bacillus* and *Amphibacillus* isolates have been studied for potential chromium (VI) bioreduction (Ibrahim et al. 2011a, b). To study how heavy metal affects both *Halomonas* sp. SL01 and SL28 would be of interest in the future. Experiments could include chromium, lead or arsenic bioreduction assays that eventually will determine if these isolates could be employed in bioremediation techniques. The assays should also look at different contaminated environments: soils and hypersaline lake water or seawater. Growth, siderophore production, heavy metal concentration over time and gene up or down regulation could be some of the variables to measure and analyze. Future projects on genome composition are discussed ahead.

Due to current low cost we could consider sequencing and annotating both isolates genomes. We could characterize genes that participate in different metabolic reactions of the cell. After annotating the genomes, then, by utilizing bioinformatics, we

could determine gene products and functions. In theory, this will provide information of which genes and their products (enzymes) may be involved in i.e. bioremediation of heavy metals, amphiphilic siderophore production and iron uptake among other metabolic processes. Siderophores in general are synthesized by non-ribosomal peptidyl synthetases (NRPSs) (Crosa 2004). These enzymes have different domains each one with specialized functions: adenylation, peptidyl carrier protein and condensation. Enterobactin, myxochelin, exochelin, vibriobactin and yersiniabactin synthetases are the most studied NRPSs. It would be interesting to validate NRPS presence and domain composition in the strains (SL01 and SL28) studied. For iron uptake, studies should focus on halochelin and sodachelin transport. Siderophore receptor, ferric binding proteins and ABC transporters genes and structure should be identified by genomic, proteomic and biophysical analyses. Siderophore receptors have β-barrel (transmembrane) and cork domains. The enterobactin receptors FhuA, FecA and FepA are the most studied and crystal structures have been obtained. It should be of interest to elucidate halochelin and sodachelin receptors on *Halomonas* sp. SL01 and SL28, respectively, compare the structures to previously described siderophore receptors.

Siderophores not only could participate in the ferric iron uptake but also as a biocontrol strategy that increases the survival of the producing microorganism. Rhizobial-synthesized siderophores have been found to inhibit the growth of plant pathogens and increase plant growth. Halochelins and sodachelins effects on plants associated with soda lakes shores should be investigated in an attempt to describe future biocontrol strategies. This could determine if there is any agricultural potential for amphiphilic siderophores either as biocontrol or growth promoting natural product.

Other organisms produce short peptides, called antimicrobial peptides, which have antimicrobial and immunomodulator properties. These peptides (i.e.

cephalosporins, echinomycin, valinomycins, and erythromycins) resemble in the primary structure to the polar head group of amphiphilic siderophores like halochelins or sodachelins. Could be possible that halochelins or sodachelins have antimicrobial properties against pathogens? Simple biological assays utilizing pure halochelins or sodachelins extracts against pathogenic microorganisms could determine if antimicrobial properties belong to these amphiphilic siderophores. The experiments could also determine and measure minimum inhibitory concentrations of halochelins or sodachelins. Another question that arises: will the fatty acid tail interfere or enhance the antimicrobial properties of halochelins or sodachelins? Hydrolysis of the fatty acyl moiety should follow and compre the functionality and antimicrobial properties of the head group *versus* the amphiphile. The antimicrobial properties of sodachelins and halochelins should be investigated for future applications in agriculture and biomedicine, developing novel methods to control plant pathogens or natural antibiotics.

Siderophores are small iron chelating compounds. However previous research done described the chelation of other metals by siderophores (Puskin 1977, Harris et al. 2007, Mullen et al. 2007, Owen et al. 2007). Harris and co-workers described the chelation of borate to vibriferrin, rhizoferrin and petrobactin. The conformation of the B-siderophore complex was different from the iron-siderophore complexes and this may be to distinguish iron uptake from boron uptake (Harris et al. 2007). Desferrioxamine B could also chelate uranium (VI) (Mullen et al. 2007). Although uranium complexation by siderophores may seem unclear there is the possibility that this could describe eventually how the complexation occurs and if bioremediation applications could develop. Phospholipid membranes also chelate divalent cations like manganese (Puskin 1977). It might be of interest to determine if micelles or vesicles formed by halochelins or sodachelins could actually bind other metals (Cd, U, Pb, Zn, La or Mn) and determine

conformational changes in the complex when compared to iron-siderophore complexes. Metal chelation has focused on Fe-siderophore complexes and their micelle-to-vesicle transitions caused by other cations. Observation and studies of other metal-amphiphilic siderophores should take place to discover other conformational patterns and effects. Eventual applications are soil, fresh water or marine bioremediation and heavy metal chelation therapies.

Biochemical and biophysical constants and properties characterization should be addressed on halochelins and sodachelins. Dissociation constants should be determined and compared to other metals, especially divalent cations like iron. Solubility constants could be also studied and determined and check for membrane portioning. The information obtained would provide a clear idea of how amphiphilic siderophores interact with iron and other metals as well as how the complexes are transported across biological membranes.

Siderophores are shuttled to the extracellular space and should be functional for eventual internalization for iron uptake. This functionality could be hindered by different enzymes, environmental conditions, or light. Photoreactivity has been described in some marine amphiphilic siderophores (Barbeau et al. 2003). Iron-bounded marinobactins and aquachelins react with light to cleave the fatty acyl moiety from the head group and reduce ferric iron. The head group still maintains affinity for ferric iron but with a higher dissociation constant than the acylated headgroup. In future experiments we should study the possibilities of amphiphilic siderophore photoreactivity and observe if the micelle or vesicle forms could protect the fatty acid from cleaving from the head group. This could provide information on the biogeochemical cycling of iron in soap lakes and also a siderophore evolution explanation.

Micelle-to-vesicle formation will help us undertand how this structural conformations could be applied in biomedicine or as biotechnological entities. Siderophore-antibiotic conjugates have been reported as “Trojan horse” delivery system (Ghosh & Miller 1993, Miller 1995, Ghosh et al. 1996). The disadvantage is that the complex is not protected from enzymes that may degrade the antimicrobial or the complex. In contrast, utilizing vesicles or micelles could hinder this degradation effect. Lliposomes delivery systems have been studied previously as therapeutics for bacterial infections or tumors. In infectious disease models polymyxin B liposomes on *P. aeruginosa*’s bacterial burden was reduced and prolonged survival of animals was observed (He et al. 2013). In tumor biology research, toxicity assays revealed drug-loaded liposome binding to tumors and size reduction of metastatic tumor was observed. (Qin et al. 2014). Due to the paramagnetic properties of iron, iron-mediated vesicle formation could also lead to the utilization of these structures as magnetic-responsive biomaterials for biomedical imaging applications (Quarta et al. 2008, Liu et al. 2012). Future studies on amphiphilic properties of halochelin and sodachelin should focus on determining the potential as antimicrobials or antitumorals carriers and imaging agents. The studies should observe how the drug could be incorporated in the vesicle. Emulsion preparations could help in the final formulation of the drug-loaded vesicle delivery system and drug loading experiments would determine that amount of drug incorporated in the system. Description of the system at pharcokinetical and pharmacological levels is of importance for potential utilization as drug carriers. Vesicle-microbe and vesicle-tumor interactions should be studied to characterize pharmacodynamical properties of drug-loaded amphiphilic siderophore vesicles or micelles. Stability of the drug-loaded siderophore vesicle is also of interest. Future studies should look at different storage conditions (pH of solution, temperature, solvents, time of storage) and determine which

one (s) help maintain the delivery system functionality and overall properties. Another important question to ask is if drug bioavailability is affected by amphiphilic vesicle delivery systems. *In vivo* bioavailability studies on mice or laboratory animals could be employed to answer this question.

Scientists must pay close attention to co-regulatory metabolic pathways in halophiles. Control and genetic regulation of metabolic pathways is of importance for cell survival and wise use of enzymatic machinery. There is evidence that both osmotic stress response and iron transport in *Chromohalobacter salexigens* are regulated at the transcriptional level by the iron transport regulatory protein, Fur (Argandona et al. 2010). There could be a direct relationship of osmotic stress and iron uptake systems in the *Halomonas* isolates. Research should also focus on oxidative stress responses, quorum sensing mechanisms, biofilm formation and how all these metabolic processes affect one another and iron uptake regulatory circuitry. Biofilm formation has been linked to iron uptake of microorganisms and it would be interesting if *Halomonas* sp. SL01 or SL28 produces more siderophore in biofilm than planktonic form. In terms of quorum sensing research, analyses should focus at the amphiphilic siderophore's fatty acyl moiety and determine if there is any relationship with acyl-homoserine lactone production (quorum sensing) and ferric iron uptake regulation.

This research described the physiological optimization of amphiphilic siderophore production and iron-mediated vesicle self assembly. There is still more work to be done in terms of strain characterization by genomics and proteomics. Experiments on metal chelation with amphiphilic siderophores and the potential biotechnological applications must start in order to understand better the biology and biogeochemical purpose of siderophores in extreme environments. With recent advances in molecular biology,

biochemistry and biophysics it would be possible to describe in detail amphiphilic siderophore regulation, synthesis and transport.

REFERENCES CITED

REFERENCES CITED

Abdul-Tehrani H, Hudson AJ, Chang YS, Timms AR, Hawkins C, Williams JM, Harrison PM, Guest JR, Andrews SC (1999) Ferritin mutants of Escherichia coli are iron deficient and growth impaired, and fur mutants are iron deficient. Journal of Bacteriology 181:1415-1428

Abergel RJ, Wilson MK, Arceneaux JEL, Hoette TM, Strong RK, Byers BR, Raymond KN (2006) Anthrax pathogen evades the mammalian immune system through stealth siderophore production. Proceedings of the National Academy of Sciences of the United States of America 103:18499-18503

Achard MES, Chen KWW, Sweet MJ, Watts RE, Schroder K, Schembri MA, McEwan AG (2013) An antioxidant role for catecholate siderophores in Salmonella. Biochemical Journal 454:543-549

Alhariri M, Azghani A, Omri A (2013) Liposomal antibiotics for the treatment of infectious diseases. Expert Opinion on Drug Delivery 10:1515-1532

Amin S, Green D, Kupper F, Carrano C (2009) Vibrioferrin, an Unusual Marine Siderophore: Iron Binding, Photochemistry, and Biological Implications. Inorganic Chemistry 48:11451-11458

Amin SA, Green DH, Al Waheeb D, Gaerdes A, Carrano CJ (2012) Iron transport in the genus Marinobacter. Biometals 25:135-147

Anderson I, Scheuner C, Goker M, Mavromatis K, Hooper SD, Porat I, Klenk HP, Ivanova N, Kyrpides N (2011) Novel Insights into the Diversity of Catabolic Metabolism from Ten Haloarchaeal Genomes. Plos One 6:12

Andrews SC, Robinson AK, Rodriguez-Quinones F (2003) Bacterial iron homeostasis. Fems Microbiology Reviews 27:215-237

Argandona M, Nieto JJ, Iglesias-Guerra F, Calderon MI, Garcia-Estepa R, Vargas C (2010) Interplay between Iron Homeostasis and the Osmotic Stress Response in the Halophilic Bacterium Chromohalobacter salexigens. Applied and Environmental Microbiology 76:3575-3589

Aston JE, Peyton BM (2007) Response of Halomonas campisalis to saline stress: changes in growth kinetics, compatible solute production and membrane phospholipid fatty acid composition. Fems Microbiology Letters 274:196-203

Baceva K, Stafilov T, Matevski V (2014) BIOACCUMULATION OF HEAVY METALS BY ENDEMIC VIOLA SPECIES FROM THE SOIL IN THE VICINITY OF THE As-Sb-Tl MINE "ALLCHAR", REPUBLIC OF MACEDONIA. International Journal of Phytoremediation 16:347-365

Banin E, Vasil ML, Greenberg EP (2005) Iron and Pseudomonas aeruginosa biofilm formation. Proceedings of the National Academy of Sciences of the United States of America 102:11076-11081

Barbeau K, Rue EL, Bruland KW, Butler A (2001) Photochemical cycling of iron in the surface ocean mediated by microbial iron(III)-binding ligands. Nature 413:409-413

Barbeau K, Rue EL, Trick CG, Bruland KT, Butler A (2003) Photochemical reactivity of siderophores produced by marine heterotrophic bacteria and cyanobacteria based on characteristic Fe(III) binding groups. Limnology and Oceanography 48:1069-1078

Barbeau K, Zhang GP, Live DH, Butler A (2002) Petrobactin, a photoreactive siderophore produced by the oil-degrading marine bacterium Marinobacter hydrocarbonoclasticus. Journal of the American Chemical Society 124:378-379

Barelmann I, Fernandez DU, Budzikiewicz H, Meyer JM (2003) The pyoverdine from Pseudomonas chlororaphis D-TR133 showing mutual acceptance with the pyoverdine of Pseudomonas fluorescens CHA0. Biometals 16:263-270

Basu S, Deobagkar DD, Matondkar SGP, Furtado I (2013) Culturable Bacterial Flora Associated with the Dinoflagellate Green Noctiluca miliaris During Active and Declining Bloom Phases in the Northern Arabian Sea. Microbial Ecology 65:934-954

Bednarova L, Brandel J, d'Hardemare A, Bednar J, Serratrice G, Pierre J (2008) Vesicles to concentrate iron in low-iron media: An attempt to mimic marine siderophores. Chemistry-a European Journal 14:3680-3686

Bergeron A, Pucci L, Bezzi P, Regazzi R (2014) Analysis of Synaptic-Like Microvesicle Exocytosis of B-Cells Using a Live Imaging Technique. Plos One 9

Bergeron RJ, Bharti N, Singh S, McManis JS, Wiegand J, Green LG (2009) Vibriobactin Antibodies: A Vaccine Strategy. Journal of Medicinal Chemistry 52:3801-3813

Bergeron RJ, Liu ZR, McManis JS, Wiegand J (1992) STRUCTURAL ALTERATIONS IN DESFERRIOXAMINE COMPATIBLE WITH IRON CLEARANCE IN ANIMALS. Journal of Medicinal Chemistry 35:4739-4744

Berti AD, Thomas MG (2009) Analysis of Achromobactin Biosynthesis by Pseudomonas syringae pv. syringae B728a. Journal of Bacteriology 191:4594-4604

Bertrand S, Larcher G, Landreau A, Richomme P, Duval O, Bouchara JP (2009) Hydroxamate siderophores of Scedosporium apiospermum. Biometals 22:1019-1029

Bister B, Bischoff D, Nicholson GJ, Valdebenito M, Schneider K, Winkelmann G, Hantke K, Sussmuth RD (2004) The structure of salmochelins: C-glucosylated enterobactins of Salmonella enterica. Biometals 17:471-481

Boiteau RM, Fitzsimmons JN, Repeta DJ, Boyle EA (2013) Detection of Iron Ligands in Seawater and Marine Cyanobacteria Cultures by High-Performance Liquid Chromatography-Inductively Coupled Plasma-Mass Spectrometry. Analytical Chemistry 85:4357-4362

Bonde GJ (1967) POLLUTION OF A MARINE ENVIRONMENT. Journal Water Pollution Control Federation 39:R45-&

Bossier P, Verstraete W (1986) DETECTION OF SIDEROPHORES IN SOIL BY A DIRECT BIOASSAY. Soil Biology & Biochemistry 18:481-486

Bou-Abdallah F, Lewin AC, Le Brun NE, Moore GR, Chasteen ND (2002) Iron detoxification properties of Escherichia coli bacterioferritin - Attenuation of oxyradical chemistry. Journal of Biological Chemistry 277:37064-37069

Boyer E, Bergevin I, Malo D, Gros P, Cellier MFM (2002) Acquisition of Mn(II) in addition to Fe(II) is required for full virulence of Salmonella enterica serovar Typhimurium. Infection and Immunity 70:6032-6042

Braud A, Jezequel K, Bazot S, Lebeau T (2009) Enhanced phytoextraction of an agricultural Cr- and Pb-contaminated soil by bioaugmentation with siderophore-producing bacteria. Chemosphere 74:280-286

Butler A, Martinez J, Barbeau K (2001) Reactivity of new self-assembling amphiphilic siderophores and alpha-hydroxy acid-containing siderophores from oceanic bacteria. Journal of Inorganic Biochemistry 86:30-30

Butler A, Theisen R (2010a) Iron(III)-siderophore coordination chemistry: Reactivity of marine siderophores. Coordination Chemistry Reviews 254:288-296

Butler A, Theisen RM (2010b) Iron(III)-siderophore coordination chemistry: Reactivity of marine siderophores. Coordination Chemistry Reviews 254:288-296

Carpenter C, Payne SM (2014) Regulation of iron transport systems in Enterobacteriaceae in response to oxygen and iron availability. Journal of inorganic biochemistry 133:110-117

Carr SA, Vogel SW, Dunbar RB, Brandes J, Spear JR, Levy R, Naish TR, Powell RD, Wakeham SG, Mandernack KW (2013) Bacterial abundance and composition in marine sediments beneath the Ross Ice Shelf, Antarctica. Geobiology 11:377-395

Challis GL, Ravel J (2000) Coelichelin, a new peptide siderophore encoded by the Streptomyces coelicolor genome: structure prediction from the sequence of its non-ribosomal peptide synthetase. Fems Microbiology Letters 187:111-114

Chemin M, Brun P-M, Lecommandoux S, Sandre O, Le Meins J-F (2012) Hybrid polymer/lipid vesicles: fine control of the lipid and polymer distribution in the binary membrane. Soft Matter 8:2867-2874

Cheung J, Beasley FC, Liu S, Lajoie GA, Heinrichs DE (2009) Molecular characterization of staphyloferrin B biosynthesis in Staphylococcus aureus. Molecular Microbiology 74:594-608

Christiaen SEA, Matthijs N, Zhang X-H, Nelis HJ, Bossier P, Coenye T (2014) Bacteria that inhibit quorum sensing decrease biofilm formation and virulence in Pseudomonas aeruginosa PAO1. Pathogens and Disease 70:271-279

Chuang CY, Santschi PH, Ho YF, Conte MH, Guo LD, Schumann D, Ayranov M, Li YH (2013) Role of biopolymers as major carrier phases of Th, Pa, Pb, Po, and Be radionuclides in settling particles from the Atlantic Ocean. Marine Chemistry 157:131-143

Cobessi D, Celia H, Pattus F (2005a) Crystal structure at high resolution of ferric-pyochelin and its membrane receptor FptA from Pseudomonas aeruginosa. Journal of Molecular Biology 352:893-904

Cobessi D, Celia H, Wirth C, Schalk I, Pattus F (2005b) Structures of iron-siderophore outer membrane receptors from P. aeruginosa. European Biophysics Journal 34:642-642

Cohen SM, O'Sullivan B, Raymond KN (2000) Mixed hydroxypyridinonate ligands as iron chelators. Inorganic Chemistry 39:4339-4346

Conzonno VH, Ulibarrena J (2010) Hydrochemistry of Lakes of the Patagonian Province of Tierra del Fuego (Argentina). Environmental Earth Sciences 59:1431-1436

Cornelis P, Matthijs S, Van Oeffelen L (2009) Iron uptake regulation in Pseudomonas aeruginosa. Biometals 22:15-22

Cotton JL, Tao J, Balibar CJ (2009) Identification and Characterization of the Staphylococcus aureus Gene Cluster Coding for Staphyloferrin A. Biochemistry 48:1025-1035

COX C, RINEHART K, MOORE M, COOK J (1981) PYOCHELIN - NOVEL STRUCTURE OF AN IRON-CHELATING GROWTH PROMOTER FOR PSEUDOMONAS-AERUGINOSA. Proceedings of the National Academy of Sciences of the United States of America-Biological Sciences 78:4256-4260

Crivellato E, Candussio L, Rosati AM, Decorti G, Klugmann FB, Mallardi F (1999) Kinetics of doxorubicin handling in the LLC-PK1 kidney epithelial cell line is mediated by both vesicle formation and P-glycoprotein drug transport. Histochemical Journal 31:635-643

Crosa JH (2004) Iron transport in bacteria, Vol. ASM Press, Washington, DC

De la Rosa-Garcia SC, Munoz-Garcia AA, Barahona-Perez LF, Gamboa-Angulo MM (2007) Antimicrobial properties of moderately halotolerant bacteria from cenotes of the Yucatan peninsula. Letters in Applied Microbiology 45:289-294

De Souza M-J, Bharathi PAL, Nair S, Chandramohan D (2007) "Trade-off" in Antarctic bacteria: limnetic psychrotrophs concede multiple enzyme expressions for multiple metal resistance. Biometals 20:821-828

Demirkanli DI, Molz FJ, Kaplan DI, Fjeld RA (2009) Soil-Root Interactions Controlling Upward Plutonium Transport in Variably Saturated Soils. Vadose Zone Journal 8:574-585

Dertz EA, Stintzi A, Raymond KN (2006) Siderophore-mediated iron transport in Bacillus subtilis and Corynebacterium glutamicum. Journal of Biological Inorganic Chemistry 11:1087-1097

Dhungana S, Michalczyk R, Boukhalfa H, Lack JG, Koppisch AT, Fairlee JM, Johnson MT, Ruggiero CE, John SG, Cox MM, Browder CC, Forsythe JH, Vanderberg LA, Neu MP, Hersman LE (2007) Purification and characterization of rhodobactin: a mixed ligand siderophore from Rhodococcus rhodochrous strain OFS. Biometals 20:853-867

Dimise EJ, Widboom PF, Bruner SD (2008) Structure elucidation and biosynthesis of fuscachelins, peptide siderophores from the moderate thermophile Thermobifida fusca. Proceedings of the National Academy of Sciences of the United States of America 105:15311-15316

Dimkpa CO, Svatos A, Dabrowska P, Schmidt A, Boland W, Kothe E (2008) Involvement of siderophores in the reduction of metal-induced inhibition of auxin synthesis in Streptomyces spp. Chemosphere 74:19-25

Dirnitriu PA, Pinkart HC, Peyton BM, Mormile MR (2008) Spatial and temporal patterns in the microbial diversity of a meromictic soda lake in Washington State. Applied and Environmental Microbiology 74:4877-4888

Drechsel H, Metzger J, Freund S, Jung G, Boelaert JR, Winkelmann G (1991) RHIZOFERRIN - A NOVEL SIDEROPHORE FROM THE FUNGUS RHIZOPUS-MICROSPORUS VAR RHIZOPODIFORMIS. Biology of Metals 4:238-243

Duckworth OW, Holmstrom SJM, Pena J, Sposito G (2009) Biogeochemistry of iron oxidation in a circumneutral freshwater habitat. Chemical Geology 260:149-158

Edberg F, Kalinowski BE, Holmstrom SJM, Holm K (2010) Mobilization of metals from uranium mine waste: the role of pyoverdines produced by Pseudomonas fluorescens. Geobiology 8:278-292

Edmondson WT, Anderson GC (1965) Some features of saline lakes in Central Washington. Limnol Oceanogr 10:R87-R96

Ejje N, Soe CZ, Gu J, Codd R (2013) The variable hydroxamic acid siderophore metabolome of the marine actinomycete Salinispora tropica CNB-440. Metallomics 5:1519-1528

Emmerich M, Bhansali A, Loesekann-Behrens T, Schroeder C, Kappler A, Behrens S (2012) Abundance, Distribution, and Activity of Fe(II)-Oxidizing and Fe(III)-Reducing Microorganisms in Hypersaline Sediments of Lake Kasin, Southern Russia. Applied and Environmental Microbiology 78:4386-4399

Farkas G, Gazso LG, Diosi G (2000) Characterization of subterranean bacteria in the Hungarian Upper Permian Siltstone (Aleurolite) Formation. Canadian Journal of Microbiology 46:559-564

Farrand AJ, Reniere ML, Ingmer H, Frees D, Skaar EP (2013) Regulation of Host Hemoglobin Binding by the Staphylococcus aureus Clp Proteolytic System. Journal of Bacteriology 195:5041-5050

Ferguson AD, Braun V, Fiedler HP, Coulton JW, Diederichs K, Welte W (2000) Crystal structure of the antibiotic albomycin in complex with the outer membrane transporter FhuA. Protein Science 9:956-963

Ferguson AD, Chakraborty R, Smith BS, Esser L, van der Helm D, Deisenhofer J (2002) Structural basis of gating by the outer membrane transporter FecA. Science 295:1715-1719

Ferguson AD, Hofmann E, Coulton JW, Diederichs K, Welte W (1998) Siderophore-mediated iron transport: Crystal structure of FhuA with bound lipopolysaccharide. Science 282:2215-2220

Ferguson AD, Kodding J, Walker G, Bos C, Coulton JW, Diederichs K, Braun V, Welte W (2001) Active transport of an antibiotic rifamycin derivative by the outer-membrane protein FhuA. Structure 9:707-716

Fernandez L, Mendez J, Guijarro JA (2007) Molecular virulence mechanisms of the fish pathogen Yersinia ruckeri. Veterinary Microbiology 125:1-10

Fernandez-Real JM, Manco M (2014) Effects of iron overload on chronic metabolic diseases. The lancet Diabetes & endocrinology 2:513-526

Fineran PC, Slater H, Everson L, Hughes K, Salmond GPC (2005) Biosynthesis of tripyrrole and beta-lactam secondary metabolites in Serratia: integration of quorum sensing with multiple new regulatory components in the control of prodigiosin and carbapenem antibiotic production. Molecular Microbiology 56:1495-1517

Fisher CR, Davies NMLL, Wyckoff EE, Feng Z, Oaks EV, Payne SM (2009) Genetics and Virulence Association of the Shigella flexneri Sit Iron Transport System. Infection and Immunity 77:1992-1999

Flannery AR, Renberg RL, Andrews NW (2013) Pathways of iron acquisition and utilization in Leishmania. Current Opinion in Microbiology 16:716-721

Fox JT, Thomson DU, Drouillard JS, Thornton AB, Burkhardt DT, Emery DA, Nagaraja TG (2009) Efficacy of Escherichia coli O157:H7 Siderophore Receptor/Porin Proteins-Based Vaccine in Feedlot Cattle Naturally Shedding E. coli O157. Foodborne Pathogens and Disease 6:893-899

Gadd GM (1996) Influence of microorganisms on the environmental fate of radionuclides. Endeavour 20:150-156

Gao B, Lu J, Hao H, Yin S, Yu X, Wang Q, Sun K (2014) Heavy Metals Pollution and Pb Isotopic Signatures in Surface Sediments Collected from Bohai Bay, North China. Scientific World Journal

Garenaux A, Caza M, Dozois CM (2011) The Ins and Outs of siderophore mediated iron uptake by extra-intestinal pathogenic Escherichia coli. Veterinary Microbiology 153:89-98

Gauglitz J, Butler A (2013a) Amino acid variability in the peptide composition of a suite of amphiphilic peptide siderophores from an open ocean Vibrio species. Journal of Biological Inorganic Chemistry 18:489-497

Gauglitz JM, Butler A (2013b) Amino acid variability in the peptide composition of a suite of amphiphilic peptide siderophores from an open ocean Vibrio species. Journal of Biological Inorganic Chemistry 18:489-497

Gauglitz JM, Zhou HJ, Butler A (2012) A suite of citrate-derived siderophores from a marine Vibrio species isolated following the Deepwater Horizon oil spill. Journal of Inorganic Biochemistry 107:90-95

Gbadebo AM, Ekwue YA (2014) Heavy metal contamination in tailings and rocksamples from an abandoned goldminein southwestern Nigeria. Environmental Monitoring and Assessment 186:165-174

Geetha SJ, Joshi SJ (2013) Engineering Rhizobial Bioinoculants: A Strategy to Improve Iron Nutrition. Scientific World Journal:15

Gehring AM, Bradley KA, Walsh CT (1997) Enterobactin biosynthesis in Escherichia coli: Isochorismate lyase (EntB) is a bifunctional enzyme that is phosphopantetheinylated by EntD and then acylated by EntE using ATP and 2,3-dihydroxybenzoate. Biochemistry 36:8495-8503

Gehring AM, Mori I, Perry RD, Walsh CT (1998) The nonribosomal peptide synthetase HMWP2 forms a thiazoline ring during biogenesis of yersiniabactin, an iron-chelating virulence factor of Yersinia pestis. Biochemistry 37:11637-11650

Ghosh A, Ghosh M, Niu C, Malouin F, Moellmann U, Miller MJ (1996) Iron transport-mediated drug delivery using mixed-ligand siderophore-beta-lactam conjugates. Chemistry & Biology 3:1011-1019

Ghosh A, Miller MJ (1993) SYNTHESIS OF NOVEL CITRATE-BASED SIDEROPHORES AND SIDEROPHORE-BETA-LACTAM CONJUGATES - IRON TRANSPORT-MEDIATED DRUG-DELIVERY SYSTEMS. Journal of Organic Chemistry 58:7652-7659

Ghozlan H, Deif H, Abu Kandil R, Sabry S (2006) Biodiversity of moderately halophilic bacteria in hypersaline habitats in Egypt. Journal of General and Applied Microbiology 52:63-72

Gledhill M, McCormack P, Ussher S, Achterberg E, Mantoura R, Worsfold P (2004) Production of siderophore type chelates by mixed bacterioplankton populations in nutrient enriched seawater incubations. Marine Chemistry 88:75-83

Goodwin JF, Whitten CF (1965) CHELATION OF FERROUS SULPHATE SOLUTIONS BY DESFERRIOXAMINE B. Nature 205:281-&

GrayOwen SD, Schryvers AB (1996) Bacterial transferrin and lactoferrin receptors. Trends in Microbiology 4:185-191

Guan L, Santander J, Mellata M, Zhang Y, Curtiss R (2013) Identification of an iron acquisition machinery in Flavobacterium columnare. Diseases of Aquatic Organisms 106:129-138

Guerinot ML, Meidl EJ, Plessner O (1990) CITRATE AS A SIDEROPHORE IN BRADYRHIZOBIUM-JAPONICUM. Journal of Bacteriology 172:3298-3303

Gull M, Hafeez FY (2012) Characterization of siderophore producing bacterial strain Pseudomonas fluorescens Mst 8.2 as plant growth promoting and biocontrol agent in wheat. African Journal of Microbiology Research 6:6308-6318

Han AW, Sandy M, Fishman B, Trindade-Silva AE, Soares CAG, Distel DL, Butler A, Haygood MG (2013) Turnerbactin, a Novel Triscatecholate Siderophore from the Shipworm Endosymbiont Teredinibacter turnerae T7901. Plos One 8

Hannauer M, Schaefer M, Hoegy F, Gizzi P, Wehrung P, Mislin GLA, Budzikiewicz H, Schalk IJ (2012) Biosynthesis of the pyoverdine siderophore of Pseudomonas aeruginosa involves precursors with a myristic or a myristoleic acid chain. Febs Letters 586:96-101

Harris W, Amin S, Kupper F, Green D, Carrano C (2007) Borate binding to siderophores: Structure and stability. Journal of the American Chemical Society 129:12263-12271

Haygood MG, Holt PD, Butler A (1993) AEROBACTIN PRODUCTION BY A PLANKTONIC MARINE VIBRIO SP. Limnology and Oceanography 38:1091-1097

He J, Abdelraouf K, Ledesma KR, Chow DSL, Tam VH (2013) Pharmacokinetics and efficacy of liposomal polymyxin B in a murine pneumonia model. International Journal of Antimicrobial Agents 42:559-564

Heesemann J, Hantke K, Vocke T, Saken E, Rakin A, Stojiljkovic I, Berner R (1993) VIRULENCE OF YERSINIA-ENTEROCOLITICA IS CLOSELY ASSOCIATED WITH SIDEROPHORE PRODUCTION, EXPRESSION OF AN IRON-REPRESSIBLE OUTER-MEMBRANE POLYPEPTIDE OF 65000 DA AND PESTICIN SENSITIVITY. Molecular Microbiology 8:397-408

Holt P, Reid R, Lewis B, Luther G, Butler A (2005) Iron(III) coordination chemistry of alterobactin A: A siderophore from the marine bacterium Alteromonas luteoviolacea. Inorganic Chemistry 44:7671-7677

Homann V, Edwards K, Webb E, Butler A (2009a) Siderophores of Marinobacter aquaeolei: petrobactin and its sulfonated derivatives. Biometals 22:565-571

Homann V, Sandy M, Tincu J, Templeton A, Tebo B, Butler A (2009b) Loihichelins A-F, a Suite of Amphiphilic Siderophores Produced by the Marine Bacterium Halomonas LOB-5. Journal of Natural Products 72:884-888

Ibrahim ASS, El-Tayeb MA, Elbadawi YB, Al-Salamah AA (2011a) Bioreduction of Cr (VI) by potent novel chromate resistant alkaliphilic Bacillus sp strain KSUCr5 isolated from hypersaline Soda lakes. African Journal of Biotechnology 10:7207-7218

Ibrahim ASS, El-Tayeb MA, Elbadawi YB, Al-Salamah AA (2011b) Isolation and characterization of novel potent Cr(VI) reducing alkaliphilic Amphibacillus sp KSUCr3 from hypersaline soda lakes. Electronic Journal of Biotechnology 14

Ilari A, Stefanini S, Chiancone E, Tsernoglou D (2000) The dodecameric ferritin from Listeria innocua contains a novel intersubunit iron-binding site. Nature Structural Biology 7:38-43

Israelachvili JN, Marcelja S, Horn RG (1980) PHYSICAL PRINCIPLES OF MEMBRANE ORGANIZATION. Quarterly Reviews of Biophysics 13:121-200

Ito Y, Butler A (2005) Structure of synechobactins, new siderophores of the marine cyanobacterium Synechococcus sp PCC 7002. Limnology and Oceanography 50:1918-1923

Ito Y, Ishida K, Okada S, Murakami M (2004) The absolute stereochemistry of anachelins, siderophores from the cyanobacterium Anabaena cylindrica. Tetrahedron 60:9075-9080

Kadirvel M, Fanimarvasti F, Forbes S, McBain A, Gardiner JM, Brown GD, Freeman S (2014) Inhibition of quorum sensing and biofilm formation in Vibrio harveyi by 4-fluoro-DPD; a novel potent inhibitor of AI-2 signalling. Chemical Communications 50:5000-5002

Kammler M, Schon C, Hantke K (1993) CHARACTERIZATION OF THE FERROUS IRON UPTAKE SYSTEM OF ESCHERICHIA-COLI. Journal of Bacteriology 175:6212-6219

Kanoh K, Kamino K, Leleo G, Adachi K, Shizuri Y (2003) Pseudoalterobactin A and B, new siderophores excreted by marine bacterium Pseudoalteromonas sp KP20-4. Journal of Antibiotics 56:871-875

Karatayev AY, Burlakova LE, Dodson SI (2008) Community analysis of Belarusian lakes: correlations of species diversity with hydrochemistry. Hydrobiologia 605:99-112

Kingsley R, Rabsch W, Williams PH, Reissbrodt R (1994) IRON SUPPLY IN SALMONELLAE IN DIAGNOSIS, EPIDEMIOLOGY, AND IN THE PROCESS OF INFECTION. Immunitat Und Infektion 22:10-14

Kline T, Fromhold M, McKennon TE, Cai S, Treiberg J, Ihle N, Sherman D, Schwan W, Hickey MJ, Warrener P, Witte PR, Brody LL, Goltry L, Barker LM, Anderson SU, Tanaka SK, Shawar RM, Nguyen LY, Langhorne M, Bigelow A, Embuscado L, Naeemi E (2000) Antimicrobial effects of novel siderophores linked to beta-lactam antibiotics. Bioorganic & Medicinal Chemistry 8:73-93

Kobayakawa F, Kodani S (2012) Screening of Streptomycetes for Production of Desferrioxamines. Journal of Pure and Applied Microbiology 6:1553-1558

Kodani S, Bicz J, Song L, Deeth RJ, Ohnishi-Kameyama M, Yoshida M, Ochi K, Challis GL (2013) Structure and biosynthesis of scabichelin, a novel tris-hydroxamate siderophore produced by the plant pathogen Streptomyces scabies 87.22. Organic & Biomolecular Chemistry 11:4686-4694

Konetschnyrapp S, Jung G, Raymond KN, Meiwes J, Zahner H (1992) SOLUTION THERMODYNAMICS OF THE FERRIC COMPLEXES OF NEW DESFERRIOXAMINE SIDEROPHORES OBTAINED BY DIRECTED FERMENTATION. Journal of the American Chemical Society 114:2224-2230

Konings AF, Martin LW, Sharples KJ, Roddam LF, Latham R, Reid DW, Lamont IL (2013) Pseudomonas aeruginosa Uses Multiple Pathways To Acquire Iron during Chronic Infection in Cystic Fibrosis Lungs. Infection and Immunity 81:2697-2704

Kontogiannopoulos KN, Tsermentseli SK, Assimopoulou AN, Papageorgiou VP (2014) Sterically stabilized liposomes as a potent carrier for shikonin. Journal of Liposome Research 24:230-240

Kreutzer MF, Kage H, Nett M (2012) Structure and Biosynthetic Assembly of Cupriachelin, a Photoreactive Siderophore from the Bioplastic Producer Cupriavidus necator H16. Journal of the American Chemical Society 134:5415-5422

Kreutzer MF, Nett M (2012) Genomics-driven discovery of taiwachelin, a lipopeptide siderophore from Cupriavidus taiwanensis. Organic & Biomolecular Chemistry 10:9338-9343

Krewulak KD, Vogel HJ (2008) Structural biology of bacterial iron uptake. Biochimica Et Biophysica Acta-Biomembranes 1778:1781-1804

Krieg S, Huche F, Diederichs K, Izadi-Pruneyre N, Lecroisey A, Wandersman C, Delepelaire P, Welte W (2009) Heme uptake across the outer membrane as revealed by crystal structures of the receptor-hemophore complex. Proceedings of the National Academy of Sciences of the United States of America 106:1045-1050

Lawlor MS, O'Connor C, Miller VL (2007) Yersiniabactin is a virulence factor for Klebsiella pneumoniae during pulmonary infection. Infection and Immunity 75:1463-1472

Lee KC, Carlson PA, Goldstein AS, Yager P, Gelb MH (1999) Protection of a decapeptide from proteolytic cleavage by lipidation and self-assembly into high-axial-ratio microstructures: A kinetic and structural study. Langmuir 15:5500-5508

Lewenza S, Conway B, Greenberg EP, Sokol PA (1999) Quorum sensing in Burkholderia cepacia: Identification of the LuxRI homologs CepRI. Journal of Bacteriology 181:748-756

Limozin L, Barmann M, Sackmann E (2003) On the organization of self-assembled actin networks in giant vesicles. European Physical Journal E 10:319-330

Lin S-Y, Hameed A, Liu Y-C, Hsu Y-H, Lai W-A, Chen W-M, Shen F-T, Young C-C (2013a) Pseudomonas sagittaria sp nov., a siderophore-producing bacterium isolated from oil-contaminated soil. International Journal of Systematic and Evolutionary Microbiology 63:2410-2417

Lin TX, Xu CH, Tang M, Guan QL, Gong MF (2013b) Siderophore Producing by Endophytic Bacterial Strain YBS106 with Antifungal Activity against Fusarium oxysporum. Journal of Pure and Applied Microbiology 7:2091-2096

LIU P, SHOKRANI F (1978) BIOLOGICAL-ACTIVITIES OF PYOCHELINS - IRON-CHELATING AGENTS OF PSEUDOMONAS-AERUGINOSA. Infection and Immunity 22:878-890

Liu Y, Shi M, Xu M, Yang H, Wu C (2012) Multifunctional nanoparticles of Fe3O4@SiO2(FITC)/PAH conjugated the recombinant plasmid of pIRSE2-EGFP/VEGF(165) with dual functions for gene delivery and cellular imaging. Expert Opinion on Drug Delivery 9:1197-1207

Luo M, Fadeev E, Groves J (2005) Mycobactin-mediated iron acquisition within macrophages. Nature Chemical Biology 1:149-153

Luo XZ, Wu SX, Liang YQ (2002) Vesicle formation induced by metal ions from micelle-forming sodium hexadecylimino diacetate in dilute aqueous. Chemical Communications:492-493

Luther GW, Wu JF (1997) What controls dissolved iron concentrations in the world ocean? a comment. Marine Chemistry 57:173-179

Machold O (1971) LAMELLAR PROTEINS OF GREEN AND CHLOROTIC CHLOROPLASTS AS AFFECTED BY IRON DEFICIENCY AND ANTIBIOTICS. Biochimica Et Biophysica Acta 238:324-&

Manczak H, Szuflicka K (1974) HYDRO BACTERIOLOGICAL CORRELATIONS IN THE ODER RIVER. Polskie Archiwum Hydrobiologii 21:101-108

Mariotti P, Malito E, Biancucci M, Lo Surdo P, Mishra RPN, Nardi-Dei V, Savino S, Nissum M, Spraggon G, Grandi G, Bagnli F, Bttomley MJ (2013) Structural and functional characterization of the Staphylococcus aureus virulence factor and vaccine candidate FhuD2. Biochemical Journal 449:683-693

Martin J, Ito Y, Homann V, Haygood M, Butler A (2006) Structure and membrane affinity of new amphiphilic siderophores produced by Ochrobactrum sp SP18. Journal of Biological Inorganic Chemistry 11:633-641

Martinez J, Butler A (2007) Marine amphiphilic siderophores: Marinobactin structure, uptake, and microbial partitioning. Journal of Inorganic Biochemistry 101:1692-1698

Martinez J, Carter-Franklin J, Mann E, Martin J, Haygood M, Butler A (2003) Structure and membrane affinity of a suite of amphiphilic siderophores produced by a marine bacterium. Proceedings of the National Academy of Sciences of the United States of America 100:3754-3759

Martinez J, Zhang G, Holt P, Jung H, Carrano C, Haygood M, Butler A (2000) Self-assembling amphiphilic siderophores from marine bacteria. Science 287:1245-1247

Martinez JS, Haygood MG, Butler A (2001) Identification of a natural desferrioxamine siderophore produced by a marine bacterium. Limnology and Oceanography 46:420-424

Matlakowska R, Sklodowska A (2009) The culturable bacteria isolated from organic-rich black shale potentially useful in biometallurgical procedures. Journal of Applied Microbiology 107:858-866

Matthijs S, Tehrani K, Laus G, Jackson R, Cooper R, Cornelis P (2007) Thioquinolobactin, a Pseudomonas siderophore with antifungal and anti-Pythium activity. Environmental Microbiology 9:425-434

Meiwes J, Fiedler HP, Haag H, Zahner H, Konetschny-Rapp S, Jung G (1990) Isolation and characterization of staphyloferrin A, a compound with siderophore activity from Staphylococcus hyicus DSM 20459. FEMS microbiology letters 55:201-205

Meyer JM, Van VT, Stintzi A, Berge O, Winkelmann G (1995) ORNIBACTIN PRODUCTION AND TRANSPORT-PROPERTIES IN STRAINS OF BURKHOLDERIA-VIETNAMIENSIS AND BURKHOLDERIA-CEPACIA (FORMERLY PSEUDOMONAS-CEPACIA). Biometals 8:309-317

Miller MJ (1995) SYNTHESIS AND STUDIES OF MICROBIAL IRON CHELATORS (SIDEROPHORES) AND DRUG CONJUGATES. Abstracts of Papers of the American Chemical Society 209:353-ORGN

Miller MJ, Walz AJ, Zhu H, Wu CR, Moraski G, Mollmann U, Tristani EM, Crumbliss AL, Ferdig MT, Checkley L, Edwards RL, Boshoff HI (2011) Design, Synthesis, and Study of a Mycobactin-Artemisinin Conjugate That Has Selective and Potent Activity against Tuberculosis and Malaria. Journal of the American Chemical Society 133:2076-2079

Minkwitz A, Berg G (2001) Comparison of antifungal activities and 16S ribosomal DNA sequences of clinical and environmental isolates of Stenotrophomonas maltophilia. Journal of Clinical Microbiology 39:139-145

Minnick AA, McKee JA, Dolence EK, Miller MJ (1992) IRON TRANSPORT-MEDIATED ANTIBACTERIAL ACTIVITY OF AND DEVELOPMENT OF RESISTANCE TO HYDROXAMATE AND CATECHOL SIDEROPHORE-CARBACEPHALOSPORIN CONJUGATES. Antimicrobial Agents and Chemotherapy 36:840-850

Mishra AK, Shukla SK, Yadav DV, Awasthi SK (2014) Iron, Manganese and Sulphur Uptake and Nutrients Availability in Sugarcane Based System in Subtropical India. Sugar Tech 16:300-310

Moeschlin S, Schnider U (1963) TREATMENT OF PRIMARY AND SECONDARY HEMOCHROMATOSIS AND ACUTE IRON POISONING WITH A NEW, POTENT IRON-ELIMINATING AGENT (DESFERRIOXAMINE-B). New England Journal of Medicine 269:57-&

Moll H, Glorius M, Johnsson A, Schaefer M, Budzikiewicz H, Pedersen K, Bernhard G (2010) Neptunium(V) complexation by natural pyoverdins and related model compounds. Radiochimica Acta 98:571-576

Mollmann U, Ghosh A, Dolence EK, Dolence JA, Ghosh M, Miller MJ, Reissbrodt R (1998) Selective growth promotion and growth inhibition of Gram-negative and Gram-positive bacteria by synthetic siderophore-beta-lactam conjugates. Biometals 11:1-12

Mollmann U, Heinisch L, Bauernfeind A, Kohler T, Ankel-Fuchs D (2009) Siderophores as drug delivery agents: application of the "Trojan Horse" strategy. Biometals 22:615-624

Moore CH, Foster LA, Gerbig DG, Dyer DW, Gibson BW (1995) IDENTIFICATION OF ALCALIGIN AS THE SIDEROPHORE PRODUCED BY BORDETELLA-PERTUSSIS AND B-BRONCHISEPTICA. Journal of Bacteriology 177:1116-1118

Morgenthau A, Pogoutse A, Adamiak P, Moraes TF, Schryvers AB (2013) Bacterial receptors for host transferrin and lactoferrin: molecular mechanisms and role in host-microbe interactions. Future Microbiology 8:1575-1585

Mullen L, Gong C, Czerwinski K (2007) Complexation of uranium(VI) with the siderophore desferrioxamine B. Journal of Radioanalytical and Nuclear Chemistry 273:683-688

Nagata T, Oobo T, Aozasa O (2013) Efficacy of a bacterial siderophore, pyoverdine, to supply iron to Solanum lycopersicum plants. Journal of Bioscience and Bioengineering 115:686-690

Nair A, Juwarkar AA, Singh SK (2007) Production and characterization of siderophores and its application in arsenic removal from contaminated soil. Water Air and Soil Pollution 180:199-212

Naito K, Suzuki M, Matsui M, Imai I (2004) Secretion of iron-complexing ligands from Closterium aciculare (Charophyceae, Chlorophyta) under iron-deficient conditions. Phycologia 43:632-634

Neilands JB (1995) SIDEROPHORES - STRUCTURE AND FUNCTION OF MICROBIAL IRON TRANSPORT COMPOUNDS. Journal of Biological Chemistry 270:26723-26726

Nicola AM, Frases S, Casadevall A (2009) Lipophilic Dye Staining of Cryptococcus neoformans Extracellular Vesicles and Capsule. Eukaryotic Cell 8:1373-1380

Nishio T, Ishida Y (1990) PRODUCTION OF DIHYDROXAMATE SIDEROPHORE ALCALIGIN BY ALCALIGENES-XYLOSOXIDANS SUBSP XYLOSOXIDANS. Agricultural and Biological Chemistry 54:1837-1839

Nishio T, Tanaka N, Hiratake J, Katsube Y, Ishida Y, Oda J (1988) ISOLATION AND STRUCTURE OF THE NOVEL DIHYDROXAMATE SIDEROPHORE ALCALIGIN. Journal of the American Chemical Society 110:8733-8734

Noinaj N, Cornelissen CN, Buchanan SK (2013) Structural insight into the lactoferrin receptors from pathogenic Neisseria. Journal of Structural Biology 184:83-92

Norman CS (1964) The treatment of iron over load with desferrioxa-mine B. Irish J Med Sci 457:13-18

Norton CF, Grant WD (1988) SURVIVAL OF HALOBACTERIA WITHIN FLUID INCLUSIONS IN SALT CRYSTALS. Journal of General Microbiology 134:1365-1373

Nuesch J, Bachmann E, Huetter R, Zaehner H C 21.10. Biosynthesis and assay methods of Desferri-oxamine B. 67. 1962. C 2110 Biosynthesis and assay methods of Desferri-oxamine B 67 1962

Oliveira PH, Batagov A, Ward J, Baganz F, Krabben P (2006) Identification of erythrobactin, a hydroxamate-type siderophore produced by Saccharopolyspora erythraea. Letters in Applied Microbiology 42:375-380

Owen JG, Ackerley DF (2011) Characterization of pyoverdine and achromobactin in Pseudomonas syringae pv. phaseolicola 1448a. Bmc Microbiology 11

Owen T, Pynn R, Hammouda B, Butler A (2007) Metal-dependent self-assembly of a microbial surfactant. Langmuir 23:9393-9400

Owen T, Pynn R, Martinez J, Butler A (2005) Micelle-to-vesicle transition of an iron-chelating microbial surfactant, marinobactin E. Langmuir 21:12109-12114

Owen T, Webb S, Butler A (2008) XAS study of a metal-induced phase transition by a microbial surfactant. Langmuir 24:4999-5002

Packiavathy IASV, Sasikumar P, Pandian SK, Veera Ravi A (2013) Prevention of quorum-sensing-mediated biofilm development and virulence factors production in Vibrio spp. by curcumin. Applied Microbiology and Biotechnology 97:10177-10187

Pattus F, Abdallah M (2000) Siderophores and iron-transport in microorganisms. Journal of the Chinese Chemical Society 47:1-20

Payne KA, Rofail D, Baladi JF, Viala M, Abetz L, Desrosiers MP, Lordan N, Ishak K, Proskorovsky I (2008) Iron chelation therapy: Clinical effectiveness, economic burden and quality of life in patients with iron overload. Advances in Therapy 25:725-742

Payne SM, Mey AR (2010) Iron uptake in Shigella and Escherichia coil. Iron Uptake and Homeostasis in Microorganisms:87-100

Petrik M, Franssen GM, Haas H, Laverman P, Hoertnagl C, Schrettl M, Helbok A, Lass-Floerl C, Decristoforo C (2012) Preclinical evaluation of two Ga-68-siderophores as potential radiopharmaceuticals for Aspergillus fumigatus infection imaging. European Journal of Nuclear Medicine and Molecular Imaging 39:1175-1183

Pollock J, Weber KA, Lack J, Achenbach LA, Mormile MR, Coates JD (2007) Alkaline iron(III) reduction by a novel alkaliphilic, halotolerant, Bacillus sp isolated from salt flat sediments of Soap Lake. Applied Microbiology and Biotechnology 77:927-934

Puskin JS (1977) DIVALENT-CATION BINDING TO PHOSPHOLIPIDS - EPR STUDY. Journal of Membrane Biology 35:39-55

Qin C, He B, Dai W, Zhang H, Wang X, Wang J, Zhang X, Wang G, Yin L, Zhang Q (2014) Inhibition of Metastatic Tumor Growth and Metastasis via Targeting Metastatic Breast Cancer by Chlorotoxin-Modified Liposomes. Molecular pharmaceutics 11:3233-3241

Quadri LEN, Keating TA, Patel HM, Walsh CT (1999) Assembly of the Pseudomonas aeruginosa nonribosomal peptide siderophore pyochelin: In vitro reconstitution of aryl-4,2-bisthiazoline synthetase activity from PchD, PPchE, and PchF. Biochemistry 38:14941-14954

Quarta A, Di Corato R, Manna L, Argentiere S, Cingolani R, Barbarella G, Pellegrino T (2008) Multifunctional nanostructures based on inorganic nanoparticles and oligothiophenes and their exploitation for cellular studies. Journal of the American Chemical Society 130:10545-10555

Raina S, De Vizio D, Palonen EK, Odell M, Brandt AM, Soini JT, Keshavarz T (2012) Is quorum sensing involved in lovastatin production in the filamentous fungus Aspergillus terreus? Process Biochemistry 47:843-852

Rastogi A, Mishra BK, Singh M, Mishra R, Shukla S (2014) Role of micronutrients on quantitative traits and prospects of its accumulation in linseed (Linum usitatissimum L.). Archives of Agronomy and Soil Science 60:1389-1409

Ratledge C, Ewing M (1996) The occurrence of carboxymycobactin, the siderophore of pathogenic mycobacteria, as a second extracellular siderophore in Mycobacterium smegmatis. Microbiology-Uk 142:2207-2212

Ravari SB, Heidarzadeh N (2014) Isolation and characterization of rhizosphere auxin producing Bacilli and evaluation of their potency on wheat growth improvement. Archives of Agronomy and Soil Science 60:895-905

Raymond KN, Dertz EA (2004) Biochemical and physical properties of siderophores. In: Iron transport in bacteria, Book 1. ASM Press, Washington, DC

Reilly JF, Horne AJ, Miller CD (2000) Nitrate removal from a drinking water supply with large free-surface constructed wetlands prior to groundwater recharge. Ecological Engineering 14:33-47

Rivault F, Liebert C, Burger A, Hoegy F, Abdallah MA, Schalk IJ, Mislin GLA (2007) Synthesis of pyochelin-norfloxacin conjugates. Bioorganic & Medicinal Chemistry Letters 17:640-644

Robbel L, Helmetag V, Knappe TA, Marahiel MA (2011) Consecutive Enzymatic Modification of Ornithine Generates the Hydroxamate Moieties of the Siderophore Erythrochelin. Biochemistry 50:6073-6080

Robbel L, Knappe TA, Linne U, Xie X, Marahiel MA (2010) Erythrochelin - a hydroxamate-type siderophore predicted from the genome of Saccharopolyspora erythraea. Febs Journal 277:663-676

Rosconi F, Davyt D, Martinez V, Martinez M, Abin-Carriquiry JA, Zane H, Butler A, de Souza EM, Fabiano E (2013) Identification and structural characterization of serobactins, a suite of lipopeptide siderophores produced by the grass endophyte Herbaspirillum seropedicae. Environmental Microbiology 15:916-927

Rout ME, Chrzanowski TH, Westlie TK, DeLuca TH, Callaway RM, Holben WE (2013) BACTERIAL ENDOPHYTES ENHANCE COMPETITION BY INVASIVE PLANTS. American Journal of Botany 100:1726-1737

Sagar S, Dwivedi A, Yadav S, Tripathi M, Kaistha SD (2012) Hexavalent chromium reduction and plant growth promotion by Staphylococcus arlettae Strain Cr11. Chemosphere 86:847-852

Sahay H, Mahfooz S, Singh AK, Singh S, Kaushik R, Saxena AK, Arora DK (2012) Exploration and characterization of agriculturally and industrially important haloalkaliphilic bacteria from environmental samples of hypersaline Sambhar lake, India. World Journal of Microbiology & Biotechnology 28:3207-3217

Sampaio AFS, Silva M, Dornas WC, Costa DC, Silva ME, dos Santos RC, de Lima WG, Pedrosa ML (2014) Iron toxicity mediated by oxidative stress enhances tissue damage in an animal model of diabetes. Biometals 27:349-361

Sandy M, Butler A (2009) Microbial Iron Acquisition: Marine and Terrestrial Siderophores. Chemical Reviews 109:4580-4595

Sandy M, Butler A (2011) Chrysobactin Siderophores Produced by Dickeya chrysanthemi EC16. Journal of Natural Products 74:1207-1212

Sandy M, Han A, Blunt J, Munro M, Haygood M, Butler A (2010) Vanchrobactin and Anguibactin Siderophores Produced by Vibrio sp DS40M4. Journal of Natural Products 73:1038-1043

Sayyed RZ, Gangurde NS, Patel PR, Joshi SA, Chincholkar SB (2010) Siderophore production by Alcaligenes faecalis and its application for growth promotion in Arachis hypogaea. Indian Journal of Biotechnology 9:302-307

Schurmann P (1966) The influence of mineral salt deficiency on chlorophyll formation and the relationship of chlorophyll a and b in green algae. Ber Schweiz Bot Ges 76:59-96

Schwyn B, Neilands JB (1987) UNIVERSAL CHEMICAL-ASSAY FOR THE DETECTION AND DETERMINATION OF SIDEROPHORES. Analytical Biochemistry 160:47-56

Seyedsayamdost MR, Traxler MF, Zheng S-L, Kolter R, Clardy J (2011) Structure and Biosynthesis of Amychelin, an Unusual Mixed-Ligand Siderophore from Amycolatopsis sp. AA4. Journal of the American Chemical Society 133:11434-11437

Shah S, Karkhanis V, Desai A (1992) ISOLATION AND CHARACTERIZATION OF SIDEROPHORE, WITH ANTIMICROBIAL ACTIVITY, FROM AZOSPIRILLUM-LIPOFERUM M. Current Microbiology 25:347-351

Silva-Stenico ME, Pamplona Silva CS, Lorenzi AS, Shishido TK, Etchegaray A, Lira SP, Beraldo Moraes LA, Fiore MF (2011) Non-ribosomal peptides produced by Brazilian cyanobacterial isolates with antimicrobial activity. Microbiological Research 166:161-175

Smith CA, Phiefer CB, MacNaughton SJ, Peacock A, Burkhalter RS, Kirkegaard R, White DC (2000) Quantitative lipid biomarker detection of unculturable microbes and chlorine exposure in water distribution system biofilms. Water Research 34:2683-2688

Soe CZ, Codd R (2014) Unsaturated Macrocyclic Dihydroxamic Acid Siderophores Produced by Shewanella putrefaciens Using Precursor-Directed Biosynthesis. Acs Chemical Biology 9:945-956

Sonier MB, Contreras DA, Treble RG, Weger HG (2012) Two distinct pathways for iron acquisition by iron-limited cyanobacterial cells: evidence from experiments using siderophores and synthetic chelators. Botany-Botanique 90:181-190

Sorokin DY, Berben T, Melton ED, Overmars L, Vavourakis CD, Muyzer G (2014) Microbial diversity and biogeochemical cycling in soda lakes. Extremophiles 18:791-809

Sorokin DY, Foti M, Pinkart HC, Muyzer G (2007) Sulfur-oxidizing bacteria in Soap Lake (Washington State), a meromictic, haloalkaline lake with an unprecedented high sulfide content. Applied and Environmental Microbiology 73:451-455

Souto A, Montaos MA, Balado M, Osorio CR, Rodriguez J, Lemos ML, Jimenez C (2013) Synthesis and antibacterial activity of conjugates between norfloxacin and analogues of the siderophore vanchrobactin. Bioorganic & Medicinal Chemistry 21:295-302

Stephan H, Freund S, Beck W, Jung G, Meyer JM, Winkelmann G (1993) ORNIBACTINS - A NEW FAMILY OF SIDEROPHORES FROM PSEUDOMONAS. Biometals 6:93-100

Stevens DA, Hamilton JR, Johnson N, Kim KK, Lee JS (2009) Halomonas, a Newly Recognized Human Pathogen Causing Infections and Contamination in a Dialysis Center Three New Species. Medicine 88:244-249

Stintzi A, Barnes C, Xu L, Raymond KN (2000) Microbial iron transport via a siderophore shuttle: A membrane ion transport paradigm. Proceedings of the National Academy of Sciences of the United States of America 97:10691-10696

Stintzi A, Raymond KN (2000) Amonabactin-mediated iron acquisition from transferrin and lactoferrin by Aeromonas hydrophila: direct measurement of individual microscopic rate constants. Journal of Biological Inorganic Chemistry 5:57-66

Suo Z, Walsh CT, Miller DA (1999) Tandem heterocyclization activity of the multidomain 230 kDa HMWP2 subunit of Yersinia pestis yersiniabactin synthetase: interaction of the 1-1382 and 1383-2035 fragments. Biochemistry 38:14023-14035

Tal-Gan Y, Stacy DM, Foegen MK, Koenig DW, Blackwell HE (2013) Highly Potent Inhibitors of Quorum Sensing in Staphylococcus aureus Revealed Through a Systematic Synthetic Study of the Group-III Autoinducing Peptide. Journal of the American Chemical Society 135:7869-7882

Tani A, Akita M, Murase H, Kimbara K (2011) Culturable bacteria in hydroponic cultures of moss Racomitrium japonicum and their potential as biofertilizers for moss production. Journal of Bioscience and Bioengineering 112:32-39

Tara N, Afzal M, Ansari TM, Tahseen R, Iqbal S, Khan QM (2014) COMBINED USE OF ALKANE-DEGRADING AND PLANT GROWTH-PROMOTING BACTERIA ENHANCED PHYTOREMEDIATION OF DIESEL CONTAMINATED SOIL. International Journal of Phytoremediation 16:1268-1277

Telford JR, Raymond KN (1997) Amonabactin: a family of novel siderophores from a pathogenic bacterium. Journal of Biological Inorganic Chemistry 2:750-761

Thieme J, Kilcoyne D, Tyliszczak T, Haselwandter K (2013) Spatially resolved NEXAFS spectroscopy of siderophores in biological matrices. In: Journal of Physics Conference Series. Proc 11th International Conference on X-ray Microscopy (XRM). Iop Publishing Ltd, BRISTOL

Thomas M, Castignetti D (2009) Examination of anthrax lethal factor inhibition by siderophores, small hydroxamates, and protamine. Journal of Microbiology Immunology and Infection 42:284-289

Tomaras AP, Crandon JL, McPherson CJ, Banevicius MA, Finegan SM, Irvine RL, Brown MF, O'Donnell JP, Nicolau DP (2013) Adaptation-Based Resistance to Siderophore-Conjugated Antibacterial Agents by Pseudomonas aeruginosa. Antimicrobial Agents and Chemotherapy 57:4197-4207

Tong Y, Guo M (2009) Bacterial heme-transport proteins and their heme-coordination modes. Archives of Biochemistry and Biophysics 481:1-15

Tsolis RM, Baumler AJ, Heffron F, Stojiljkovic I (1996) Contribution of TonB- and Feo-mediated iron uptake to growth of Salmonella typhimurium in the mouse. Infection and Immunity 64:4549-4556

Valdebenito M, Crumbliss AL, Winkelmann G, Hantke K (2006) Environmental factors influence the production of enterobactin, salmochelin, aerobactin, and yersiniabactin in Escherichia coli strain Nissle 1917. International Journal of Medical Microbiology 296:513-520

VanEngelen MR, Peyton BM, Mormile MR, Pinkart HC (2008) Fe(III), Cr(VI), and Fe(III) mediated Cr(VI) reduction in alkaline media using a Halomonas isolate from Soap Lake, Washington. Biodegradation 19:841-850

Vasavi HS, Arun AB, Rekha P-D (2014) Anti-quorum sensing activity of Psidium guajava L. flavonoids against Chromobacterium violaceum and Pseudomonas aeruginosa PAO1. Microbiology and immunology 58:286-293

Vraspir JM, Holt PD, Butler A (2011) Identification of new members within suites of amphiphilic marine siderophores. Biometals 24:85-92

Wang Y, Wilks JC, Danhorn T, Ramos I, Croal L, Newman DK (2011) Phenazine-1-Carboxylic Acid Promotes Bacterial Biofilm Development via Ferrous Iron Acquisition. Journal of Bacteriology 193:3606-3617

Wang Y, Zhang XH, Austin B (2010) Comparative analysis of the phenotypic characteristics of high- and low-virulent strains of Edwardsiella tarda. Journal of Fish Diseases 33:985-994

Weaver EA, Wyckoff EE, Mey AR, Morrison R, Payne SM (2013) FeoA and FeoC Are Essential Components of the Vibrio cholerae Ferrous Iron Uptake System, and FeoC Interacts with FeoB. Journal of Bacteriology 195:4826-4835

Wencewicz TA, Long TE, Mollmann U, Miller MJ (2013) Trihydroxamate Siderophore-Fluoroquinolone Conjugates Are Selective Sideromycin Antibiotics that Target Staphylococcus aureus. Bioconjugate Chemistry 24:473-486

White AJ, Snow GA (1969) ISOLATION OF MYCOBACTINS FROM VARIOUS MYCOBACTERIA - PROPERTIES OF MYCOBACTINS S AND H. Biochemical Journal 111:785-&

Williams P, Griffiths E (1992) BACTERIAL TRANSFERRIN RECEPTORS - STRUCTURE, FUNCTION AND CONTRIBUTION TO VIRULENCE. Medical Microbiology and Immunology 181:301-322

Wolff-Boenisch D, Traina SJ (2007) The effect of desferrioxamine B on the desorption of U(VI) from Georgia kaolinite KGa-1b and its ligand-promoted dissolution at pH 6 and 25 degrees C. Chemical Geology 242:278-287

Woo S-M, Kim S-D (2008) Structural Identification of Siderophore(AH18) from Bacillus subtilis AH18, a Biocontrol agent of Phytophthora Blight Disease in Red-pepper. Korean Journal of Microbiology and Biotechnology 36:326-335

Xu G, Martinez J, Groves J, Butler A (2002) Membrane affinity of the amphiphilic marinobactin siderophores. Journal of the American Chemical Society 124:13408-13415

Yanagawa K, Morono Y, de Beer D, Haeckel M, Sunamura M, Futagami T, Hoshino T, Terada T, Nakamura K-i, Urabe T, Rehder G, Boetius A, Inagaki F (2013) Metabolically active microbial communities in marine sediment under high-CO2 and low-pH extremes. Isme Journal 7:555-567

Yasumoto-Hirose M, Nishijima M, Ngirchechol MK, Kanoh K, Shizuri Y, Miki W (2006) Isolation of marine bacteria by in situ culture on media-supplemented polyurethane foam. Marine Biotechnology 8:227-237

Yu XM, Ai CX, Xin L, Zhou GF (2011) The siderophore-producing bacterium, Bacillus subtilis CAS15, has a biocontrol effect on Fusarium wilt and promotes the growth of pepper. European Journal of Soil Biology 47:138-145

Yue WW, Grizot S, Buchanan SK (2003) Structural evidence for iron-free citrate and ferric citrate binding to the TonB-dependent outer membrane transporter FecA. Journal of Molecular Biology 332:353-368

Zane HK, Butler A (2013) Isolation, Structure Elucidation, and Iron-Binding Properties of Lystabactins, Siderophores Isolated from a Marine Pseudoalteromonas sp. Journal of Natural Products 76:648-654

Zane HK, Naka H, Rosconi F, Sandy M, Haygood MG, Butler A (2014) Biosynthesis of Amphi-enterobactin Siderophores by Vibrio harveyi BAA-1116: Identification of a Bifunctional Nonribosomal Peptide Synthetase Condensation Domain. Journal of the American Chemical Society 136:5615-5618

Zhang LB, Sun W, Cai WG, Zhang Z, Gu YG, Chen HG, Ma SW, Jia XP (2013) Differential response of two ferritin subunit genes (VpFer1 and VpFer2) from Venerupis philippinarum following pathogen and heavy metals challenge. Fish & Shellfish Immunology 35:1658-1662

Zhao L, Wang F, Zhao J (2014) Identification and functional characteristics of chlorpyrifos-degrading and plant growth promoting bacterium Acinetobacter calcoaceticus. Journal of Basic Microbiology 54:457-463

Zhu JY, Zhang JX, Li Q, Han T, Xie JP, Hu YH, Chai LY (2013) Phylogenetic analysis of bacterial community composition in sediment contaminated with multiple heavy metals from the Xiangjiang River in China. Marine Pollution Bulletin 70:134-139

Zhu WM, Wilks A, Stojiljkovic I (2000) Degradation of heme in gram-negative bacteria: the product of the hemO gene of Neisseriae is a heme oxygenase. Journal of Bacteriology 182:6783-6790

APPENDICES

APPENDIX A

RAW DATA FOR GROWTH CURVES AND SIDEROPHORE PRODUCTION

RAW DATA FOR GROWTH CURVES AND SIDEROPHORE PRODUCTION

Table A1. Optical densities for *Halomonas* sp. SL01 at room temperature and different SLM NaCl % (w/v) treatments. [a]Standard deviation.

SL01 Cultive	Time (h)	Optical Density					
		1	2	3	Average	Std Dev[a]	Control
1.0 % NaCl	0	0.000	0.000	0.000	0.000	0.000	0.000
	24	0.308	0.307	0.304	0.306	0.002	0.001
	48	0.374	0.391	0.395	0.387	0.011	0.000
	71	0.431	0.445	0.449	0.442	0.009	0.000
5.0 % NaCl	0	0.000	0.000	0.000	0.000	0.000	0.000
	24	0.254	0.283	0.247	0.261	0.019	0.001
	53	0.680	0.607	0.587	0.625	0.049	0.000
	76	0.478	0.465	0.504	0.482	0.020	0.000
	99.5	0.355	0.392	0.436	0.394	0.041	0.000
	119	0.353	0.518	0.430	0.434	0.083	0.000
	144	0.600	0.577	0.413	0.530	0.102	0.000
10.0 % NaCl	0	0.000	0.000	0.000	0.000	0.000	0.000
	24.5	0.103	0.100	0.094	0.099	0.005	0.000
	29.5	0.089	0.097	0.095	0.094	0.004	0.000
	46.5	0.143	0.152	0.101	0.132	0.027	0.000
	53.5	0.197	0.240	0.208	0.215	0.022	0.000
	71.5	0.660	0.647	0.641	0.649	0.010	0.000
	77.5	0.620	0.615	0.600	0.612	0.010	0.000
	96	0.612	0.581	0.530	0.574	0.041	0.000

Table A2. Chrome Azurol Sulfonate assay of siderophore production for *Halomonas* sp. SL01 at room temperature and different SLM NaCl % (w/v) treatments. [a]Standard deviation.

SL01 Cultive	Time (h)	CAS Assay									
		1	Siderophore Conc. (µM)	2	Siderophore Conc. (µM)	3	Siderophore Conc. (µM)	Average (µM)	Std Dev[a] (µM)	Negative	Negative Conc. (µM)
1.0 % NaCl	0	0.964	0.0	0.959	0.0	0.920	0.0	0.0	0.0	0.978	0.0
	24	0.768	1.7	0.745	2.2	0.735	2.3	2.1	0.3	0.919	0.0
	48	0.071	14.3	0.059	14.5	0.058	14.5	14.5	0.1	0.923	0.0
	71	0.214	14.7	0.156	16.0	0.180	15.4	15.3	0.7	0.959	0.0
5.0 % NaCl	0	0.899	0.0	0.976	0.0	0.905	0.0	0.0	0.0	0.967	0.0
	24	0.895	0.0	0.988	0.0	0.915	0.0	0.0	0.0	0.970	0.0
	53	0.070	14.3	0.056	14.6	0.055	14.6	14.5	0.2	0.978	0.0
	76	0.215	39.0	0.358	30.4	0.277	35.3	34.9	4.3	0.986	0.0
	99.5	0.171	41.7	0.285	34.8	0.234	37.9	38.1	3.4	0.959	0.0
	119	0.224	38.5	0.336	31.8	0.240	37.5	35.9	3.6	0.945	0.0
	144	0.259	36.4	0.384	28.9	0.366	30.0	31.7	4.1	0.976	0.0
10.0 % NaCl	0	1.439	0.0	1.403	0.0	1.393	0.0	0.0	0.0	1.421	0.0
	24.5	1.427	0.0	1.421	0.0	1.431	0.0	0.0	0.0	1.437	0.0
	29.5	1.454	0.0	1.447	0.0	1.451	0.0	0.0	0.0	1.42	0.0
	46.5	1.224	0.0	1.241	0.0	1.279	0.0	0.0	0.0	1.405	0.0
	53.5	0.964	0.0	0.984	0.0	1.091	0.0	0.0	0.0	1.342	0.0
	71.5	0.421	10.0	0.443	9.5	0.694	3.8	7.8	3.4	1.078	0.0
	77.5	0.267	21.5	0.269	21.5	0.331	19.2	20.7	1.3	1.054	0.0
	96	0.407	16.5	0.266	21.6	0.272	21.4	19.8	2.9	1.025	0.0

Table A3. Optical densities for *Halomonas* sp. SL01 at 37 °C and different SLM NaCl % (w/v) treatments. [a]Standard deviation.

SL01 Cultive	Time (h)	Optical Density					
		1	2	3	Average	Std Dev[a]	Control
1.0 % NaCl	0	0.000	0.000	0.000	0.000	0.000	0.000
	47.5	0.000	0.000	0.000	0.000	0.000	0.000
	66.5	0.000	0.000	0.000	0.000	0.000	0.000
	90.6	0.013	0.002	0.000	0.005	0.007	0.000
	120	0.111	0.112	0.000	0.074	0.064	0.000
	138.5	0.090	0.098	0.000	0.063	0.054	0.000
5.0 % NaCl	0	0.000	0.000	0.000	0.000	0.000	0.000
	24	0.281	0.296	0.329	0.302	0.025	0.000
	53	0.245	N/Av	0.422	0.334	0.125	0.001
	76	0.369	N/Av	0.481	0.425	0.079	0.001
	99.5	0.406	N/Av	0.378	0.392	0.020	0.000
	119	0.414	N/Av	0.325	0.370	0.063	0.000
	144	0.363	N/Av	0.305	0.334	0.041	0.000
10.0 % NaCl	0	0.000	0.000	0.000	0.000	0.000	0.000
	24	0.347	0.363	0.344	0.351	0.010	0.000
	48	0.659	0.673	0.634	0.655	0.020	0.000
	72	0.682	0.718	0.613	0.671	0.053	0.000
	91.5	0.619	0.515	0.355	0.496	0.133	0.000
	115.5	0.484	0.407	0.332	0.408	0.076	0.000
	121.5	0.470	0.400	0.331	0.400	0.070	0.000

Table A4. Chrome Azurol Sulfonate assay of siderophore production for *Halomonas* sp. SL01 at 37 °C and different SLM NaCl % (w/v) treatments. [a]Standard deviation.

SL01 Cultive	Time (h)	CAS Assay									
		1	Siderophore Conc. (µM)	2	Siderophore Conc. (µM)	3	Siderophore Conc. (µM)	Average (µM)	Std Dev[a] (µM)	Negative	Negative Conc. (µM)
1.0 % NaCl	0	1.278	0.0	1.254	0.0	1.301	0.0	0.0	0.0	1.356	0.0
	47.5	1.291	0.0	1.285	0.0	1.293	0.0	0.0	0.0	1.341	0.0
	66.5	1.272	0.0	1.292	0.0	1.278	0.0	0.0	0.0	1.342	0.0
	90.6	1.305	0.0	1.307	0.0	1.201	0.0	0.0	0.0	1.345	0.0
	120	1.415	0.0	1.305	0.0	1.293	0.0	0.0	0.0	1.326	0.0
	138.5	1.304	0.0	1.306	0.0	1.316	0.0	0.0	0.0	1.417	0.0
5.0 % NaCl	0	0.996	0.0	0.989	0.0	1.010	0.0	0.0	0.0	0.980	0.0
	24	0.059	29.0	0.062	28.9	0.058	29.1	29.0	0.1	0.960	0.0
	53	0.231	38.1	N/Av	N/Av	0.202	39.8	38.9	1.2	0.982	0.0
	76	0.246	37.2	N/Av	N/Av	0.185	40.8	39.0	2.6	0.940	0.0
	99.5	0.291	34.5	N/Av	N/Av	0.193	40.3	37.4	4.2	0.971	0.0
	119	0.290	34.5	N/Av	N/Av	0.264	36.1	35.3	1.1	0.974	0.0
	144	0.341	31.5	N/Av	N/Av	0.561	18.2	24.8	9.3	0.980	0.0
10.0 % NaCl	0	0.920	0.0	0.913	0.0	0.901	0.0	0.0	0.0	0.930	0.0
	24	0.914	0.0	0.923	0.0	0.927	0.0	0.0	0.0	0.955	0.0
	48	0.059	14.5	0.059	14.5	0.059	14.5	14.5	0.0	0.979	0.0
	72	0.111	17.0	0.078	17.7	0.232	14.3	16.3	1.8	0.968	0.0
	91.5	0.485	27.2	0.396	32.6	0.348	35.5	31.8	4.2	1.075	0.0
	115.5	0.540	23.8	0.520	25.0	0.396	32.6	27.2	4.8	1.078	0.0
	121.5	0.543	23.6	0.521	25.0	0.453	29.1	25.9	2.9	1.096	0.0

Table A5. Maximum siderophore production data obtained for *Halomonas* sp. SL01. [a]Average; [b]Standard deviation.

NaCl Concentration (% w/v)	Maximum Siderophore Production (µM)			
	Temperature (°C)			
	25 (Av.)[a]	37 (Av.)[a]	25 (S.D.)[b]	37 (S.D.)[b]
1	15.3	0.0	0.7	0.0
5	38.1	39.0	3.4	2.6
10	20.7	31.8	1.3	4.2

Table A6. Optical Optical densities for *Halomonas* sp. SL28 at room temperature and different SLM NaCl % (w/v) treatments. [a]Standard deviation.

SL28 Cultive	Time (h)	Optical Density					
		1	2	3	Average	Std Dev[a]	Control
1.0 % NaCl	0.0	0.000	0.000	0.000	0.000	0.000	0.000
	18.5	0.002	0.007	0.006	0.005	0.003	0.000
	44.0	0.062	0.168	0.138	0.123	0.055	0.000
	90.5	0.204	0.220	0.216	0.213	0.008	0.000
	114.5	0.190	0.218	0.212	0.207	0.015	0.000
	138.5	0.182	0.216	0.207	0.202	0.018	0.000
	162.5	0.181	0.215	0.210	0.202	0.018	0.000
5.0 % NaCl	0.0	0.000	0.000	0.000	0.000	0.000	0.000
	21.0	0.157	0.140	0.156	0.151	0.010	0.000
	42.0	0.431	0.397	0.443	0.424	0.024	0.000
	50.5	0.515	0.535	0.541	0.530	0.014	0.000
	67.0	0.574	0.620	0.617	0.604	0.026	0.000
	75.0	0.543	0.606	0.571	0.573	0.032	0.000
	89.0	0.556	0.607	0.593	0.585	0.026	0.000
	97.0	0.583	0.621	0.611	0.605	0.020	0.001
10.0 % NaCl	0.0	0.000	0.000	0.000	0.000	0.000	0.000
	24.0	0.098	0.093	0.093	0.095	0.003	0.000
	48.0	0.246	0.232	0.241	0.240	0.007	0.000
	72.0	0.644	0.625	0.629	0.633	0.010	0.011
	96.0	0.764	0.760	0.754	0.759	0.005	0.000
	120.0	0.833	0.846	0.835	0.838	0.007	0.000

Table A7. Chrome Azurol Sulfonate assay of siderophore production for *Halomonas* sp. SL28 at room temperature and different SLM NaCl % (w/v) treatments. [a]Standard deviation.

SL28 Cultive	Time (h)	CAS Assay									
		1	Siderophore Conc. (µM)	2	Siderophore Conc. (µM)	3	Siderophore Conc. (µM)	Average (µM)	Std Dev[a] (µM)	Negative	Negative Conc. (µM)
1.0 % NaCl	0.0	1.123	0.0	1.2	0.0	1.134	0.0	0.0	0.0	0.956	0.0
	18.5	1.258	0.0	1.291	0.0	1.249	0.0	0.0	0.0	1.319	0.0
	44.0	1.235	0.0	1.249	0.0	1.236	0.0	0.0	0.0	1.334	0.0
	90.5	1.235	0.0	1.254	0.0	1.230	0.0	0.0	0.0	1.300	0.0
	114.5	1.175	0.0	1.168	0.0	1.170	0.0	0.0	0.0	1.263	0.0
	138.5	1.197	0.0	1.125	0.0	1.134	0.0	0.0	0.0	1.313	0.0
	162.5	1.150	0.0	1.036	1.7	1.073	0.8	0.8	0.9	1.299	0.0
5.0 % NaCl	0.0	0.999	0.0	0.978	0.0	0.950	0.0	0.0	0.0	0.925	0.0
	21.0	0.884	0.0	0.889	0.0	0.887	0.0	0.0	0.0	0.878	0.0
	42.0	0.797	1.2	0.864	0.0	0.740	2.2	1.2	1.1	0.909	0.0
	50.5	0.667	3.6	0.751	2.0	0.585	5.0	3.6	1.5	0.911	0.0
	67.0	0.555	5.6	0.581	5.1	0.478	7.0	5.9	1.0	0.906	0.0
	75.0	0.557	5.5	0.555	5.6	0.437	7.7	6.3	1.2	0.915	0.0
	89.0	0.513	6.3	0.551	5.7	0.420	8.0	6.7	1.2	0.895	0.0
	97.0	0.527	6.1	0.573	5.3	0.434	7.8	6.4	1.3	0.919	0.0
10.0 % NaCl	0.0	0.901	0.0	0.956	0.0	0.900	0.0	0.0	0.0	0.905	0.0
	24.0	0.891	0.0	0.885	0.0	0.887	0.0	0.0	0.0	0.888	0.0
	48.0	0.925	0.0	0.805	1.1	0.904	0.0	0.4	0.6	0.913	0.0
	72.0	0.741	2.2	0.782	1.5	0.777	1.6	1.8	0.4	0.922	0.0
	96.0	0.307	10.0	0.196	12.0	0.255	11.0	11.0	1.0	0.906	0.0
	120.0	0.246	11.1	0.114	13.5	0.187	12.2	12.3	1.2	0.899	0.0

Table A8. Maximum siderophore production data obtained for *Halomonas* sp. SL28. [a]Average; [b]Standard deviation.

NaCl Concentration (% w/v)	Maximum Siderophore Production (µM)			
	Temperature (°C)			
	25 (Av.)[a]	37 (Av.)[a]	25 (S.D.)[b]	37 (S.D.)[b]
1.0	0.8	0.0	0.9	0.0
5.0	6.7	0.0	1.2	0.0
10.0	12.3	14.8	1.2	0.0

Table A9. Optical densities of different SLM pH treatments at 37 °C and 5% (w/v) NaCl for *Halomonas* sp. SL01. [a]Standard deviation.

SL01 Cultive (pH)	Time (h)	Optical Density					
		1	2	3	Average	Std. Dev.[a]	Control
8	0	0.000	0.000	0.000	0.000	0.000	0.000
	22.5	0.323	0.297	0.161	0.260	0.087	0.000
	49	0.444	0.465	0.281	0.397	0.101	0.000
	95	0.376	0.402	0.253	0.344	0.080	0.000
	119	0.337	0.365	0.211	0.304	0.082	0.000
	151	0.281	0.327	0.191	0.266	0.069	0.000
	167	0.262	0.316	0.190	0.256	0.063	0.000
9	0	0.000	0.000	0.000	0.000	0.000	0.000
	24	0.281	0.296	0.329	0.302	0.025	0.000
	53	0.245	N/Av	0.422	0.334	0.125	0.001
	76	0.369	N/Av	0.481	0.425	0.079	0.001
	99.5	0.406	N/Av	0.378	0.392	0.020	0.000
	119	0.414	N/Av	0.325	0.370	0.063	0.000
	144	0.363	N/Av	0.305	0.334	0.041	0.000
10	0	0.000	0.000	0.000	0.000	0.000	0.000
	24.5	0.000	0.000	0.000	0.000	0.000	0.000
	44.5	0.000	0.000	0.000	0.000	0.000	0.000
	53	0.000	0.000	0.000	0.000	0.000	0.000
	69	0.000	0.000	0.000	0.000	0.000	0.000
	143	0.194	0.009	0.001	0.068	0.109	0.000
	168	0.194	0.294	0.195	0.228	0.057	0.000
	189	0.196	0.220	0.245	0.220	0.025	0.000
	213	0.161	0.179	0.181	0.174	0.011	0.000
	236.5	0.149	0.161	0.165	0.158	0.008	0.000
11	0	0.000	0.000	0.000	0.000	0.000	0.000
	28	0.000	0.000	0.000	0.000	0.000	0.000
	47.5	0.187	0.000	0.000	0.062	0.108	0.000
	71	0.208	0.035	0.000	0.081	0.111	0.000
	98.5	0.178	0.168	0.000	0.115	0.100	0.000
	143.5	0.162	0.158	0.000	0.107	0.092	0.000
	167	0.123	0.118	0.000	0.080	0.070	0.000

Table A10. Chrome Azurol Sulfonate assay for siderophore production of different SLM pH treatments (8 and 9) at 37 °C and 5% (w/v) NaCl for *Halomonas* sp. SL01. [a]Standard deviation.

SL01 Cultive (pH)	Time (h)	CAS Assay									
		1	Siderophore Conc. (µM)	2	Siderophore Conc. (µM)	3	Siderophore Conc. (µM)	Average (µM)	Std. Dev. (µM)[a]	Negative	Negative Conc. (µM)
8	0	1.072	0.0	1.073	0.0	1.075	0.0	0.0	0.0	1.081	0.0
	22.5	0.736	8.4	0.821	6.2	0.988	2.1	5.6	3.2	1.032	1.0
	49	0.487	29.1	0.302	38.3	0.476	29.7	32.4	5.2	1.062	0.5
	95	0.646	21.2	0.536	26.7	0.601	23.4	23.8	2.8	1.074	0.0
	119	0.645	21.3	0.543	26.3	0.605	23.2	23.6	2.6	1.074	0.0
	151	0.344	19.9	0.221	23.2	0.339	20.1	21.1	1.8	1.073	0.8
	167	0.406	18.3	0.287	21.4	0.402	18.4	19.4	1.8	1.072	0.8
9	0	0.996	0.0	0.989	0.0	1.010	0.0	0.0	0.0	0.980	0.0
	24	0.059	29.0	0.062	28.9	0.058	29.1	29.0	0.1	0.960	0.0
	53	0.231	38.1	N/Av	N/Av	0.202	39.8	38.9	1.2	0.982	0.0
	76	0.246	37.2	N/Av	N/Av	0.185	40.8	39.0	2.6	0.940	0.0
	99.5	0.291	34.5	N/Av	N/Av	0.193	40.3	37.4	4.2	0.971	0.0
	119	0.290	34.5	N/Av	N/Av	0.264	36.1	35.3	1.1	0.974	0.0
	144	0.341	31.5	N/Av	N/Av	0.561	18.2	24.8	9.3	0.980	0.0

Table A11. Chrome Azurol Sulfonate assay for siderophore production of different SLM pH treatments (10 and 11) at 37 °C and 5% (w/v) NaCl for *Halomonas* sp. SL01. [a]Standard deviation.

SL01 Cultive (pH)	Time (h)	CAS Assay									
		1	Siderophore Conc. (µM)	2	Siderophore Conc. (µM)	3	Siderophore Conc. (µM)	Average (µM)	Std. Dev. (µM)[a]	Negative	Negative Conc. (µM)
10	0	1.102	0.0	1.200	0.0	1.245	0.0	0.0	0.0	1.345	0.0
	24.5	1.363	0.0	1.397	0.0	1.443	0.0	0.0	0.0	1.495	0.0
	44.5	1.341	0.0	1.390	0.0	1.464	0.0	0.0	0.0	1.502	0.0
	53	1.325	0.0	1.340	0.0	1.421	0.0	0.0	0.0	1.455	0.0
	69	1.326	0.0	1.381	0.0	1.429	0.0	0.0	0.0	1.460	0.0
	143	1.173	0.0	1.307	0.0	1.390	0.0	0.0	0.0	1.480	0.0
	168	0.613	12.9	0.979	3.2	1.173	0.0	6.4	9.1	1.474	0.0
	189	0.927	4.6	0.930	4.5	0.567	14.1	9.3	6.7	1.446	0.0
	213	0.759	9.0	0.915	4.9	1.074	0.7	4.9	5.9	1.497	0.0
	236.5	0.818	7.5	0.956	3.8	1.055	1.2	4.4	4.4	1.454	0.0
11	0	1.203	0.0	1.210	0.0	1.204	0.0	0.0	0.0	1.234	0.0
	28	1.587	0.0	1.641	0.0	1.665	0.0	0.0	0.0	1.657	0.0
	47.5	1.324	0.0	1.623	0.0	1.672	0.0	0.0	0.0	1.613	0.0
	71	0.613	12.9	1.590	0.0	1.652	0.0	6.4	9.1	1.635	0.0
	98.5	0.549	14.6	1.228	0.0	1.682	0.0	7.3	10.3	1.639	0.0
	143.5	0.646	12.0	0.887	5.7	1.656	0.0	6.0	8.5	1.637	0.0
	167	0.685	11.0	0.461	16.9	1.612	0.0	5.5	7.8	1.636	0.0

Table A12. Optical densities of different SLM pH treatments at room temperature and 10% (w/v) NaCl for *Halomonas* sp. SL28. [a]Standard deviation.

SL28 Cultive (pH)	Time (h)	Optical Density					
		1	2	3	Average	Std Dev[a]	Control
8	0	0.000	0.000	0.000	0.000	0.000	0.000
	24	0.044	0.046	0.038	0.043	0.004	0.000
	48	0.278	0.269	0.269	0.272	0.005	0.000
	72	0.554	0.577	0.568	0.566	0.012	0.000
	96	0.674	0.687	0.723	0.695	0.025	0.000
	168	0.658	0.633	0.663	0.651	0.016	0.000
	192	0.615	0.599	0.612	0.609	0.009	0.000
9	0	0.000	0.000	0.000	0.000	0.000	0.000
	24.0	0.098	0.093	0.093	0.095	0.003	0.000
	48.0	0.246	0.232	0.241	0.240	0.007	0.000
	72.0	0.644	0.625	0.629	0.633	0.010	0.011
	96.0	0.764	0.760	0.754	0.759	0.005	0.000
	120.0	0.833	0.846	0.835	0.838	0.007	0.000
10	0	0.000	0.000	0.000	0.000	0.000	0.000
	24	0.013	0.011	0.018	0.014	0.004	0.000
	48	0.068	0.045	0.055	0.056	0.012	0.000
	72	0.244	0.268	0.261	0.258	0.012	0.000
	97.5	0.285	0.299	0.273	0.286	0.013	0.000
	117.5	0.372	0.398	0.367	0.379	0.017	0.000
	138.5	0.429	0.435	0.419	0.428	0.008	0.000
	164.5	0.397	0.398	0.385	0.393	0.007	0.000
	189	0.371	0.369	0.363	0.368	0.004	0.000
11	0	0.000	0.000	0.000	0.000	0.000	0.000
	23.5	0.000	0.002	0.002	0.001	0.001	0.000
	47	0.002	0.003	0.002	0.002	0.001	0.002
	72	0.007	0.006	0.004	0.006	0.002	0.000
	95.5	0.012	0.004	0.002	0.006	0.005	0.000
	118.5	0.002	0.002	0.007	0.004	0.003	0.000
	144	0.029	0.051	0.023	0.034	0.015	0.001
	173	0.162	0.161	0.112	0.145	0.029	0.000
	196	0.185	0.255	0.184	0.208	0.041	0.003
	219.5	0.208	0.256	0.189	0.218	0.035	0.000
	239	0.182	0.232	0.174	0.196	0.031	0.000

Table A13. Chrome Azurol Sulfonate assay for siderophore production of different SLM pH treatments (8 and 9) at room temperature and 10% (w/v) NaCl for *Halomonas* sp. SL28. [a]Standard deviation.

SL28 Cultive (pH)	Time (h)	CAS Assay									
		1	Siderophore Conc. (µM)	2	Siderophore Conc. (µM)	3	Siderophore Conc. (µM)	Average (µM)	Std Dev (µM)[a]	Negative	Negative Conc. (µM)
8	0	1.000	0.0	1.000	0.0	1.000	0.0	0.0	0	1.000	0.0
	24	0.960	0.0	0.953	0.0	0.980	0.0	0.0	0.0	0.951	0.0
	48	0.945	0.0	1.045	0.0	0.924	0.0	0.0	0.0	0.962	0.0
	72	0.526	6.1	0.790	1.3	0.836	0.5	2.7	3.0	0.942	0.0
	96	0.061	14.5	0.148	12.9	0.338	9.5	12.3	2.6	0.966	0.0
	168	0.275	40.0	0.293	38.9	0.248	41.6	40.2	1.4	1.069	0.0
	192	0.223	43.2	0.289	39.1	0.239	42.2	41.5	2.1	1.078	0.0
9	0	1.000	0.0	1.000	0.0	1.000	0.0	0.0	0.0	1.000	0.0
	24.0	0.891	0.0	0.885	0.0	0.887	0.0	0.0	0.0	0.888	0.0
	48.0	0.925	0.0	0.805	1.1	0.904	0.0	0.4	0.6	0.913	0.0
	72.0	0.741	2.2	0.782	1.5	0.777	1.6	1.8	0.4	0.922	0.0
	96.0	0.307	10.0	0.196	12.0	0.255	11.0	11.0	1.0	0.906	0.0
	120.0	0.246	11.1	0.114	13.5	0.187	12.2	12.3	1.2	0.899	0.0

Table A14. Chrome Azurol Sulfonate assay for siderophore production of different SLM pH treatments (10 and 11) at room temperature and 10% (w/v) NaCl for *Halomonas* sp. SL28. [a]Standard deviation.

SL28 Cultive (pH)	Time (h)	CAS Assay									
		1	Siderophore Conc. (µM)	2	Siderophore Conc. (µM)	3	Siderophore Conc. (µM)	Average (µM)	Std Dev (µM)[a]	Negative	Negative Conc. (µM)
10	0	1.000	0.0	1.000	0.0	1.000	0.0	0.0	0.0	1.000	0.0
	24	0.940	0.0	0.924	0.0	0.945	0.0	0.0	0.0	0.953	0.0
	48	0.947	0.0	0.945	0.0	0.930	0.0	0.0	0.0	0.960	0.0
	72	1.043	0.0	0.935	0.0	0.924	0.0	0.0	0.0	0.978	0.0
	97.5	0.837	0.5	0.851	0.2	0.675	3.4	1.4	1.8	1.026	0.0
	117.5	0.809	1.0	0.816	0.9	0.521	6.2	2.7	3.0	0.976	0.0
	138.5	0.648	3.9	0.704	2.9	0.434	7.8	4.9	2.6	0.981	0.0
	164.5	0.685	3.2	0.723	2.6	0.370	8.9	4.9	3.5	1.028	0.0
	189	0.714	2.7	0.739	2.3	0.383	8.7	4.6	3.6	1.028	0.0
11	0	1.000	0.0	1.000	0.0	1.000	0.0	0.0	0.0	1.000	0.0
	23.5	0.952	0.0	0.971	0.0	0.966	0.0	0.0	0.0	1.009	0.0
	47	0.939	0.0	0.952	0.0	1.006	0.0	0.0	0.0	1.007	0.0
	72	0.946	0.0	0.954	0.0	0.979	0.0	0.0	0.0	0.966	0.0
	95.5	0.930	0.0	0.933	0.0	0.954	0.0	0.0	0.0	0.976	0.0
	118.5	0.953	0.0	0.946	0.0	0.998	0.0	0.0	0.0	0.980	0.0
	144	0.912	0.0	0.926	0.0	0.926	0.0	0.0	0.0	0.969	0.0
	173	0.888	0.0	0.925	0.0	0.922	0.0	0.0	0.0	0.956	0.0
	196	0.620	4.4	0.698	3.0	0.723	2.6	3.3	1.0	0.977	0.0
	219.5	0.216	11.7	0.123	13.4	0.406	8.3	11.1	2.6	0.933	0.0
	239	0.069	14.3	0.058	14.5	0.119	13.4	14.1	0.6	0.904	0.0

APPENDIX B

HPLC, MASS SPECTROMETRY AND FAME DATA FOR HALOCHELINS B, C AND E

HPLC, MASS SPECTROMETRY AND FAME DATA FOR HALOCHELINS B, C AND E

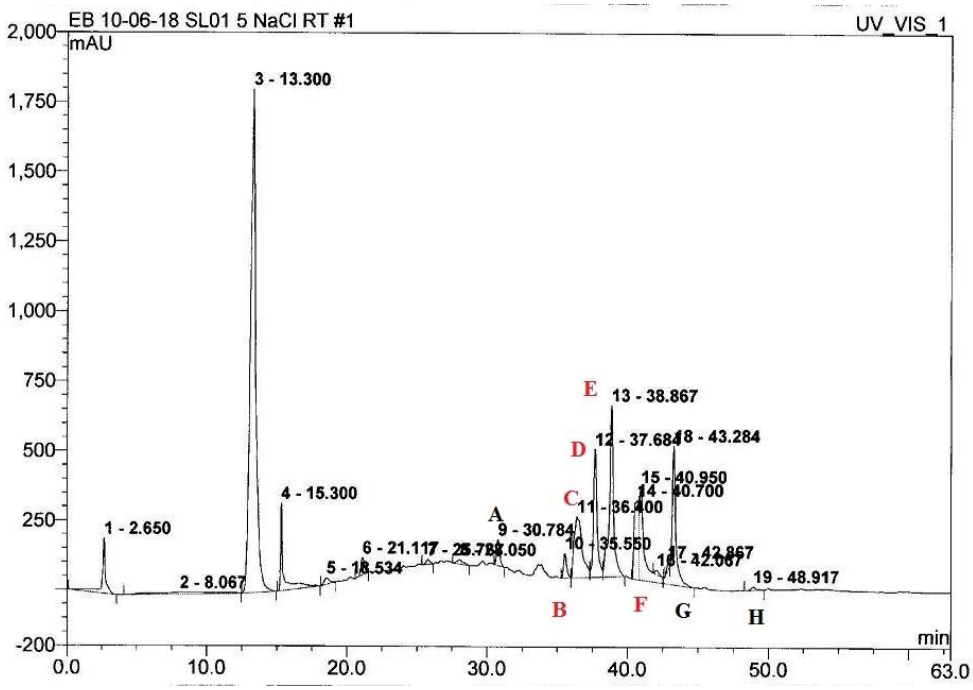

Figure B1. HPLC chromatogram of *Halomonas* sp. SL01 produced fractions with their retention times. Red letters (B through F) indicates iron-chelation active fractions, suggesting siderophore presence. Black letters represents no iron chelation activity (fractions A and H) or poor solubility in water (fraction G).

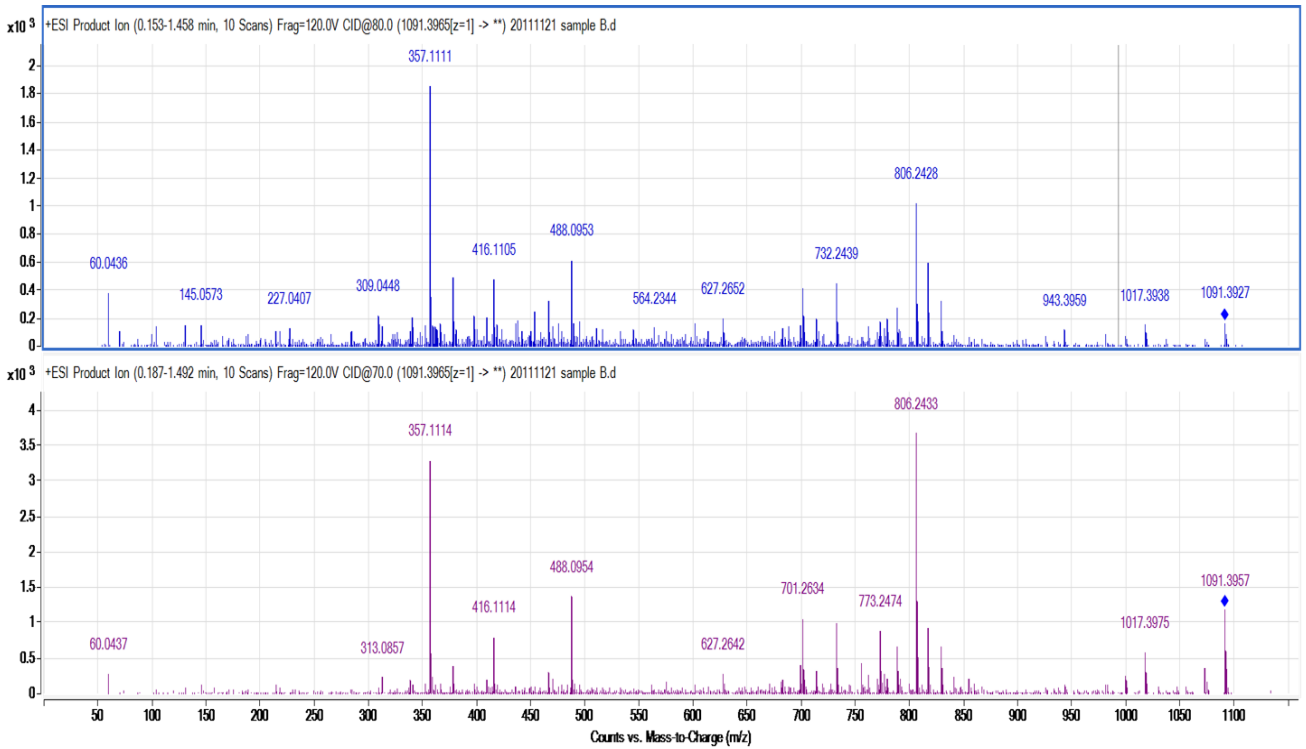

Figure B2. QTOF mass spectra with ESI showing mass to charge ratio (*m/z*) vs. relative abundance for Halochelin B. Top spectrum was performed at collision induced dissociation (CID) of 80 and the bottom spectrum at a CID of 70 and 120 V. Parent ion was detected at 1091.40 amu and is identified with a blue diamond.

Table B1. Mass to charge (m/z) ratios for Halochelin B at CID 70 (Z=1).

Halochelin B			
m/z	**Abundance**	**Abundance (%)**	**Maximum Abundance**
60.0436	376.5	20.29	376.5
309.0448	219.2	11.81	219.2
340.0878	211.5	11.4	211.5
357.1111	1855.5	100	1855.5
358.1137	351.7	18.96	351.7
378.0654	487	26.25	487
379.0634	170.3	9.18	170.3
397.1076	217.9	11.74	217.9
409.1083	204.3	11.01	204.3
416.1105	477.1	25.71	477.1
436.0836	166.4	8.97	166.4
438.1954	189.5	10.21	189.5
454.1266	251.2	13.54	251.2
466.127	321.8	17.34	321.8
488.0953	614.3	33.11	614.3
489.1001	167.9	9.05	167.9
495.2163	176.4	9.51	176.4
627.2652	196.4	10.58	196.4
701.2628	407.9	21.98	407.9
702.2529	219.7	11.84	219.7
714.234	195.5	10.54	195.5
732.2439	450.8	24.3	450.8
733.2427	178.3	9.61	178.3
773.245	179.3	9.66	179.3
779.3221	194	10.46	194
788.2333	272	14.66	272
806.2428	1017.1	54.81	1017.1
807.2451	304.2	16.4	304.2
808.2415	173.7	9.36	173.7
817.2999	599	32.28	599
818.3023	242.3	13.06	242.3
829.2994	325.6	17.55	325.6
1091.393	166.7	8.98	166.7

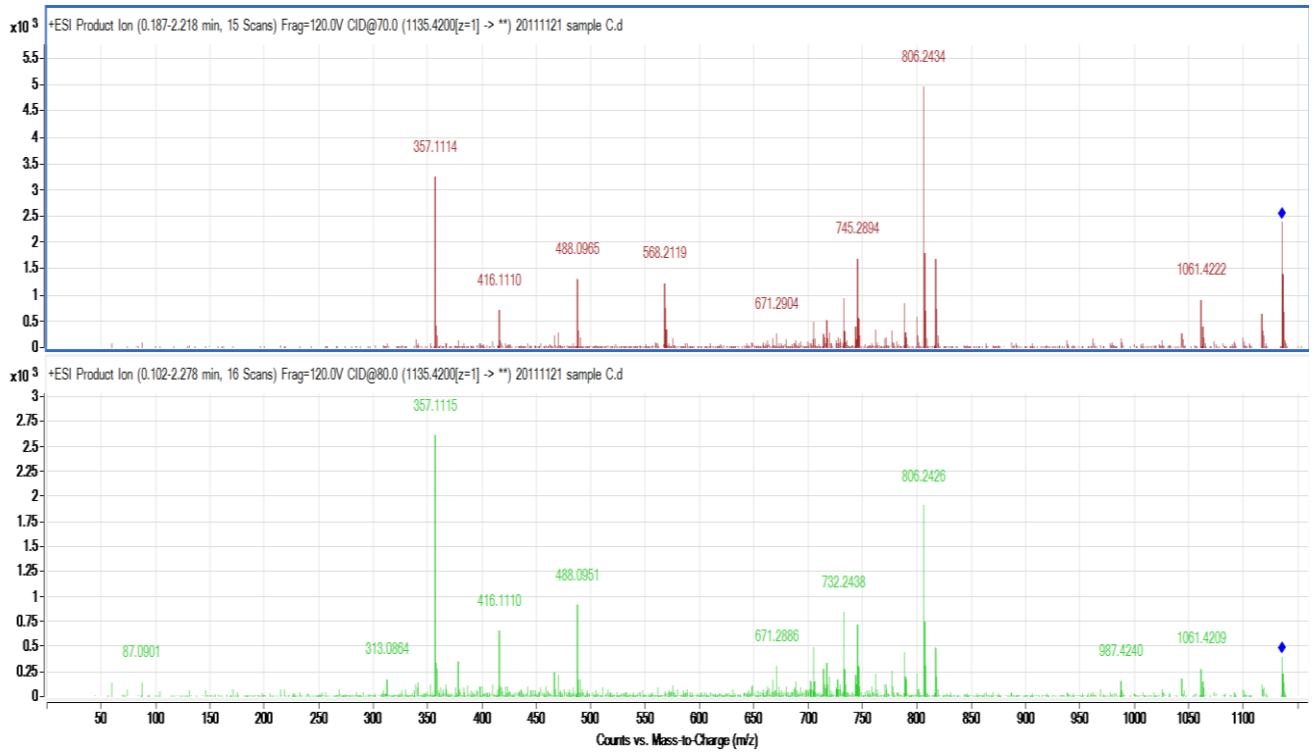

Figure B3. QTOF mass spectra with ESI showing mass to charge ratio (m/z) vs. relative abundance for Halochelin C. Top spectrum was performed at collision induced dissociation (CID) of 70 and the bottom spectrum at a CID of 80 and 120 V. Parent ion was detected at 1135.42 amu and is identified with a blue diamond.

Table B2. Mass to charge (m/z) ratios for Halochelin C at CID 70 (Z=1).

Halochelin C			
m/z	**Abundance**	**Abundance (%)**	**Maximum Abundance**
357.1114	3257.6	65.63	3257.6
358.1141	413.7	8.33	413.7
416.111	724	14.59	724
488.0965	1316.3	26.52	1316.3
568.2119	1229.3	24.77	1229.3
568.7145	752.4	15.16	752.4
569.2143	355.1	7.15	355.1
705.1778	483.6	9.74	483.6
717.1776	530	10.68	530
732.2443	928.4	18.7	928.4
743.2722	406.1	8.18	406.1
745.2894	1699.2	34.23	1699.2
746.2913	550.2	11.08	550.2
788.2326	840.2	16.93	840.2
799.2634	586.5	11.82	586.5
806.2434	4963.7	100	4963.7
807.2459	1796.3	36.19	1796.3
808.2449	689.5	13.89	689.5
817.2729	1691.2	34.07	1691.2
818.2754	713	14.36	713
1061.422	914.4	18.42	914.4
1062.425	407.1	8.2	407.1
1117.41	636.6	12.82	636.6
1135.421	2390.2	48.15	2390.2
1136.424	1398.2	28.17	1398.2
1137.425	655.4	13.2	655.4

Table B3. Mass to charge (m/z) ratios for Halochelin C at CID 20 (Z=2).

Halochelin C			
m/z	**Abundance**	**Abundance (%)**	**Maximum Abundance**
60.0438	1206.7	18.85	1206.7
87.0907	342.3	5.35	342.3
104.0328	1599.9	24.99	1599.9
114.0533	617.7	9.65	617.7
131.0796	2848.8	44.5	2848.8
189.0837	349.9	5.46	349.9
198.182	651.1	10.17	651.1
218.1104	574.3	8.97	574.3
330.1858	830.6	12.97	830.6
394.616	780	12.18	780
403.6216	3078.2	48.08	3078.2
404.1229	1103	17.23	1103
404.6252	336	5.25	336
469.1306	524.1	8.19	524.1
481.1305	358.3	5.6	358.3
531.211	357.2	5.58	357.2
550.1991	375.8	5.87	375.8
559.2054	1357.6	21.21	1357.6
559.7067	850	13.28	850
560.21	349.2	5.45	349.2
568.211	6401.9	100	6401.9

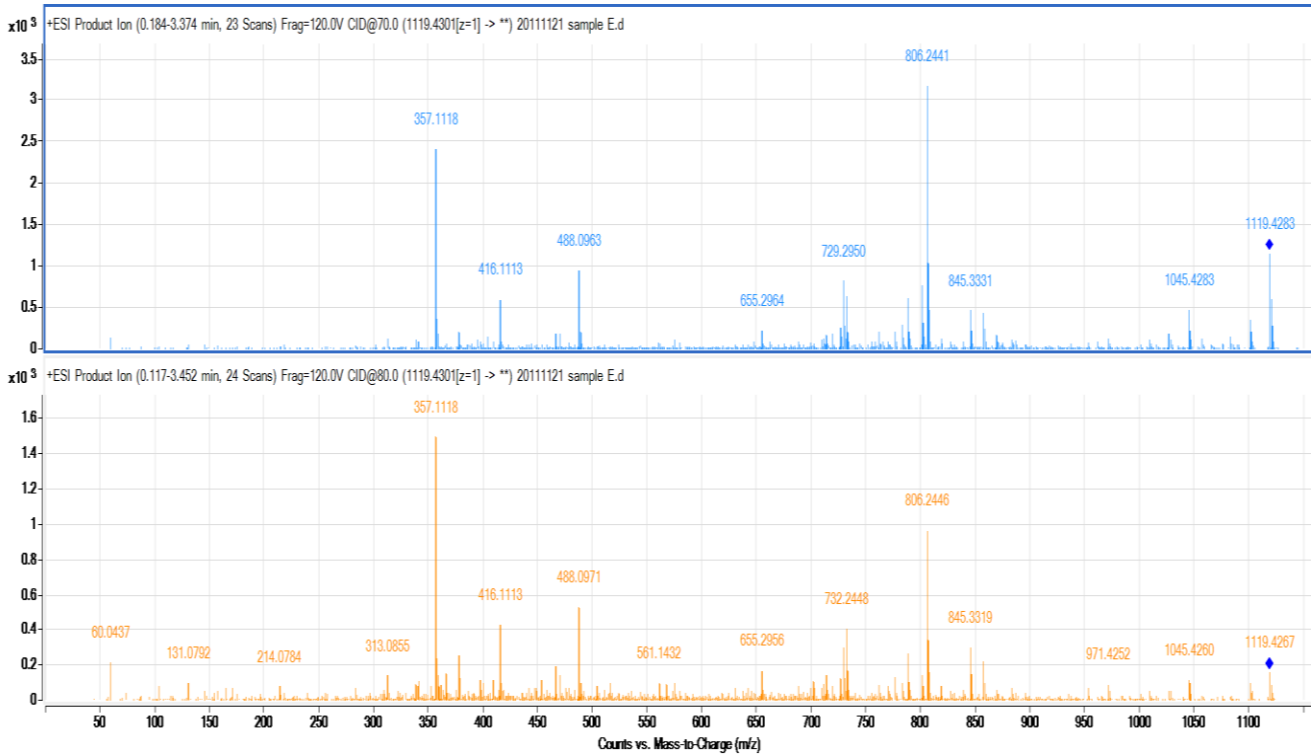

Figure B4. QTOF mass spectra with ESI showing mass to charge ratio (m/z) vs. relative abundance for Halochelin E. Top spectrum was performed at collision induced dissociation (CID) of 70 and the bottom spectrum at a CID of 80 and 120 V. Parent ion was detected at 1119.43 amu and is identified with a blue diamond.

Table B4. Mass to charge (m/z) ratios for Halochelin E at CID 80 (Z=1).

Halochelin E							
m/z	Abundance	Abundance (%)	Maximum Abundance	m/z	Abundance	Abundance (%)	Maximum Abundance
60.0437	211.4	14.13	211.4	727.2776	124.1	8.3	124.1
313.0855	136.4	9.12	136.4	729.2945	298	19.93	298
341.1374	109.3	7.31	109.3	730.2951	123.9	8.29	123.9
357.1118	1495.7	100	1495.7	732.2448	407.3	27.23	407.3
358.1157	240.3	16.06	240.3	733.2479	169.6	11.34	169.6
359.1112	139.2	9.31	139.2	776.2318	133.7	8.94	133.7
366.0659	150.8	10.08	150.8	788.2344	261.1	17.45	261.1
378.0659	257.3	17.2	257.3	789.2321	101.9	6.81	101.9
379.0658	122.3	8.17	122.3	801.2788	138.1	9.24	138.1
397.1059	109.7	7.34	109.7	806.2446	965.8	64.58	965.8
409.1072	116.5	7.79	116.5	807.2462	339.6	22.71	339.6
416.1113	429.3	28.7	429.3	807.3523	125.8	8.41	125.8
454.1273	111.8	7.47	111.8	808.2447	156.4	10.46	156.4
466.1282	194.8	13.02	194.8	845.3319	298.4	19.95	298.4
470.0863	138	9.23	138	846.3347	145.6	9.73	145.6
488.0971	527.4	35.26	527.4	857.3321	219.2	14.66	219.2
655.2956	167	11.17	167	1045.426	113.4	7.58	113.4
702.2316	102.3	6.84	102.3	1119.427	160.7	10.75	160.7
714.2345	143.8	9.61	143.8				

Table B5. Mass to charge (m/z) ratios for Halochelin E at CID 30 (Z=2).

Halochelin E			
m/z	**Abundance**	**Abundance (%)**	**Maximum Abundance**
57.0694	267.4	6.78	267.4
60.0438	592.3	15.01	592.3
86.0589	208.2	5.28	208.2
104.033	1038.5	26.32	1038.5
113.0689	212.8	5.39	212.8
114.0536	313.1	7.94	313.1
131.0796	1137	28.81	1137
189.0838	233.2	5.91	233.2
218.1102	313.5	7.94	313.5
314.1914	323.5	8.2	323.5
360.1068	249.4	6.32	249.4
385.6107	264	6.69	264
394.617	830.8	21.05	830.8
395.1172	329.3	8.34	329.3
403.6222	2575.3	65.26	2575.3
404.1235	963.8	24.42	963.8
404.6228	301.7	7.65	301.7
469.1314	566.7	14.36	566.7
469.6329	279.2	7.08	279.2
505.2028	255.1	6.46	255.1
514.2092	198.6	5.03	198.6
523.2129	224.9	5.7	224.9
542.2028	326.6	8.28	326.6
551.2087	806.3	20.43	806.3
551.7099	408.9	10.36	408.9

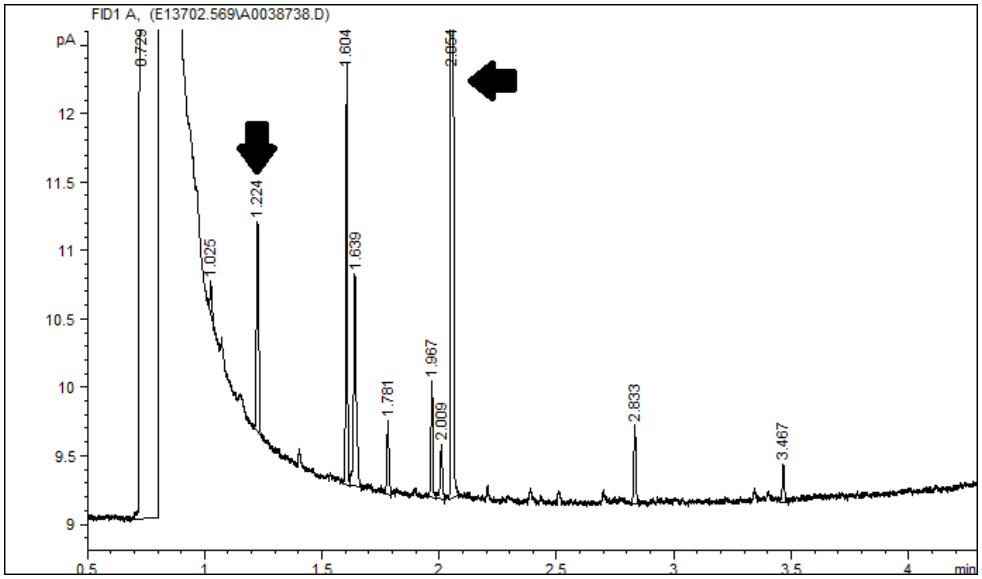

Figure B5. Gas chromatogram for fatty acid methyl ester (FAME) analysis of Halochelins B (1.224 min) and C (2.054 min). Fractions of interest are indicated with black arrows.

Table B6. FAME analysis results with the Sherlock MIS Software for fatty acid identification of Halochelins B and C. Retention times and responses of each fraction plus their respective peak names are presented. [a]Retention time (min); [b]Response in pA; [c]Area/Height ratio; [d]Response factor; [e]Equivalent chain length.

RT[a]	Response[b]	Ar/Ht[c]	RFact[d]	ECL[e]	Peak Name	Percent	Comment1	Comment2
0.7290	1.088E+9	0.018	----	6.6980	SOLVENT PEAK	----	< min rt	
1.0254	344	0.010	----	8.6768		----	< min rt	
1.2238	1982	0.011	1.122	9.9999	10:0	10.40	ECL deviates 0.000	Reference -0.001
1.6042	3520	0.009	----	11.8175	unknown 11.825	----	ECL deviates -0.008	
1.6395	2312	0.011	----	11.9697		----		
1.7810	660	0.009	----	12.5052	unknown 12.502	----	ECL deviates 0.003	
1.9672	974	0.009	----	13.1858		----		
2.0086	532	0.010	1.007	13.3272	12:1 3OH	2.50	ECL deviates 0.002	
2.0545	17590	0.009	1.003	13.4837	12:0 3OH	82.44	ECL deviates 0.001	
2.8326	689	0.009	0.954	16.0006	16:0	3.07	ECL deviates 0.001	Reference 0.001
3.4665	363	0.009	0.935	17.9996	18:0	1.59	ECL deviates 0.000	Reference 0.000

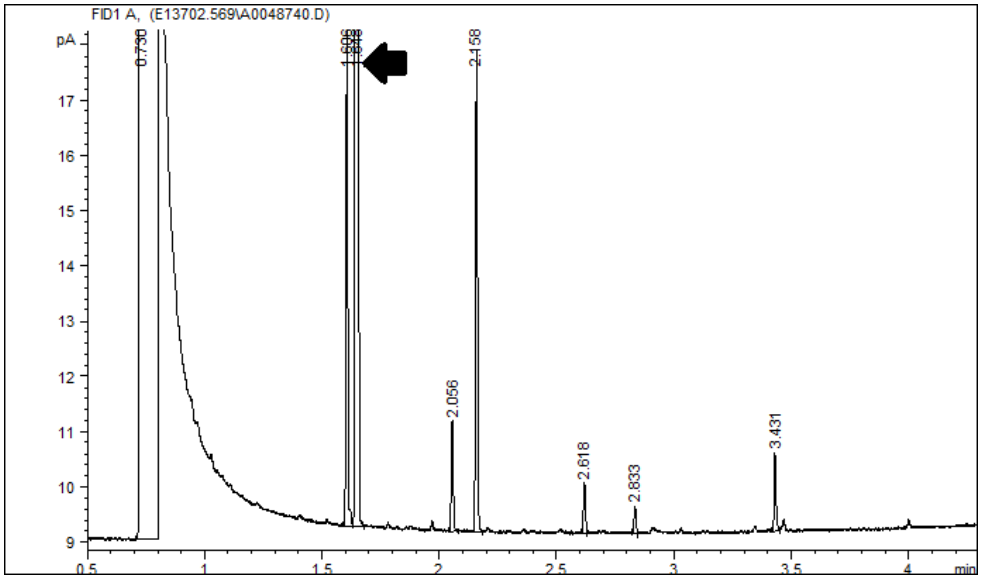

Figure B6. Gas chromatogram for fatty acid methyl ester (FAME) analysis of Halochelin E (1.648 min). Fraction of interest is indicated with black arrow.

Table B7. FAME analysis results with the Sherlock MIS Software for fatty acid identification of Halochelin E. Retention times and responses of fraction plus its respective peak name are presented. [a]Retention time (min); [b]Response in pA; [c]Area/Height ratio; [d]Response factor; [e]Equivalent chain length.

RT[a]	Response[b]	Ar/Ht[c]	RFact[d]	ECL[e]	Peak Name	Percent	Comment1	Comment2
0.7299	1.064E+9	0.018	----	6.6998	SOLVENT PEAK	----	< min rt	
1.6056	13029	0.009	----	11.8172	unknown 11.825	----	ECL deviates -0.008	
1.6482	108820	0.009	1.045	12.0000	12:0	97.59	ECL deviates 0.000	Reference 0.006
2.0558	2252	0.009	1.003	13.4837	12:0 3OH	1.94	ECL deviates 0.001	
2.1584	9521	0.008	----	13.8340		----		
2.6177	1027	0.009	----	15.3211		----		
2.8331	582	0.008	0.954	16.0000	16:0	0.48	ECL deviates 0.000	Reference 0.002
3.4314	1901	0.010	----	17.8849		----		

APPENDIX C

MASS SPECTROMETRY AND FAME DATA FOR HALOCHELINS D AND F

MASS SPECTROMETRY AND FAME DATA FOR HALOCHELINS D AND F

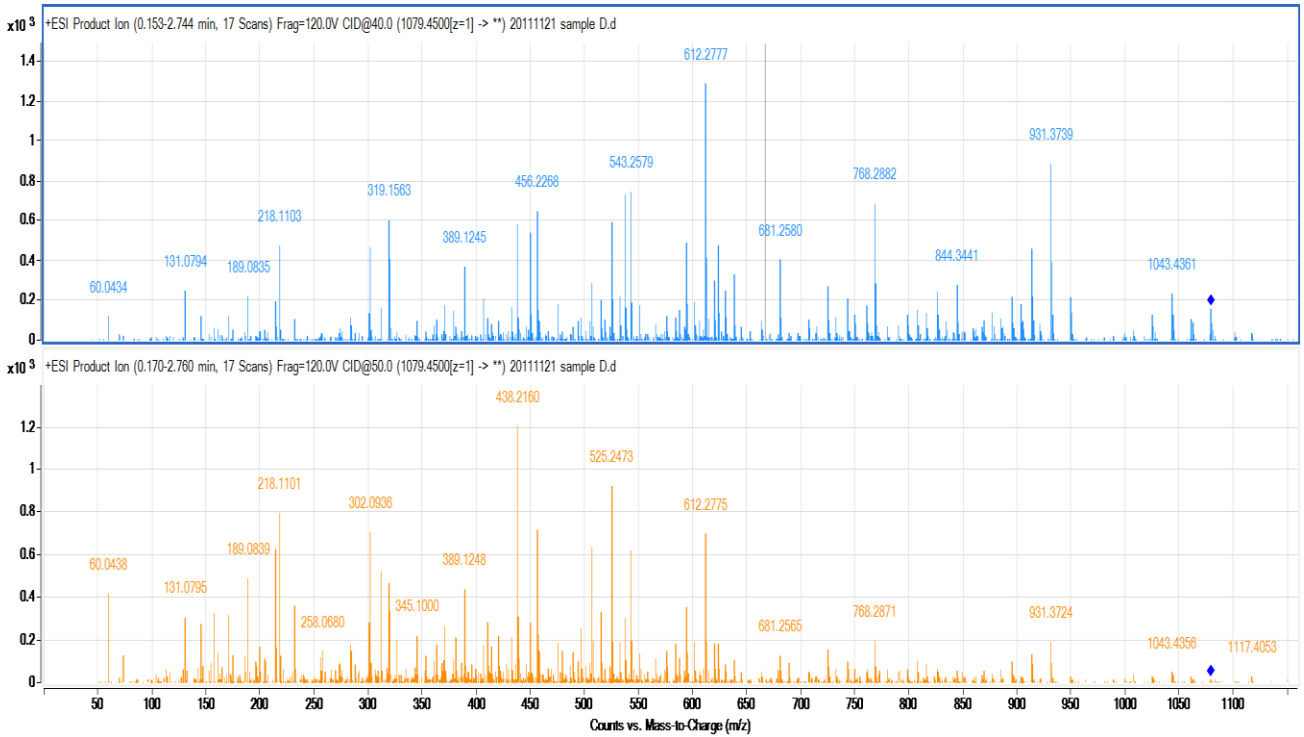

Figure C1. QTOF mass spectra with ESI showing mass to charge ratio (*m/z*) vs. relative abundance for Halochelin D. Top spectrum panel was performed at collision induced dissociation (CID) of 40 and the bottom panel at a CID of 50 (both at 120 V). Parent ion was detected at 1079.45 amu and is identified with a blue diamond.

Table C1. Mass to charge (m/z) ratios for Halochelin D at CID 30 (Z=1).

Halochelin D							
m/z	Abund.	Abund. (%)	Max. Abund.	m/z	Abund.	Abund. (%)	Max. Abund.
319.1563	670.9	29.41	670.9	320.1044	230.7	10.11	230.7
450.1753	786	34.45	786	438.2155	191.4	8.39	191.4
537.2064	895	39.23	895	451.1786	155.3	6.81	155.3
612.2776	882.2	38.67	882.2	456.227	236.4	10.36	236.4
624.2373	511.3	22.41	511.3	525.2465	262.1	11.49	262.1
630.2883	376.4	16.5	376.4	538.2079	158	6.93	158
638.2166	405	17.75	405	543.2582	293.2	12.85	293.2
681.2576	562.8	24.67	562.8	594.267	257.7	11.29	257.7
768.2882	1220.3	53.49	1220.3	613.279	275.3	12.07	275.3
769.2925	388.4	17.02	388.4	620.2052	203.9	8.94	203.9
826.3317	329.3	14.43	329.3	682.2577	175.3	7.68	175.3
844.3433	461	20.21	461	750.276	162.3	7.11	162.3
913.364	831.8	36.46	831.8	761.3079	194.4	8.52	194.4
914.3646	366.6	16.07	366.6	845.3456	175.9	7.71	175.9
931.3745	2281.5	100	2281.5	862.3499	150.3	6.59	150.3
932.3766	1137.5	49.86	1137.5	887.3512	165.6	7.26	165.6
933.3788	305.8	13.4	305.8	895.3535	201.2	8.82	201.2
949.385	1430.7	62.71	1430.7	903.3803	209.9	9.2	209.9
950.3876	719.2	31.52	719.2	905.359	244.1	10.7	244.1
1043.436	591.6	25.93	591.6	906.3632	162.7	7.13	162.7
1044.44	346.7	15.2	346.7	921.3915	216	9.47	216
1061.447	605.8	26.55	605.8	951.3923	236.2	10.35	236.2
1062.449	319.8	14.02	319.8	1025.425	151.4	6.64	151.4
1079.457	842.6	36.93	842.6	1081.463	220.9	9.68	220.9
1080.46	518.8	22.74	518.8				

Table C2. Mass to charge (m/z) ratios for Halochelin D at CID 50 (Z=1). [a]Abundance; [b]Percent abundance and [c]maximum abundance.

Halochelin D							
m/z	**Abund.[a]**	**Abund. (%)[b]**	**Max. Abund.[c]**	**m/z**	**Abund.**	**Abund. (%)**	**Max. Abund.**
60.0438	416.7	34.68	416.7	283.1341	182.9	15.22	182.9
131.0795	306	25.46	306	327.0874	196.1	16.32	196.1
157.0579	320.7	26.68	320.7	345.1	221.8	18.46	221.8
171.0735	320.2	26.64	320.2	363.1091	174.9	14.55	174.9
189.0839	485.9	40.44	485.9	371.1143	261.9	21.8	261.9
214.0787	625.3	52.04	625.3	381.1962	208.7	17.36	208.7
218.1101	795.1	66.17	795.1	407.1344	176.5	14.69	176.5
232.0891	362.3	30.15	362.3	414.1178	170.3	14.17	170.3
301.1096	282.1	23.48	282.1	420.2064	218.7	18.2	218.7
302.0936	704.4	58.62	704.4	432.1293	212.9	17.71	212.9
312.1756	519	43.19	519	457.2292	226.6	18.85	226.6
319.1554	465	38.7	465	476.1544	182.1	15.15	182.1
320.104	331.9	27.62	331.9	497.2528	251.4	20.92	251.4
389.1248	438.5	36.49	438.5	508.2413	197.4	16.43	197.4
438.216	1201.7	100	1201.7	515.1648	198.5	16.52	198.5
439.2187	310.1	25.81	310.1	526.2497	188.3	15.67	188.3
450.1408	280.6	23.35	280.6	533.1748	192.8	16.04	192.8
456.2272	719.5	59.87	719.5	544.2588	198.3	16.5	198.3
507.2369	634.2	52.77	634.2	584.2828	181	15.06	181
515.2622	333	27.71	333	602.1947	189.6	15.78	189.6
525.2473	919.9	76.55	919.9	613.2802	190.8	15.88	190.8
537.2064	303.6	25.27	303.6	620.2053	182.2	15.16	182.2
543.2574	619.2	51.53	619.2	624.2371	182.1	15.16	182.1
594.2674	352.5	29.33	352.5	768.2871	195.3	16.25	195.3
612.2775	696.7	57.98	696.7	931.3724	190.8	15.88	190.8

Table C3. Mass to charge (m/z) ratios for Halochelin D at CID 50 (Z=2).

Halochelin D			
m/z	**Abundance**	**Abundance (%)**	**Maximum Abundance**
60.0436	214.8	9.33	214.8
86.0587	128.6	5.58	128.6
104.0326	198.5	8.62	198.5
114.0531	203.8	8.85	203.8
131.0797	2303.1	100	2303.1
132.0811	142.6	6.19	142.6
218.1093	245.3	10.65	245.3
284.1801	126.4	5.49	126.4
312.1757	717.9	31.17	717.9
313.1778	187.8	8.15	187.8
384.6469	148.3	6.44	148.3
438.217	142.2	6.17	142.2
522.2212	390.5	16.95	390.5
522.7231	239.1	10.38	239.1
531.2277	592	25.71	592
531.7296	445.9	19.36	445.9
532.2293	176.5	7.66	176.5
537.2065	154.8	6.72	154.8
540.2333	1062.6	46.14	1062.6
540.735	701.5	30.46	701.5
541.236	245.5	10.66	245.5
541.7375	123.9	5.38	123.9
542.2143	145.2	6.31	145.2
543.2543	125.9	5.47	125.9
624.2353	123.2	5.35	123.2

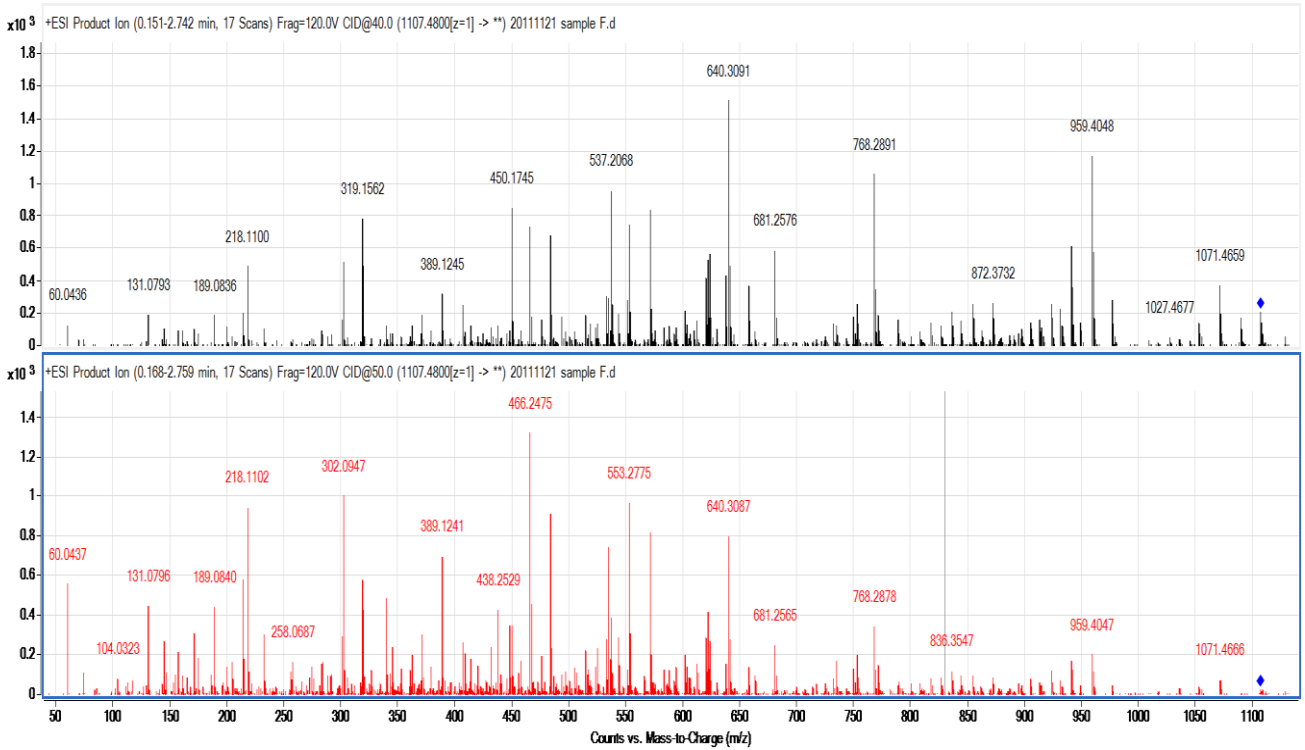

Figure C2. QTOF mass spectra with ESI showing mass to charge ratio (m/z) vs. relative abundance for Halochelin F. Top panel spectrum was performed at CID of 40 and the bottom panel spectrum at 50 (both at 120 V). Parent ion was detected at 1107.48 amu and is identified with a blue diamond.

Table C4. Mass to charge (m/z) ratios for Halochelin F at CID 30 (Z=1). [a]Abundance; [b]Percent abundance and [c]maximum abundance.

Halochelin F							
m/z	Abund.[a]	Abund. (%)[b]	Max. Abund.[c]	m/z	Abund.	Abund. (%)	Max. Abund.
450.1763	1058.6	38	1058.6	1089.478	818	29.36	818
537.2066	1122.5	40.29	1122.5	1090.479	466.5	16.74	466.5
640.3086	953.6	34.23	953.6	1107.488	1237	44.41	1237
768.2894	1527.1	54.82	1527.1	1108.491	635.2	22.8	635.2
941.3951	944.2	33.89	944.2	1109.493	260.6	9.36	260.6
959.4054	2785.7	100	2785.7	189.084	124.4	4.46	124.4
960.4083	1363.7	48.95	1363.7	218.1097	172.3	6.19	172.3
977.4161	1855.5	66.61	1855.5	302.0951	191.7	6.88	191.7
978.4191	939.4	33.72	939.4	320.1034	205.2	7.36	205.2
1089.478	818	29.36	818	451.1792	222.5	7.99	222.5
1107.488	1237	44.41	1237	466.2482	167.2	6	167.2
319.1568	744	26.71	744	551.1837	163.1	5.85	163.1
450.1763	1058.6	38	1058.6	553.2779	206.8	7.42	206.8
484.2575	252.3	9.06	252.3	572.2921	140.8	5.05	140.8
537.2066	1122.5	40.29	1122.5	620.206	217	7.79	217
538.2094	270.1	9.69	270.1	625.2398	182.4	6.55	182.4
571.2886	384.5	13.8	384.5	639.22	134.9	4.84	134.9
622.2982	232.7	8.35	232.7	659.322	182	6.53	182
624.2374	632	22.69	632	750.2793	147.9	5.31	147.9
638.217	439.2	15.77	439.2	753.317	137.6	4.94	137.6
640.3086	953.6	34.23	953.6	770.2937	121.5	4.36	121.5
641.3122	311.5	11.18	311.5	771.3259	163.7	5.88	163.7
658.3189	339.3	12.18	339.3	790.3406	121.1	4.35	121.1
681.2584	727.6	26.12	727.6	836.3523	119.4	4.29	119.4
682.26	246.8	8.86	246.8	844.3794	147.1	5.28	147.1
768.2894	1527.1	54.82	1527.1	855.3663	172	6.17	172
769.292	581.7	20.88	581.7	862.3878	131.4	4.72	131.4
789.3378	246.6	8.85	246.6	890.3807	162.3	5.82	162.3
854.3635	342.7	12.3	342.7	905.389	130.6	4.69	130.6
872.3742	466.8	16.76	466.8	915.3781	187.4	6.73	187.4
873.3761	295.4	10.61	295.4	923.3861	204.8	7.35	204.8
933.3906	271	9.73	271	924.3823	125.8	4.51	125.8
941.3951	944.2	33.89	944.2	931.4079	214.1	7.69	214.1
942.3969	444.6	15.96	444.6	934.3922	149.2	5.36	149.2
959.4054	2785.7	100	2785.7	943.4017	148.5	5.33	148.5

Table C5. Mass to charge (m/z) ratios for Halochelin F at CID 30 (Z=1, continued). [a]Abundance; [b]Percent abundance and [c]maximum abundance.

Halochelin F (Continued)							
m/z	Abund.[a]	Abund. (%)[b]	Max. Abund.[c]	m/z	Abund.	Abund. (%)	Max. Abund.
961.4107	382.5	13.73	382.5	950.423	129.6	4.65	129.6
977.4161	1855.5	66.61	1855.5	1053.456	159	5.71	159
978.4191	939.4	33.72	939.4	1054.453	130.9	4.7	130.9
979.419	327	11.74	327	1073.475	162.6	5.84	162.6
1071.467	723	25.95	723	1091.484	167.3	6.01	167.3
1072.47	445.3	15.99	445.3				

Table C6. Mass to charge (m/z) ratios for Halochelin F at CID 50 (Z=1). [a]Abundance; [b]Percent abundance and [c]maximum abundance.

Halochelin F							
m/z	Abund.[a]	Abund. (%)[b]	Max. Abund.[c]	m/z	Abund.	Abund. (%)	Max. Abund.
60.0437	556.1	42.22	556.1	450.1449	349.6	26.54	349.6
131.0796	446.5	33.9	446.5	466.2475	1317.2	100	1317.2
171.0736	310.4	23.56	310.4	467.2513	455.8	34.61	455.8
189.084	439.9	33.4	439.9	484.2579	912.7	69.29	912.7
214.0788	582.7	44.24	582.7	535.2674	739.2	56.12	739.2
218.1102	945.5	71.78	945.5	537.2063	387.4	29.41	387.4
302.0947	1001.4	76.02	1001.4	553.2775	963.6	73.15	963.6
319.156	577.8	43.86	577.8	554.283	306.7	23.28	306.7
320.1039	427.1	32.43	427.1	571.2885	815.6	61.92	815.6
340.2066	486.7	36.95	486.7	622.2988	415.2	31.52	415.2
389.1241	697.1	52.93	697.1	640.3087	798.8	60.65	798.8
438.2529	424.8	32.25	424.8	768.2878	340.2	25.83	340.2
448.237	346.3	26.29	346.3				

Table C7. Mass to charge (m/z) ratios for Halochelin F at CID 20 (Z=2).

Halochelin F			
m/z	**Abundance**	**Abundance (%)**	**Maximum Abundance**
60.044	1432.7	17.38	1432.7
104.033	2046.3	24.82	2046.3
114.0531	470.1	5.7	470.1
131.0798	2683.3	32.54	2683.3
218.1105	655.9	7.95	655.9
340.2067	829.4	10.06	829.4
394.6164	798.3	9.68	798.3
403.622	3407.1	41.32	3407.1
404.1231	1204.9	14.61	1204.9
469.1313	873.8	10.6	873.8
555.2114	449.6	5.45	449.6
564.2164	1426.4	17.3	1426.4
564.7171	736.6	8.93	736.6
573.2217	8245.4	100	8245.4
573.7231	4895.7	59.37	4895.7
574.2253	1886.3	22.88	1886.3
574.7261	547.5	6.64	547.5
806.2452	553.9	6.72	553.9

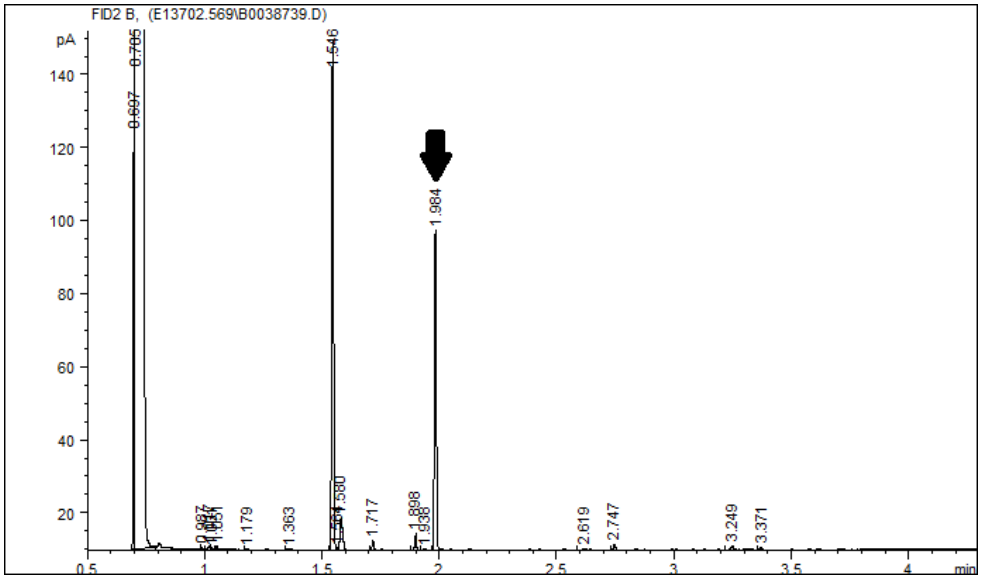

Figure C3. Gas chromatogram for fatty acid methyl ester (FAME) analysis of Halochelin D (1.9840 min). Fraction of interest is indicated with a black arrow.

Table C8. FAME analysis results with the Sherlock MIS Software for fatty acid identification of Halochelin D. Retention times and responses of each fraction plus their respective peak names are presented. [a]Retention time (min); [b]Response in pA; [c]Area/Height ratio; [d]Response factor; [e]Equivalent chain length.

RT[a]	Response[b]	Ar/Ht[c]	RFact[d]	ECL[e]	Peak Name	Percent	Comment1	Comment2
0.697	61497	0.004	----	6.6550		----	< min rt	
0.704	1.083E+9	0.017	----	6.7084	SOLVENT PEAK	----	< min rt	
0.987	890	0.012	----	8.6678		----	< min rt	
1.016	1452	0.012	----	8.8726		----	< min rt	
1.030	641	0.010	----	8.9700		----		
1.050	1202	0.010	----	9.1099		----		
1.178	537	0.010	1.220	9.9991	10:0	0.66	ECL deviates -0.001	Reference 0.001
1.363	435	0.009	1.151	11.0007	11:0	0.51	ECL deviates 0.001	Reference 0.002
1.545	143385	0.008	----	11.8164	unknown 11.825	----	ECL deviates -0.009	
1.563	422	0.006	----	11.8954		----		
1.580	13304	0.011	----	11.9691		----		
1.717	2740	0.008	----	12.5024	unknown 12.502	----	ECL deviates 0.000	
1.898	4738	0.008	----	13.1843		----		
1.938	397	0.009	1.024	13.3245	12:1 3OH	0.41	ECL deviates 0.000	
1.984	92165	0.008	1.017	13.4838	12:0 3OH	95.00	ECL deviates 0.001	
2.618	515	0.011	----	15.5912		----		
2.746	1623	0.009	0.930	16.0012	16:0	1.53	ECL deviates 0.001	Reference -0.002
3.249	1409	0.010	0.897	17.6097	18:3 w6c (6,9,12)	1.28	ECL deviates 0.010	
3.370	665	0.010	0.891	17.9990	18:0	0.60	ECL deviates -0.001	Reference -0.006

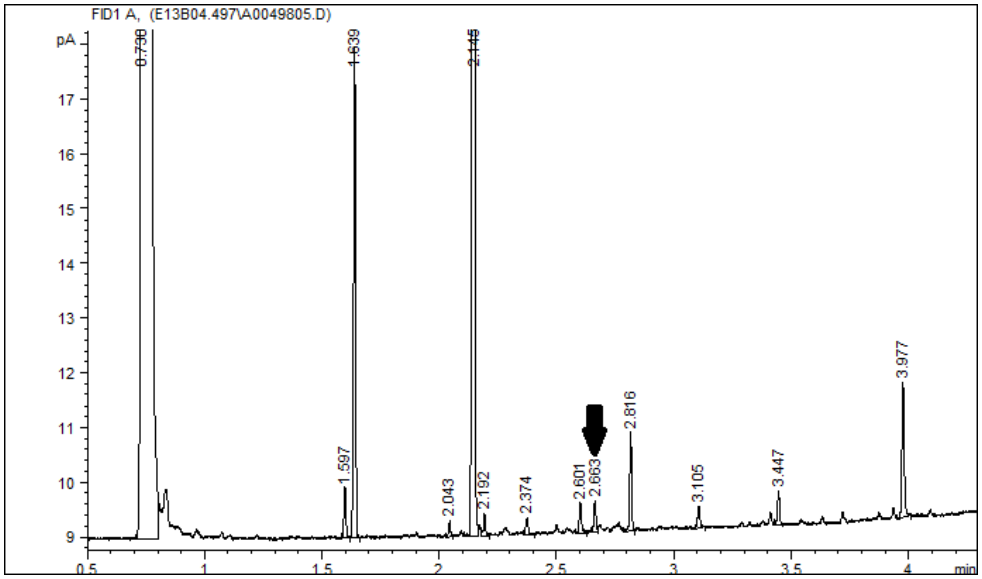

Figure C4. Gas chromatogram for FAME analysis of Halochelin F (2.663 min). Fraction of interest is indicated with a black arrow.

Table C9. FAME analysis results with the Sherlock MIS Software for fatty acid identification of Halochelin F. Retention times and responses of fraction plus its respective peak name are presented. [a]Retention time (min); [b]Response in pA; [c]Area/Height ratio; [d]Response factor; [e]Equivalent chain length.

RT[a]	Response[b]	Ar/Ht[c]	RFact[d]	ECL[e]	Peak Name	Percent	Comment1	Comment2
0.730	1.074E+09	0.020	0.000	6.676	SOLVENT PEAK	0.00	< min rt	
1.597	1093	0.009	1.045	11.817	unknown 11.825	5.72	ECL deviates -0.008	
1.639	10351	0.009	1.038	12.001	12:0	53.81	ECL deviates 0.001	Reference 0.005
2.043	375	0.009	0.989	13.485	12:0 3OH	1.86	ECL deviates 0.002	
2.145	107052	0.009	0.000	13.835		0.00		
2.192	611	0.010	0.976	13.999	14:0	2.99	ECL deviates -0.001	Reference 0.003
2.374	438	0.010	0.000	14.591		0.00		
2.601	731	0.010	0.000	15.320		0.00		
2.663	699	0.010	0.951	15.517	14:0 3OH	3.33	ECL deviates 0.002	14:0 3OH/16:1 iso
2.816	2080	0.009	0.946	16.000	16:0	9.85	ECL deviates 0.000	Reference 0.004
3.105	579	0.010	0.940	16.915	17:0 cyclopropane	2.72	ECL deviates 0.000	
3.447	792	0.010	0.938	18.001	18:0	3.72	ECL deviates 0.001	Reference 0.004
3.977	3387	0.011	0.943	19.739	20:2 w6,9c	16.00	ECL deviates 0.000	
0.000	699	0.000	0.000	0.000	Summed Feature 2	3.33	12:0 aldehyde?	unknown 10.947
0.000	0	0.000	0.000	0.000		0.00	16:1 iso I/14:0 3OH	14:0 3OH/16:1 iso

APPENDIX D

DYNAMIC LIGHT SCATTERING AND PARTICLE SIZE ANALYSIS DATA

DYNAMIC LIGHT SCATTERING AND PARTICLE SIZE ANALYSIS DATA

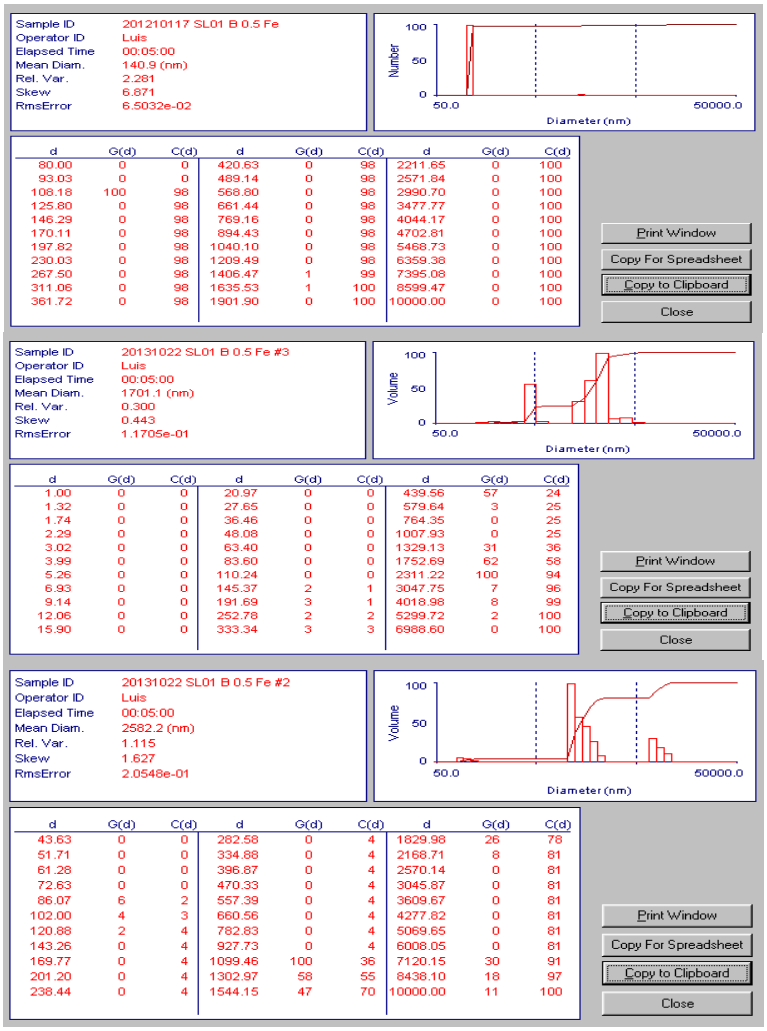

Figure D1. Particle size analysis results for *Halomonas* sp. SL01 Halochelin B at 0.5 Eq. Fe^{+3}.

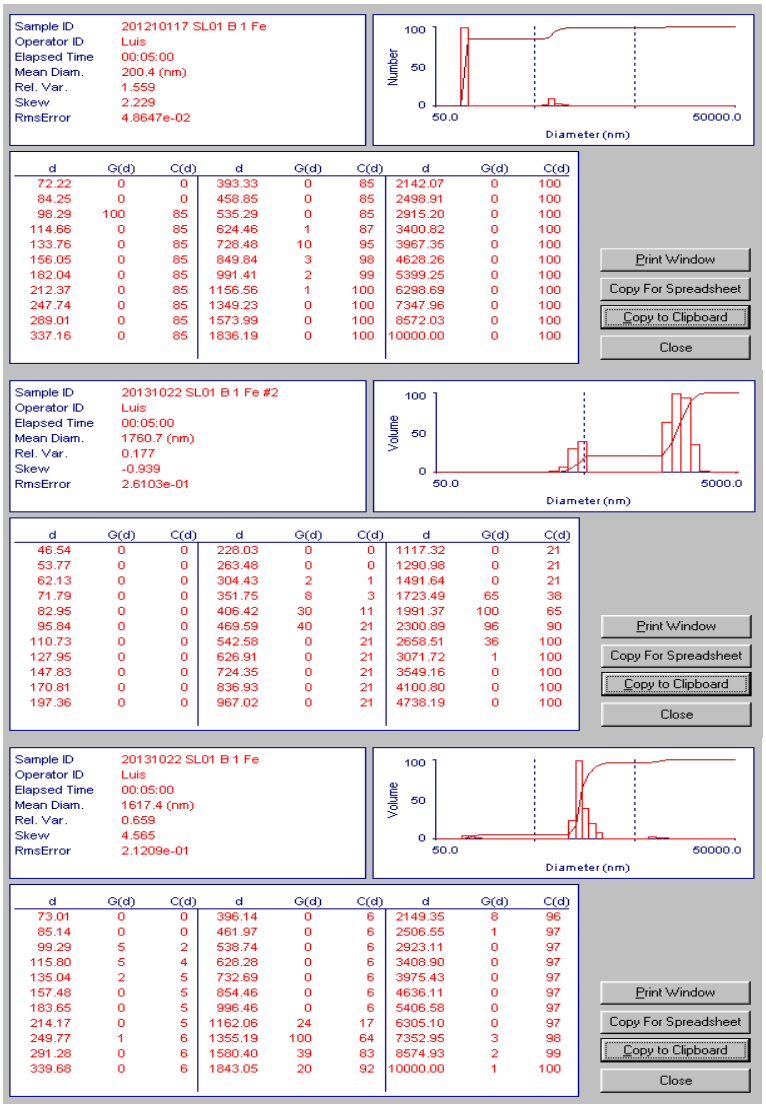

Figure D2. Particle size analysis results for *Halomonas* sp. SL01 Halochelin B at 1 Eq. Fe^{+3}.

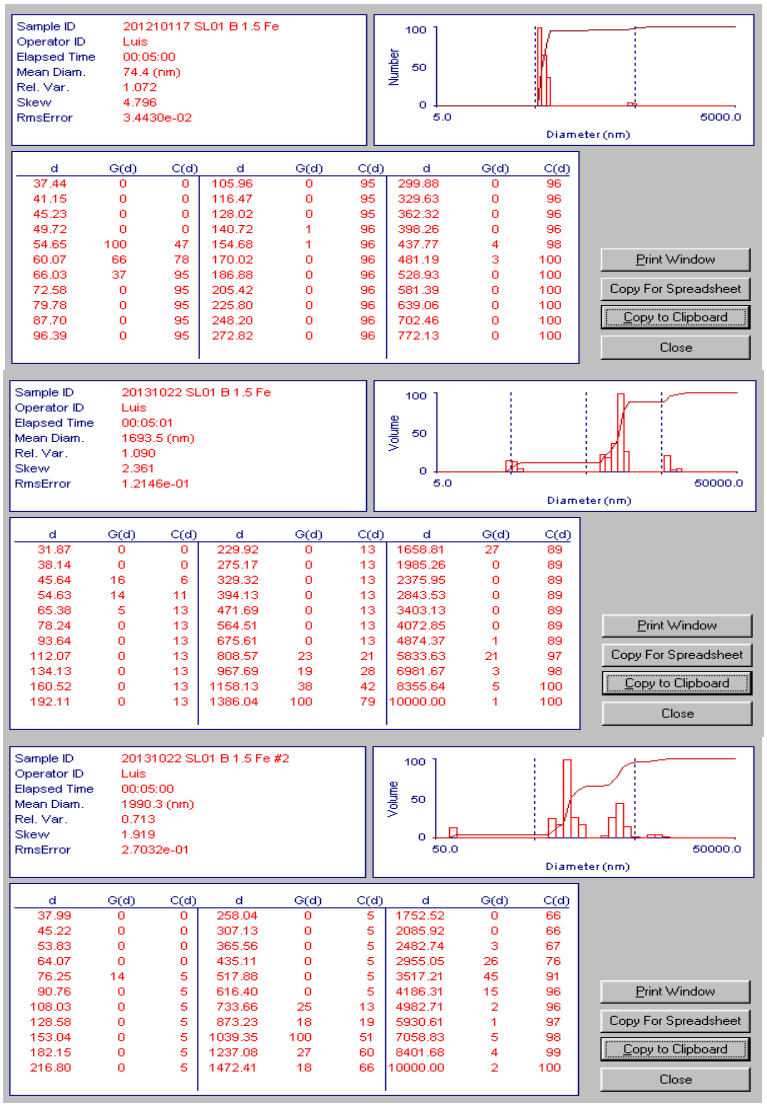

Figure D3. Particle size analysis results for *Halomonas* sp. SL01 Halochelin B at 1.5 Eq. Fe^{+3}.

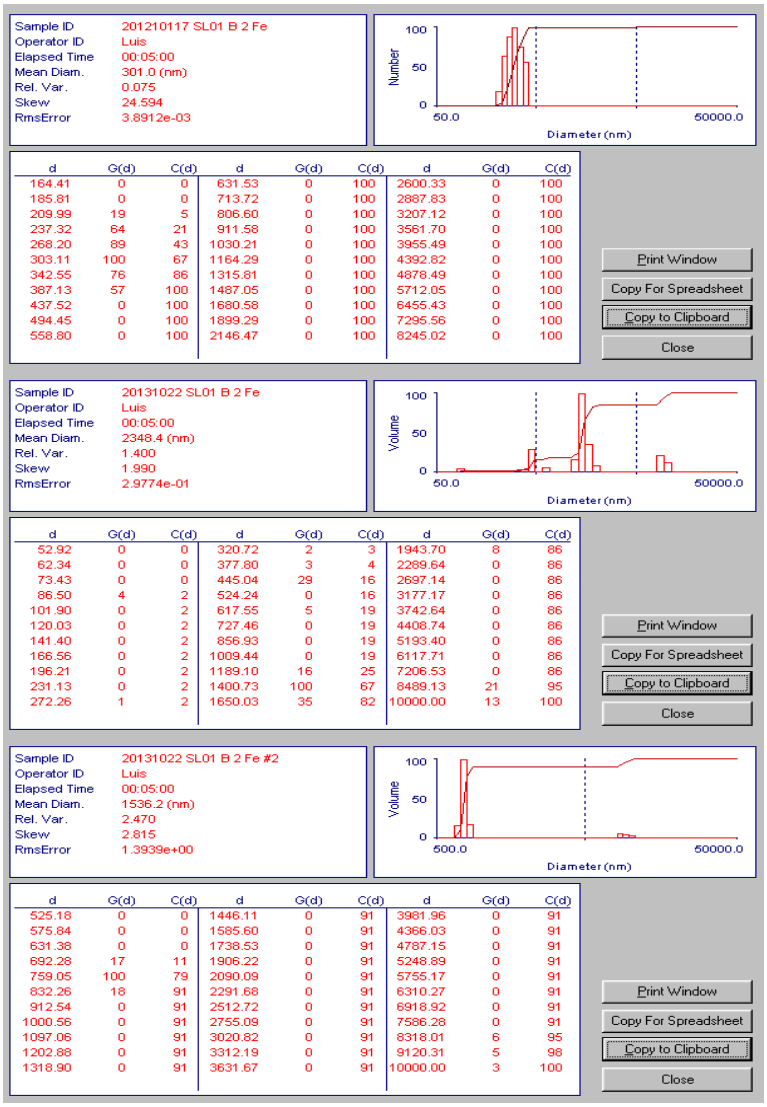

Figure D4. Particle size analysis results for *Halomonas* sp. SL01 Halochelin B at 2 Eq. Fe^{+3}.

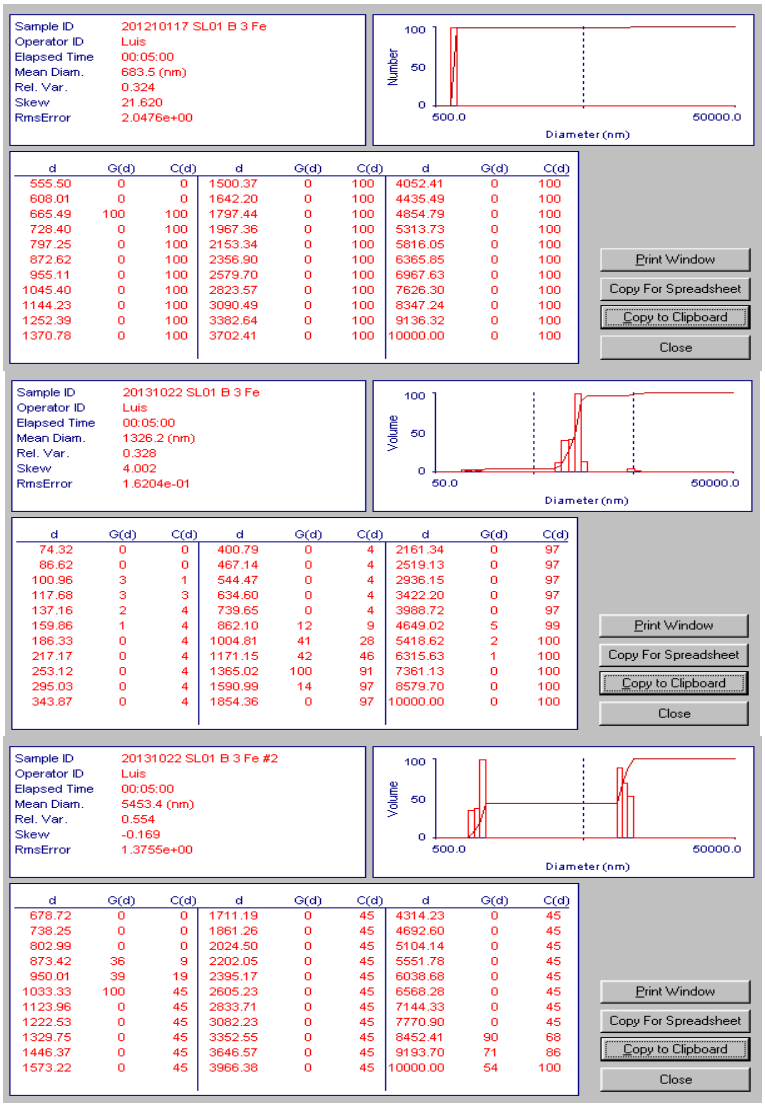

Figure D5. Particle size analysis results for *Halomonas* sp. SL01 Halochelin B at 3 Eq. Fe^{+3}.

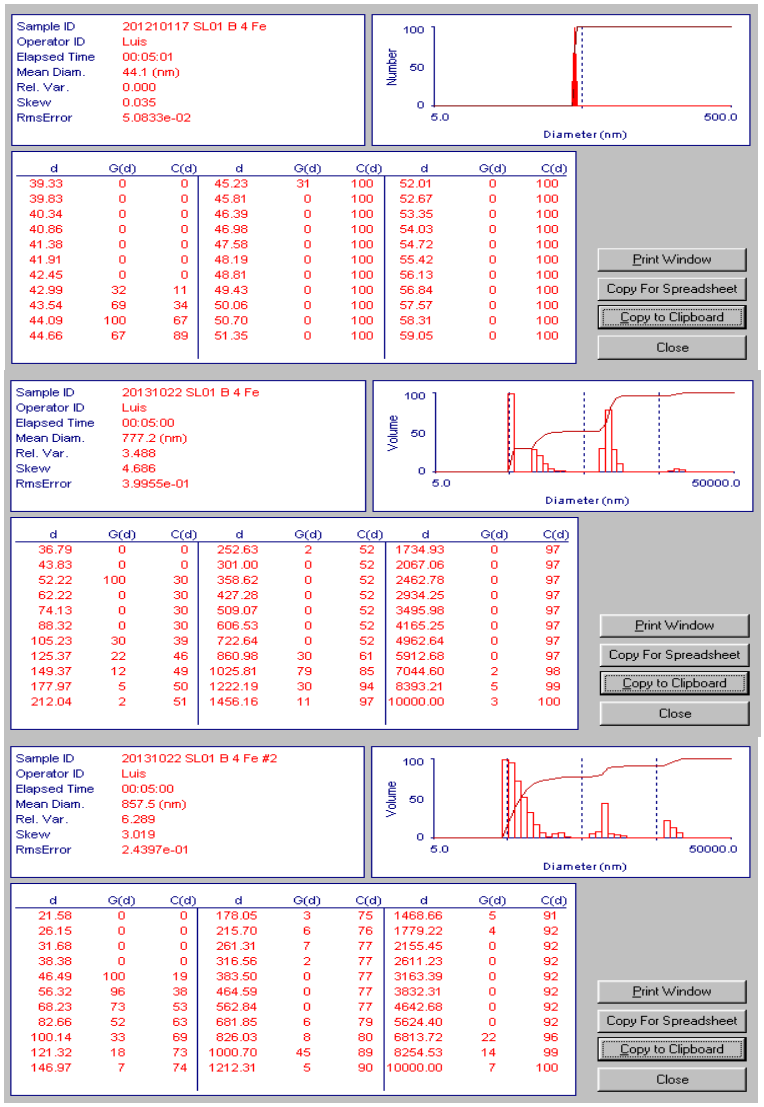

Figure D6. Particle size analysis results for *Halomonas* sp. SL01 Halochelin B at 4 Eq. Fe^{+3}.

A)

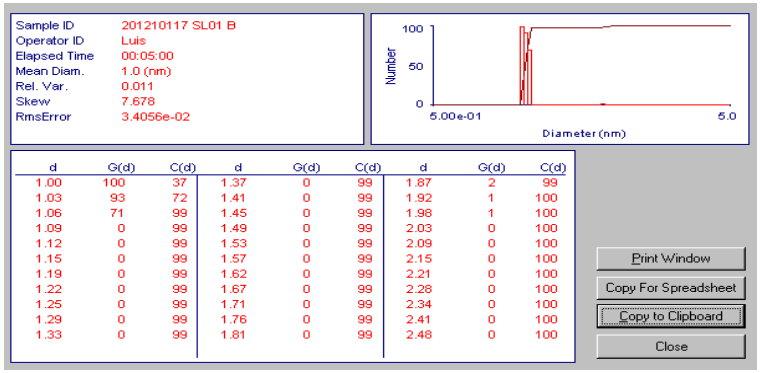

B)

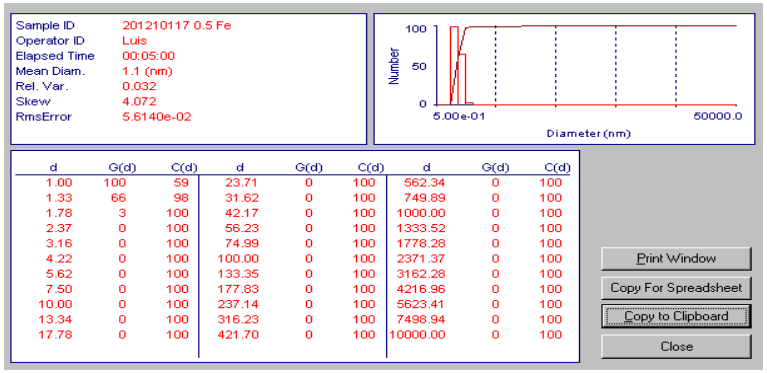

C)

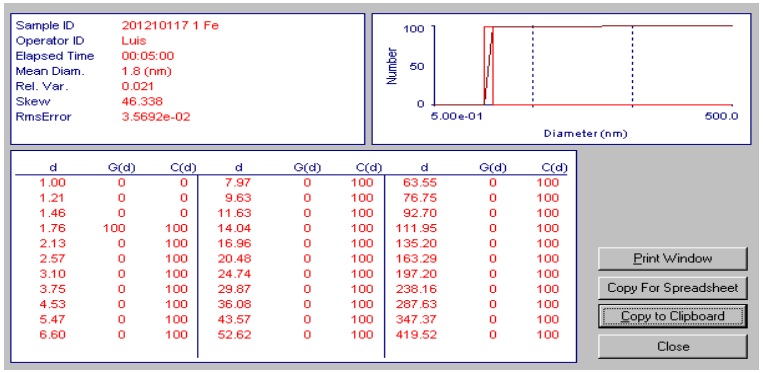

D)

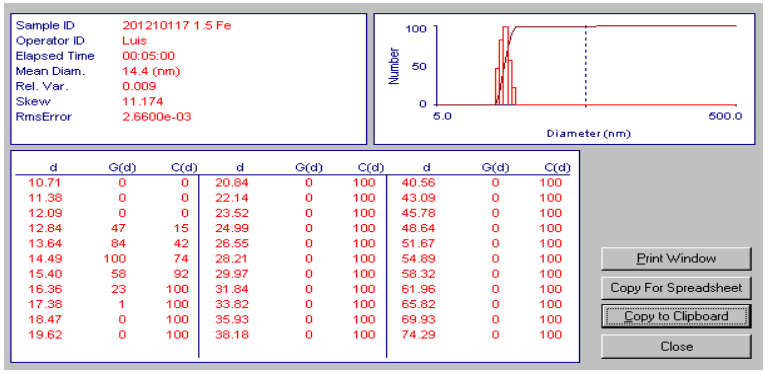

Figure D7. Particle size analysis results for *Halomonas* sp. SL01 Halochelin B without ferric iron (A) and ferric iron controls 0.5 (B), 1 (C) and 1.5 (D) Eq. Fe^{+3}.

A)

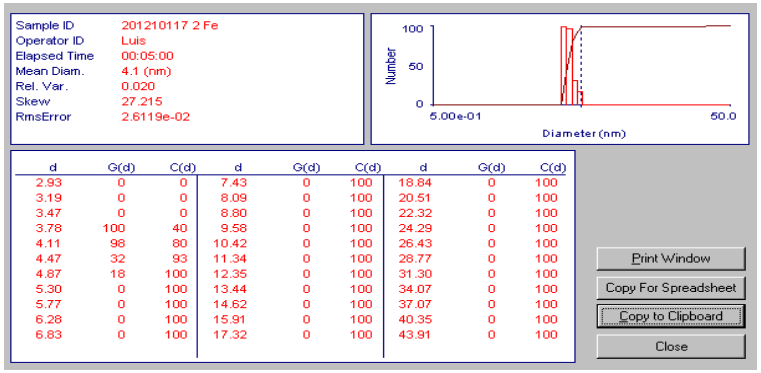

B)

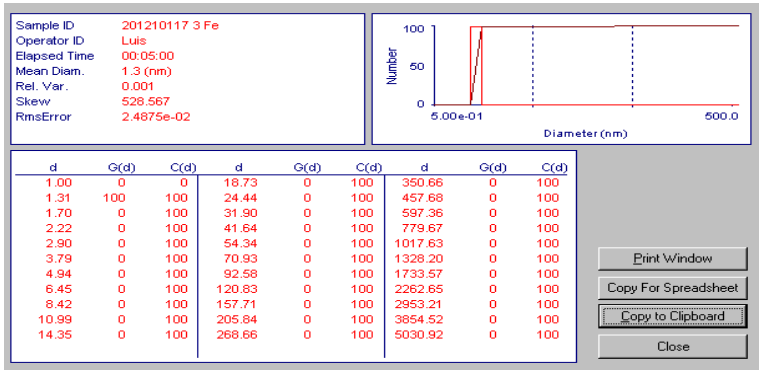

C)

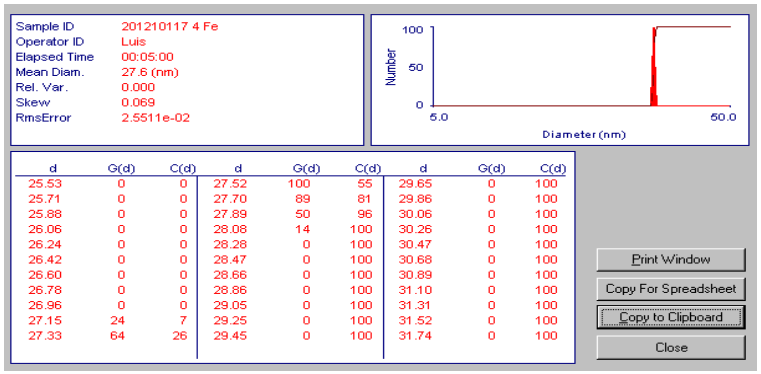

Figure D8. Particle size analysis results for ferric iron controls 2 (A), 3 (B) and 4 (C) Eq. Fe^{+3}.

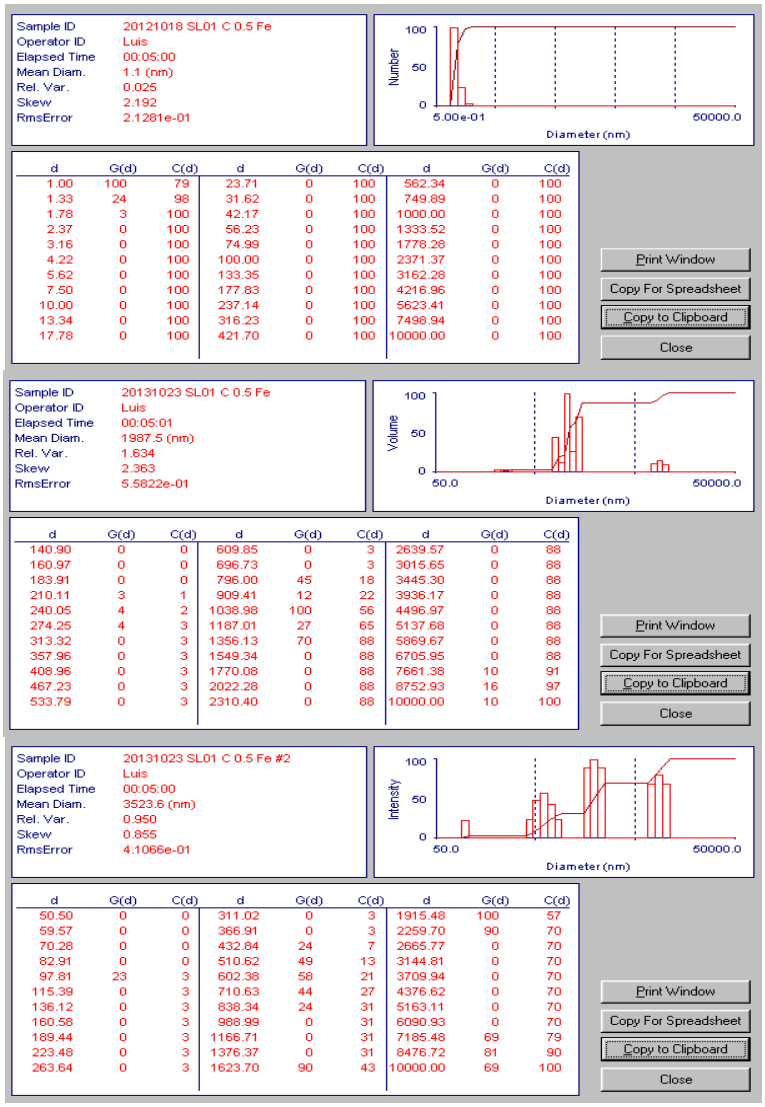

Figure D9. Particle size analysis results for *Halomonas* sp. SL01 Halochelin C at 0.5 Eq. Fe^{+3}.

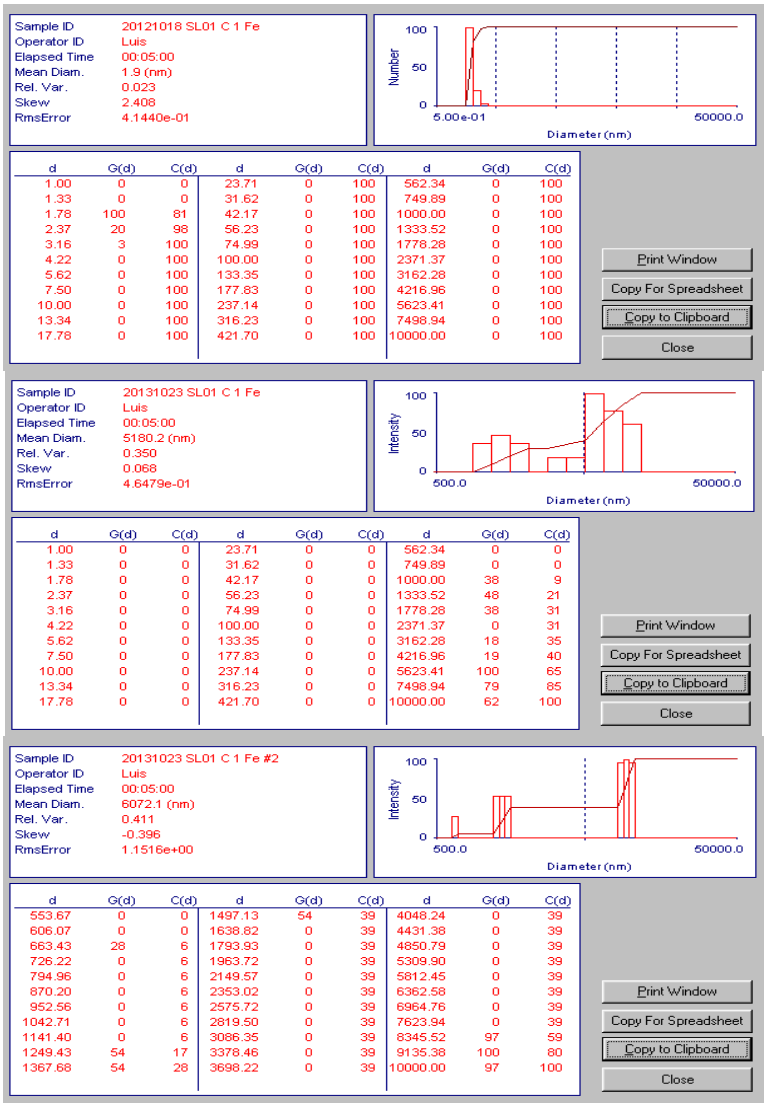

Figure D10. Particle size analysis results for *Halomonas* sp. SL01 Halochelin C at 1 Eq. Fe^{+3}.

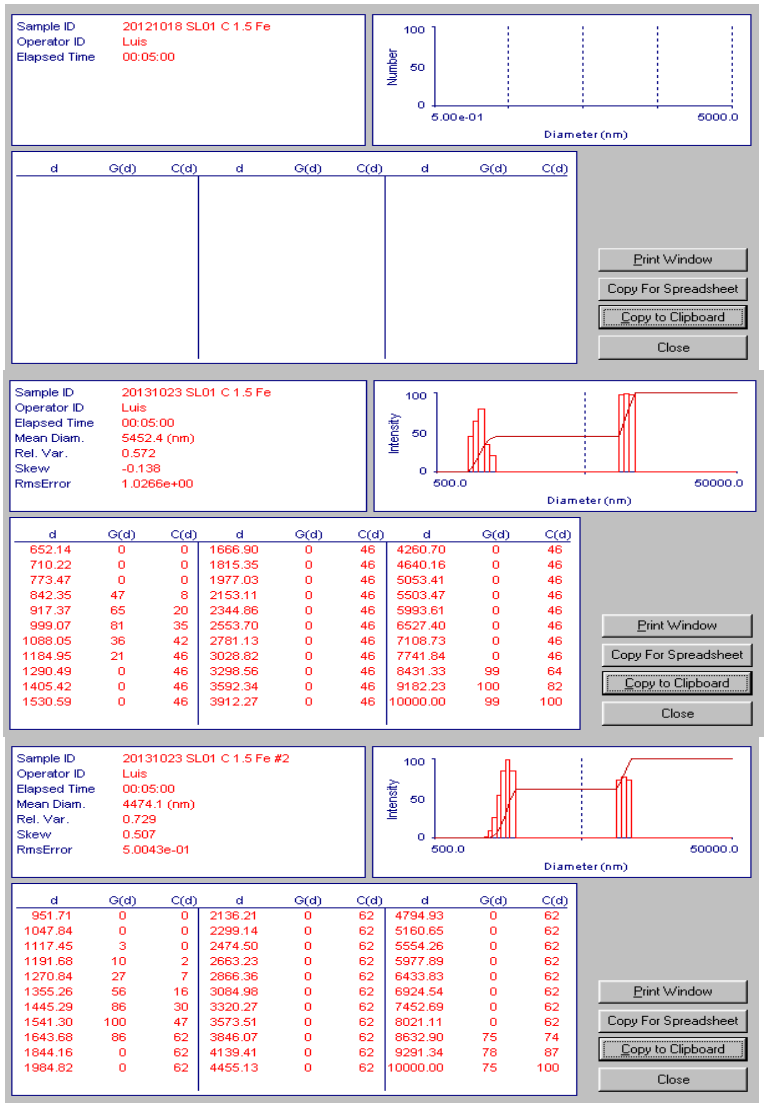

d	G(d)	C(d)	d	G(d)	C(d)	d	G(d)	C(d)
652.14	0	0	1666.90	0	46	4260.70	0	46
710.22	0	0	1815.35	0	46	4640.16	0	46
773.47	0	0	1977.03	0	46	5053.41	0	46
842.35	47	8	2153.11	0	46	5503.47	0	46
917.37	65	20	2344.86	0	46	5993.61	0	46
999.07	81	35	2553.70	0	46	6527.40	0	46
1088.05	36	42	2781.13	0	46	7108.73	0	46
1184.95	21	46	3028.82	0	46	7741.84	0	46
1290.49	0	46	3298.56	0	46	8431.33	99	64
1405.42	0	46	3592.34	0	46	9182.23	100	82
1530.59	0	46	3912.27	0	46	10000.00	99	100

d	G(d)	C(d)	d	G(d)	C(d)	d	G(d)	C(d)
951.71	0	0	2136.21	0	62	4794.93	0	62
1047.84	0	0	2299.14	0	62	5160.65	0	62
1117.45	3	0	2474.50	0	62	5554.26	0	62
1191.68	10	2	2663.23	0	62	5977.89	0	62
1270.84	27	7	2866.36	0	62	6433.83	0	62
1355.26	56	16	3084.98	0	62	6924.54	0	62
1445.29	86	30	3320.27	0	62	7452.69	0	62
1541.30	100	47	3573.51	0	62	8021.11	0	62
1643.68	86	62	3846.07	0	62	8632.90	75	74
1844.16	0	62	4139.41	0	62	9291.34	78	87
1984.82	0	62	4455.13	0	62	10000.00	75	100

Figure D11. Particle size analysis results for *Halomonas* sp. SL01 Halochelin C at 1.5 Eq. Fe^{+3}.

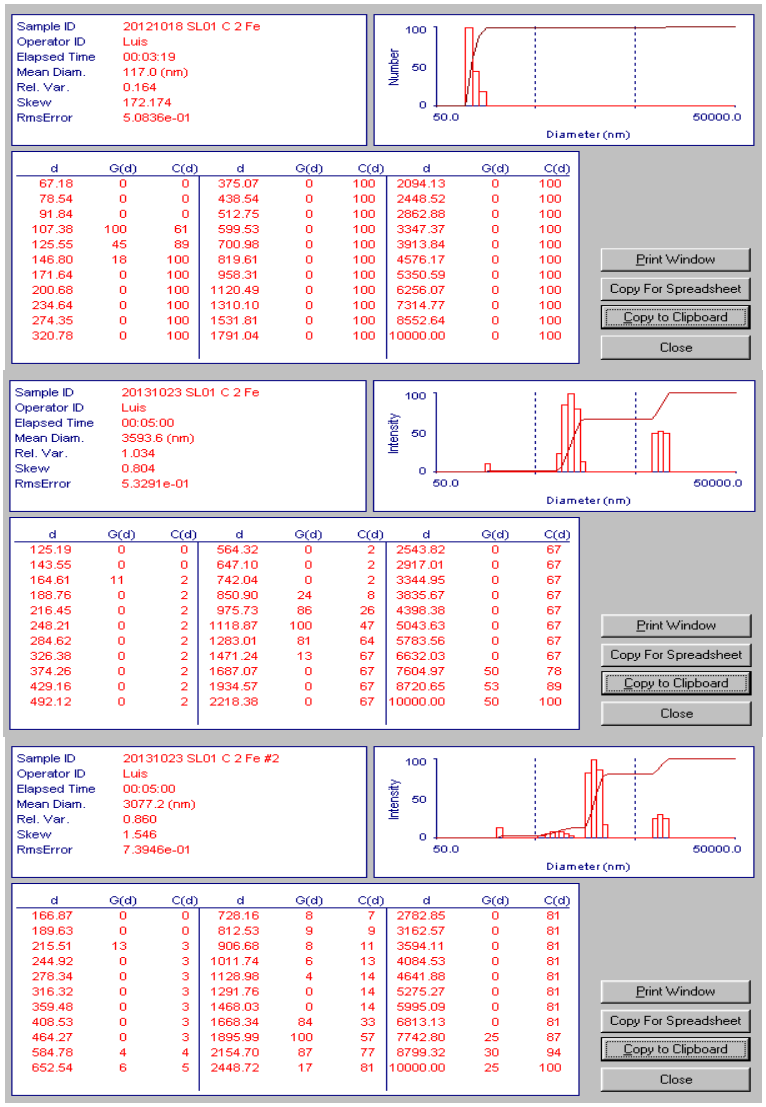

Figure D12. Particle size analysis results for *Halomonas* sp. SL01 Halochelin C at 2 Eq. Fe^{+3}.

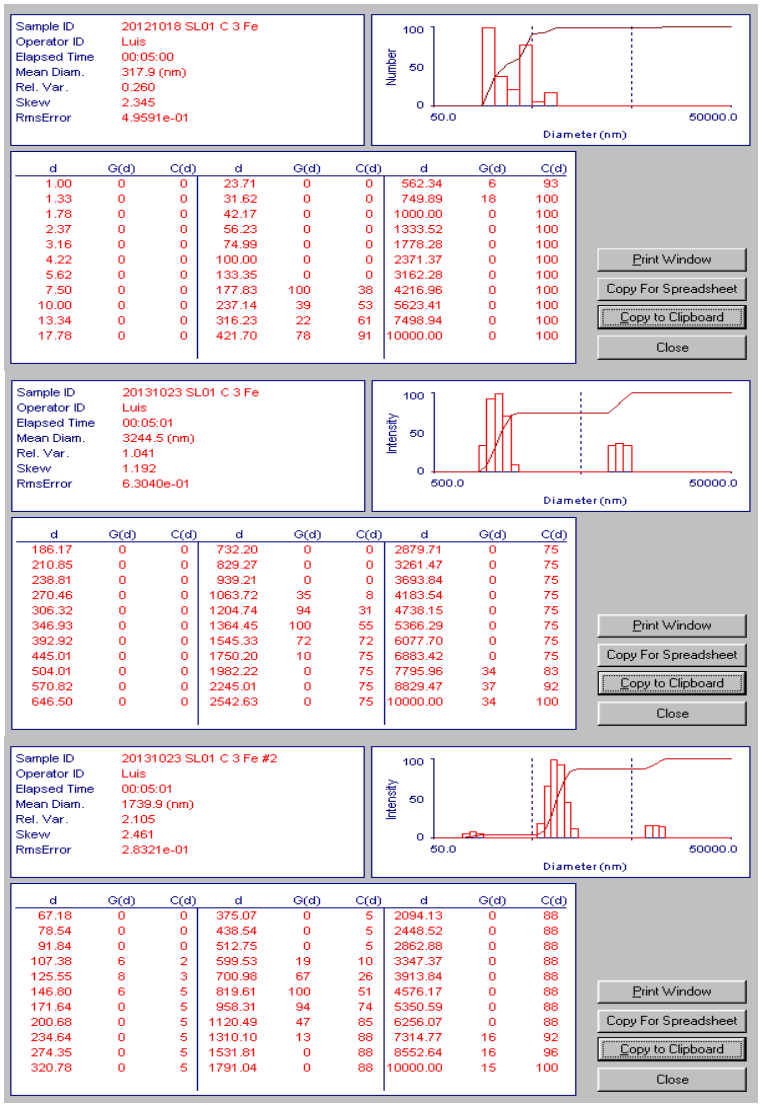

d	G(d)	C(d)	d	G(d)	C(d)	d	G(d)	C(d)
1.00	0	0	23.71	0	0	562.34	6	93
1.33	0	0	31.62	0	0	749.89	18	100
1.78	0	0	42.17	0	0	1000.00	0	100
2.37	0	0	56.23	0	0	1333.52	0	100
3.16	0	0	74.99	0	0	1778.28	0	100
4.22	0	0	100.00	0	0	2371.37	0	100
5.62	0	0	133.35	0	0	3162.28	0	100
7.50	0	0	177.83	100	38	4216.96	0	100
10.00	0	0	237.14	39	53	5623.41	0	100
13.34	0	0	316.23	22	61	7498.94	0	100
17.78	0	0	421.70	78	91	10000.00	0	100

d	G(d)	C(d)	d	G(d)	C(d)	d	G(d)	C(d)
186.17	0	0	732.20	0	0	2879.71	0	75
210.85	0	0	829.27	0	0	3261.47	0	75
238.81	0	0	939.21	0	0	3693.84	0	75
270.46	0	0	1063.72	35	8	4183.54	0	75
306.32	0	0	1204.74	94	31	4738.15	0	75
346.93	0	0	1364.45	100	55	5366.29	0	75
392.92	0	0	1545.33	72	72	6077.70	0	75
445.01	0	0	1750.20	10	75	6883.42	0	75
504.01	0	0	1982.22	0	75	7795.96	34	83
570.82	0	0	2245.01	0	75	8829.47	37	92
646.50	0	0	2542.63	0	75	10000.00	34	100

d	G(d)	C(d)	d	G(d)	C(d)	d	G(d)	C(d)
67.18	0	0	375.07	0	5	2094.13	0	88
78.54	0	0	438.54	0	5	2448.52	0	88
91.84	0	0	512.75	0	5	2862.88	0	88
107.38	6	2	599.53	19	10	3347.37	0	88
125.55	8	3	700.98	67	26	3913.84	0	88
146.80	6	5	819.61	100	51	4576.17	0	88
171.64	0	5	958.31	94	74	5350.59	0	88
200.68	0	5	1120.49	47	85	6256.07	0	88
234.64	0	5	1310.10	13	88	7314.77	16	92
274.35	0	5	1531.81	0	88	8552.64	16	96
320.78	0	5	1791.04	0	88	10000.00	15	100

Figure D13. Particle size analysis results for *Halomonas* sp. SL01 Halochelin C at 3 Eq. Fe^{+3}.

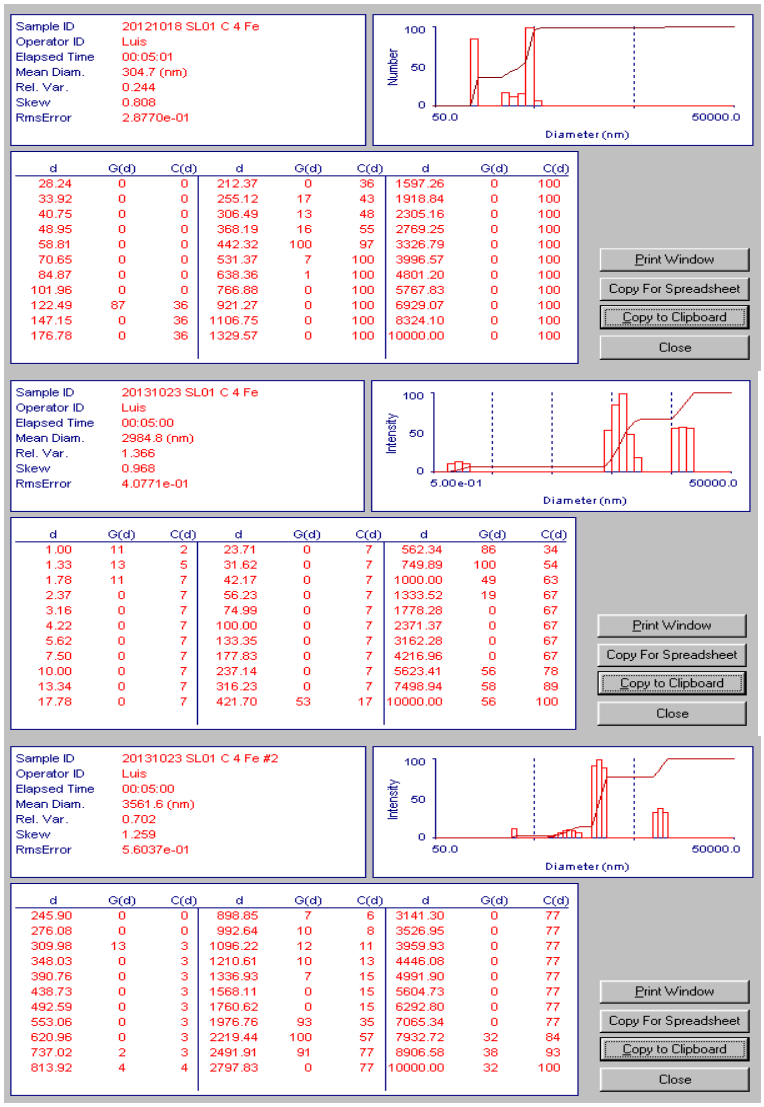

Figure D14. Particle size analysis results for *Halomonas* sp. SL01 Halochelin C at 4 Eq. Fe^{+3}.

A)

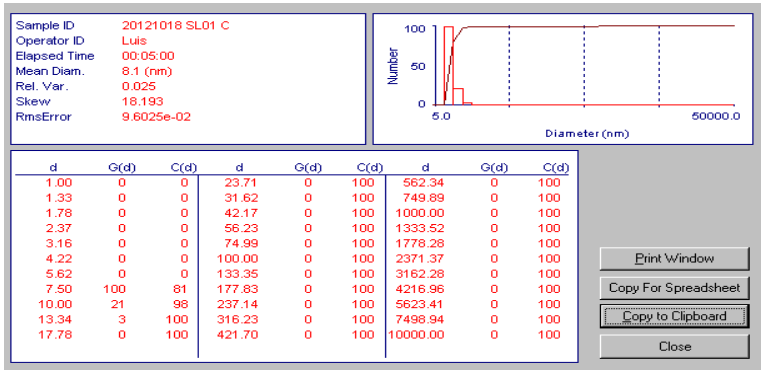

B)

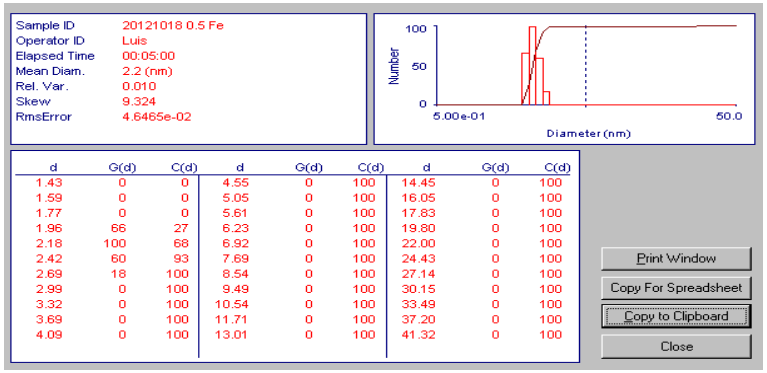

C)

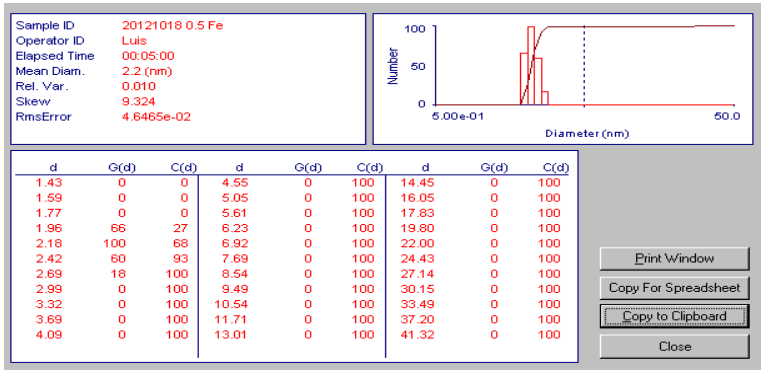

D)

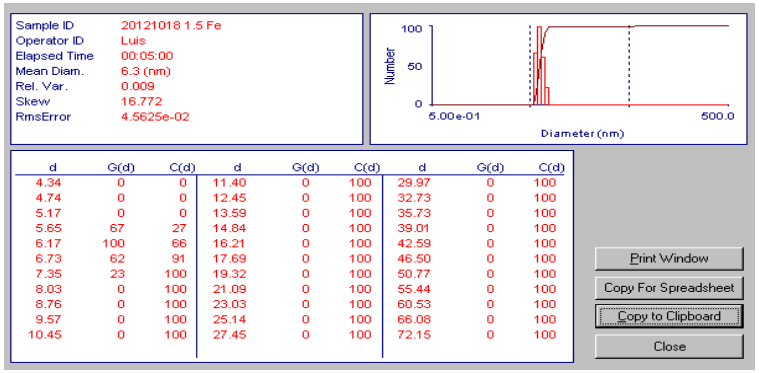

Figure D15. Particle size analysis results for *Halomonas* sp. SL01 Halochelin C without ferric iron (A) and ferric iron controls 0.5 (B), 1 (C) and 1.5 (D) Eq. Fe^{+3}.

A)

B)

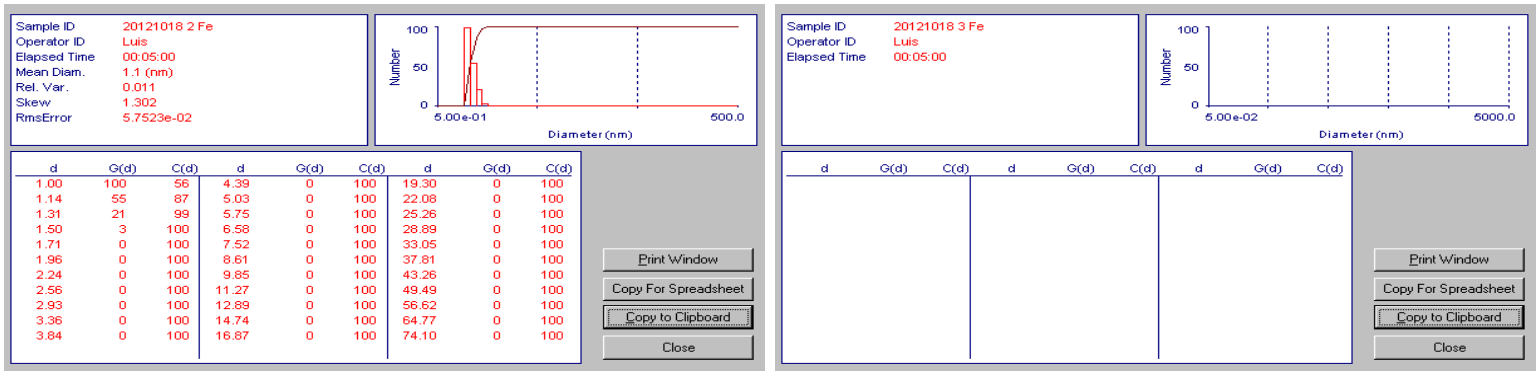

C)

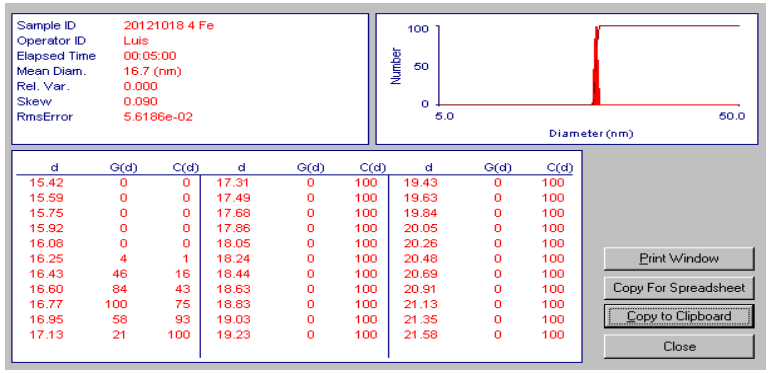

Figure D16. Particle size analysis results for ferric iron controls 2 (A), 3 (B) and 4 (C) Eq. Fe^{+3}.

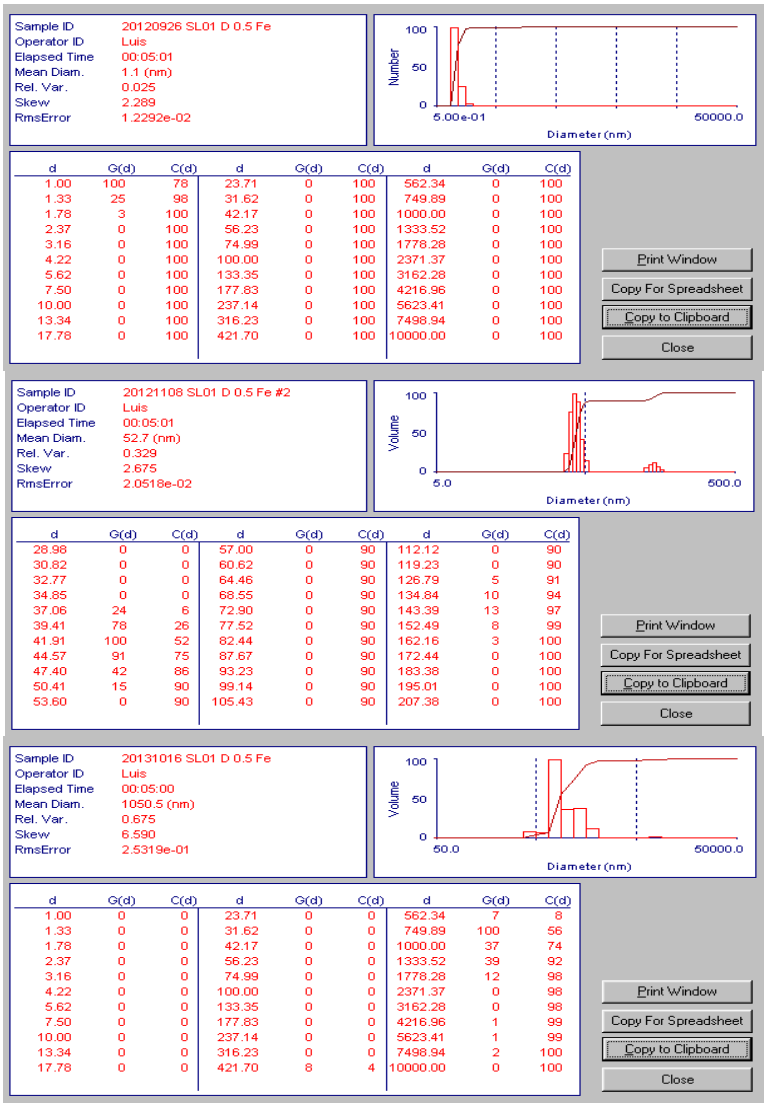

Figure D17. Particle size analysis results for *Halomonas* sp. SL01 Halochelin D at 0.5 Eq. Fe^{+3}.

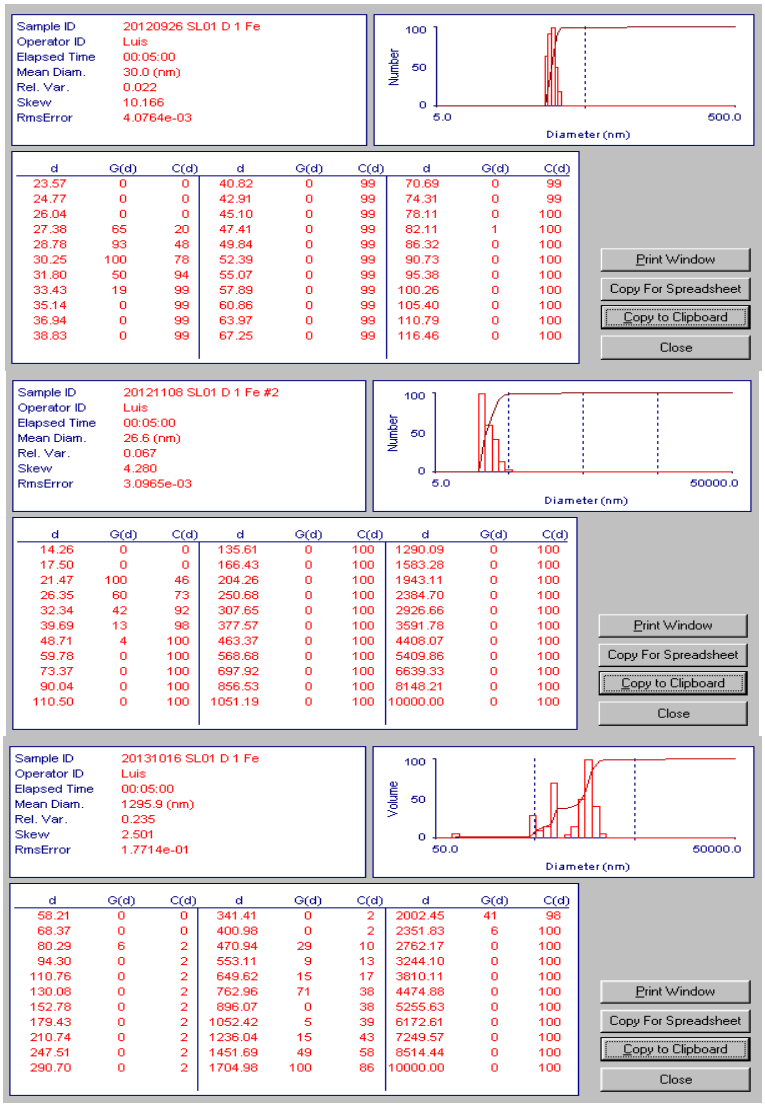

Figure D18. Particle size analysis results for *Halomonas* sp. SL01 Halochelin D at 1 Eq. Fe^{+3}.

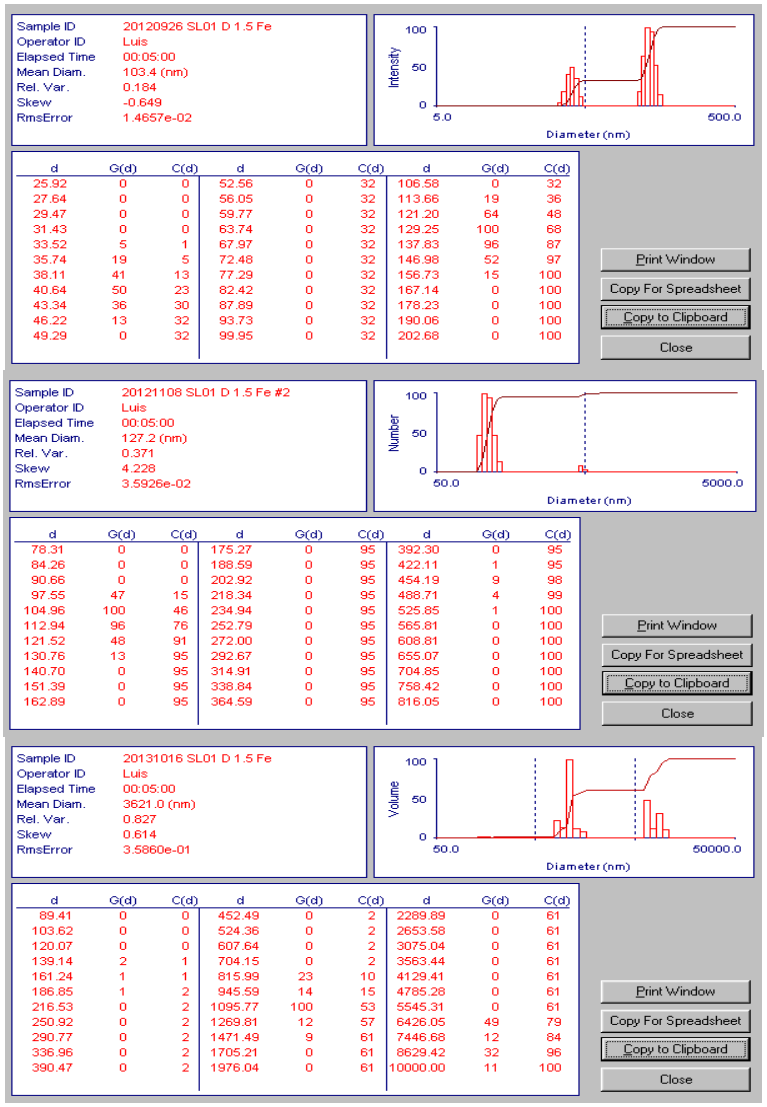

Figure D19. Particle size analysis results for *Halomonas* sp. SL01 Halochelin D at 1.5 Eq. Fe^{+3}.

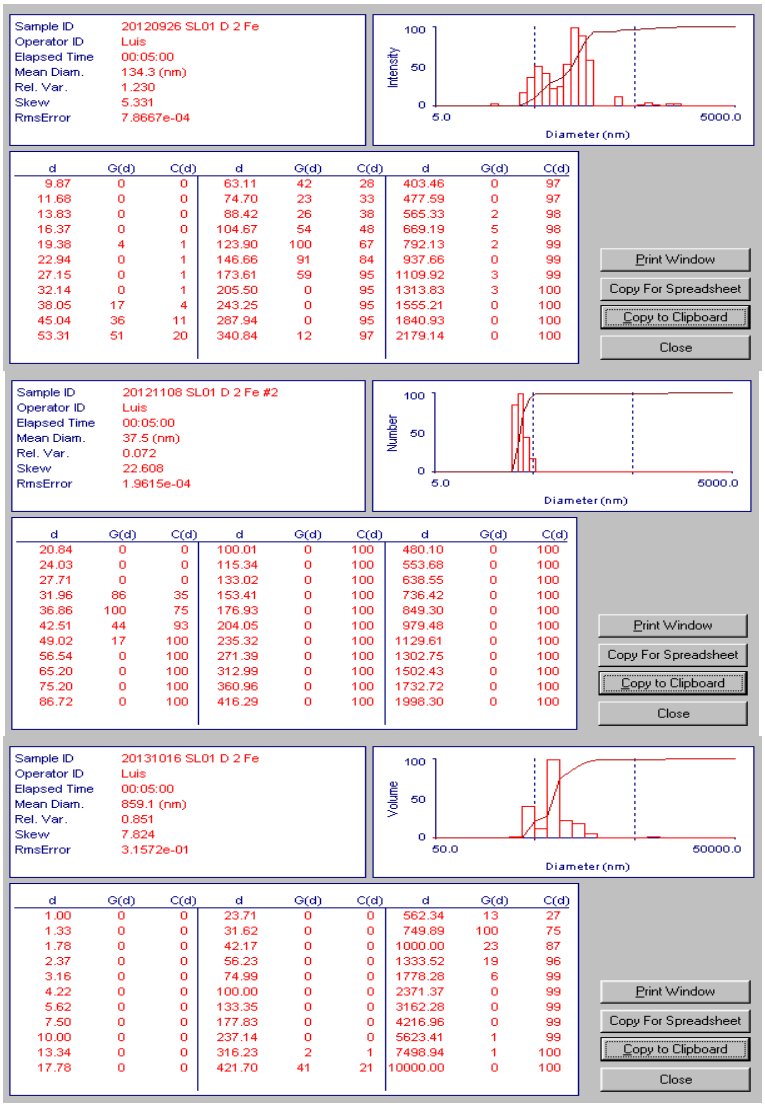

Figure D20. Particle size analysis results for *Halomonas* sp. SL01 Halochelin D at 2 Eq. Fe^{+3}.

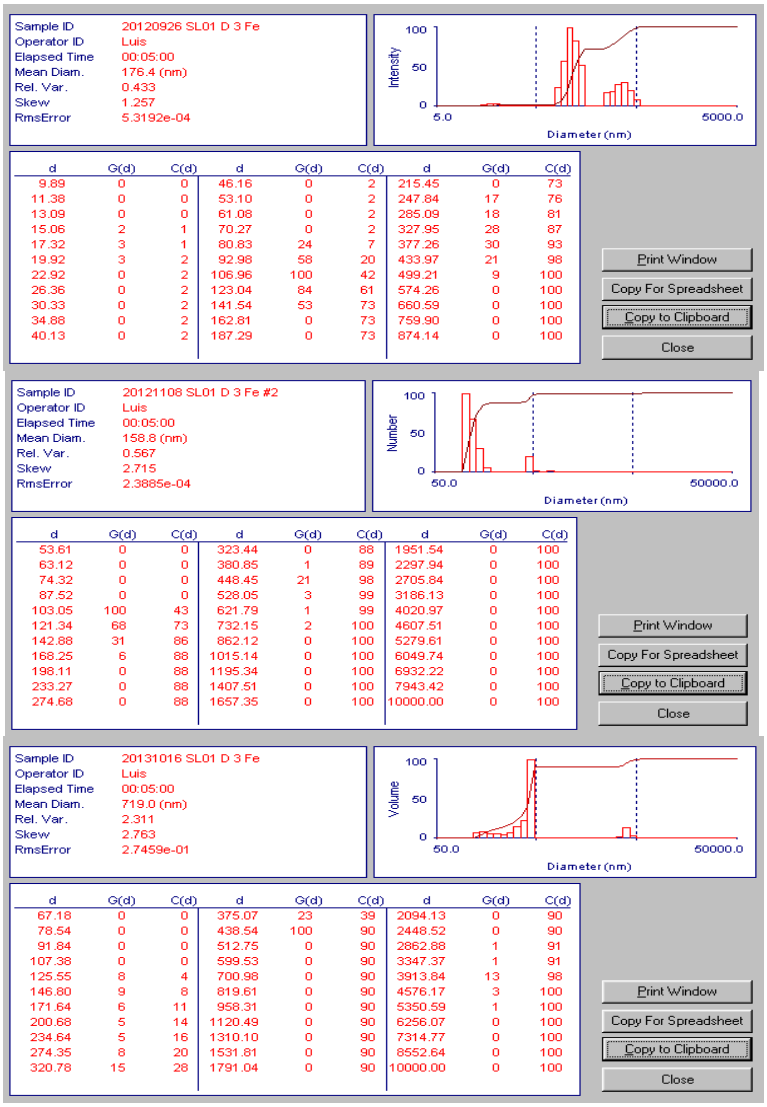

Figure D21. Particle size analysis results for *Halomonas* sp. SL01 Halochelin D at 3 Eq. Fe^{+3}.

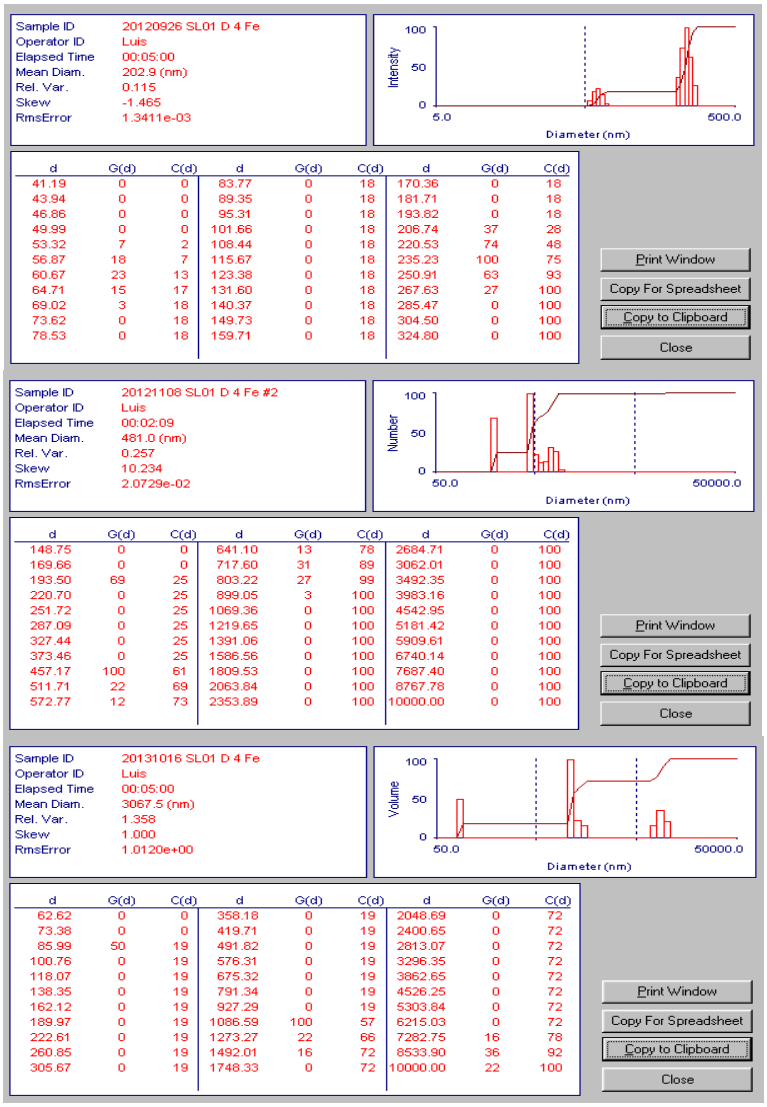

Figure D22. Particle size analysis results for *Halomonas* sp. SL01 Halochelin D at 4 Eq. Fe^{+3}.

A)

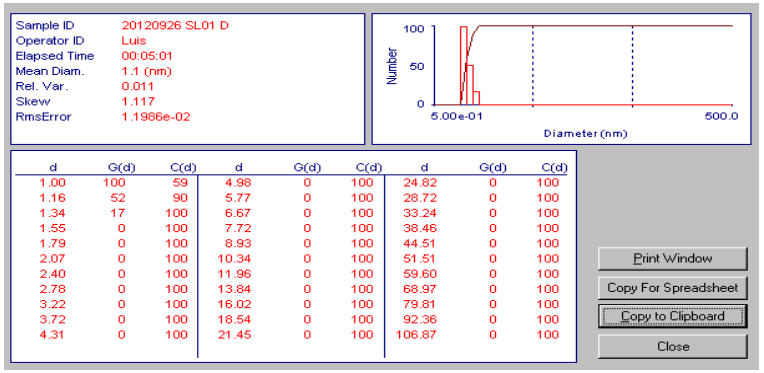

B)

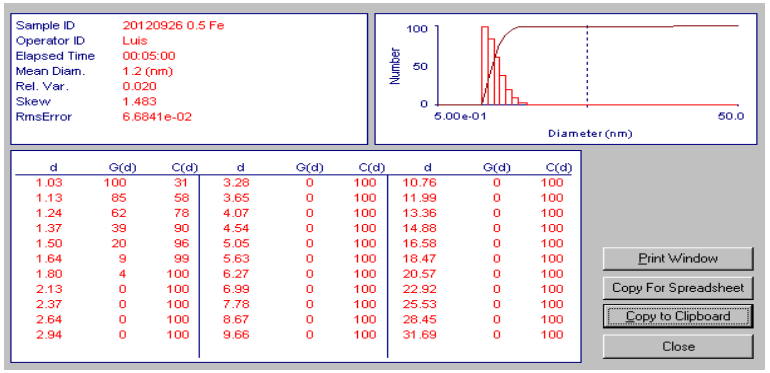

C)

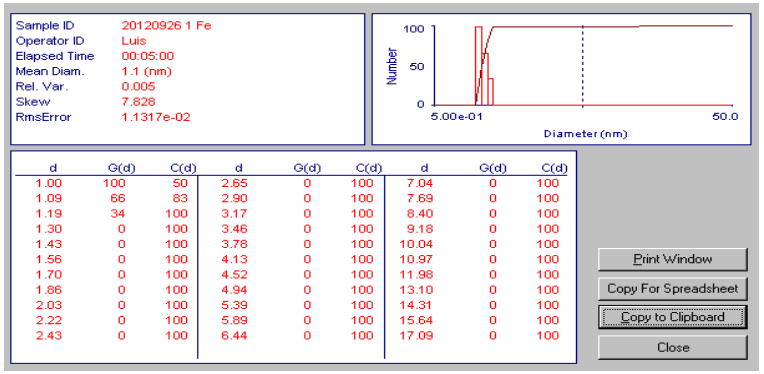

D)

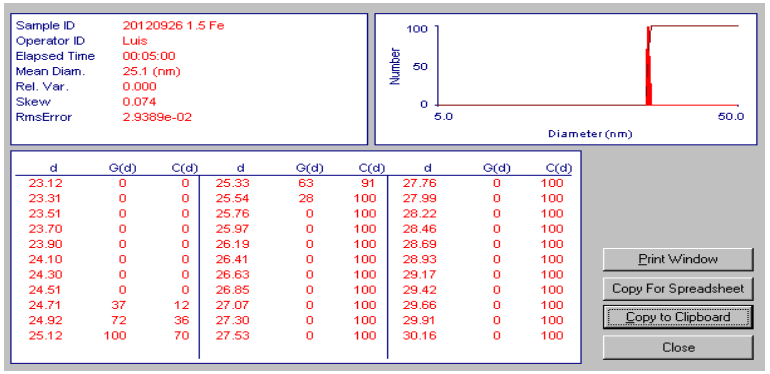

Figure D23. Particle size analysis results for *Halomonas* sp. SL01 Halochelin D without ferric iron (A) and ferric iron controls 0.5 (B), 1 (C) and 1.5 (D) Eq. Fe^{+3}.

A)

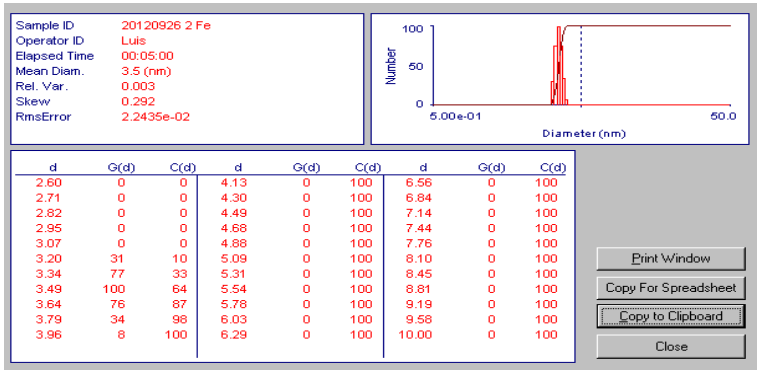

B)

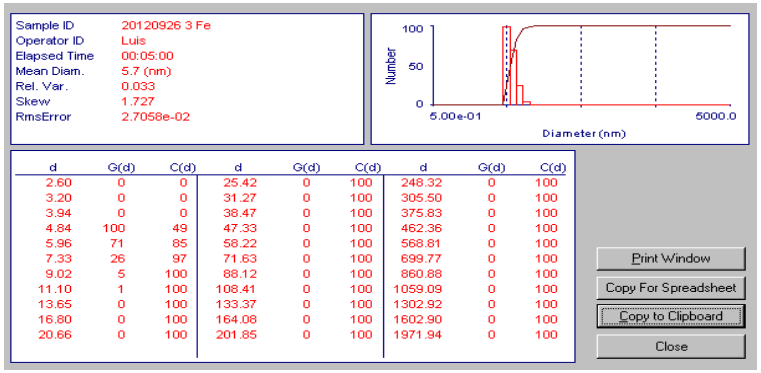

C)

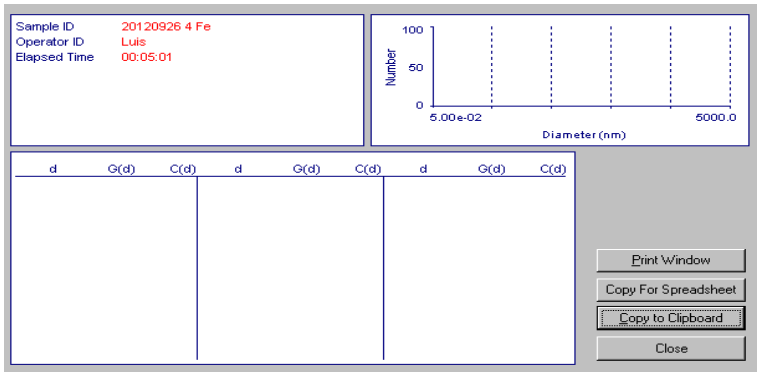

Figure D24. Particle size analysis results for ferric iron controls 2 (A), 3 (B) and 4 (C) Eq. Fe^{+3}.

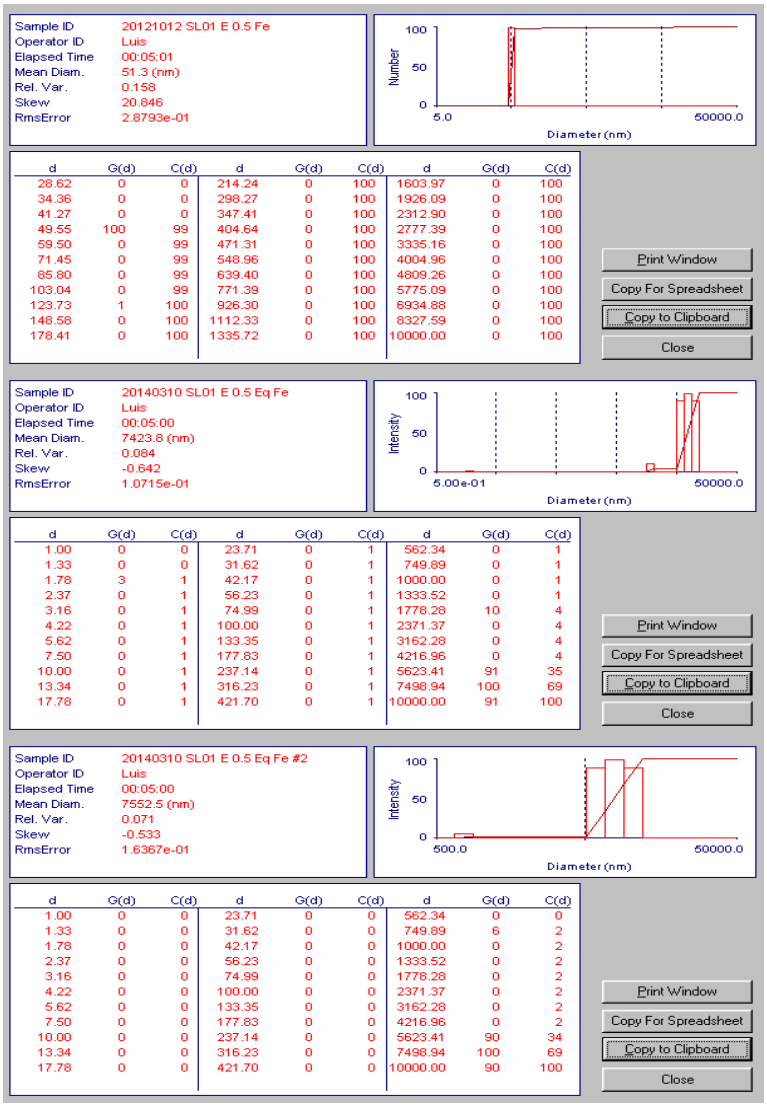

Figure D25. Particle size analysis results for *Halomonas* sp. SL01 Halochelin E at 0.5 Eq. Fe^{+3}.

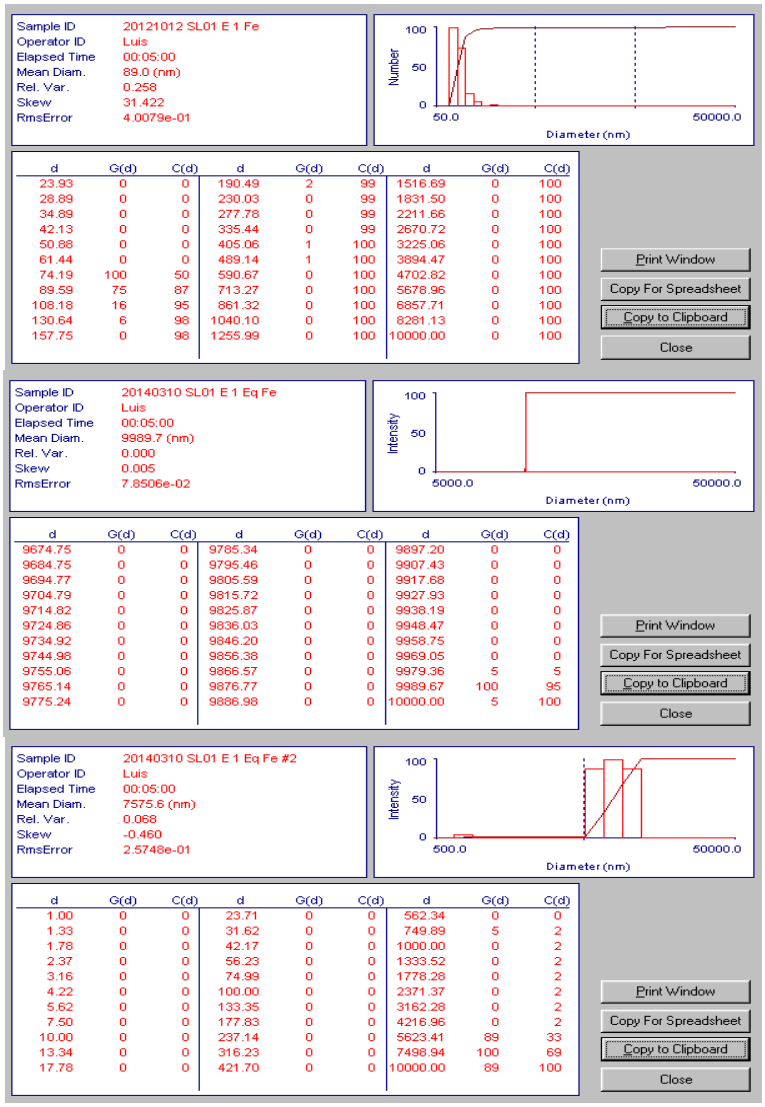

Figure D26. Particle size analysis results for *Halomonas* sp. SL01 Halochelin E at 1 Eq. Fe^{+3}.

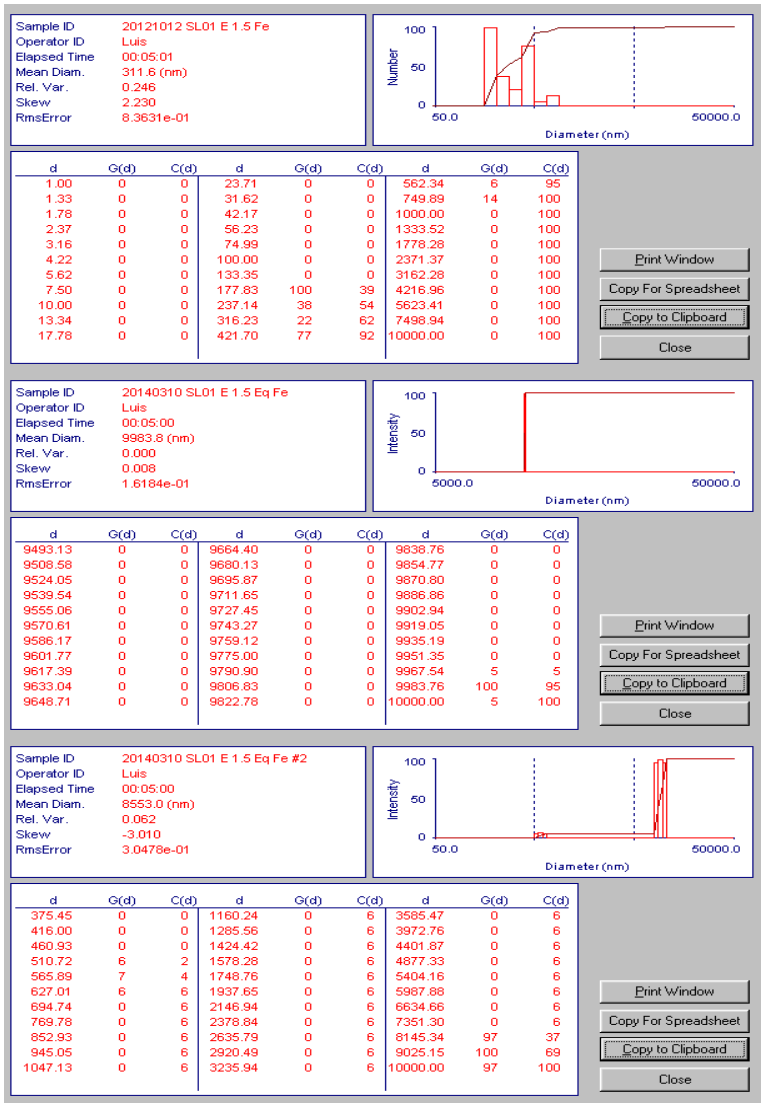

Figure D27. Particle size analysis results for *Halomonas* sp. SL01 Halochelin E at 1.5 Eq. Fe^{+3}.

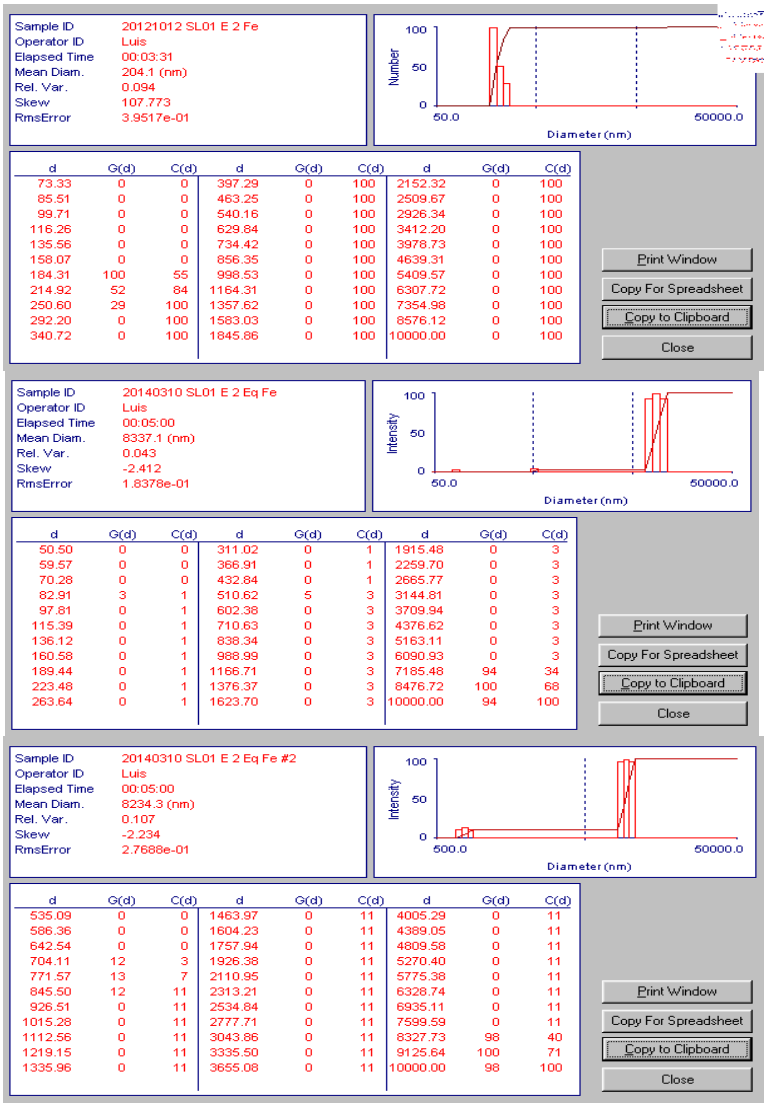

Figure D28. Particle size analysis results for *Halomonas* sp. SL01 Halochelin E at 2 Eq. Fe^{+3}.

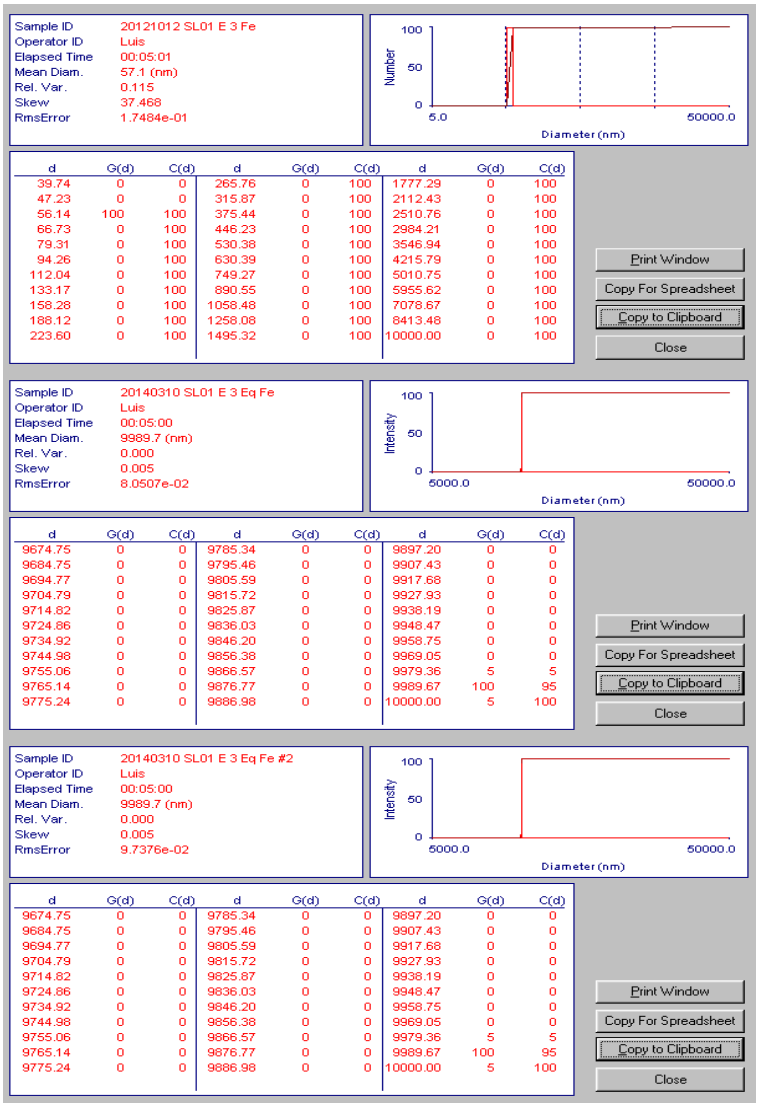

Figure D29. Particle size analysis results for *Halomonas* sp. SL01 Halochelin E at 3 Eq. Fe^{+3}.

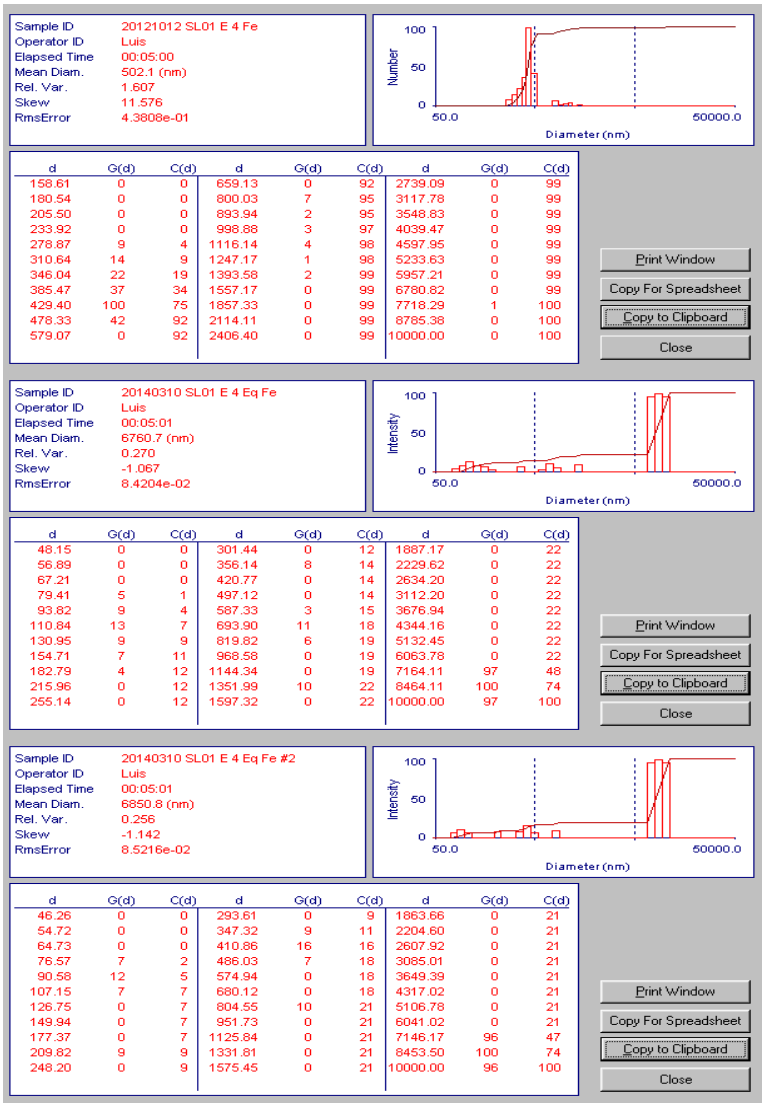

Figure D30. Particle size analysis results for *Halomonas* sp. SL01 Halochelin E at 4 Eq. Fe^{+3}.

A)

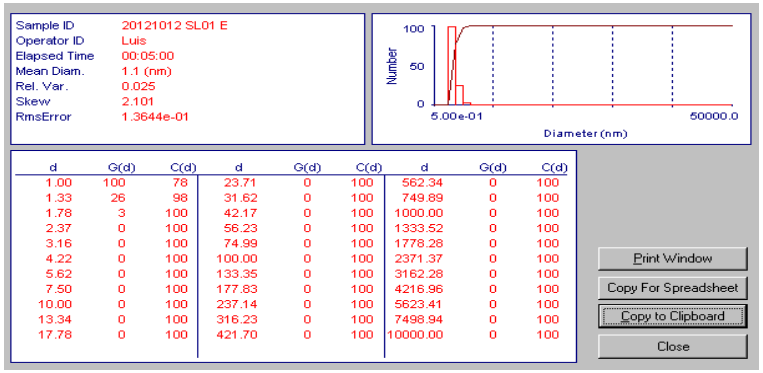

d	G(d)	C(d)	d	G(d)	C(d)	d	G(d)	C(d)
1.00	100	78	23.71	0	100	562.34	0	100
1.33	26	98	31.62	0	100	749.89	0	100
1.78	3	100	42.17	0	100	1000.00	0	100
2.37	0	100	56.23	0	100	1333.52	0	100
3.16	0	100	74.99	0	100	1778.28	0	100
4.22	0	100	100.00	0	100	2371.37	0	100
5.62	0	100	133.35	0	100	3162.28	0	100
7.50	0	100	177.83	0	100	4216.96	0	100
10.00	0	100	237.14	0	100	5623.41	0	100
13.34	0	100	316.23	0	100	7498.94	0	100
17.78	0	100	421.70	0	100	10000.00	0	100

B)

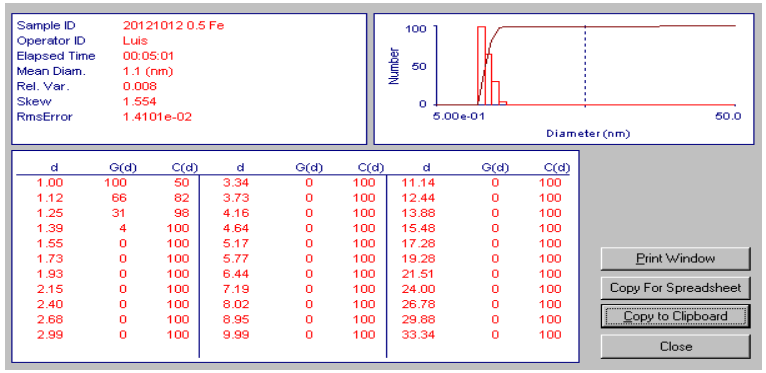

d	G(d)	C(d)	d	G(d)	C(d)	d	G(d)	C(d)
1.00	100	50	3.34	0	100	11.14	0	100
1.12	66	82	3.73	0	100	12.44	0	100
1.25	31	98	4.16	0	100	13.88	0	100
1.39	4	100	4.64	0	100	15.48	0	100
1.55	0	100	5.17	0	100	17.28	0	100
1.73	0	100	5.77	0	100	19.28	0	100
1.93	0	100	6.44	0	100	21.51	0	100
2.15	0	100	7.19	0	100	24.00	0	100
2.40	0	100	8.02	0	100	26.78	0	100
2.68	0	100	8.95	0	100	29.88	0	100
2.99	0	100	9.99	0	100	33.34	0	100

C)

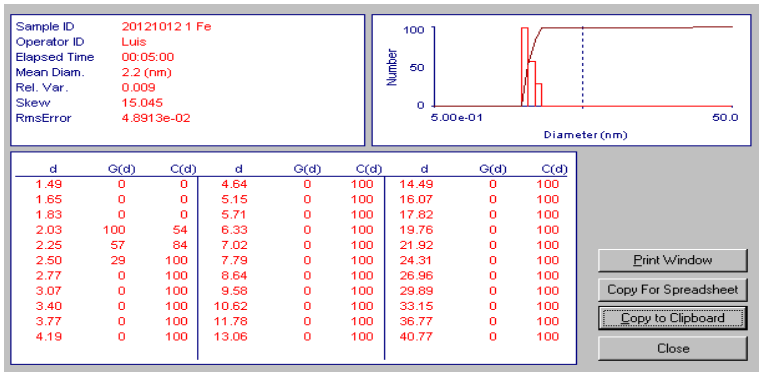

d	G(d)	C(d)	d	G(d)	C(d)	d	G(d)	C(d)
1.49	0	0	4.64	0	100	14.49	0	100
1.65	0	0	5.15	0	100	16.07	0	100
1.83	0	0	5.71	0	100	17.82	0	100
2.03	100	54	6.33	0	100	19.76	0	100
2.25	57	84	7.02	0	100	21.92	0	100
2.50	29	100	7.79	0	100	24.31	0	100
2.77	0	100	8.64	0	100	26.96	0	100
3.07	0	100	9.58	0	100	29.89	0	100
3.40	0	100	10.62	0	100	33.15	0	100
3.77	0	100	11.78	0	100	36.77	0	100
4.19	0	100	13.06	0	100	40.77	0	100

D)

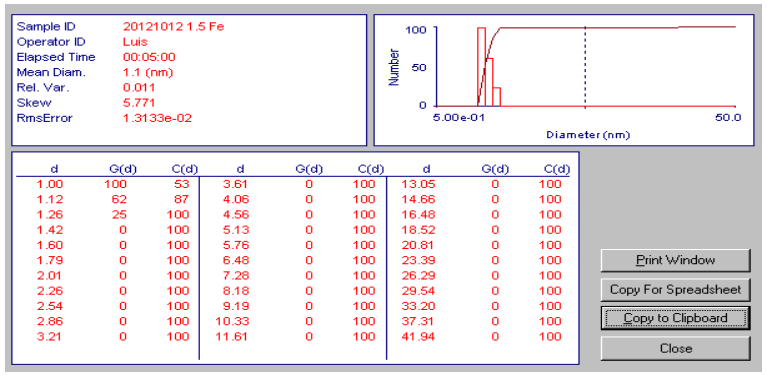

d	G(d)	C(d)	d	G(d)	C(d)	d	G(d)	C(d)
1.00	100	53	3.61	0	100	13.05	0	100
1.12	62	87	4.06	0	100	14.66	0	100
1.26	25	100	4.56	0	100	16.48	0	100
1.42	0	100	5.13	0	100	18.52	0	100
1.60	0	100	5.76	0	100	20.81	0	100
1.79	0	100	6.48	0	100	23.39	0	100
2.01	0	100	7.28	0	100	26.29	0	100
2.26	0	100	8.18	0	100	29.54	0	100
2.54	0	100	9.19	0	100	33.20	0	100
2.86	0	100	10.33	0	100	37.31	0	100
3.21	0	100	11.61	0	100	41.94	0	100

Figure D31. Particle size analysis results for *Halomonas* sp. SL01 Halochelin E without ferric iron (A) and ferric iron controls 0.5 (B), 1 (C) and 1.5 (D) Eq. Fe^{+3}.

A)

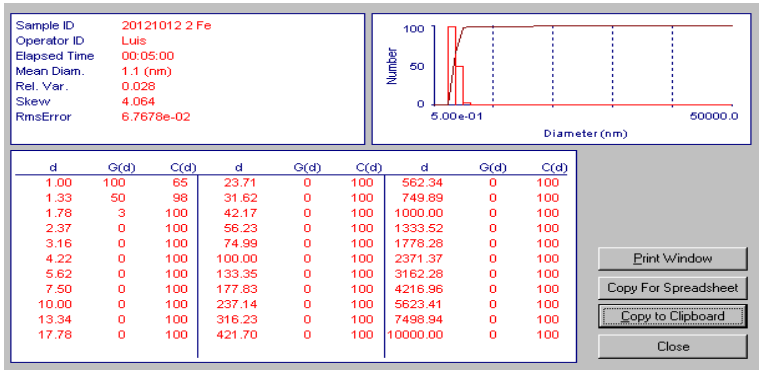

B)

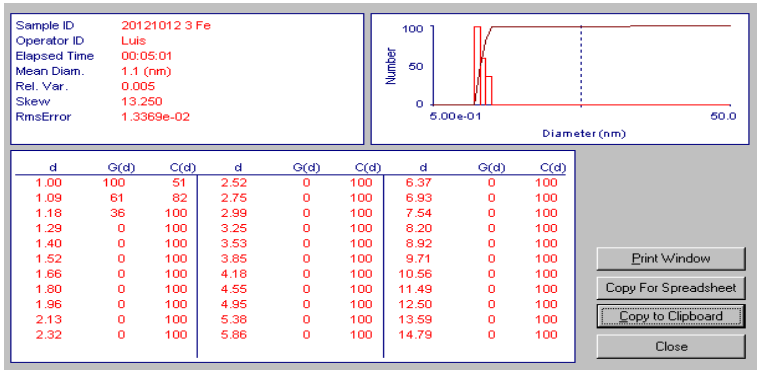

C)

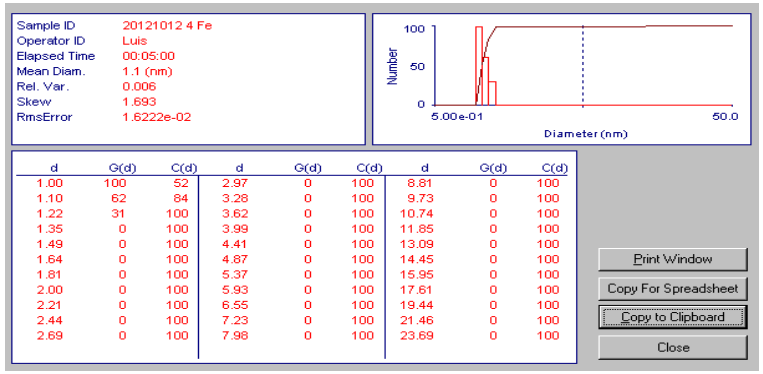

Figure D32. Particle size analysis results for ferric iron controls 2 (A), 3 (B) and 4 (C) Eq. Fe^{+3}.

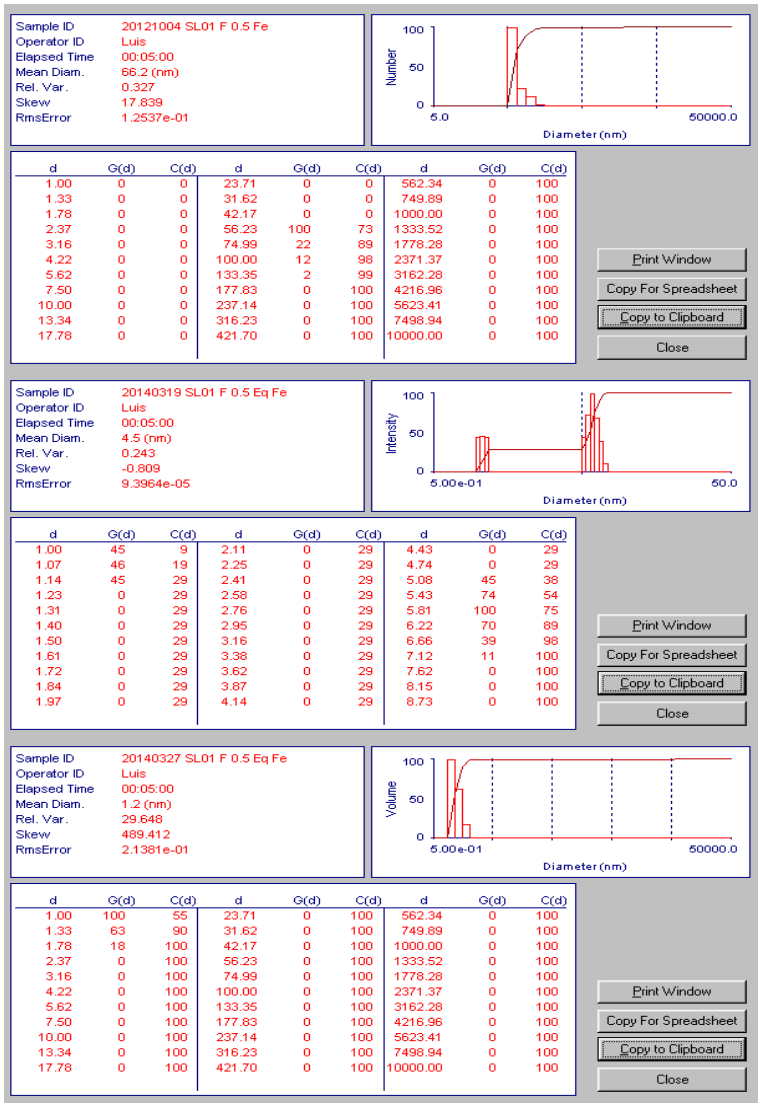

Figure D33. Particle size analysis results for *Halomonas* sp. SL01 Halochelin F at 0.5 Eq. Fe^{+3}.

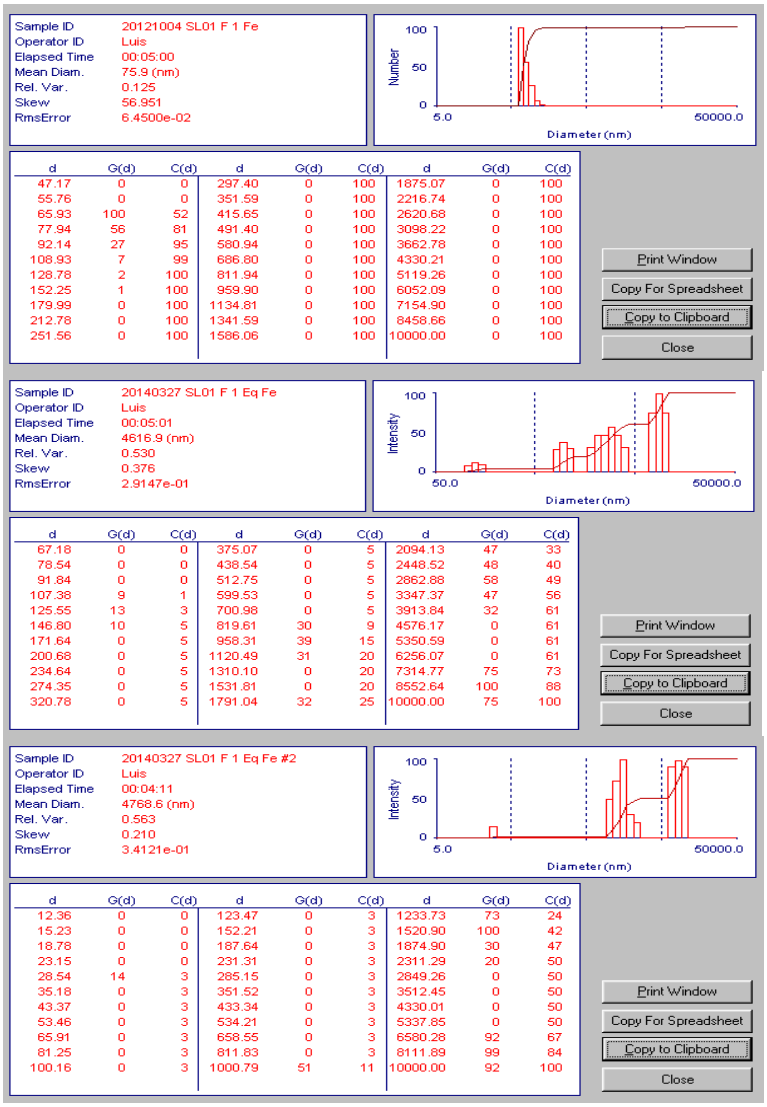

Figure D34. Particle size analysis results for *Halomonas* sp. SL01 Halochelin F at 1 Eq. Fe^{+3}.

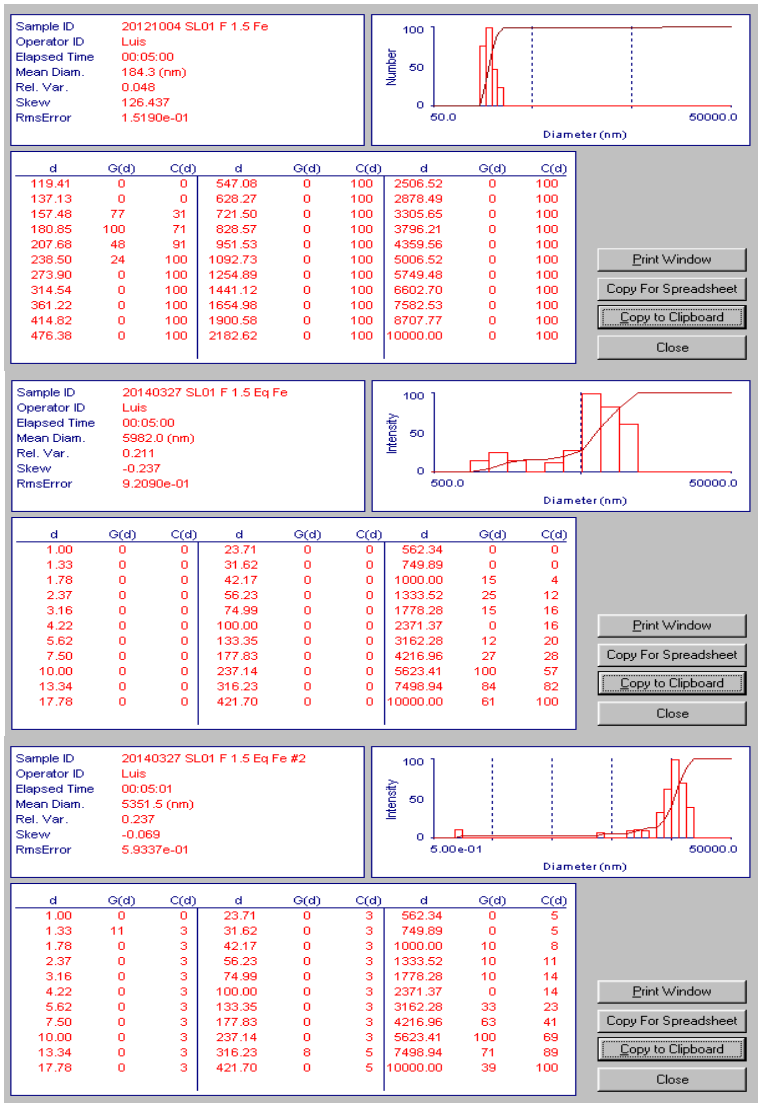

Figure D35. Particle size analysis results for *Halomonas* sp. SL01 Halochelin F at 1.5 Eq. Fe^{+3}.

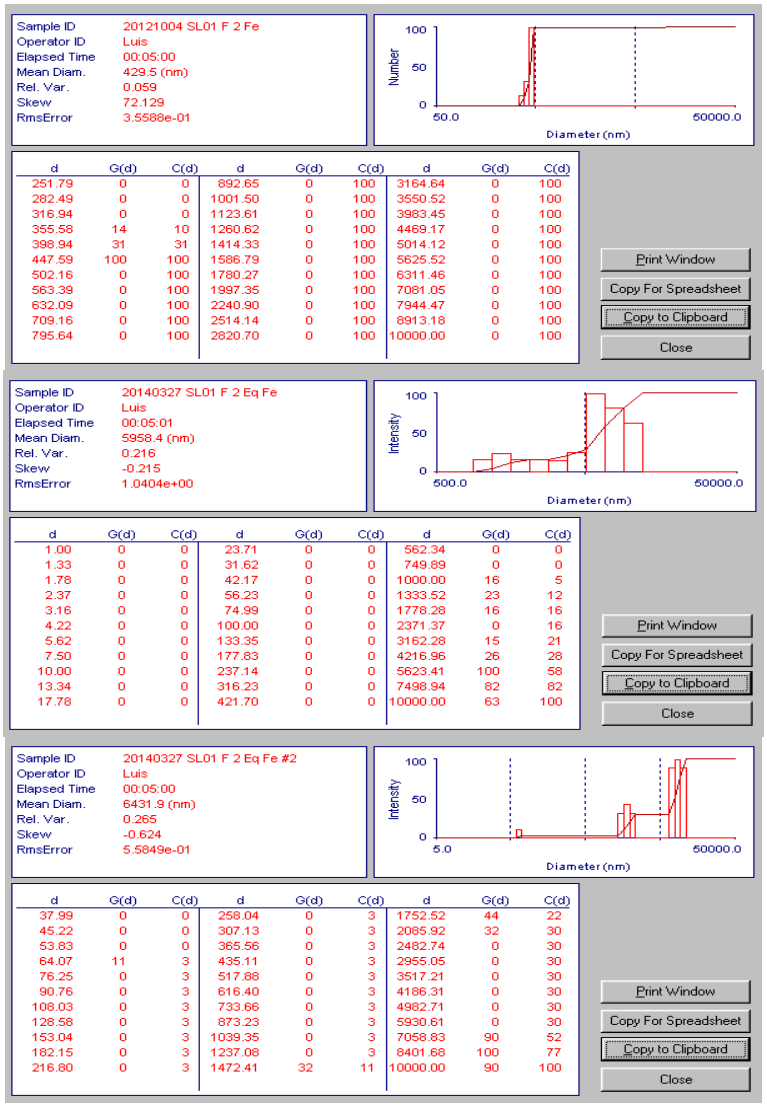

Figure D36. Particle size analysis results for *Halomonas* sp. SL01 Halochelin F at 2 Eq. Fe^{+3}.

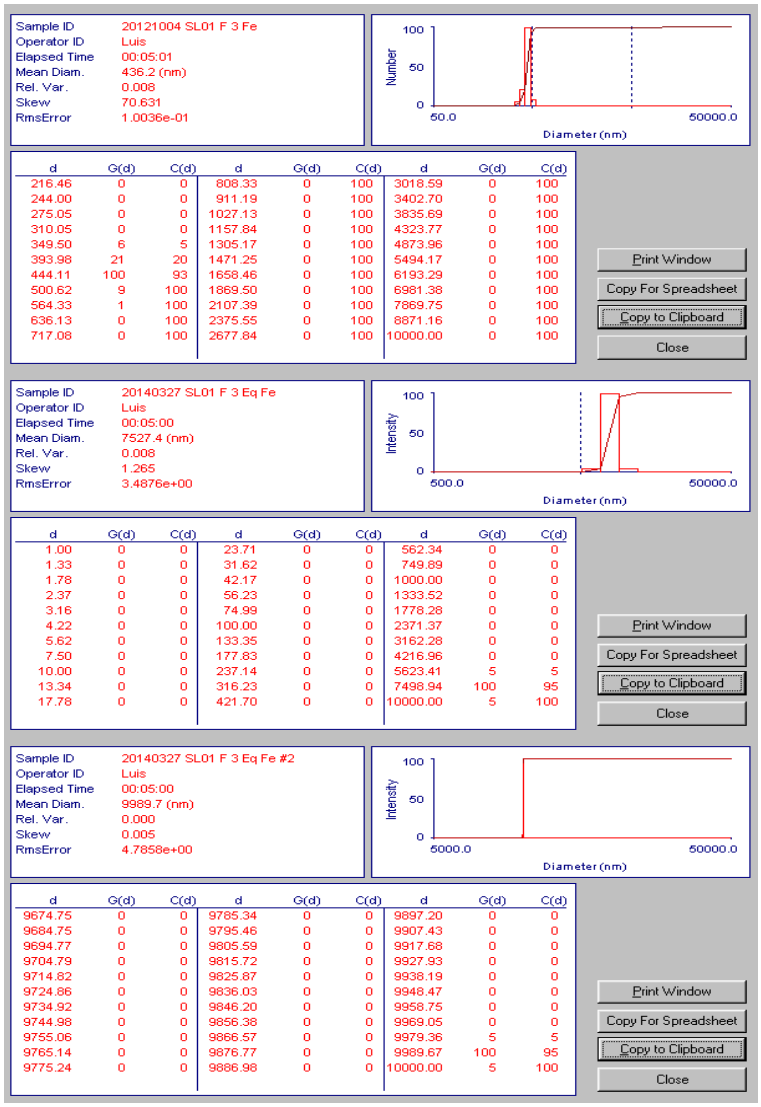

Figure D37. Particle size analysis results for *Halomonas* sp. SL01 Halochelin F at 3 Eq. Fe^{+3}.

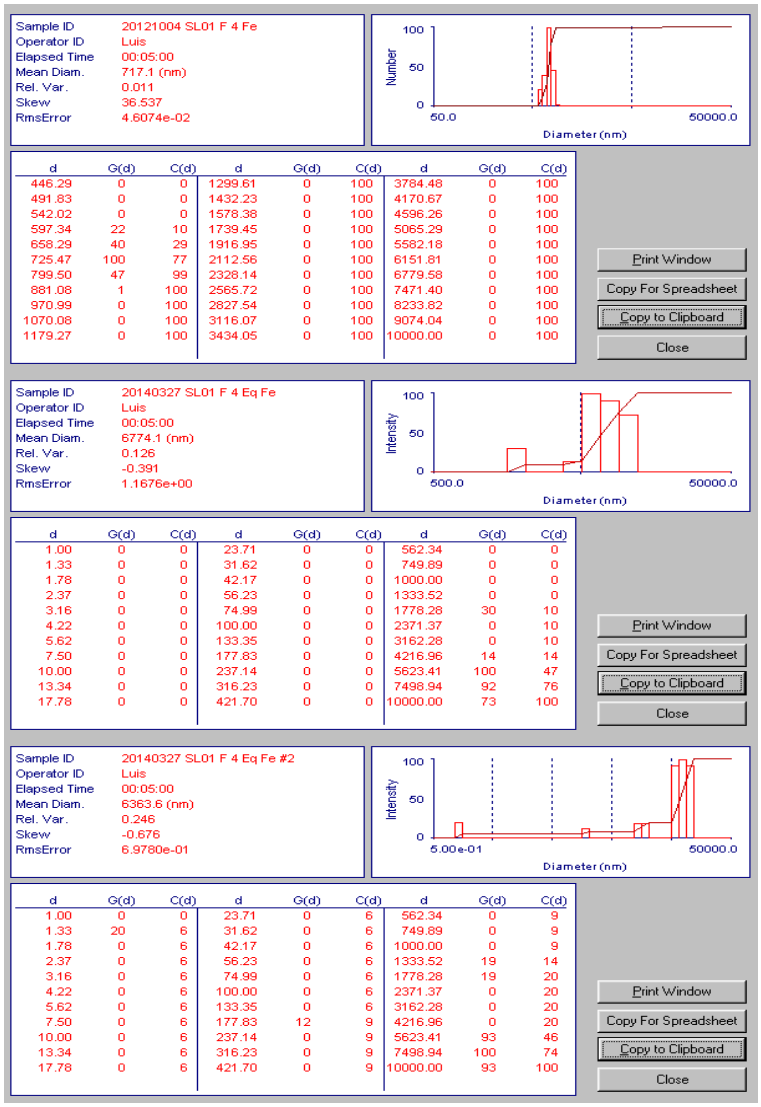

Figure D38. Particle size analysis results for *Halomonas* sp. SL01 Halochelin F at 4 Eq. Fe^{+3}.

A)

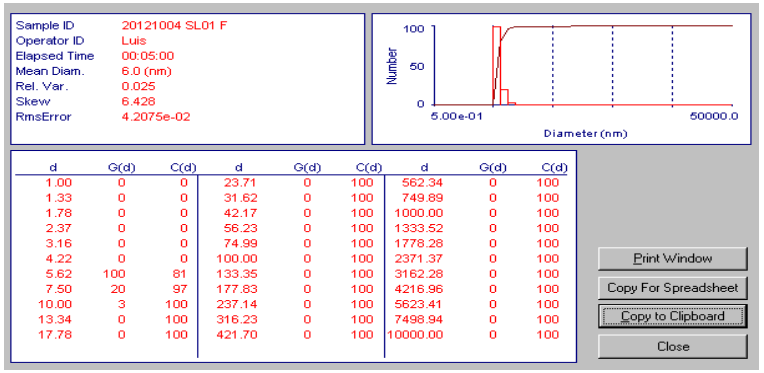

d	G(d)	C(d)	d	G(d)	C(d)	d	G(d)	C(d)
1.00	0	0	23.71	0	100	562.34	0	100
1.33	0	0	31.62	0	100	749.89	0	100
1.78	0	0	42.17	0	100	1000.00	0	100
2.37	0	0	56.23	0	100	1333.52	0	100
3.16	0	0	74.99	0	100	1778.28	0	100
4.22	0	0	100.00	0	100	2371.37	0	100
5.62	100	81	133.35	0	100	3162.28	0	100
7.50	20	97	177.83	0	100	4216.96	0	100
10.00	3	100	237.14	0	100	5623.41	0	100
13.34	0	100	316.23	0	100	7498.94	0	100
17.78	0	100	421.70	0	100	10000.00	0	100

B)

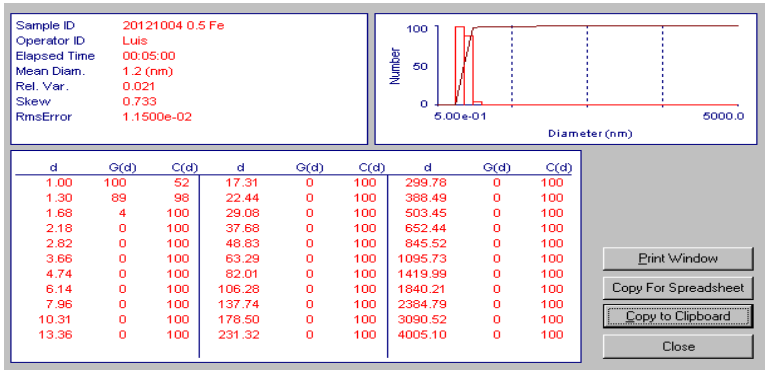

d	G(d)	C(d)	d	G(d)	C(d)	d	G(d)	C(d)
1.00	100	52	17.31	0	100	299.78	0	100
1.30	89	98	22.44	0	100	388.49	0	100
1.68	4	100	29.08	0	100	503.45	0	100
2.18	0	100	37.68	0	100	652.44	0	100
2.82	0	100	48.83	0	100	845.52	0	100
3.66	0	100	63.29	0	100	1095.73	0	100
4.74	0	100	82.01	0	100	1419.99	0	100
6.14	0	100	106.28	0	100	1840.21	0	100
7.96	0	100	137.74	0	100	2384.79	0	100
10.31	0	100	178.50	0	100	3090.52	0	100
13.36	0	100	231.32	0	100	4005.10	0	100

C)

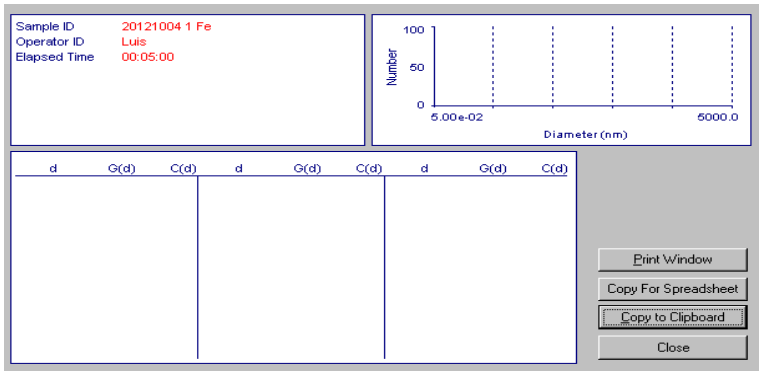

d	G(d)	C(d)	d	G(d)	C(d)	d	G(d)	C(d)

D)

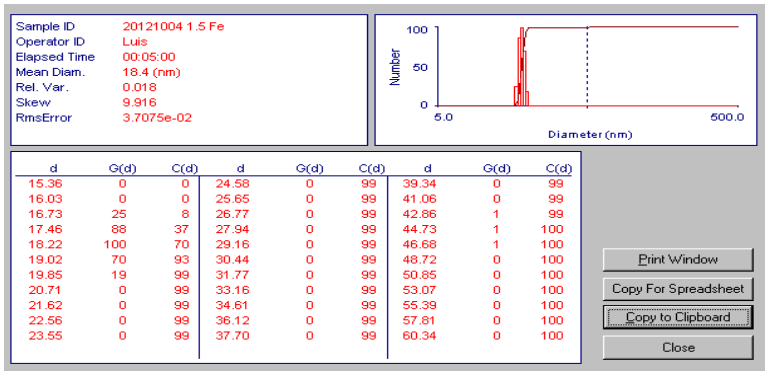

d	G(d)	C(d)	d	G(d)	C(d)	d	G(d)	C(d)
15.36	0	0	24.58	0	99	39.34	0	99
16.03	0	0	25.65	0	99	41.06	0	99
16.73	25	8	26.77	0	99	42.86	1	99
17.46	88	37	27.94	0	99	44.73	1	100
18.22	100	70	29.16	0	99	46.68	1	100
19.02	70	93	30.44	0	99	48.72	0	100
19.85	19	99	31.77	0	99	50.85	0	100
20.71	0	99	33.16	0	99	53.07	0	100
21.62	0	99	34.61	0	99	55.39	0	100
22.56	0	99	36.12	0	99	57.81	0	100
23.55	0	99	37.70	0	99	60.34	0	100

Figure D39. Particle size analysis results for *Halomonas* sp. SL01 Halochelin F without ferric iron (A) and ferric iron controls 0.5 (B), 1 (C) and 1.5 (D) Eq. Fe^{+3}.

A)

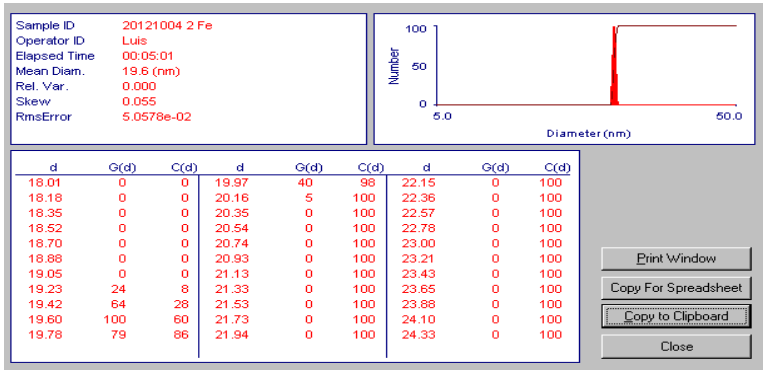

B)

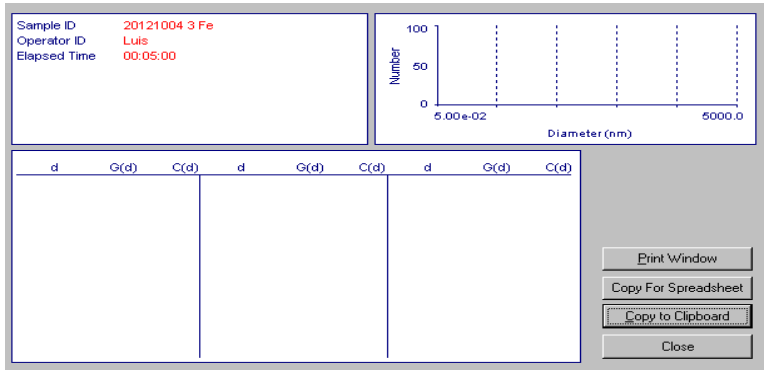

C)

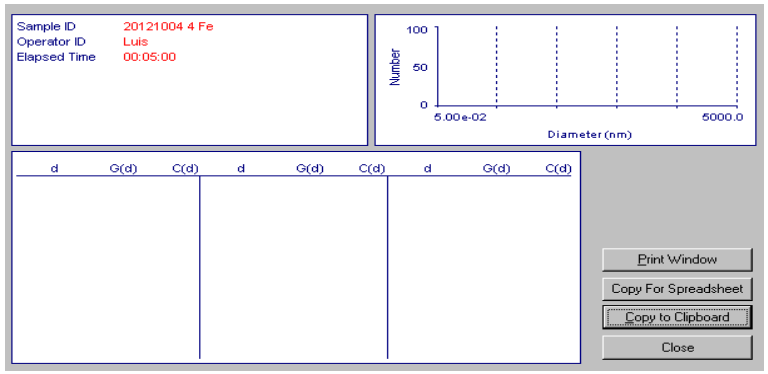

Figure D40. Particle size analysis results for ferric iron controls 2 (A), 3 (B) and 4 (C) Eq. Fe^{+3}.

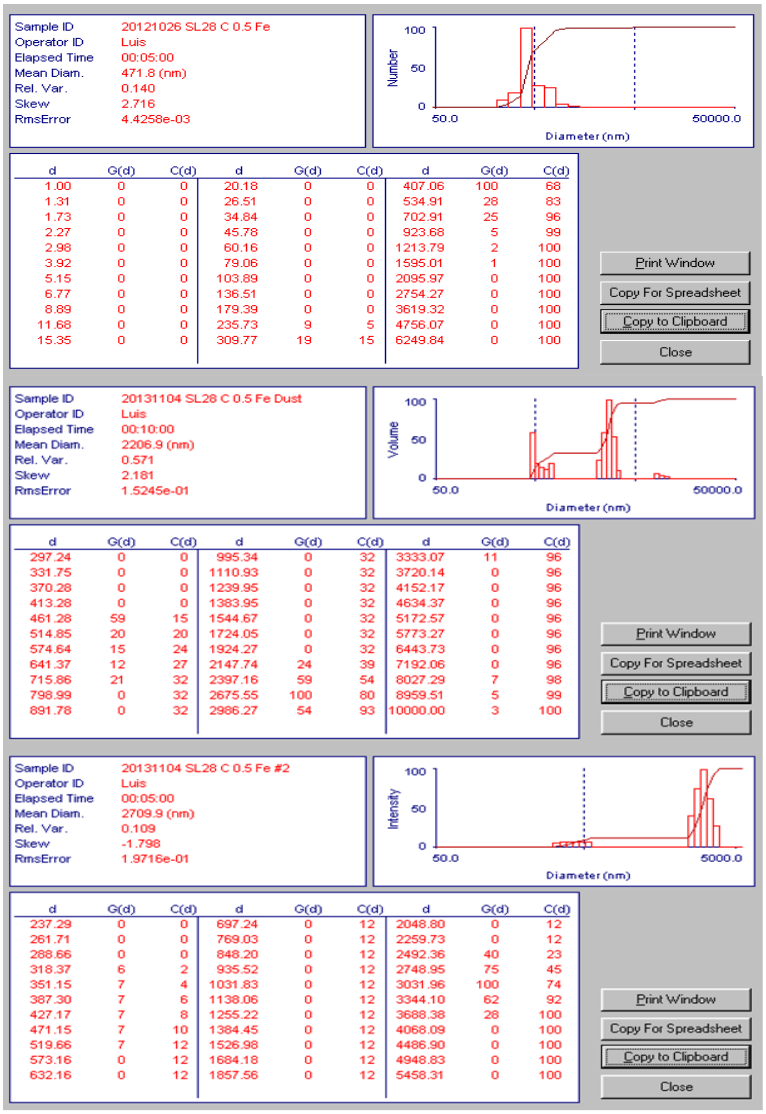

Figure D41. Particle size analysis results for *Halomonas* sp. SL28 Sodachelin C at 0.5 Eq. Fe^{+3}.

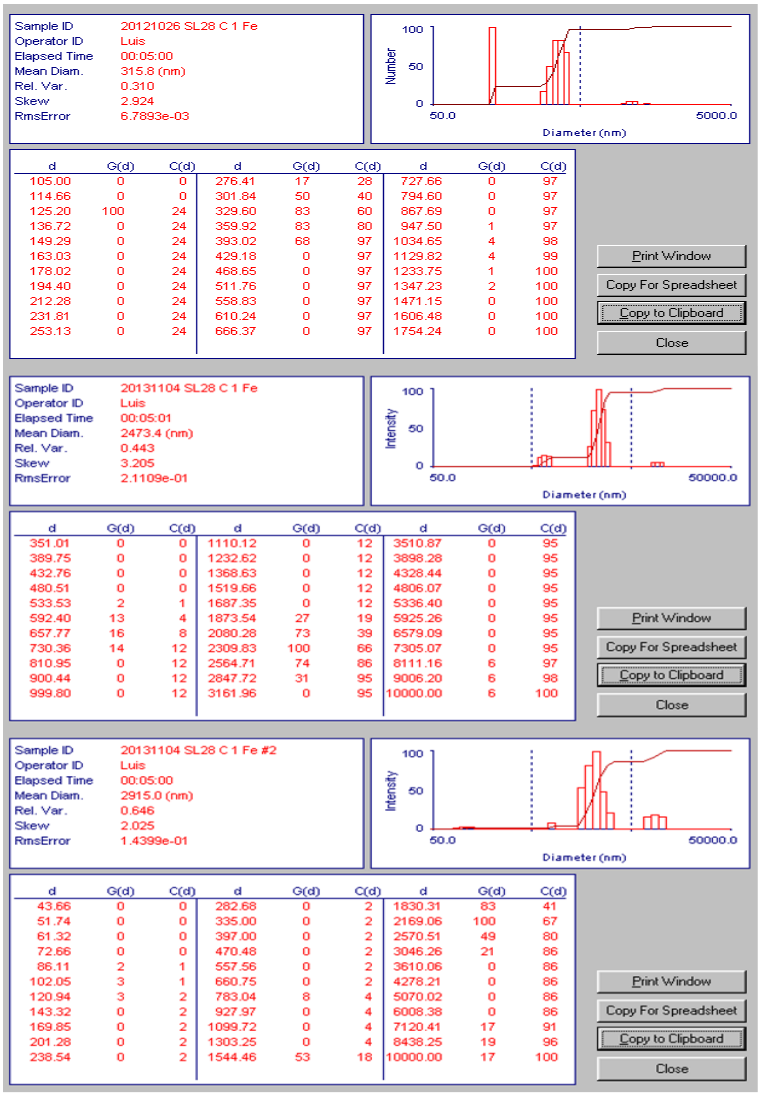

Figure D42. Particle size analysis results for *Halomonas* sp. SL28 Sodachelin C at 1 Eq. Fe^{+3}.

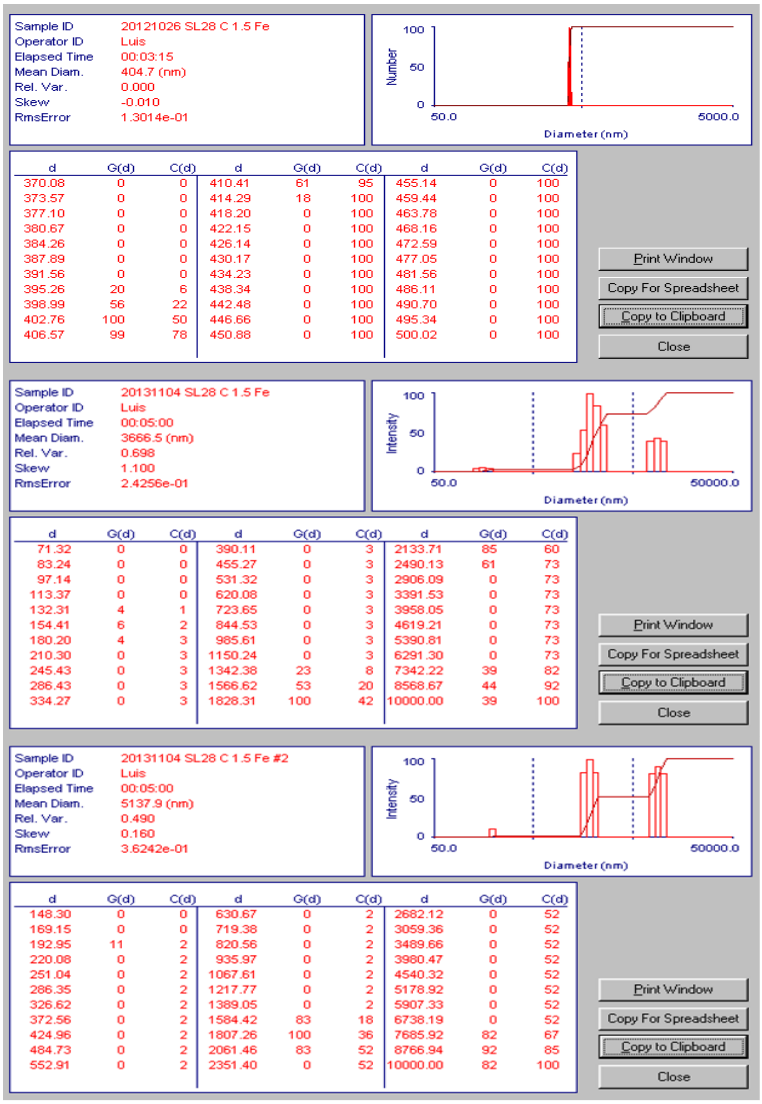

Figure D43. Particle size analysis results for *Halomonas* sp. SL28 Sodachelin C at 1.5 Eq. Fe^{+3}.

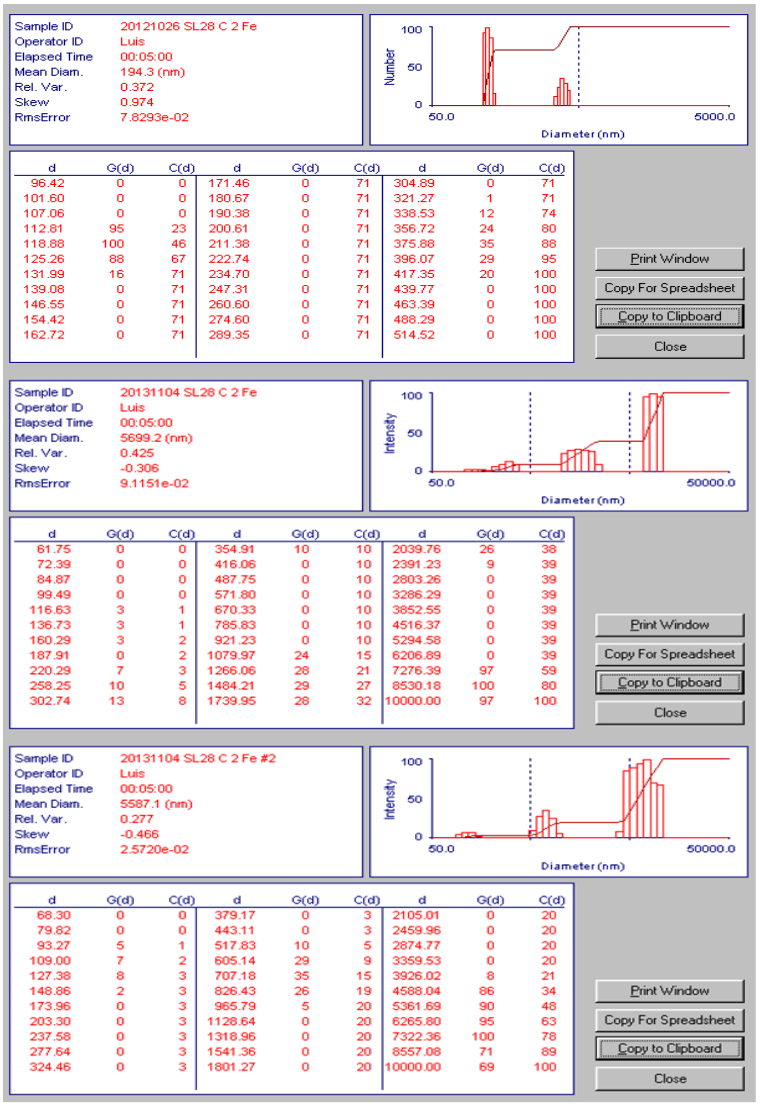

Figure D44. Particle size analysis results for *Halomonas* sp. SL28 Sodachelin C at 2 Eq. Fe^{+3}.

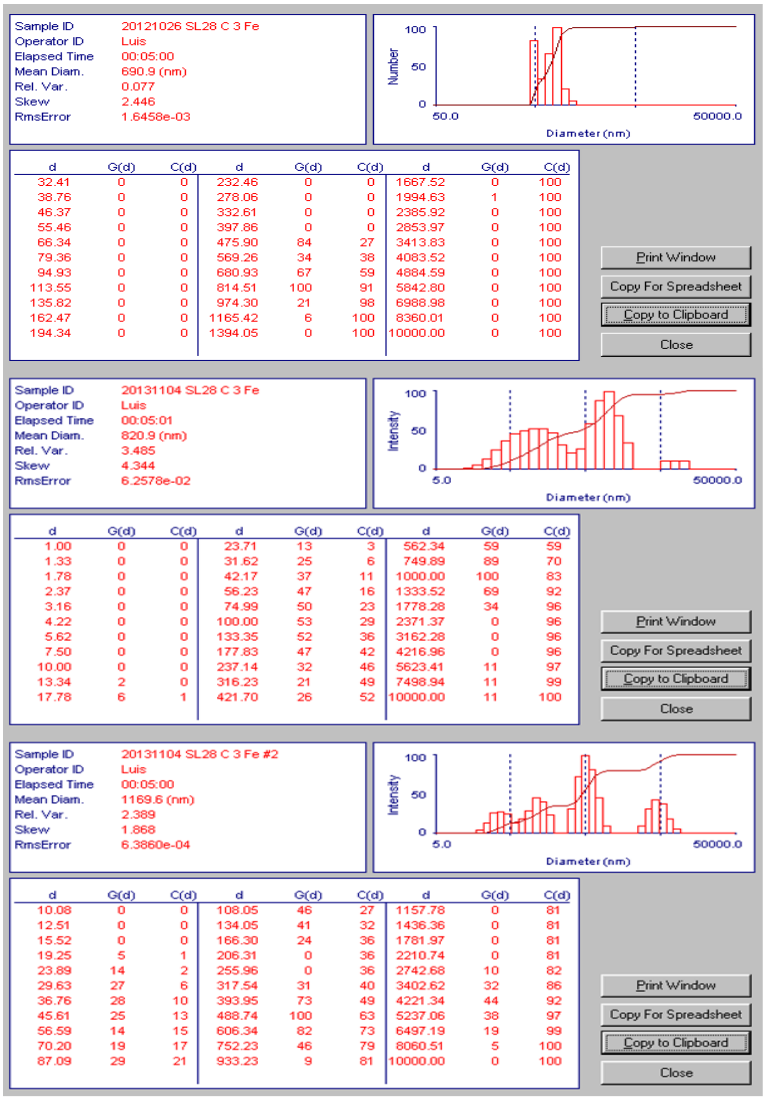

Figure D45. Particle size analysis results for *Halomonas* sp. SL28 Sodachelin C at 3 Eq. Fe^{+3}.

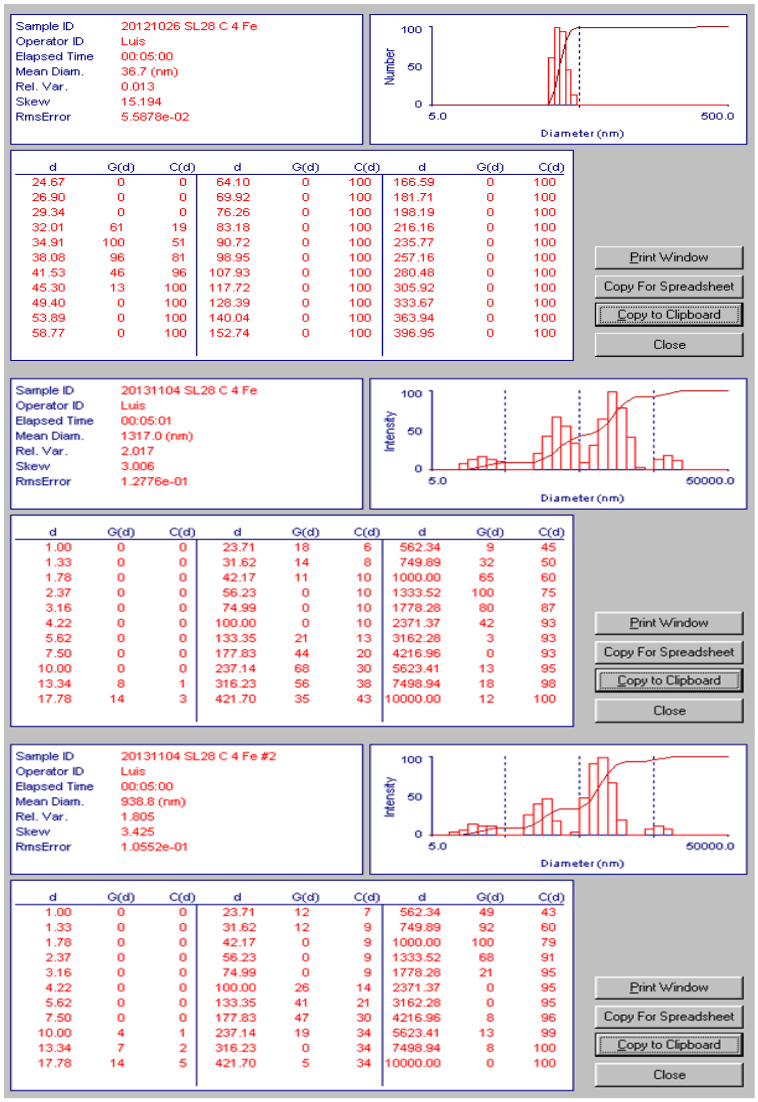

Figure D46. Particle size analysis results for *Halomonas* sp. SL28 Sodachelin C at 4 Eq. Fe^{+3}.

A)

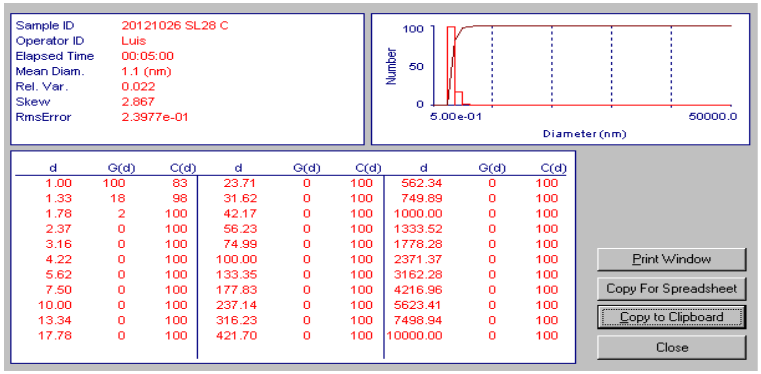

B)

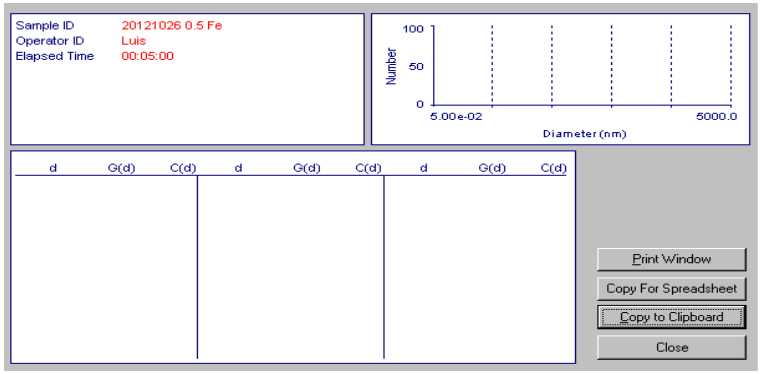

C)

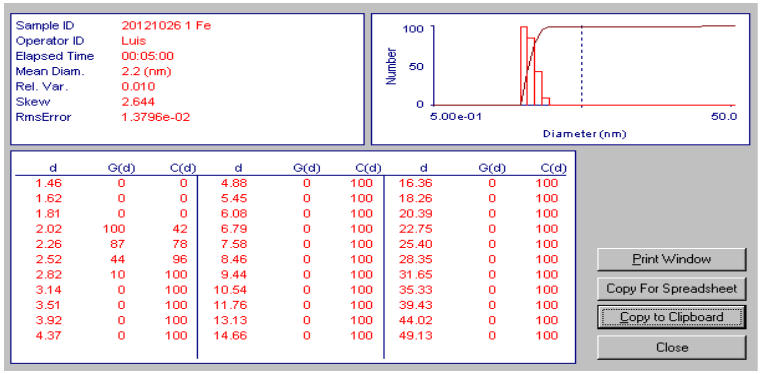

D)

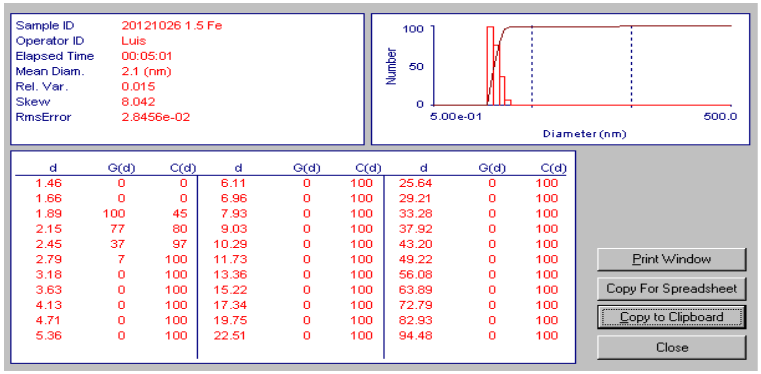

Figure D47. Particle size analysis results for *Halomonas* sp. SL28 Sodachelin C without ferric iron (A) and ferric iron controls 0.5 (B), 1 (C) and 1.5 (D) Eq. Fe^{+3}.

A)

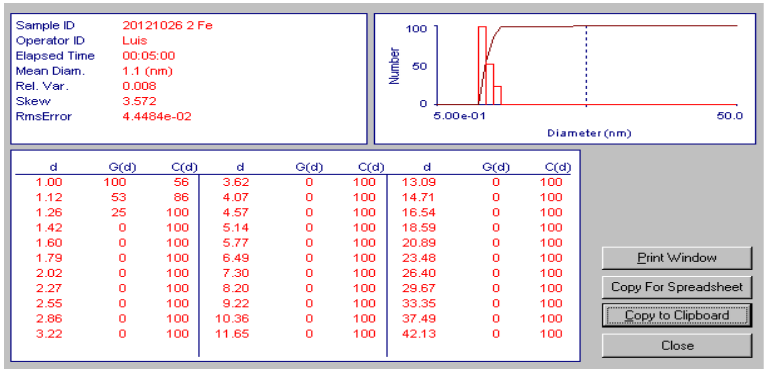

B)

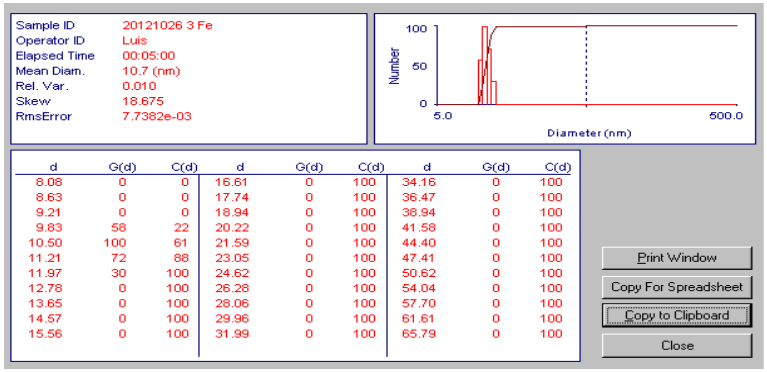

C)

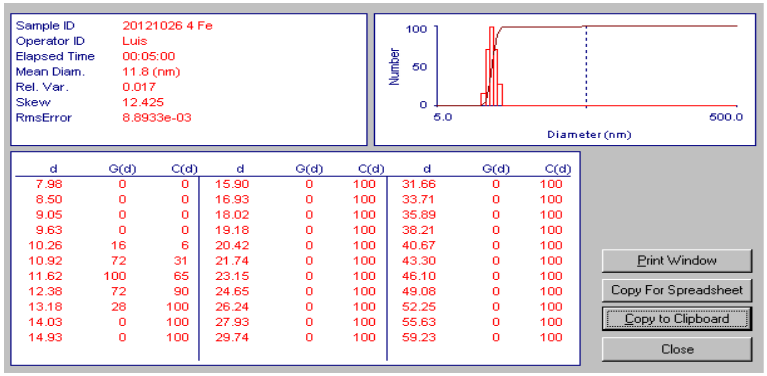

Figure D48. Particle size analysis results for ferric iron controls 2 (A), 3 (B) and 4 (C) Eq. Fe^{+3}.

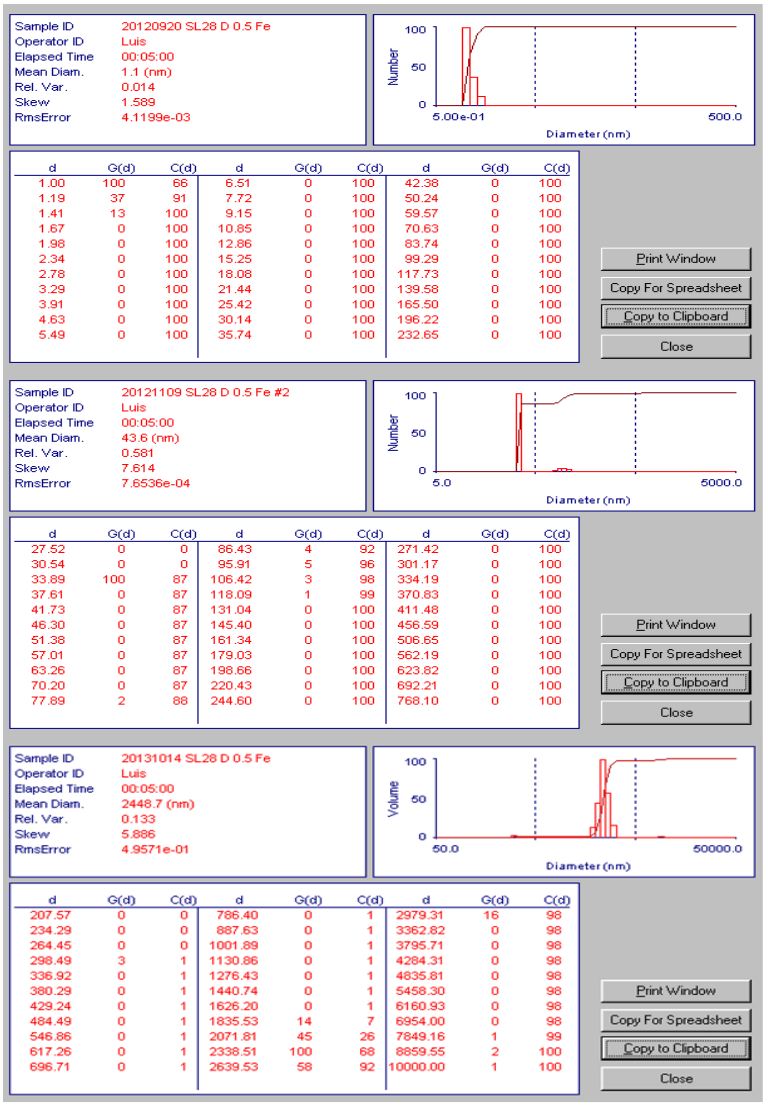

Figure D49. Particle size analysis results for *Halomonas* sp. SL28 Sodachelin D at 0.5 Eq. Fe^{+3}.

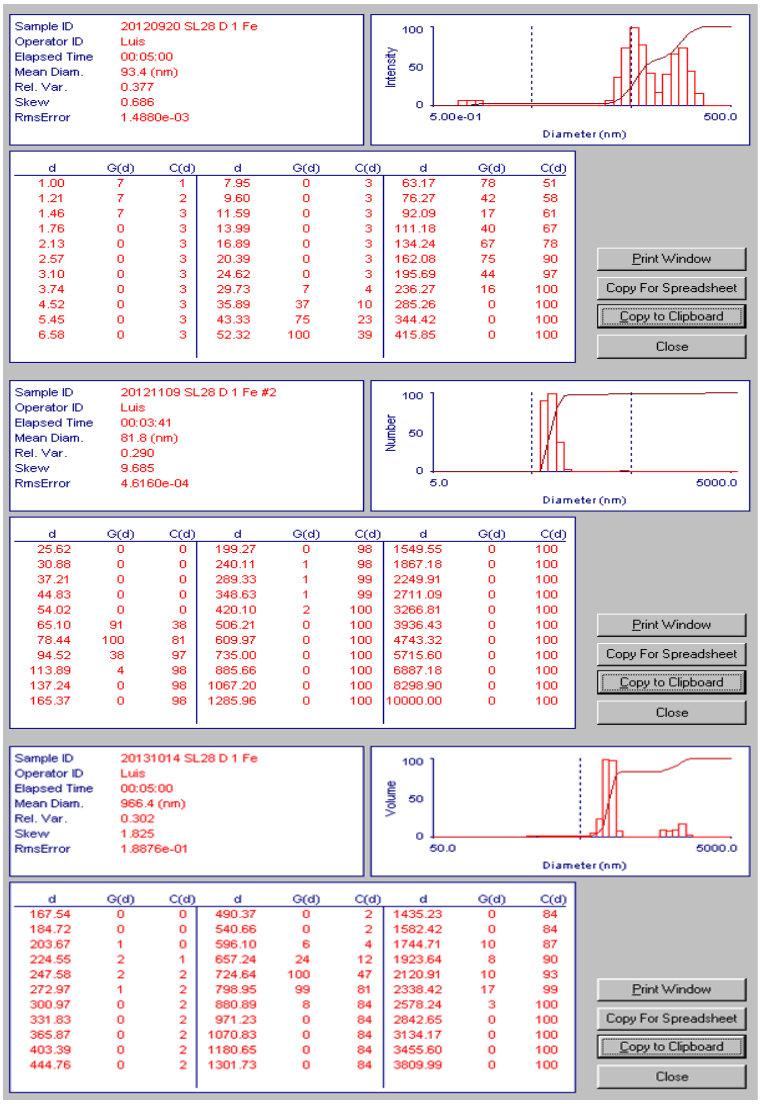

Figure D50. Particle size analysis results for *Halomonas* sp. SL28 Sodachelin D at 1 Eq. Fe^{+3}.

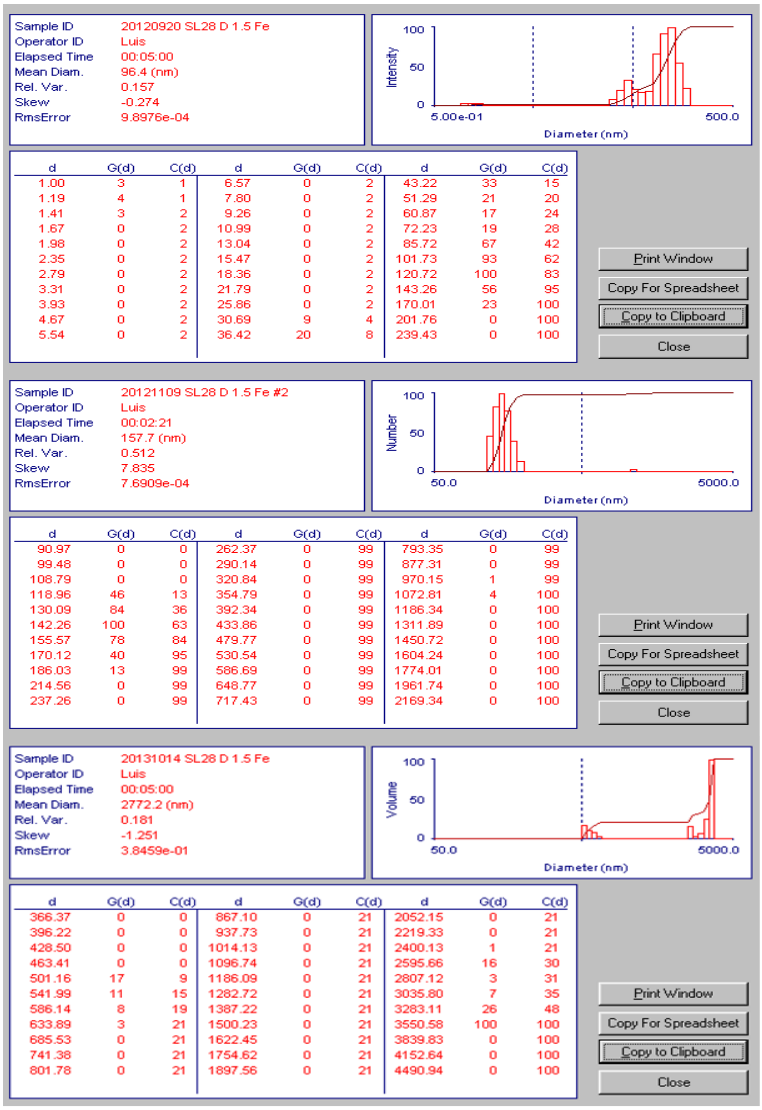

Figure D51. Particle size analysis results for *Halomonas* sp. SL28 Sodachelin D at 1.5 Eq. Fe^{+3}.

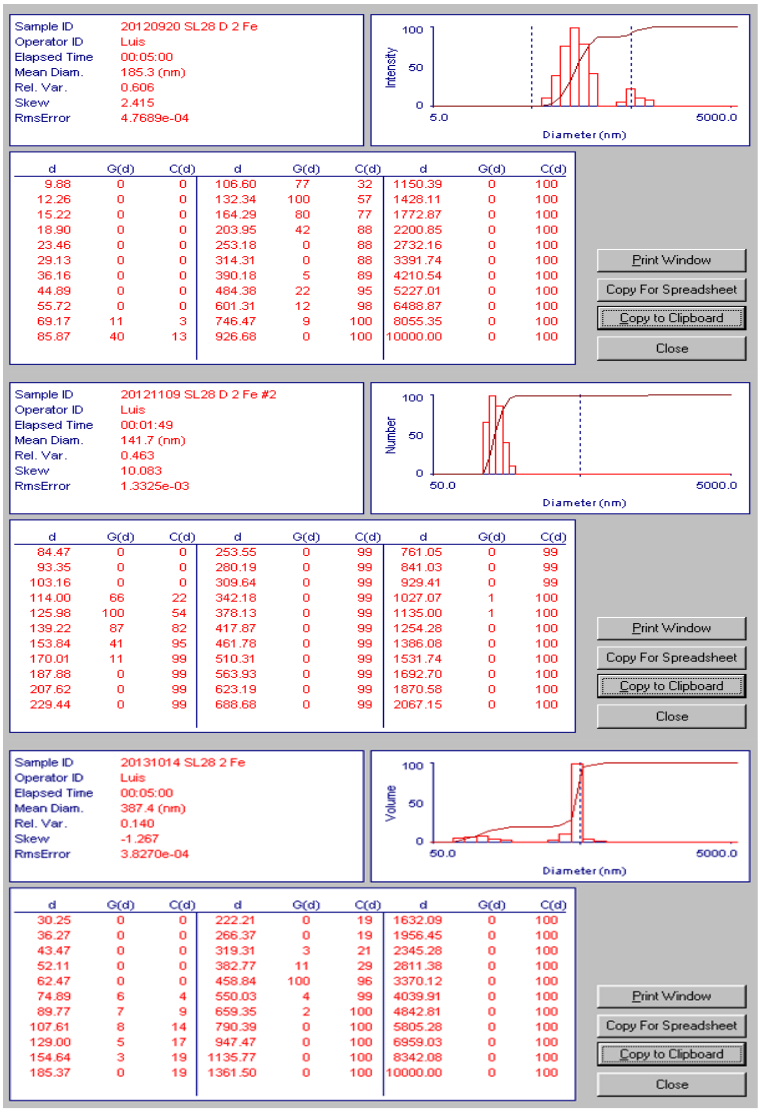

Figure D52. Particle size analysis results for *Halomonas* sp. SL28 Sodachelin D at 2 Eq. Fe^{+3}.

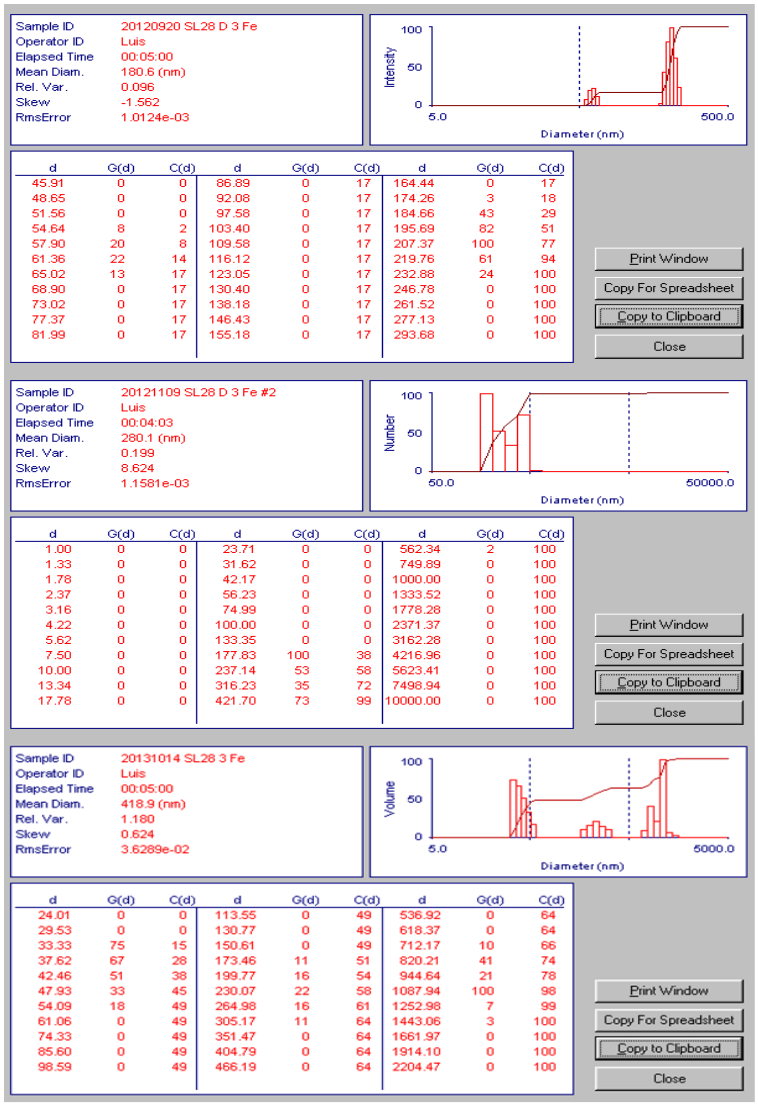

Figure D53. Particle size analysis results for *Halomonas* sp. SL28 Sodachelin D at 3 Eq. Fe^{+3}.

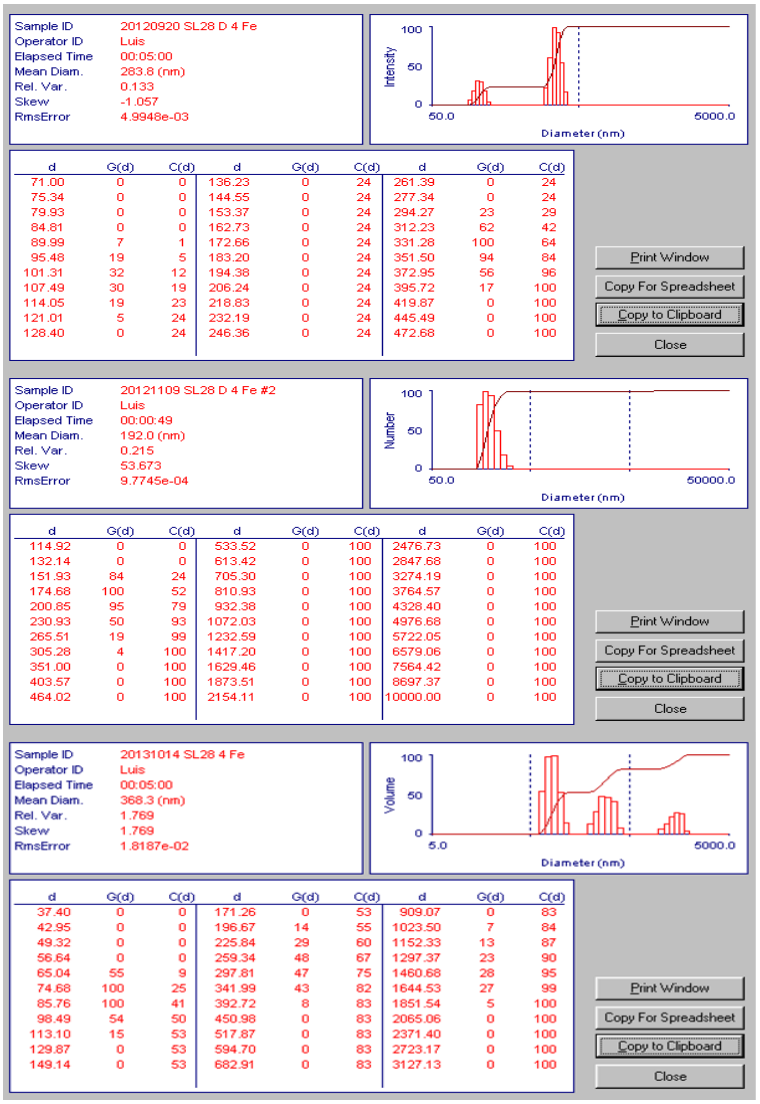

Figure D54. Particle size analysis results for *Halomonas* sp. SL28 Sodachelin D at 4 Eq. Fe^{+3}.

A)

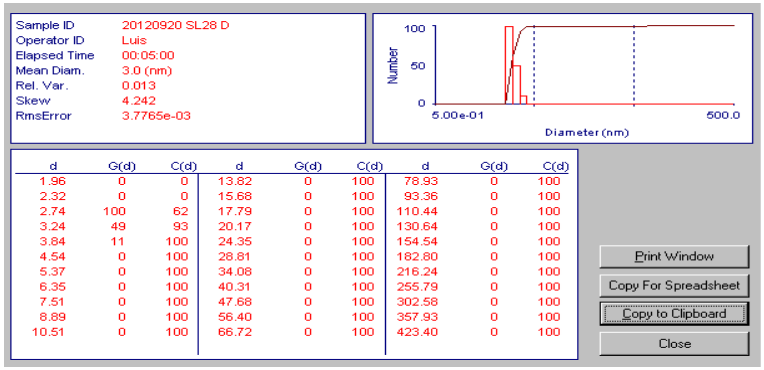

B)

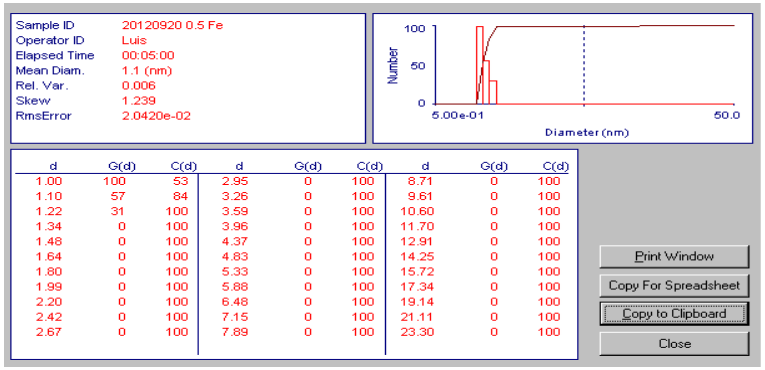

C)

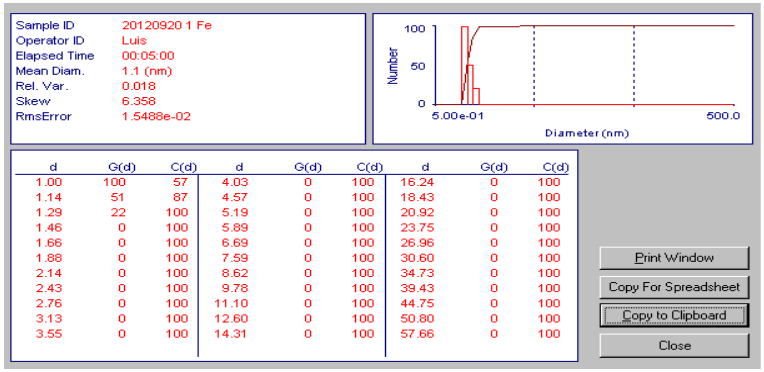

D)

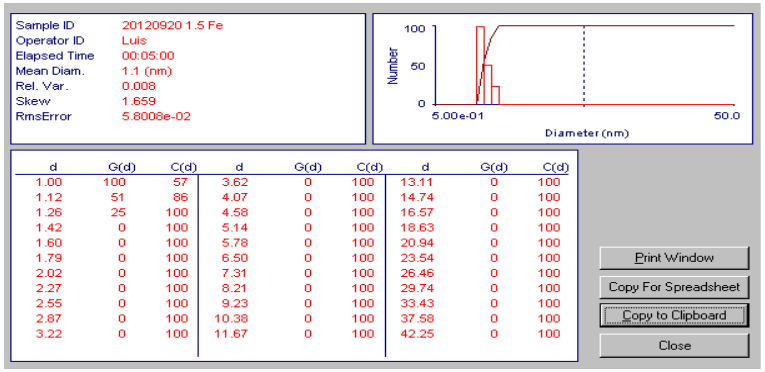

Figure D55. Particle size analysis results for *Halomonas* sp. SL28 Sodachelin D without ferric iron (A) and ferric iron controls 0.5 (B), 1 (C) and 1.5 (D) Eq. Fe^{+3}.

A)

B)

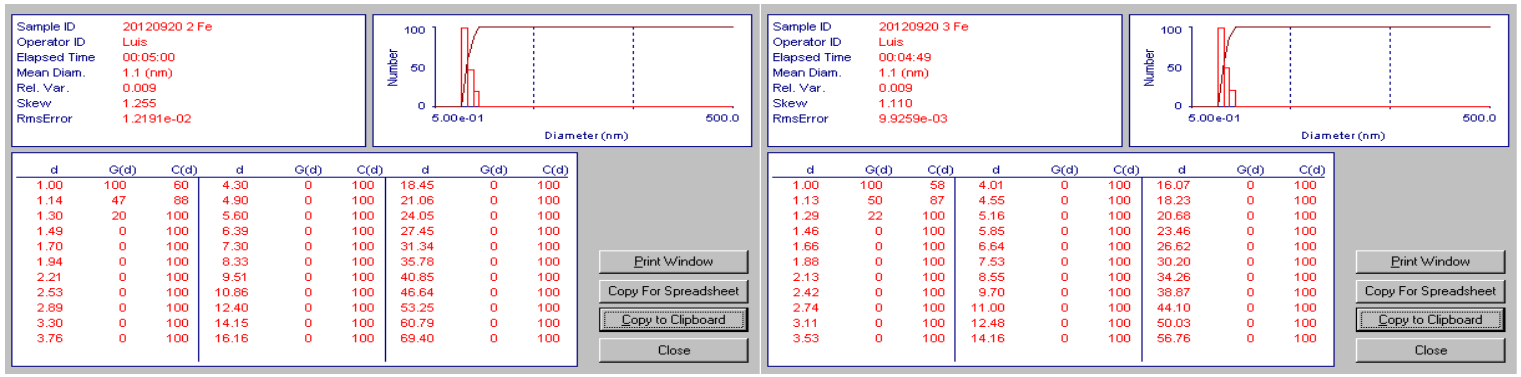

C)

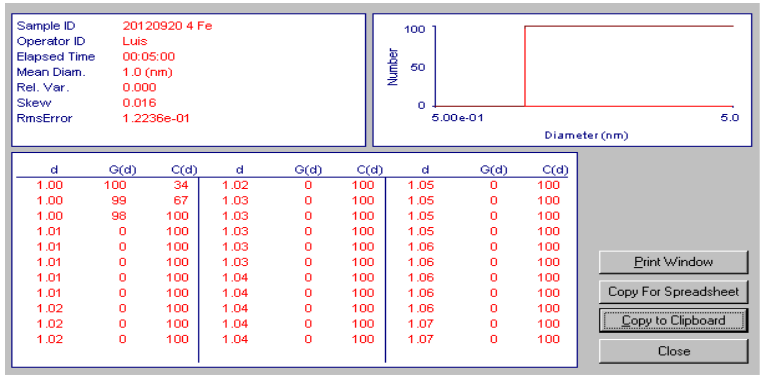

Figure D56. Particle size analysis results for ferric iron controls at 2 (A), 3 (B) and 4 (C) Eq. Fe^{+3}.

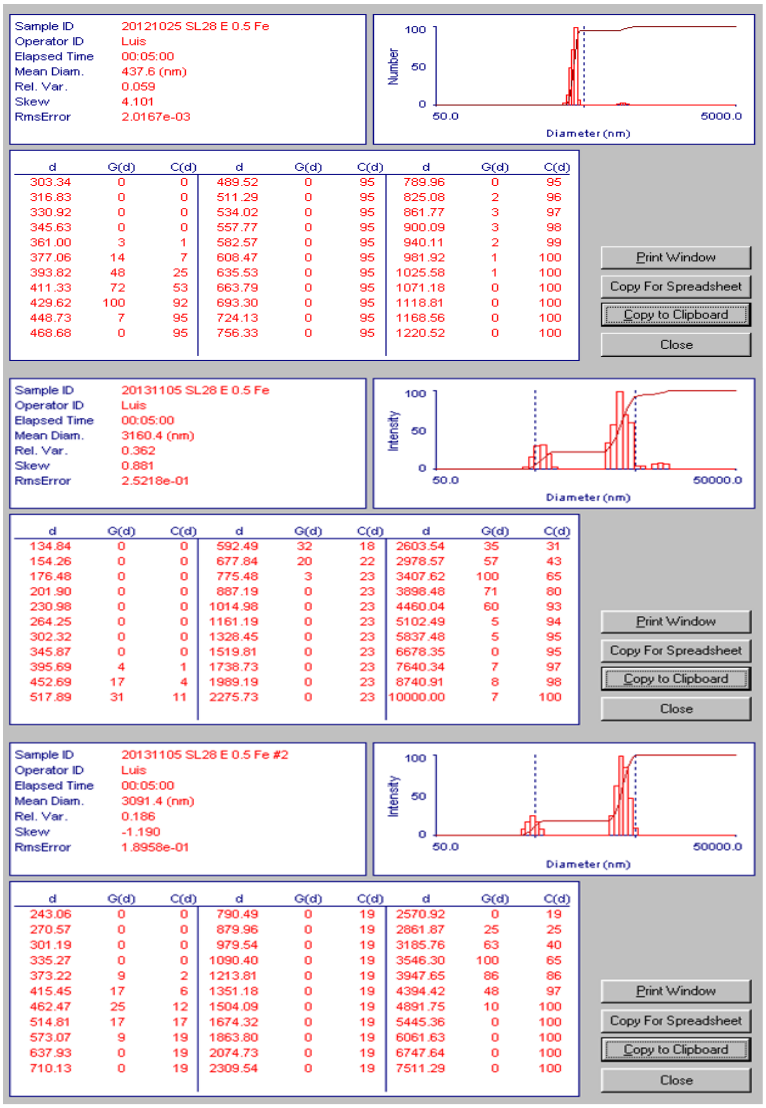

Figure D57. Particle size analysis results for *Halomonas* sp. SL28 Sodachelin E at 0.5 Eq. Fe^{+3}.

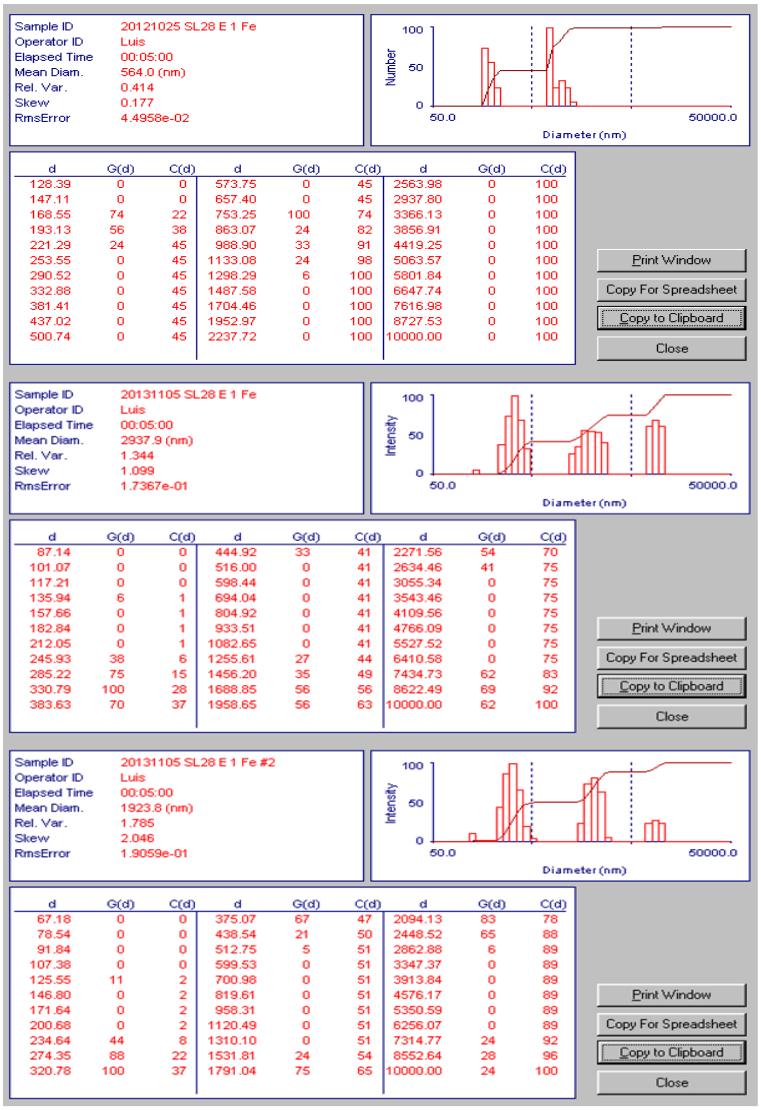

Figure D58. Particle size analysis results for *Halomonas* sp. SL28 Sodachelin E at 1 Eq. Fe^{+3}.

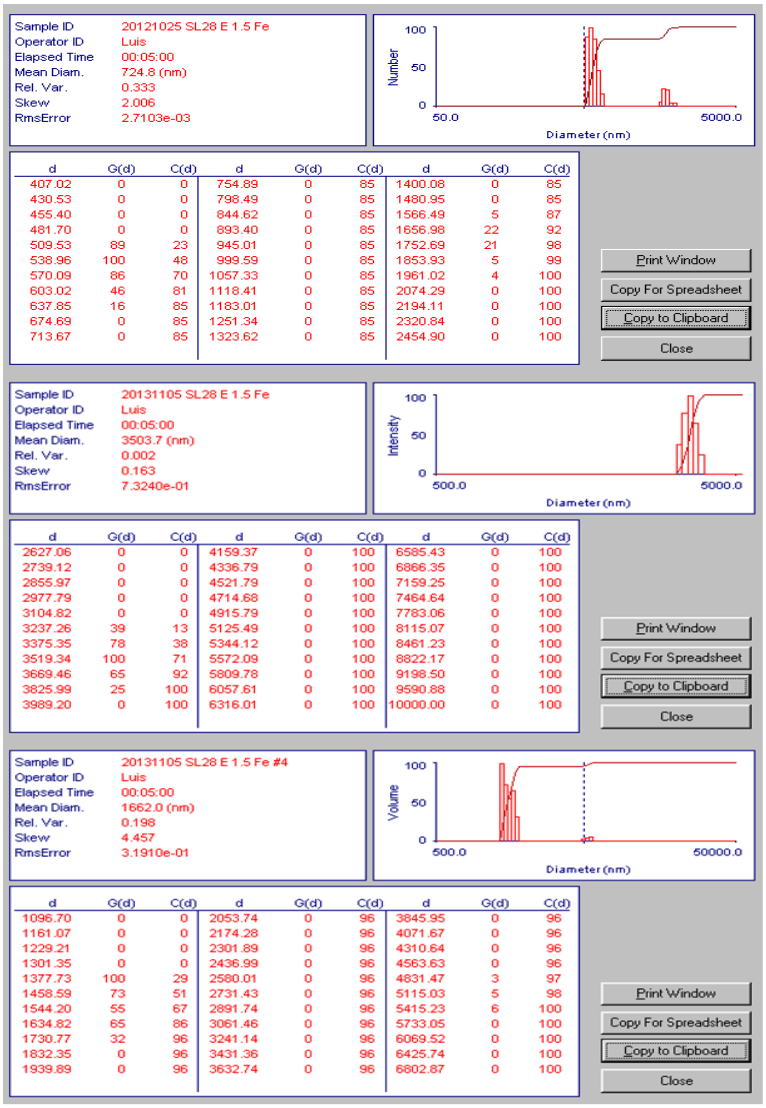

Figure D59. Particle size analysis results for *Halomonas* sp. SL28 Sodachelin E at 1.5 Eq. Fe^{+3}.

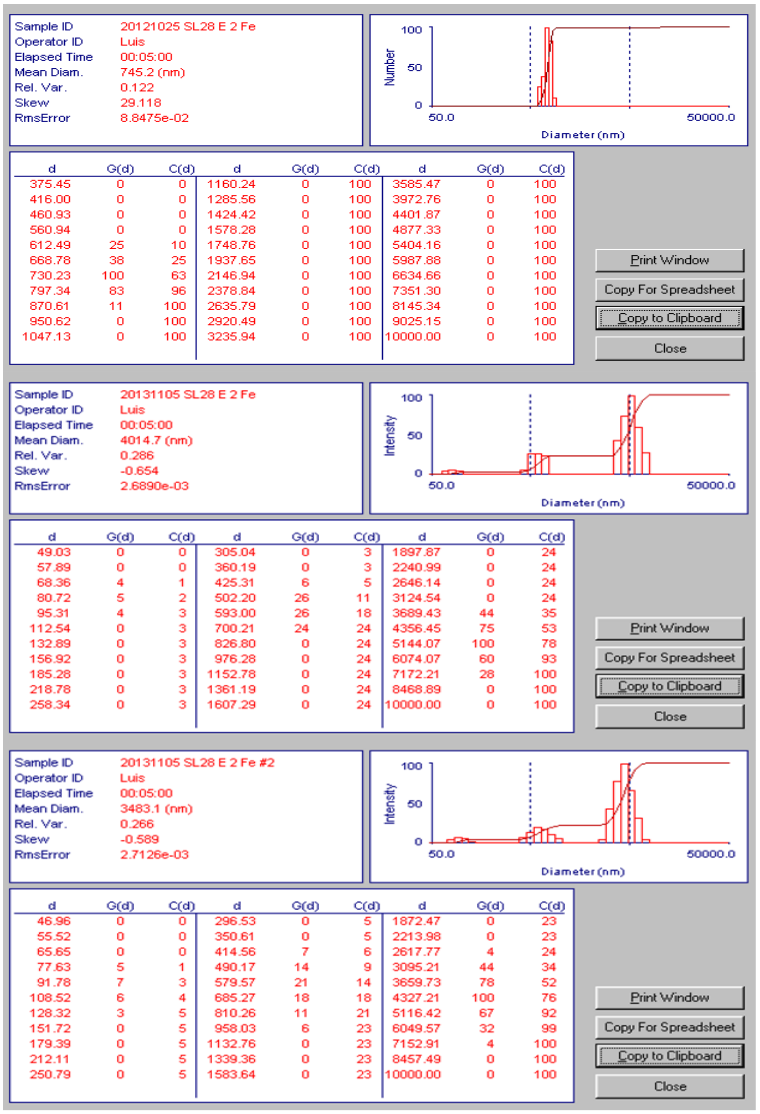

Figure D60. Particle size analysis results for *Halomonas* sp. SL28 Sodachelin E at 2 Eq. Fe^{+3}.

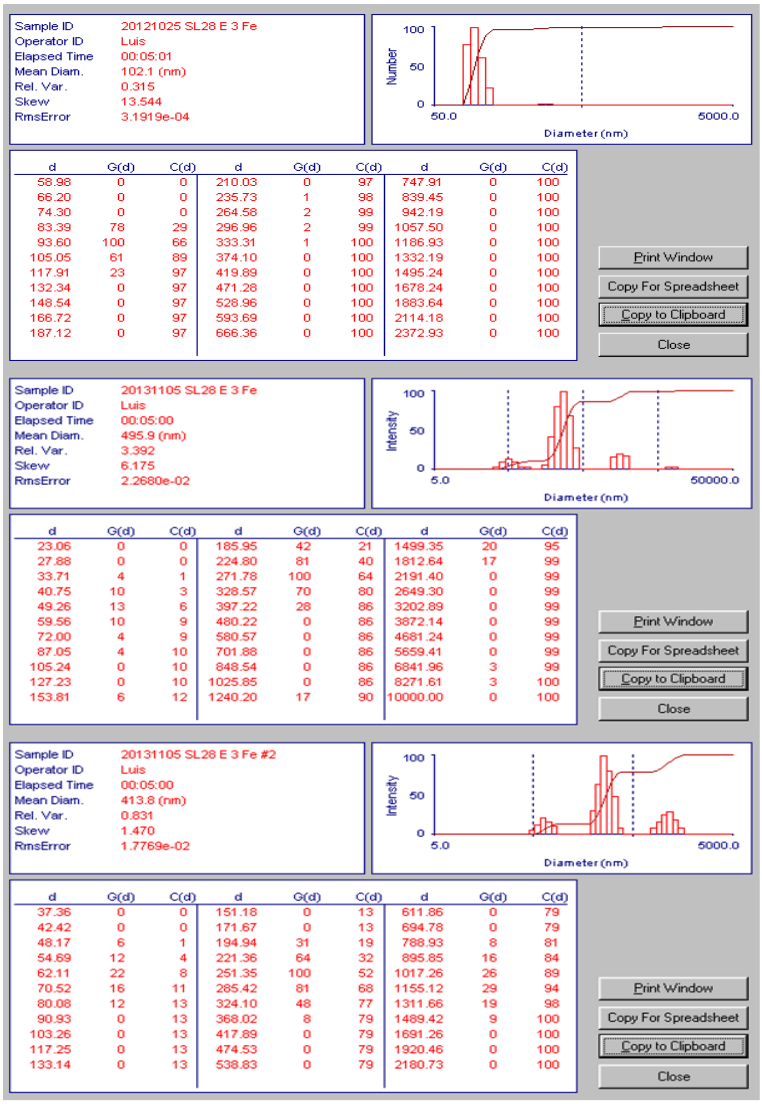

Figure D61. Particle size analysis results for *Halomonas* sp. SL28 Sodachelin E at 3 Eq. Fe^{+3}.

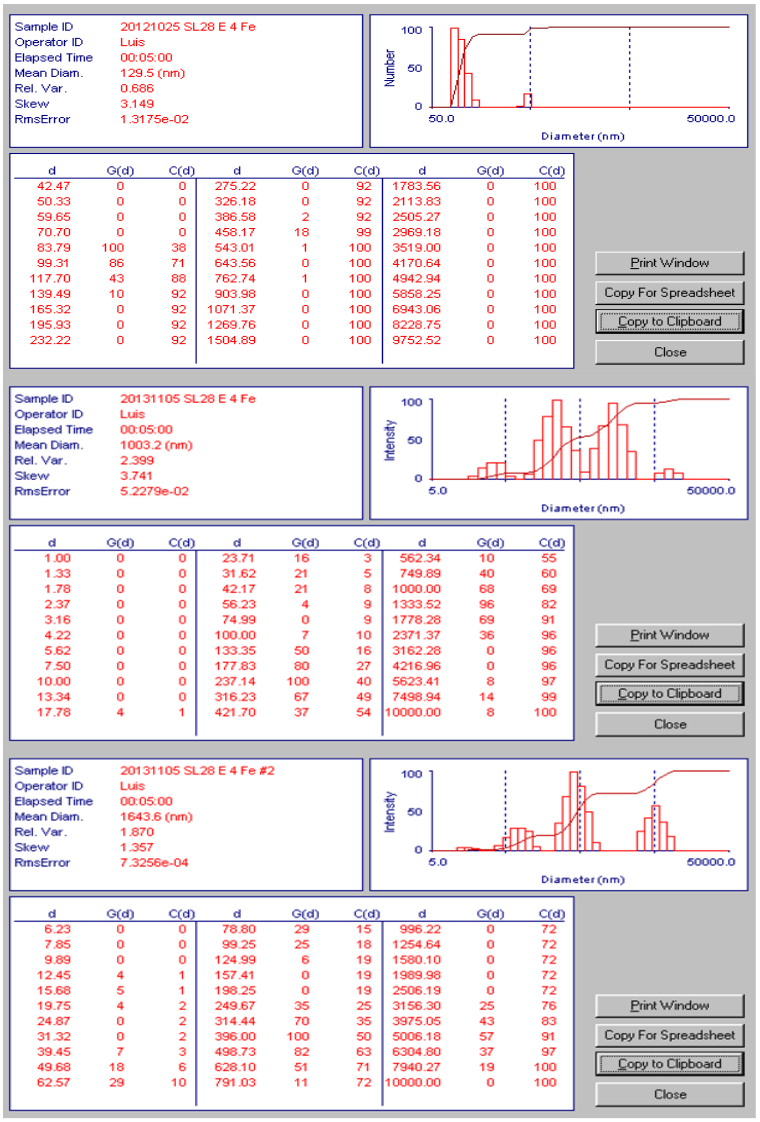

Figure D62. Particle size analysis results for *Halomonas* sp. SL28 Sodachelin E at 4 Eq. Fe^{+3}.

A)

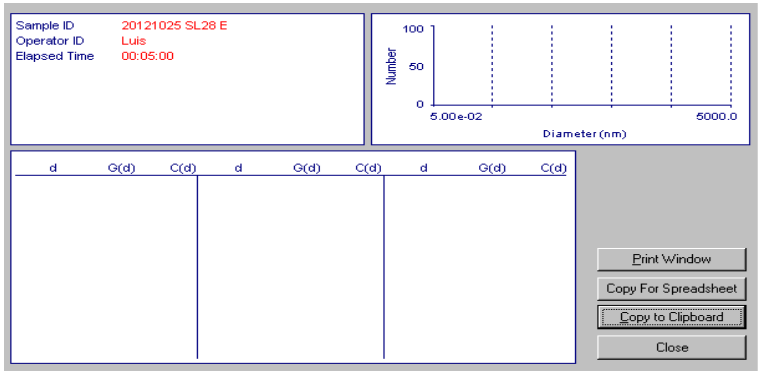

B)

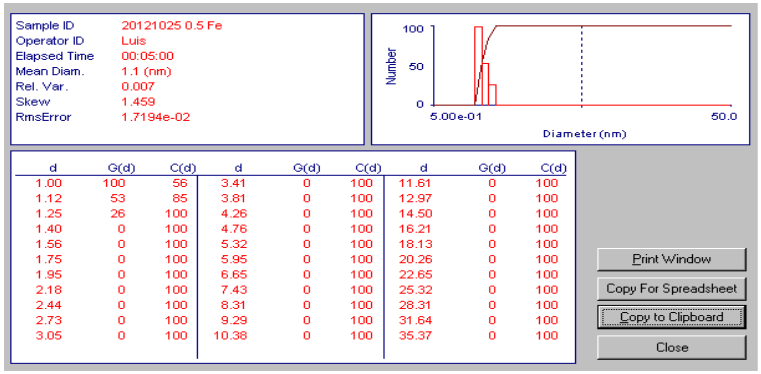

C)

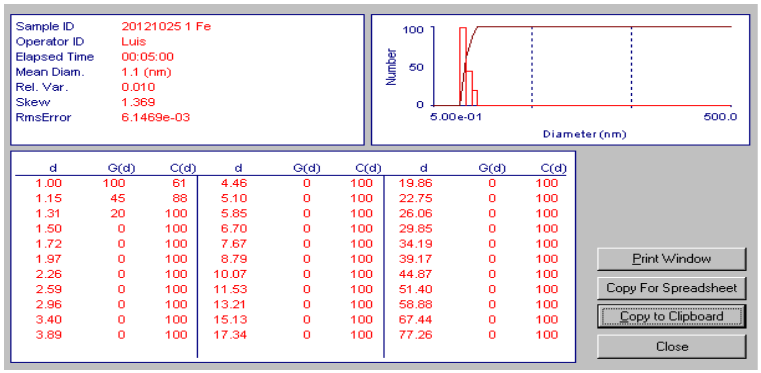

D)

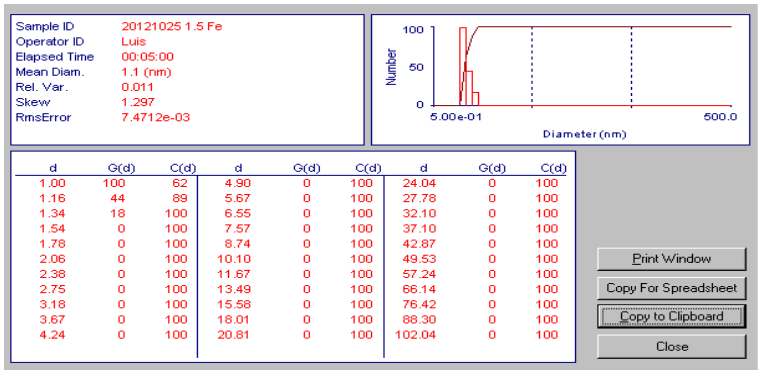

Figure D63. Particle size analysis results for *Halomonas* sp. SL28 Sodachelin E without ferric iron (A) and ferric iron controls 0.5 (B), 1 (C) and 1.5 (D) Eq. Fe^{+3}.

A)

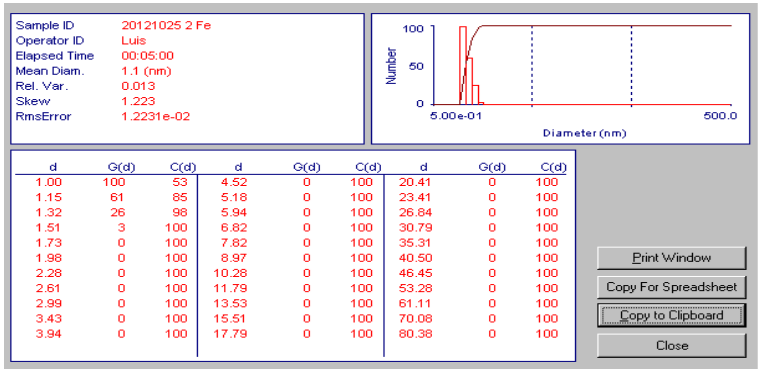

B)

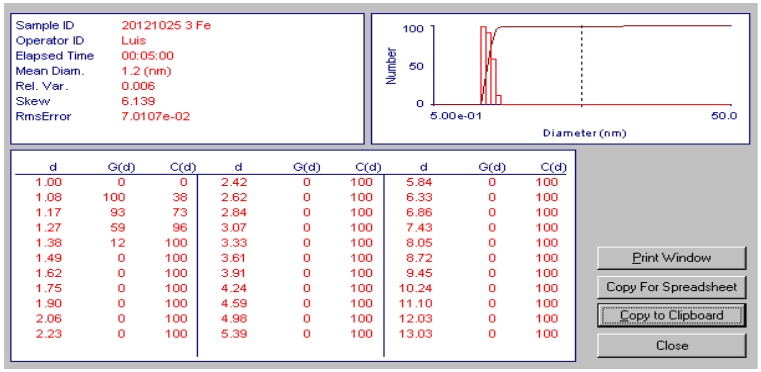

C)

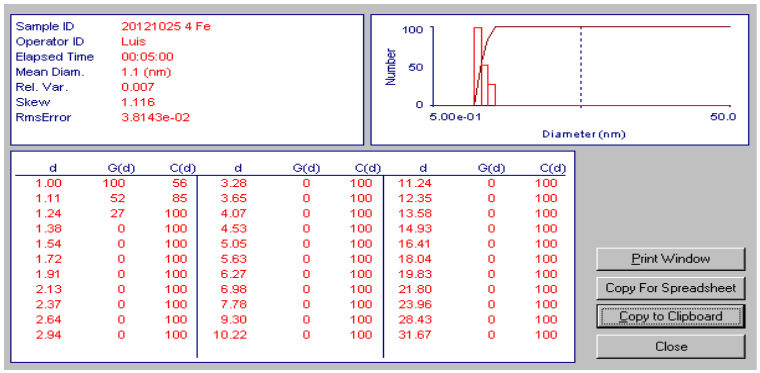

Figure D64. Particle size analysis results for ferric iron controls at 2 (A), 3 (B) and 4 (C) Eq. Fe^{+3}.

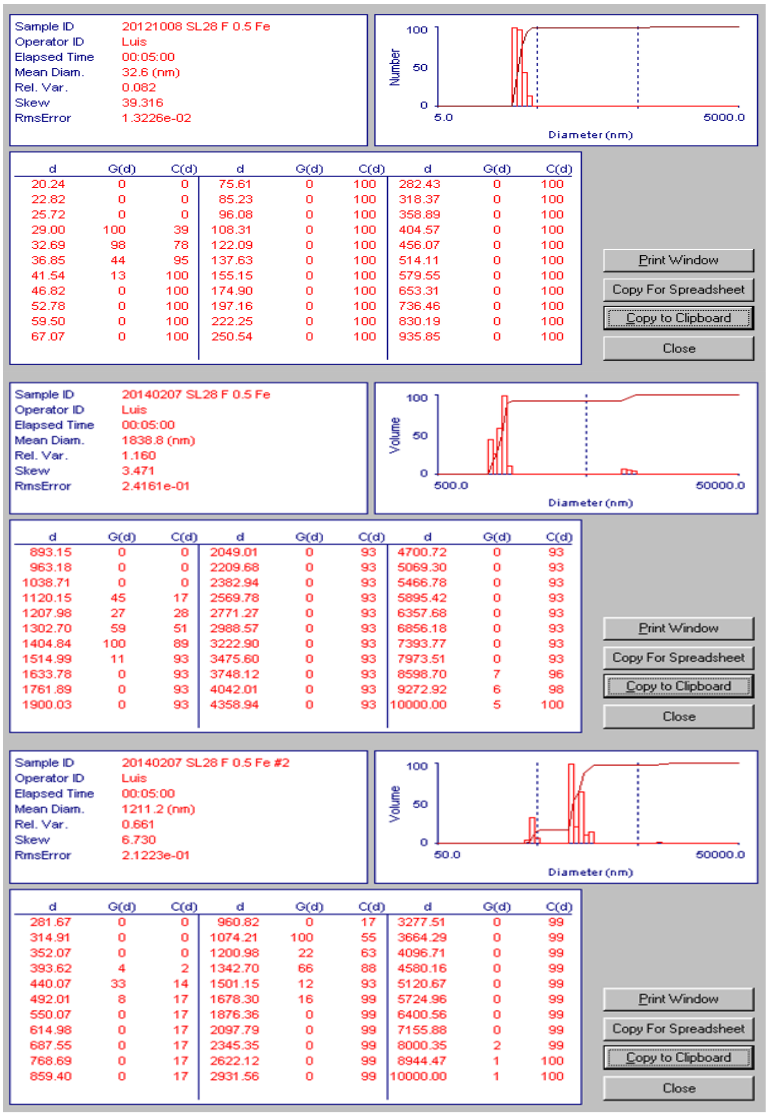

Figure D65. Particle size analysis results for *Halomonas* sp. SL28 Sodachelin F at 0.5 Eq. Fe^{+3}.

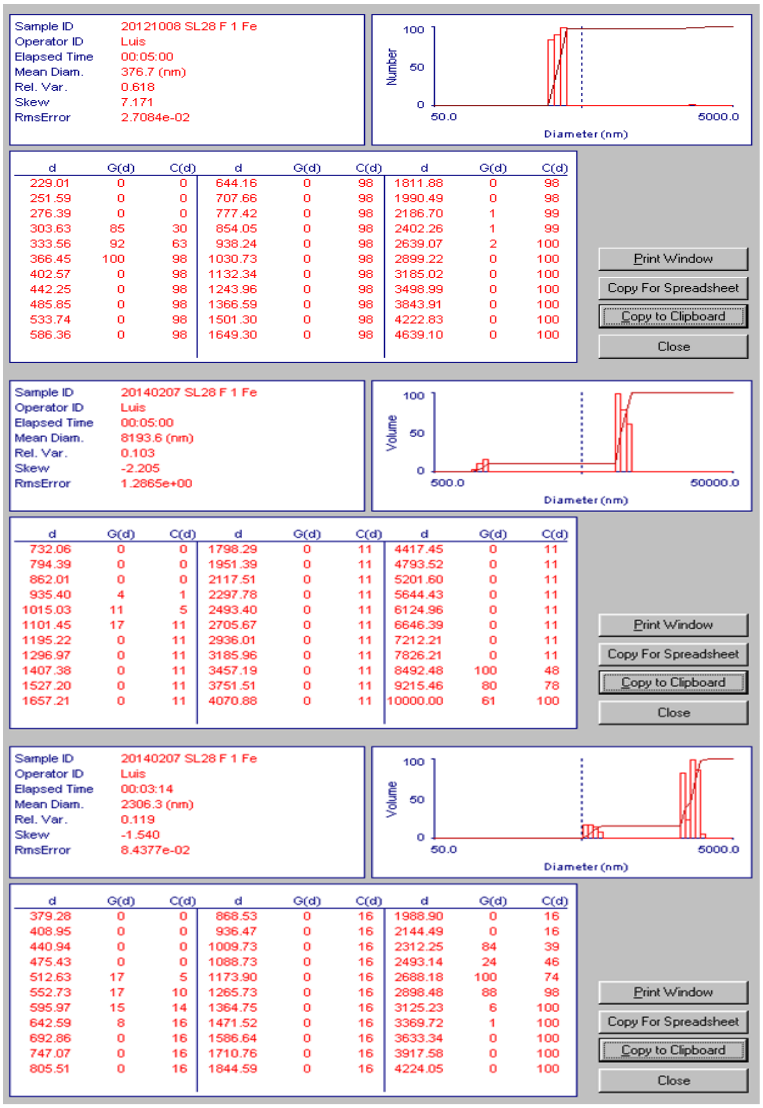

Figure D66. Particle size analysis results for *Halomonas* sp. SL28 Sodachelin F at 1 Eq. Fe^{+3}.

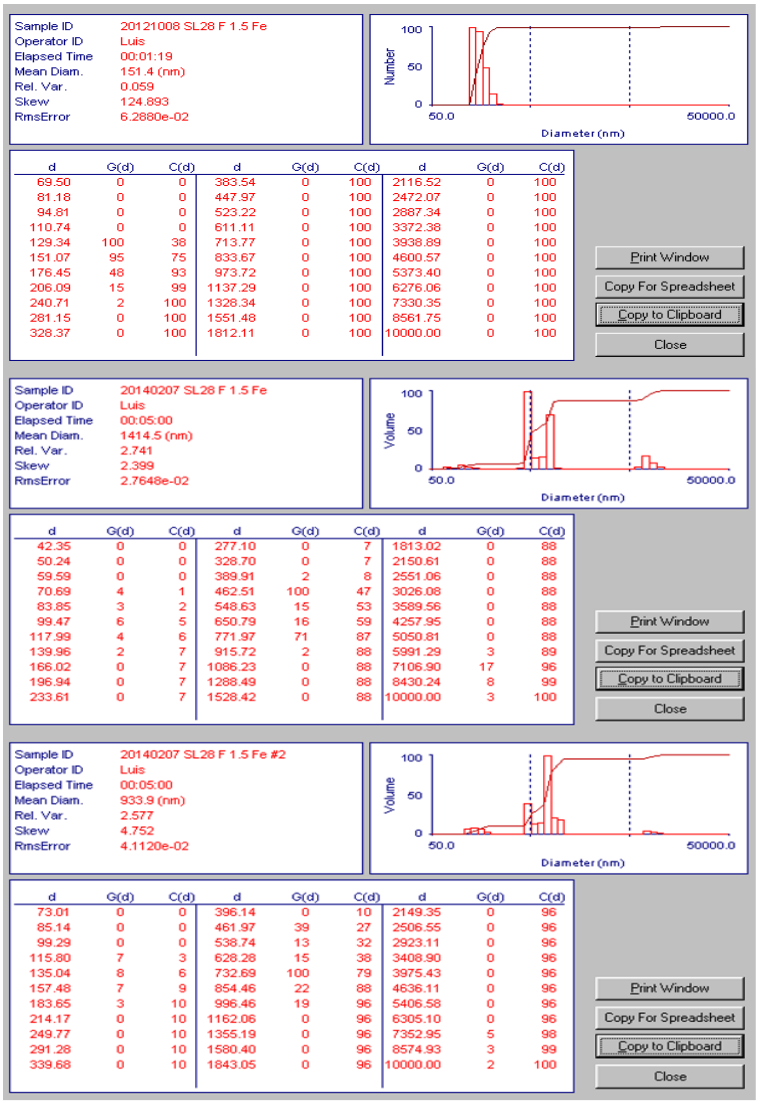

Figure D67. Particle size analysis results for *Halomonas* sp. SL28 Sodachelin F at 1.5 Eq. Fe^{+3}.

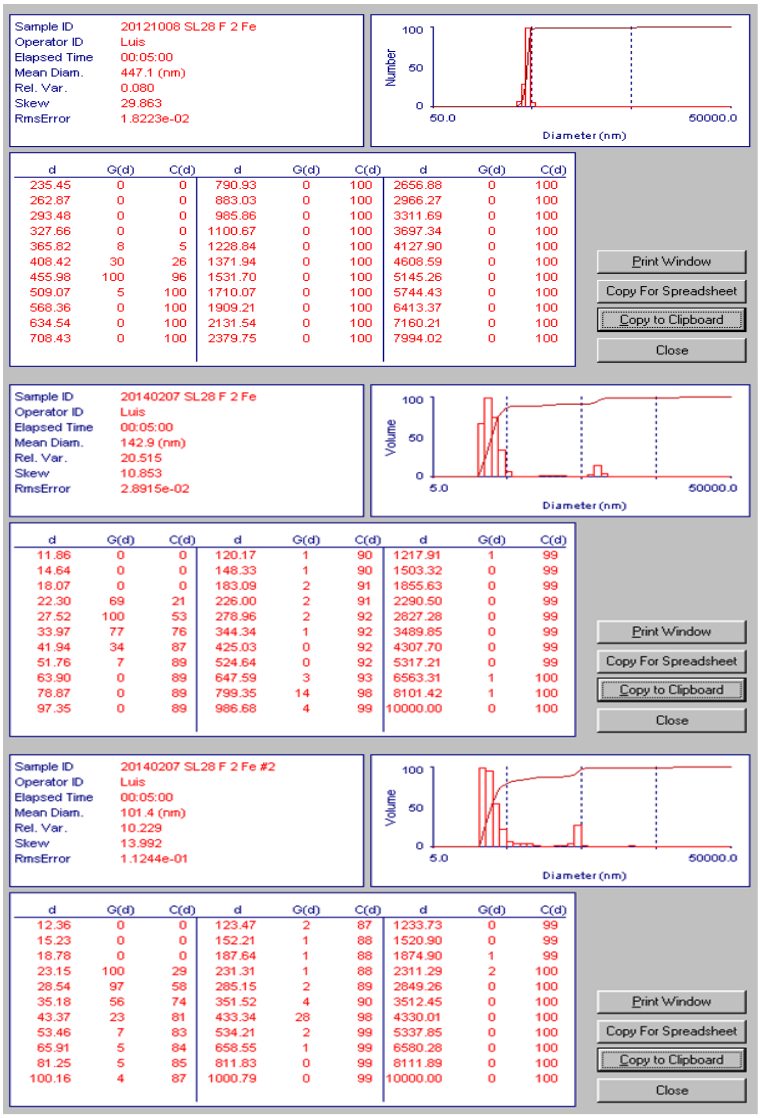

Figure D68. Particle size analysis results for *Halomonas* sp. SL28 Sodachelin F at 2 Eq. Fe^{+3}.

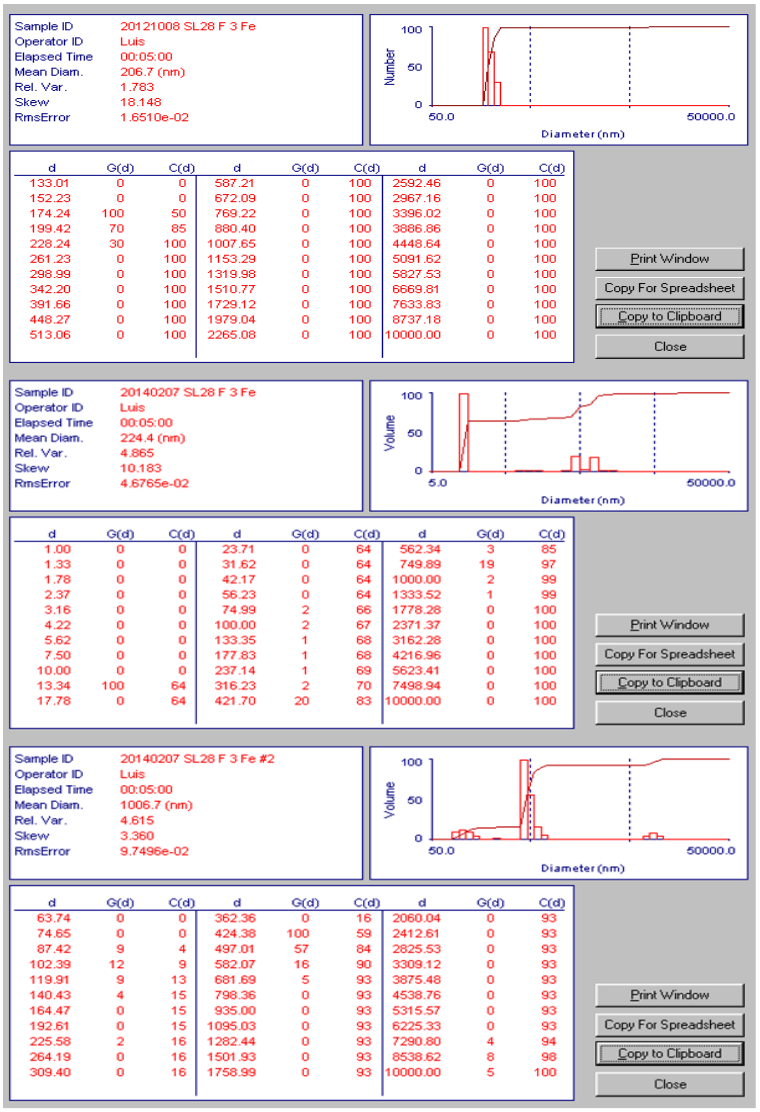

Figure D69. Particle size analysis results for *Halomonas* sp. SL28 Sodachelin F at 3 Eq. Fe^{+3}.

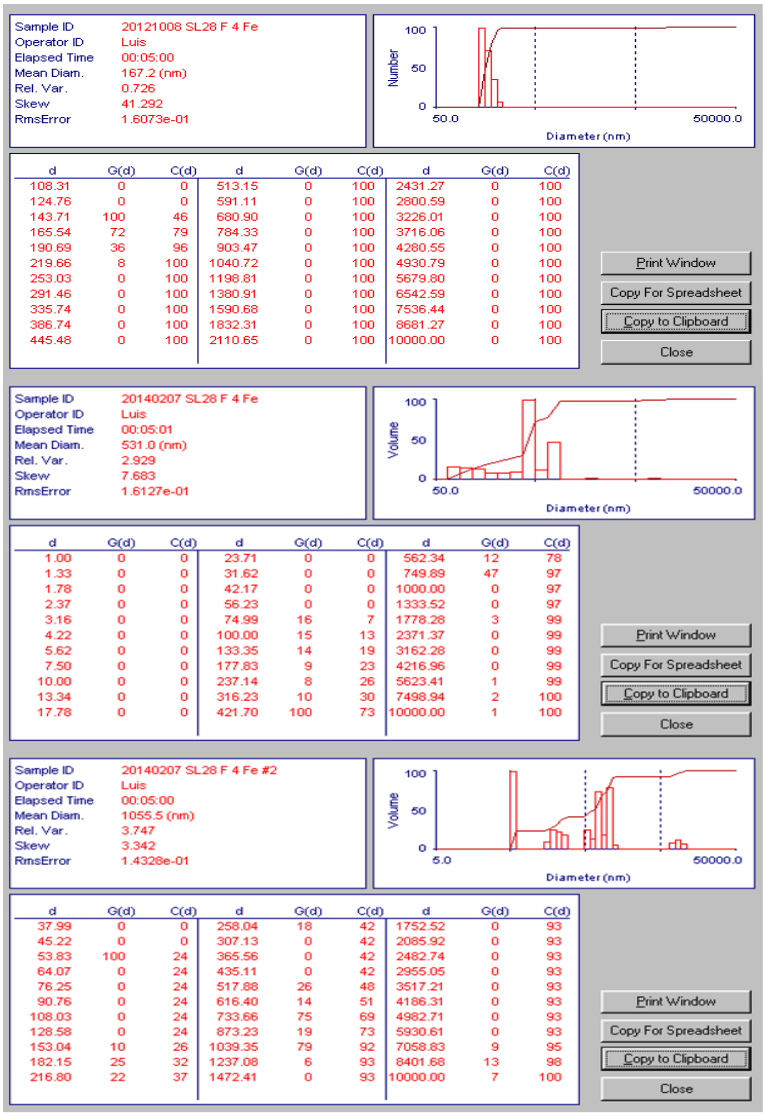

Figure D70. Particle size analysis results for *Halomonas* sp. SL28 Sodachelin F at 4 Eq. Fe^{+3}.

A)

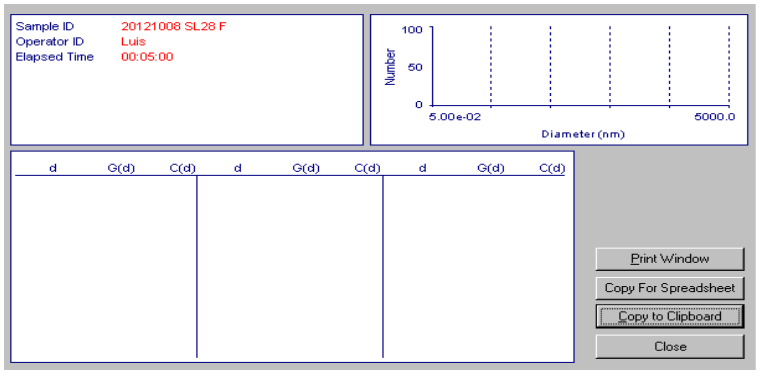

B)

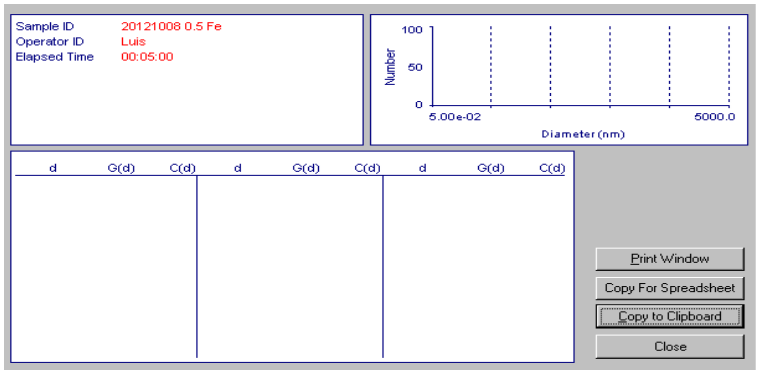

C)

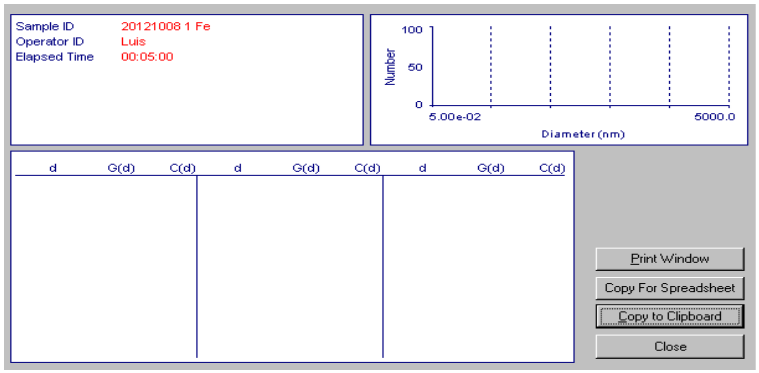

D)

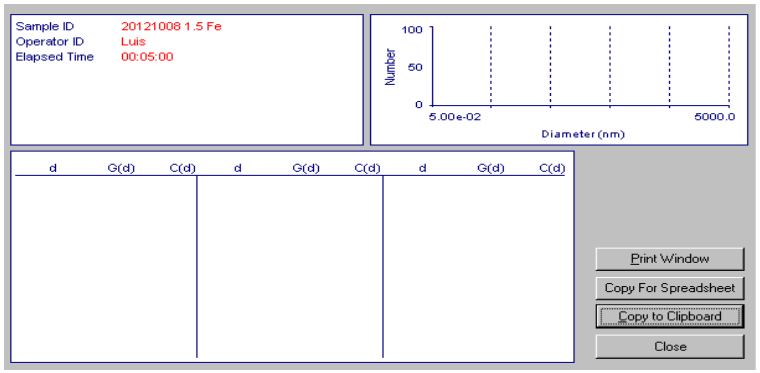

Figure D71. Particle size analysis results for *Halomonas* sp. SL28 Sodachelin F without ferric iron (A) and ferric iron controls 0.5 (B), 1 (C) and 1.5 (D) Eq. Fe^{+3}.

A)

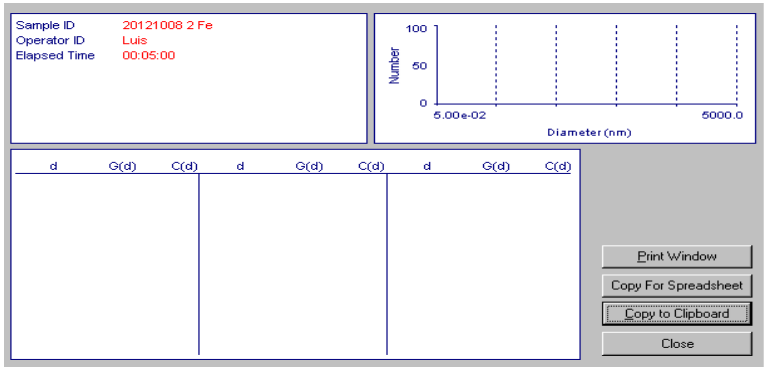

B)

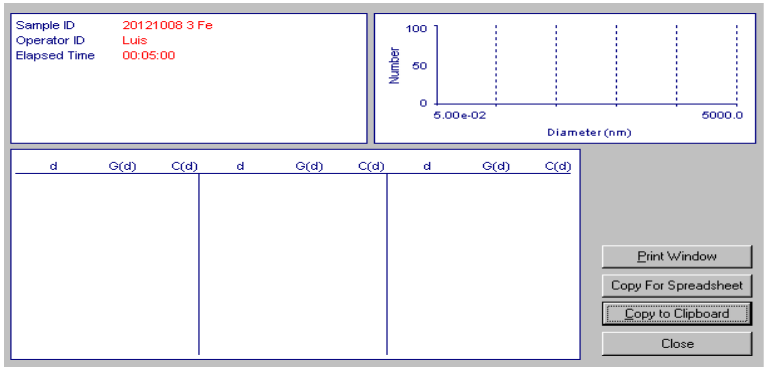

C)

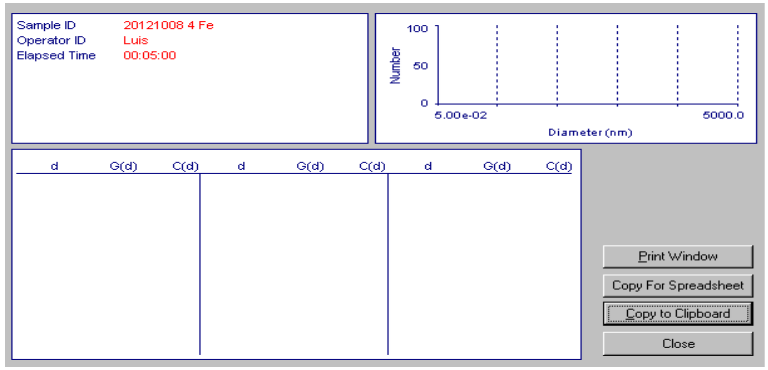

Figure D72. Particle size analysis results for ferric iron controls at 2 (A), 3 (B) and 4 (C) Eq. Fe^{+3}.

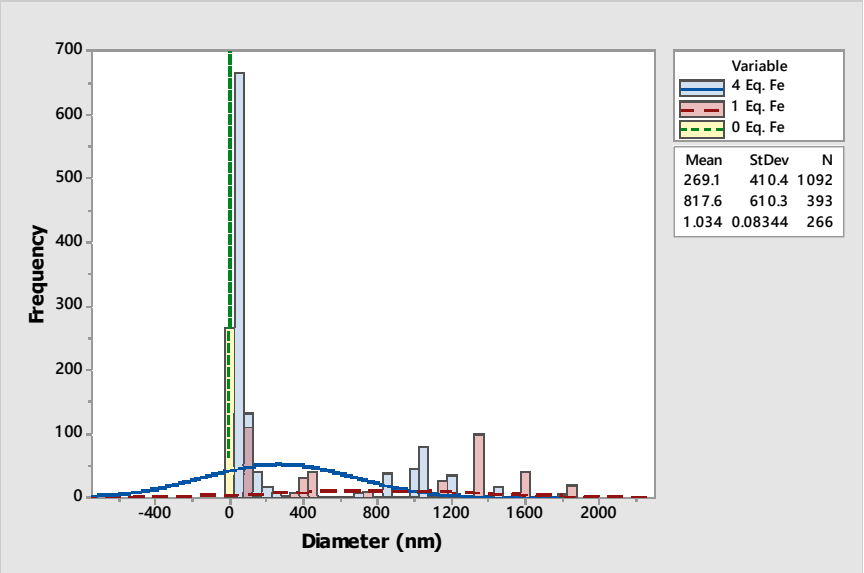

Figure D73. Particle size distribution for Halochelin B at different ferric iron equivalents.

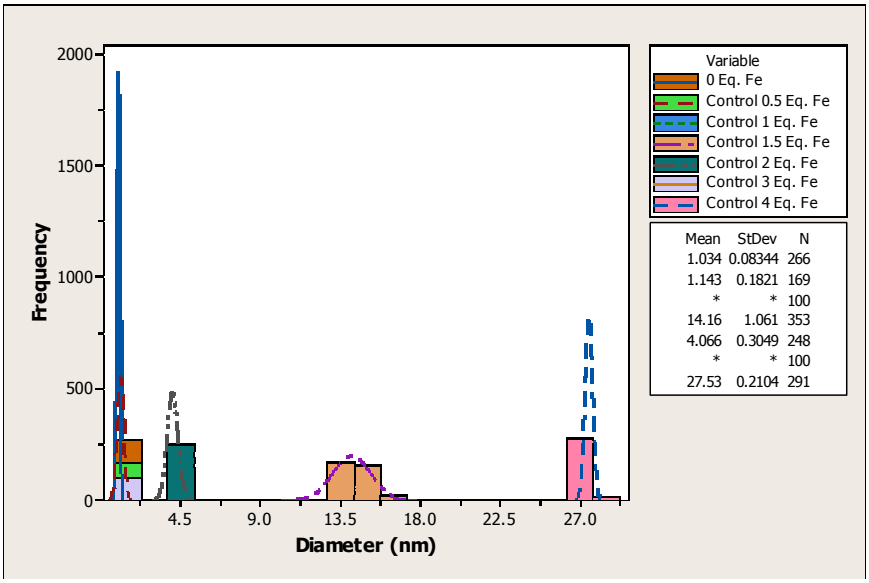

Figure D74. Particle size distribution for Halochelin B controls.

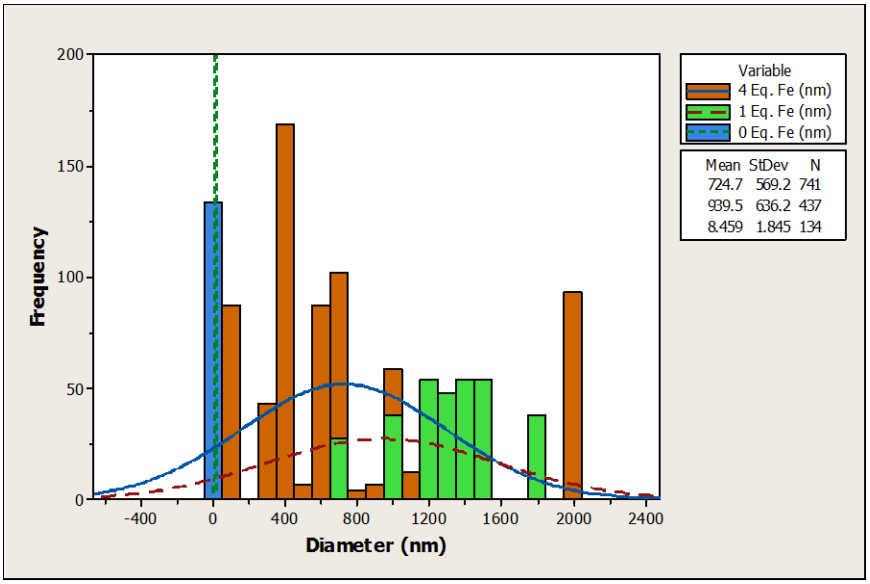

Figure D75. Particle size distribtution for Halochelin C at different ferric iron equivalents.

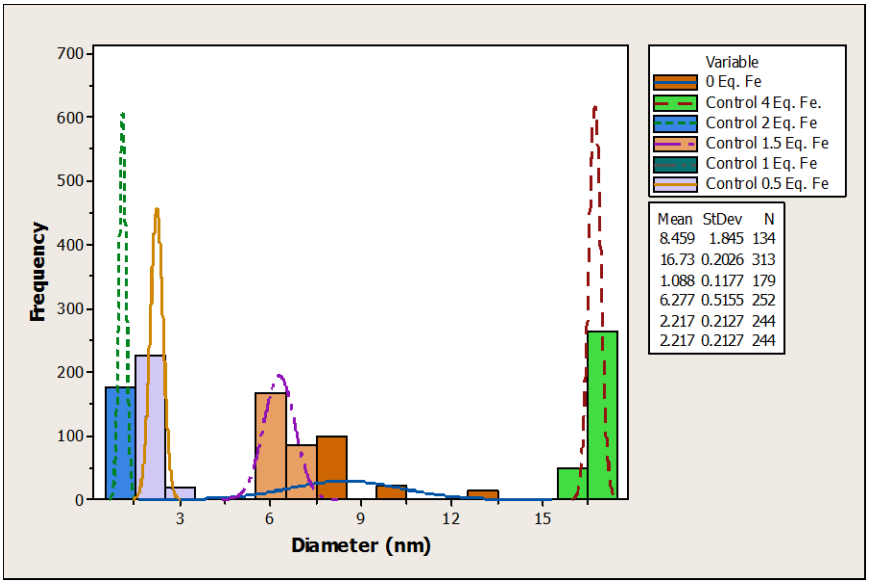

Figure D76. Particle size distribtution for Halochelin C controls.

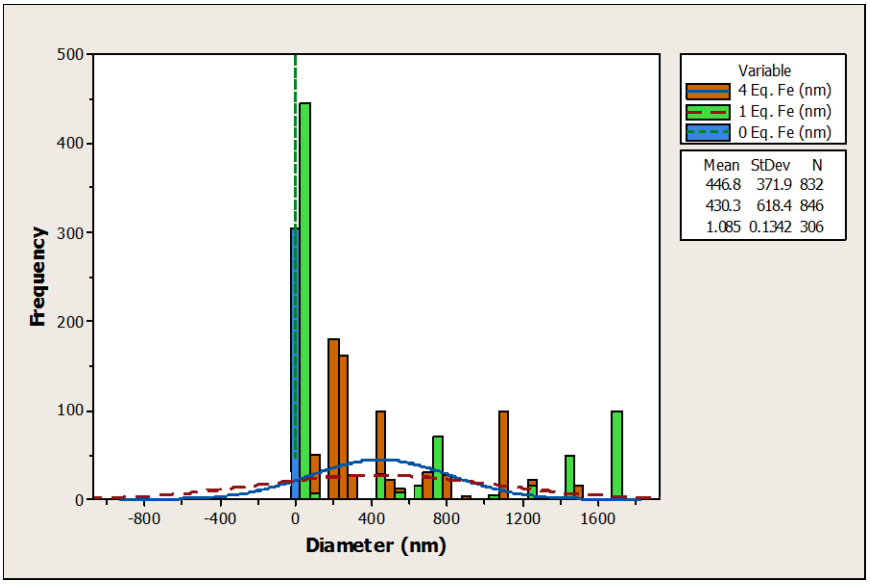

Figure D77. Particle size distribtution for Halochelin D at different ferric iron equivalents.

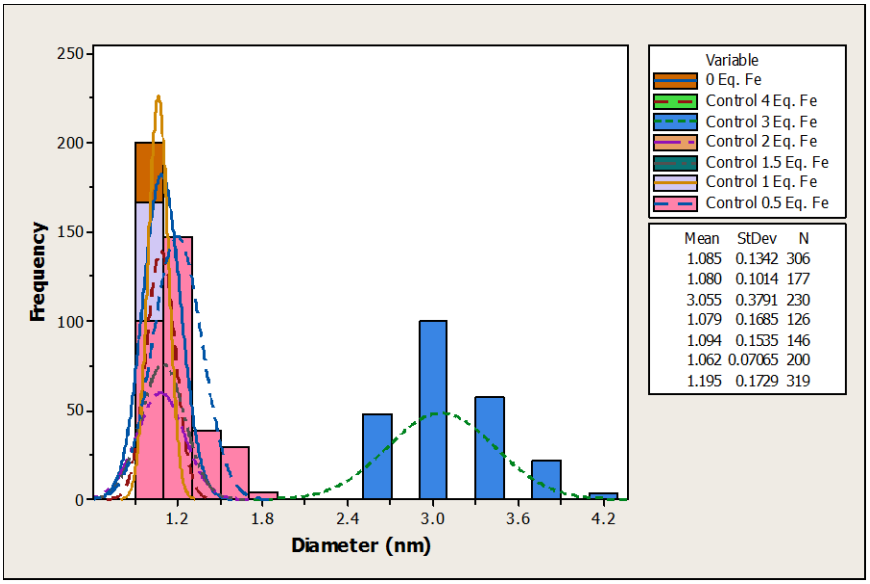

Figure D78. Particle size distribtution for Halochelin D controls.

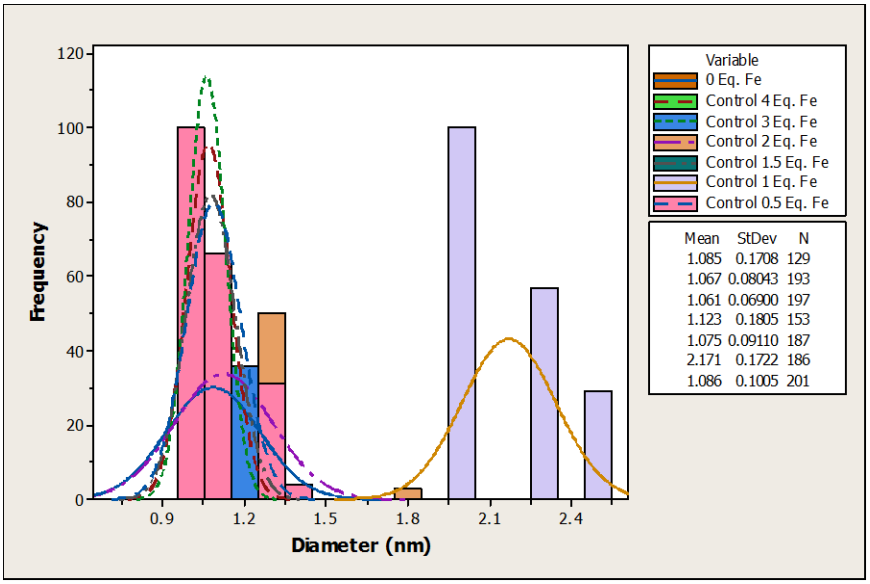

Figure D79. Particle size distribtution for Halochelin E controls.

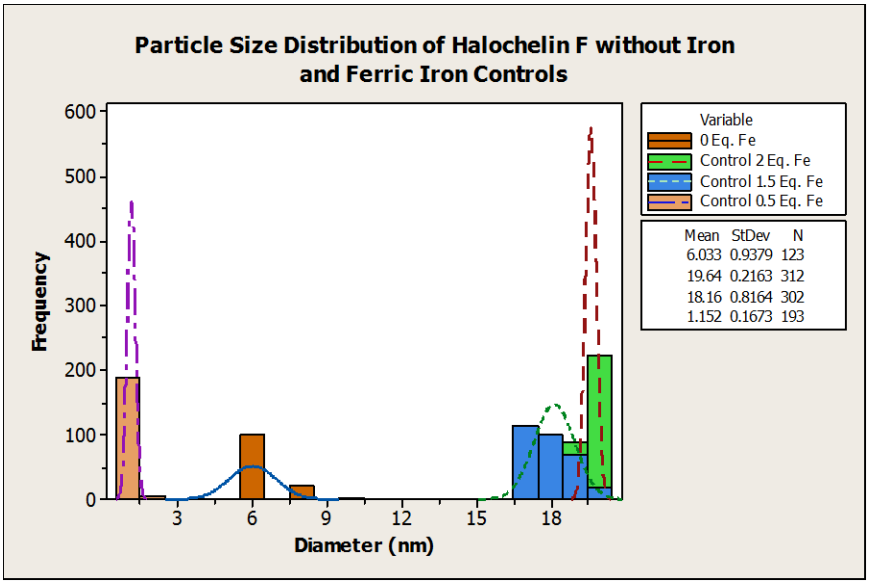

Figure D80. Particle size distribtution for Halochelin F controls.

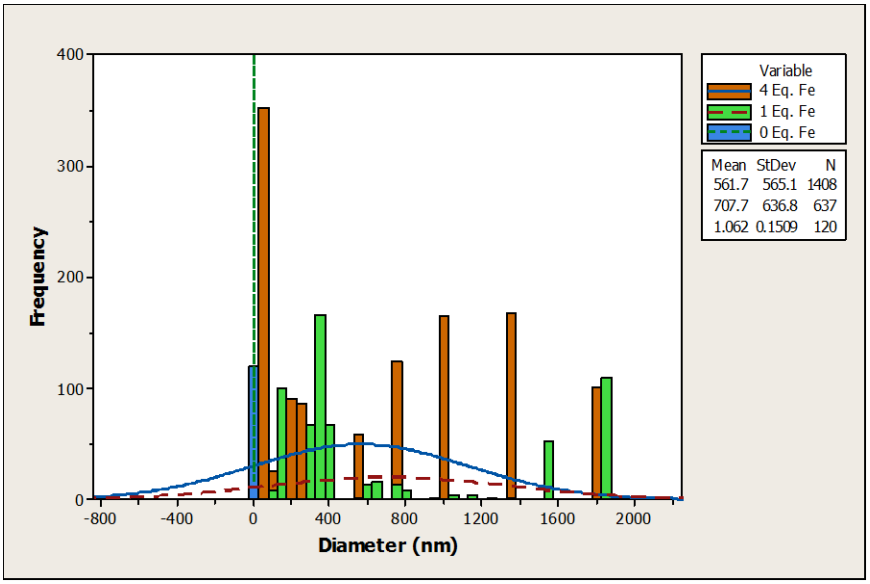

Figure D81. Particle size distribtution for Sodachelin C at different ferric iron equivalents.

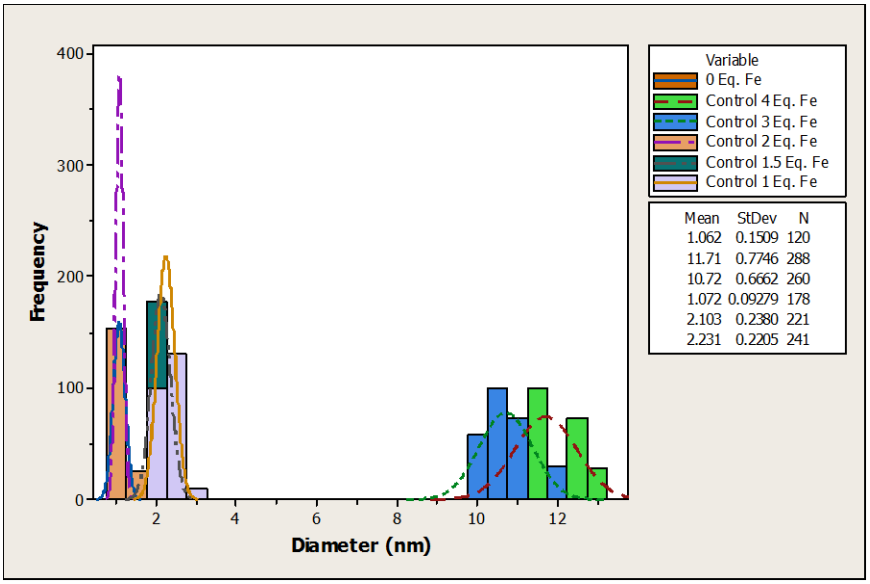

Figure D82. Particle size distribtution for Sodachelin C controls.

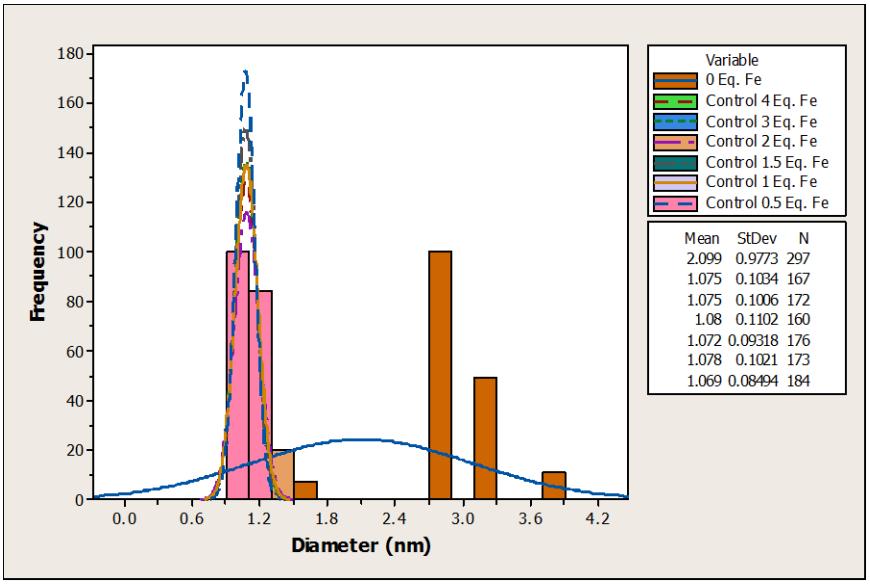

Figure D83. Particle size distribtution for Sodachelin D controls.

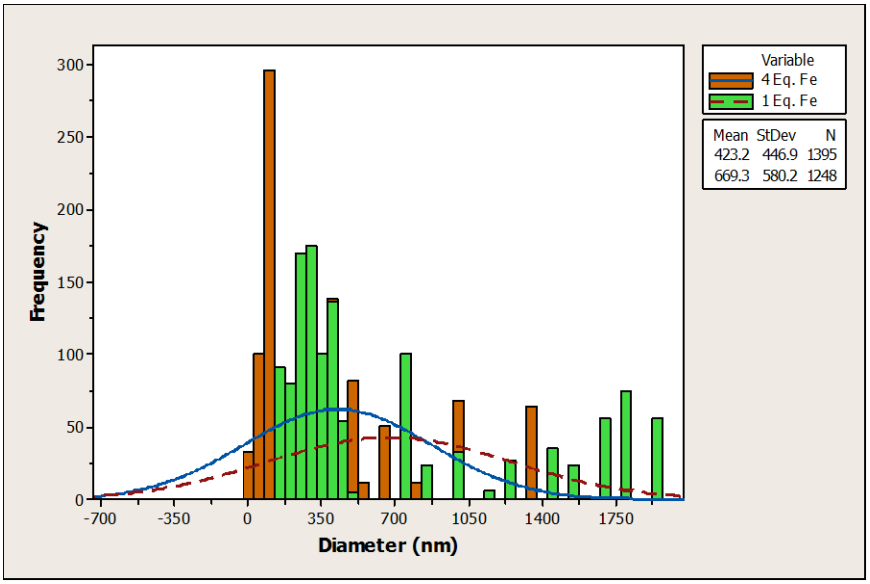

Figure D84. Particle size distribtution for Sodachelin E at different ferric iron equivalents.

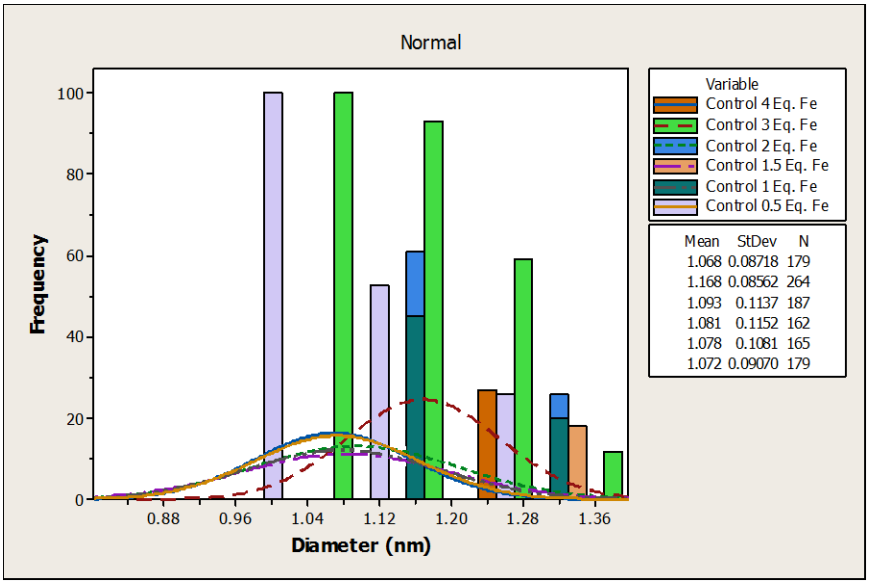

Figure D85. Particle size distribtution for Sodachelin E controls.

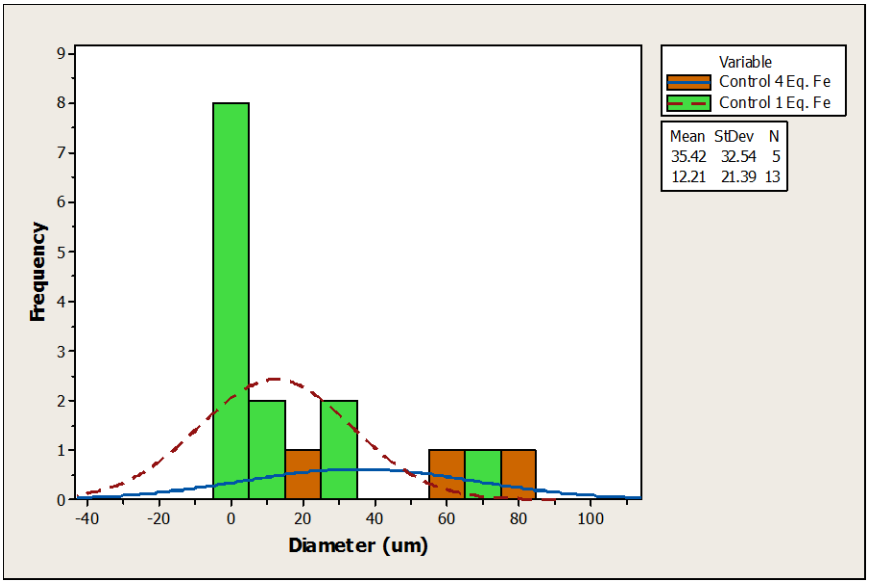

Figure D86. Particle size distribtution for Halochelin D epifluorescence microscopy controls.

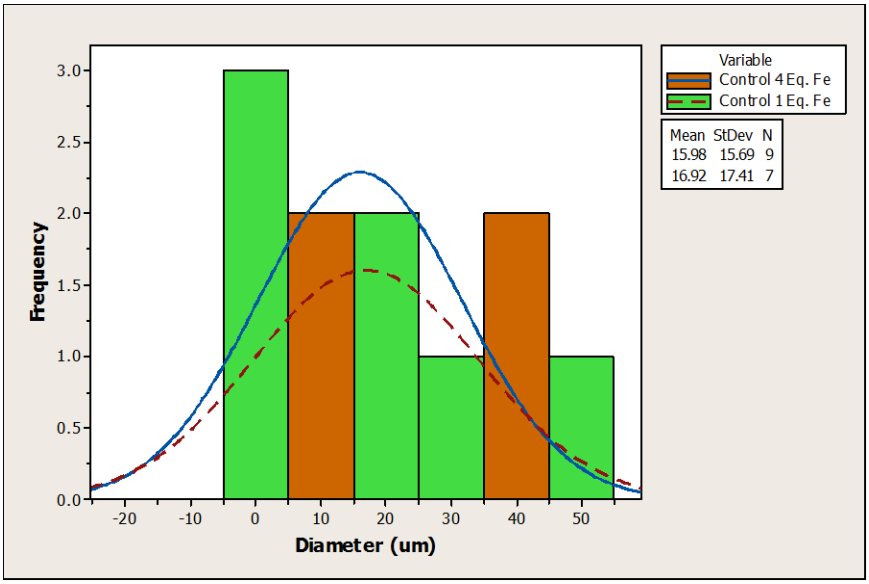

Figure D87. Particle size distribtution for Halochelin E epifluorescence microscopy controls.

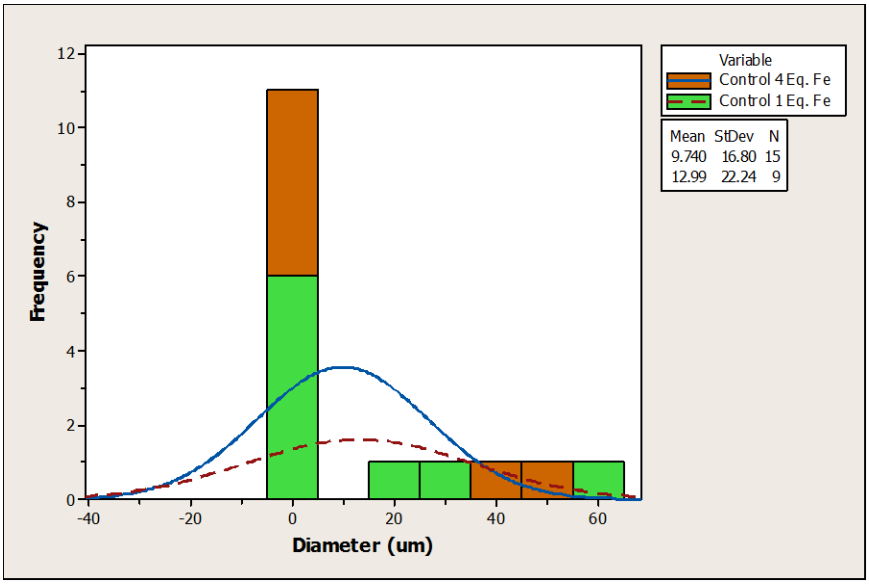

Figure D88. Particle size distribtution for Halochelin F epifluorescence microscopy controls.

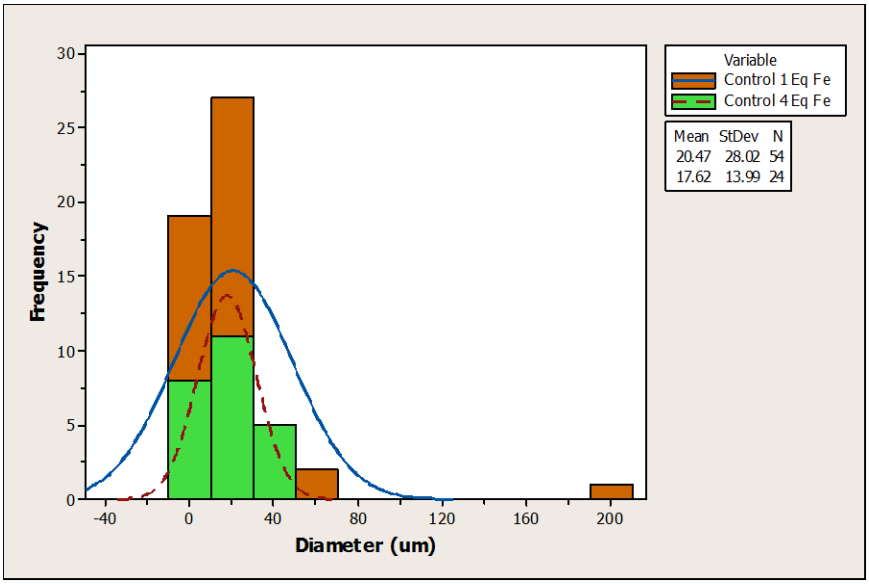

Figure D89. Particle size distribtution for Sodachelin C epifluorescence microscopy controls.

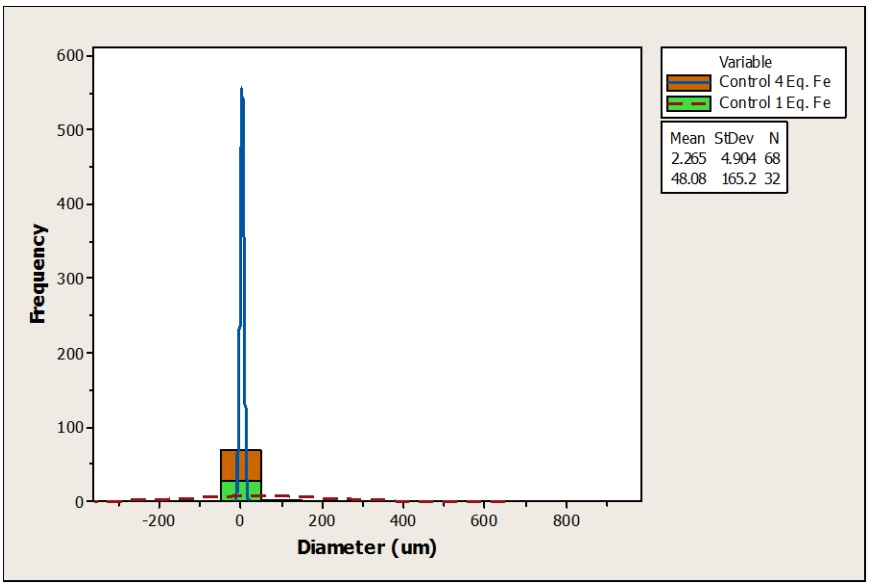

Figure D90. Particle size distribtution for Sodachelin D epifluorescence microscopy controls.

APPENDIX E

STATISTICAL ANALYSIS

One-way ANOVA: 4 Eq. Fe (nm, 1 Eq. Fe (nm, 0 Eq. Fe (nm, Control 4 Eq, ...

```
Source    DF         SS        MS       F      P
Factor     4  160446071  40111518  259.99  0.000
Error   2137  329699272    154281
Total   2141  490145343

S = 392.8   R-Sq = 32.73%   R-Sq(adj) = 32.61%



Level                     N   Mean  StDev
4 Eq. Fe (nm)          1092  269.1  410.4
1 Eq. Fe (nm)           393  817.6  610.3
0 Eq. Fe (nm)           266    1.0    0.1
Control 4 Eq. Fe (nm)   291   27.5    0.2
Control 1 Eq. Fe (nm)   100    1.8    0.0

                        Individual 95% CIs For Mean Based on
                        Pooled StDev
Level                   ---+---------+---------+---------+------
4 Eq. Fe (nm)                        (*)
1 Eq. Fe (nm)                                            (-*)
0 Eq. Fe (nm)            (-*-)
Control 4 Eq. Fe (nm)     (-*-)
Control 1 Eq. Fe (nm)   (--*--)
                        ---+---------+---------+---------+------
                           0       250       500       750

Pooled StDev = 392.8

Grouping Information Using Tukey Method

                          N   Mean  Grouping
1 Eq. Fe (nm)           393  817.6  A
4 Eq. Fe (nm)          1092  269.1    B
Control 4 Eq. Fe (nm)   291   27.5      C
Control 1 Eq. Fe (nm)   100    1.8      C
0 Eq. Fe (nm)           266    1.0      C

Means that do not share a letter are significantly different.
```

Figure E1. Statistical analysis for Halochelin B mean diameters at different ferric iron equivalents.

One-way ANOVA: 4 Eq. Fe nm, 1 Eq. Fe nm, 0 Eq. Fe nm, Control 4 Eq, ...

```
Level                    N   Mean  StDev
4 Eq. Fe (nm)          741  724.7  569.2
1 Eq. Fe (nm)          437  939.5  636.2
0 Eq. Fe (nm)          134    8.5    1.8
Control 4 Eq. Fe (nm)  313   16.7    0.2
Control 1 Eq. Fe (nm)  244    2.2    0.2

                       Individual 95% CIs For Mean Based on
                       Pooled StDev
Level                  --+---------+---------+---------+-------
4 Eq. Fe (nm)                                 (*)
1 Eq. Fe (nm)                                        (*-)
0 Eq. Fe (nm)          (-*--)
Control 4 Eq. Fe (nm)   (-*)
Control 1 Eq. Fe (nm)  (-*-)
                       --+---------+---------+---------+-------
                         0       300       600       900

Pooled StDev = 472.5


Grouping Information Using Tukey Method

                         N   Mean  Grouping
1 Eq. Fe (nm)          437  939.5  A
4 Eq. Fe (nm)          741  724.7     B
Control 4 Eq. Fe (nm)  313   16.7        C
0 Eq. Fe (nm)          134    8.5        C
Control 1 Eq. Fe (nm)  244    2.2        C

Means that do not share a letter are significantly different.
```

Figure E2. Statistical analysis for Halochelin C mean diameters at different ferric iron equivalents.

One-way ANOVA: 4 Eq. Fe (nm, 1 Eq. Fe (nm, 0 Eq. Fe (nm, Control 4 Eq, ...

```
Source    DF         SS        MS       F      P
Factor     4   92991408  23247852  125.04  0.000
Error   2356  438038014    185924
Total   2360  531029422

S = 431.2   R-Sq = 17.51%   R-Sq(adj) = 17.37%



Level                    N   Mean  StDev
4 Eq. Fe (nm)          832  446.8  371.9
1 Eq. Fe (nm)          846  430.3  618.4
0 Eq. Fe (nm)          306    1.1    0.1
Control 4 Eq. Fe (nm)  177    1.1    0.1
Control 1 Eq. Fe (nm)  200    1.1    0.1

                       Individual 95% CIs For Mean Based on
                       Pooled StDev
Level                  ----+---------+---------+---------+-----
4 Eq. Fe (nm)                                      (-*-)
1 Eq. Fe (nm)                                     (-*-)
0 Eq. Fe (nm)           (--*--)
Control 4 Eq. Fe (nm)  (---*---)
Control 1 Eq. Fe (nm)  (---*---)
                       ----+---------+---------+---------+-----
                           0       150       300       450

Pooled StDev = 431.2

Grouping Information Using Tukey Method

                         N   Mean  Grouping
4 Eq. Fe (nm)          832  446.8  A
1 Eq. Fe (nm)          846  430.3  A
0 Eq. Fe (nm)          306    1.1    B
Control 4 Eq. Fe (nm)  177    1.1    B
Control 1 Eq. Fe (nm)  200    1.1    B

Means that do not share a letter are significantly different.
```

Figure E3. Statistical analysis for Halochelin D mean diameters at different ferric iron equivalents.

One-way ANOVA: 4 Eq. Fe, 1 Eq. Fe, 0 Eq. Fe, Control 4 Eq. Fe, Control 1 Eq. Fe

```
Source    DF        SS        MS       F      P
Factor     4  40185596  10046399  387.32  0.000
Error   1108  28739516     25938
Total   1112  68925112

S = 161.1   R-Sq = 58.30%   R-Sq(adj) = 58.15%


                                    Individual 95% CIs For Mean Based on
                                    Pooled StDev
Level               N   Mean  StDev  --+---------+---------+---------+-------
4 Eq. Fe          399  419.8  257.0                                      (*)
1 Eq. Fe          206  105.2  109.3           (-*-)
0 Eq. Fe          129    1.1    0.2  (-*-)
Control 4 Eq. Fe  193    1.1    0.1  (-*-)
Control 1 Eq. Fe  186    2.2    0.2  (-*-)
                                    --+---------+---------+---------+-------
                                      0       120       240       360

Pooled StDev = 161.1

Grouping Information Using Tukey Method

                    N   Mean  Grouping
4 Eq. Fe          399  419.8  A
1 Eq. Fe          206  105.2     B
Control 1 Eq. Fe  186    2.2       C
0 Eq. Fe          129    1.1       C
Control 4 Eq. Fe  193    1.1       C

Means that do not share a letter are significantly different.
```

Figure E4. Statistical analysis for Halochelin E mean diameters at different ferric iron equivalents.

One-way ANOVA: 4 Eq. Fe, 1 Eq. Fe, 0 Eq. Fe

```
Source    DF         SS        MS       F      P
Factor     2   62835397  31417698  294.43  0.000
Error   1831  195380609    106707
Total   1833  258216006

S = 326.7   R-Sq = 24.33%   R-Sq(adj) = 24.25%


                              Individual 95% CIs For Mean Based on
                              Pooled StDev
Level        N   Mean  StDev  --+---------+---------+---------+-------
4 Eq. Fe   315  848.8  478.2                                      (*)
1 Eq. Fe  1396  611.4  297.6                           *)
0 Eq. Fe   123    6.0    0.9  (-*--)
                              --+---------+---------+---------+-------
                                0       250       500       750

Pooled StDev = 326.7


Grouping Information Using Tukey Method

             N   Mean  Grouping
4 Eq. Fe   315  848.8  A
1 Eq. Fe  1396  611.4     B
0 Eq. Fe   123    6.0       C

Means that do not share a letter are significantly different.
```

Figure E5. Statistical analysis for Halochelin F mean diameters at different ferric iron equivalents.

One-way ANOVA: 4 Eq. Fe, 1 Eq. Fe, 0 Eq. Fe, Control 4 Eq. Fe, Control 1 Eq. Fe

```
Source    DF         SS        MS       F      P
Factor     4  187264741  46816185  177.99  0.000
Error   2689  707274127    263025
Total   2693  894538867

S = 512.9   R-Sq = 20.93%   R-Sq(adj) = 20.82%
```

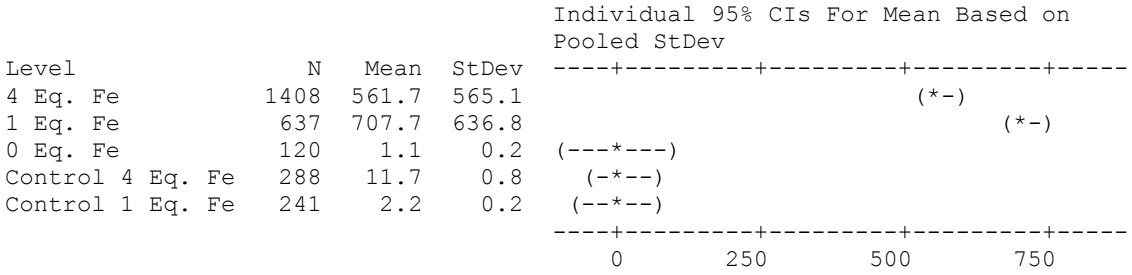


```
Pooled StDev = 512.9


Grouping Information Using Tukey Method

                    N   Mean  Grouping
1 Eq. Fe          637  707.7  A
4 Eq. Fe         1408  561.7     B
Control 4 Eq. Fe  288   11.7        C
Control 1 Eq. Fe  241    2.2        C
0 Eq. Fe          120    1.1        C

Means that do not share a letter are significantly different.
```

Figure E6. Statistical analysis for Sodachelin C mean diameters at different ferric iron equivalents.

One-way ANOVA: 4 Eq. Fe, 1 Eq. Fe, 0 Eq. Fe, Control 4 Eq. Fe, Control 1 Eq. Fe

```
Source    DF         SS        MS       F      P
Factor     4   40528642  10132161  111.35  0.000
Error   3181  289452085     90994
Total   3185  329980727

S = 301.7   R-Sq = 12.28%   R-Sq(adj) = 12.17%


                                    Individual 95% CIs For Mean Based on
                                    Pooled StDev
Level                N   Mean  StDev  ----+---------+---------+---------+-----
4 Eq. Fe          1432  297.1  334.6                                    (-*)
1 Eq. Fe          1117  258.8  340.3                               (-*-)
0 Eq. Fe           297    2.1    1.0   (--*---)
Control 4 Eq. Fe   167    1.1    0.1  (---*----)
Control 1 Eq. Fe   173    1.1    0.1  (---*----)
                                    ----+---------+---------+---------+-----
                                        0       100       200       300

Pooled StDev = 301.7

Grouping Information Using Tukey Method

                     N   Mean  Grouping
4 Eq. Fe          1432  297.1  A
1 Eq. Fe          1117  258.8     B
0 Eq. Fe           297    2.1       C
Control 1 Eq. Fe   173    1.1       C
Control 4 Eq. Fe   167    1.1       C

Means that do not share a letter are significantly different.
```

Figure E7. Statistical analysis for Sodachelin D mean diameters at different ferric iron equivalents.

One-way ANOVA: 4 Eq. Fe, 1 Eq. Fe, Control 4 Eq. Fe, Control 1 Eq. Fe

```
Source    DF         SS        MS       F      P
Factor     3  128104058  42701353  182.45  0.000
Error   2983  698170987    234050
Total   2986  826275046

S = 483.8   R-Sq = 15.50%   R-Sq(adj) = 15.42%


                                      Individual 95% CIs For Mean Based on
                                      Pooled StDev
Level                 N   Mean  StDev  ----+---------+---------+---------+-----
4 Eq. Fe           1395  423.2  446.9                          (*)
1 Eq. Fe           1248  669.3  580.2                                      (*-)
Control 4 Eq. Fe    179    1.1    0.1   (--*---)
Control 1 Eq. Fe    165    1.1    0.1  (---*---)
                                      ----+---------+---------+---------+-----
                                          0       200       400       600

Pooled StDev = 483.8


Grouping Information Using Tukey Method

                     N   Mean  Grouping
1 Eq. Fe          1248  669.3  A
4 Eq. Fe          1395  423.2    B
Control 1 Eq. Fe   165    1.1      C
Control 4 Eq. Fe   179    1.1      C

Means that do not share a letter are significantly different.
```

Figure E8. Statistical analysis for Sodachelin E mean diameters at different ferric iron equivalents.

One-way ANOVA: 4 Eq. Fe, 1 Eq. Fe

```
Source    DF         SS      MS     F      P
Factor     1     257668  257668  2.83  0.093
Error   1208  110143775   91179
Total   1209  110401442

S = 302.0   R-Sq = 0.23%   R-Sq(adj) = 0.15%


                              Individual 95% CIs For Mean Based on
                              Pooled StDev
Level       N   Mean  StDev  -------+---------+---------+---------+--
4 Eq. Fe  844  402.6  333.8  (-------*-------)
1 Eq. Fe  366  434.3  210.7          (------------*-----------)
                              -------+---------+---------+---------+--
                                   400       425       450       475

Pooled StDev = 302.0

Grouping Information Using Tukey Method

            N   Mean  Grouping
1 Eq. Fe  366  434.3  A
4 Eq. Fe  844  402.6  A

Means that do not share a letter are significantly different.
```

Figure E9. Statistical analysis for Sodachelin F mean diameters at different ferric iron equivalents.

One-way ANOVA: 4 Eq. Fe (nm), 1 Eq. Fe (nm), 0 Eq. Fe (nm)

```
Source   DF         SS       MS      F      P
Factor    2   14887059  7443529  29.01  0.000
Error   569  145978101   256552
Total   571  160865159

S = 506.5   R-Sq = 9.25%   R-Sq(adj) = 8.94%


                                  Individual 95% CIs For Mean Based on
                                  Pooled StDev
Level            N   Mean  StDev  --------+---------+---------+---------+-
4 Eq. Fe (nm)  244  904.8  655.9                              (----*-----)
1 Eq. Fe (nm)   64  714.6  484.2         (----------*---------)
0 Eq. Fe (nm)  264  562.3  318.4  (----*----)
                                  --------+---------+---------+---------+-
                                        600       720       840       960

Pooled StDev = 506.5


Grouping Information Using Tukey Method

                 N   Mean  Grouping
4 Eq. Fe (nm)  244  904.8  A
1 Eq. Fe (nm)   64  714.6    B
0 Eq. Fe (nm)  264  562.3    B

Means that do not share a letter are significantly different.
```

Figure E10. Statistical analysis for Halochelin D epifluorescence microscopy.

One-way ANOVA: 4 Eq. Fe (nm), 1 Eq. Fe (nm), 0 Eq. Fe (nm)

```
Source   DF        SS      MS      F      P
Factor    2   1902151  951076  10.11  0.000
Error   855  80416528   94054
Total   857  82318679

S = 306.7   R-Sq = 2.31%   R-Sq(adj) = 2.08%


                                    Individual 95% CIs For Mean Based on
                                    Pooled StDev
Level            N   Mean  StDev  ---------+---------+---------+---------+
4 Eq. Fe (nm)  695  563.6  320.2                              (---*---)
1 Eq. Fe (nm)   97  448.2  284.7      (---------*---------)
0 Eq. Fe (nm)   66  437.2  152.0  (-----------*-----------)
                                    ---------+---------+---------+---------+
                                           420       480       540       600

Pooled StDev = 306.7


Grouping Information Using Tukey Method

                 N   Mean  Grouping
4 Eq. Fe (nm)  695  563.6  A
1 Eq. Fe (nm)   97  448.2    B
0 Eq. Fe (nm)   66  437.2    B

Means that do not share a letter are significantly different.
```

Figure E11. Statistical analysis for Halochelin E epifluorescence microscopy.

One-way ANOVA: 4 Eq. Fe (nm), 1 Eq. Fe (nm), 0 Eq. Fe (nm)

```
Source   DF        SS     MS     F      P
Factor    2     90717  45359  1.01  0.364
Error   603  27012303  44797
Total   605  27103020

S = 211.7   R-Sq = 0.33%   R-Sq(adj) = 0.00%


                                    Individual 95% CIs For Mean Based on
                                    Pooled StDev
Level            N   Mean  StDev  -----+---------+---------+---------+----
4 Eq. Fe (nm)  460  465.8  203.7                        (---*---)
1 Eq. Fe (nm)  120  458.4  248.2                  (-------*------)
0 Eq. Fe (nm)   26  405.7  159.6  (---------------*---------------)
                                   -----+---------+---------+---------+----
                                      350       400       450       500

Pooled StDev = 211.7


Grouping Information Using Tukey Method

                 N   Mean  Grouping
4 Eq. Fe (nm)  460  465.8  A
1 Eq. Fe (nm)  120  458.4  A
0 Eq. Fe (nm)   26  405.7  A

Means that do not share a letter are significantly different.
```

Figure E12. Statistical analysis for Halochelin F epifluorescence microscopy.

One-way ANOVA: 4 Eq. Fe (nm), 1 Eq. Fe (nm), 0 Eq. Fe (nm)

```
Source   DF        SS      MS     F      P
Factor    2    530656  265328  4.11  0.017
Error   479  30885655   64479
Total   481  31416311

S = 253.9   R-Sq = 1.69%   R-Sq(adj) = 1.28%


                                    Individual 95% CIs For Mean Based on
                                    Pooled StDev
Level            N   Mean  StDev  ----+---------+---------+---------+-----
4 Eq. Fe (nm)  150  490.0  353.4                 (---------*----------)
1 Eq. Fe (nm)  175  420.8  159.1  (--------*---------)
0 Eq. Fe (nm)  157  489.7  224.7                 (---------*---------)
                                    ----+---------+---------+---------+-----
                                      400       440       480       520

Pooled StDev = 253.9


Grouping Information Using Tukey Method

                 N   Mean  Grouping
4 Eq. Fe (nm)  150  490.0  A
0 Eq. Fe (nm)  157  489.7  A
1 Eq. Fe (nm)  175  420.8    B

Means that do not share a letter are significantly different.
```

Figure E13. Statistical analysis for Sodachelin C epifluorescence microscopy.

One-way ANOVA: 4 Eq. Fe (nm), 1 Eq. Fe (nm), 0 Eq. Fe (nm)

```
Source   DF         SS      MS     F      P
Factor    2     781672  390836  2.01  0.135
Error   526  102095295  194098
Total   528  102876967

S = 440.6   R-Sq = 0.76%   R-Sq(adj) = 0.38%


                                    Individual 95% CIs For Mean Based on
                                    Pooled StDev
Level            N   Mean  StDev  --+---------+---------+---------+-------
4 Eq. Fe (nm)  405  588.5  406.8                   (--*--)
1 Eq. Fe (nm)   14  500.4  248.2  (--------------*---------------)
0 Eq. Fe (nm)  110  673.6  562.0                      (-----*----)
                                    --+---------+---------+---------+-------
                                    300       450       600       750

Pooled StDev = 440.6


Grouping Information Using Tukey Method

                 N   Mean  Grouping
0 Eq. Fe (nm)  110  673.6  A
4 Eq. Fe (nm)  405  588.5  A
1 Eq. Fe (nm)   14  500.4  A

Means that do not share a letter are significantly different.
```

Figure E14. Statistical analysis for Sodachelin D epifluorescence microscopy.

APPENDIX F

EPIFLUORESCENCE MICROSCOPY IMAGES

EPIFLUORESCENCE MICROSCOPY IMAGES

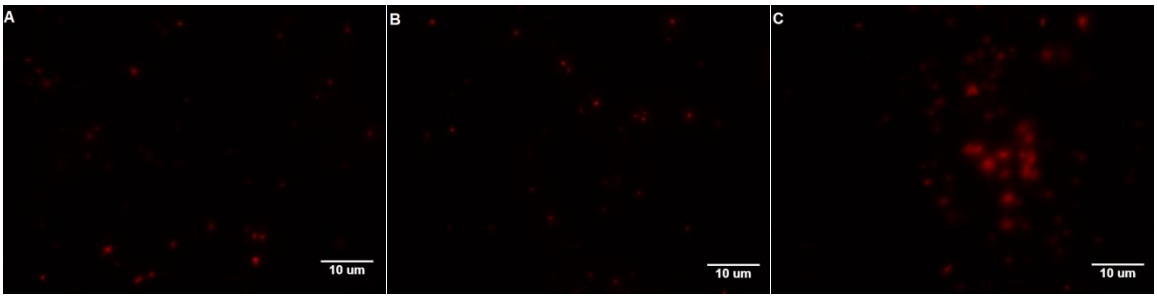

Image F1. Epifluorescence microscopy for Halochelin D without ferric iron. Magnification at 60 X; scale bars at 10 μm.

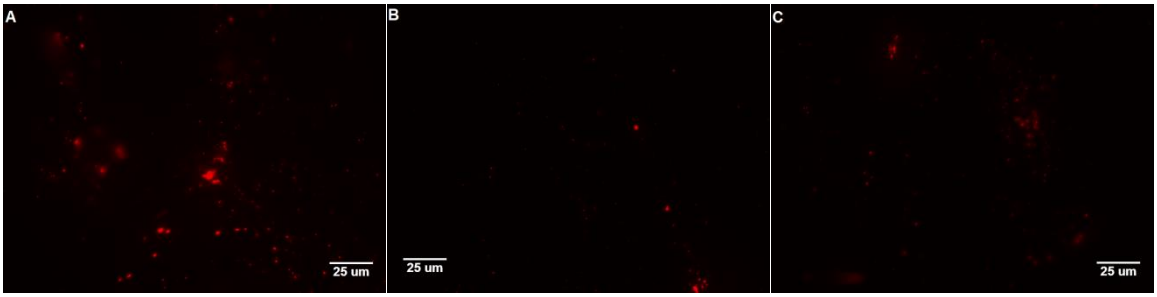

Image F2. Epifluorescence microscopy for Halochelin D without ferric iron. Magnification at 20 X; scale bars at 25 μm.

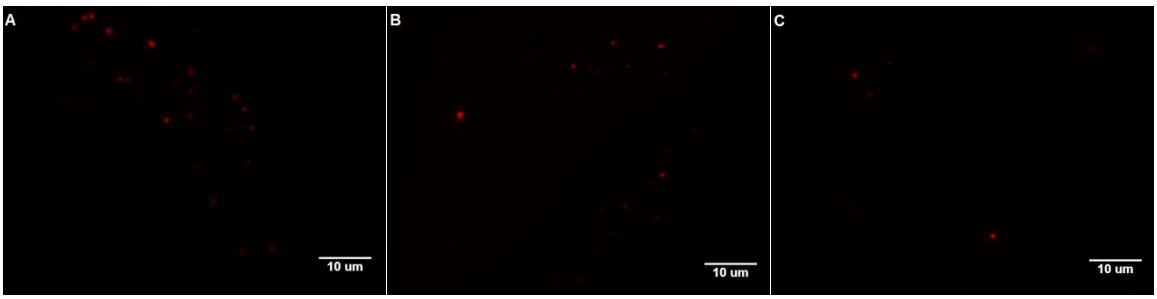

Image F3. Epifluorescence microscopy for Halochelin D with 1 Eq. Fe^{+3}. Magnification at 60 X; scale bars at 10 μm.

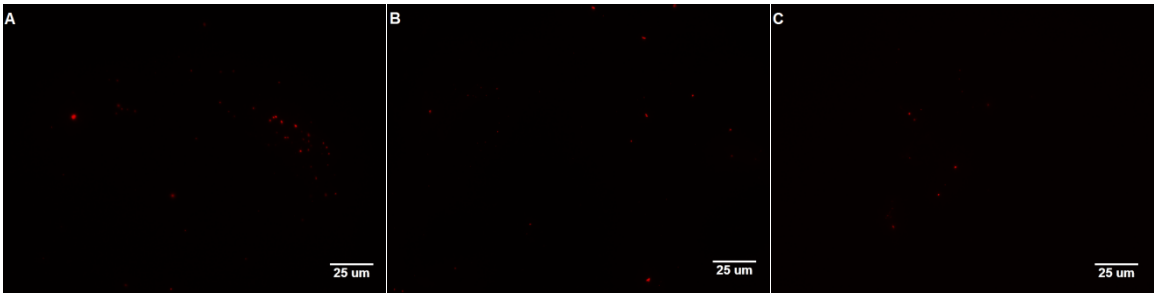

Image F4. Epifluorescence microscopy for Halochelin D with 1 Eq. Fe^{+3}. Magnification at 20 X; scale bars at 25 µm.

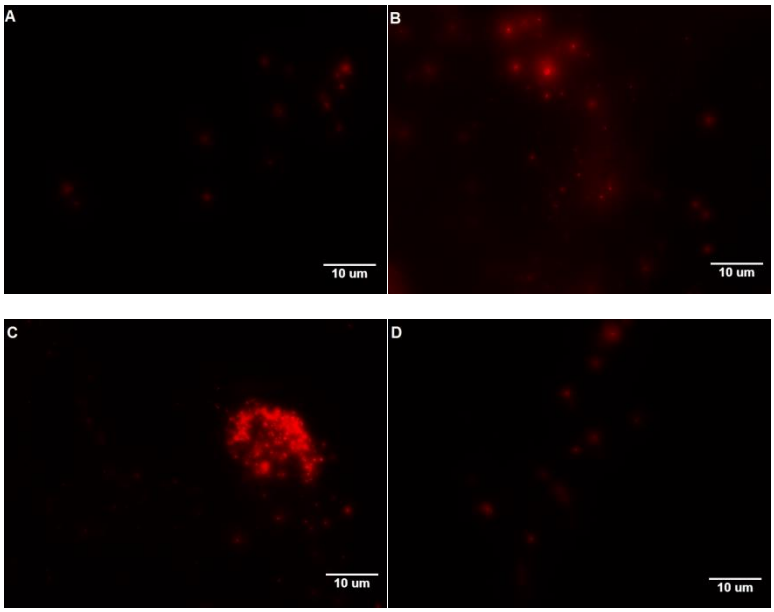

Image F5. Epifluorescence microscopy for Halochelin D with 4 Eq. Fe^{+3}. Magnification at 60 X; scale bars at 10 µm.

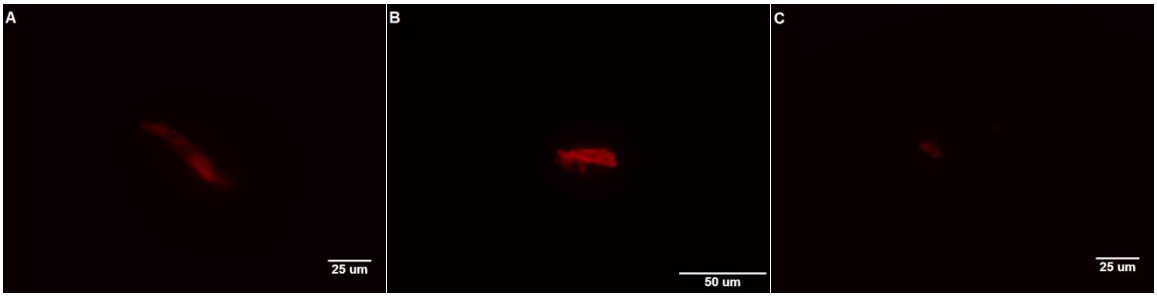

Image F6. Epifluorescence microscopy for Halochelin D 1 Eq. Fe^{+3} controls. Magnification at 20X; scale bars at 25 (A and C) and 50 µm (B).

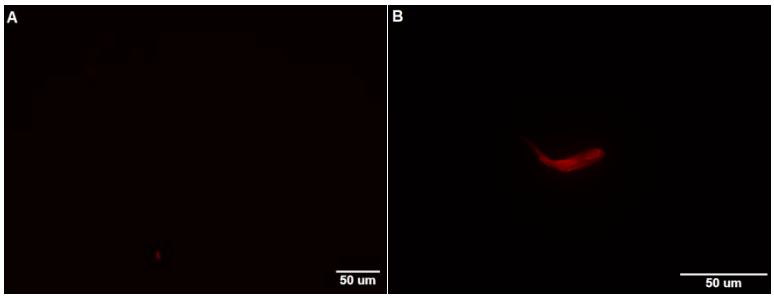

Image F7. Epifluorescence microscopy for Halochelin D 4 Eq. Fe^{+3} controls. Magnification at 10X (A) and 20X (B); scale bars at 50 µm.

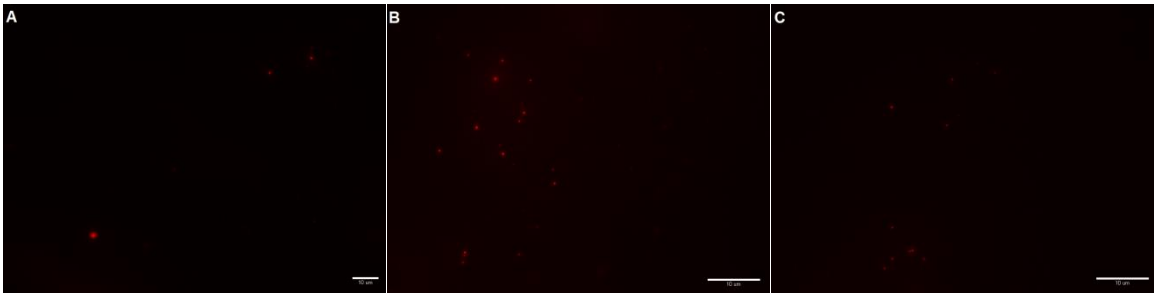

Image F8. Epifluorescence microscopy for Halochelin E without ferric iron. Magnification at 60 X; scale bars at 10 µm.

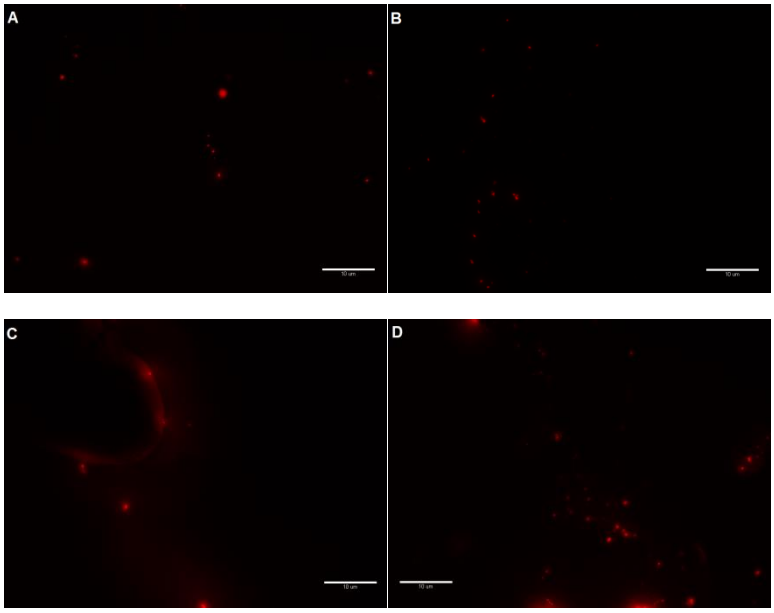

Image F9. Epifluorescence microscopy for Halochelin E with 1 Eq. Fe^{+3}. Magnification at 60 X; scale bars at 10 µm.

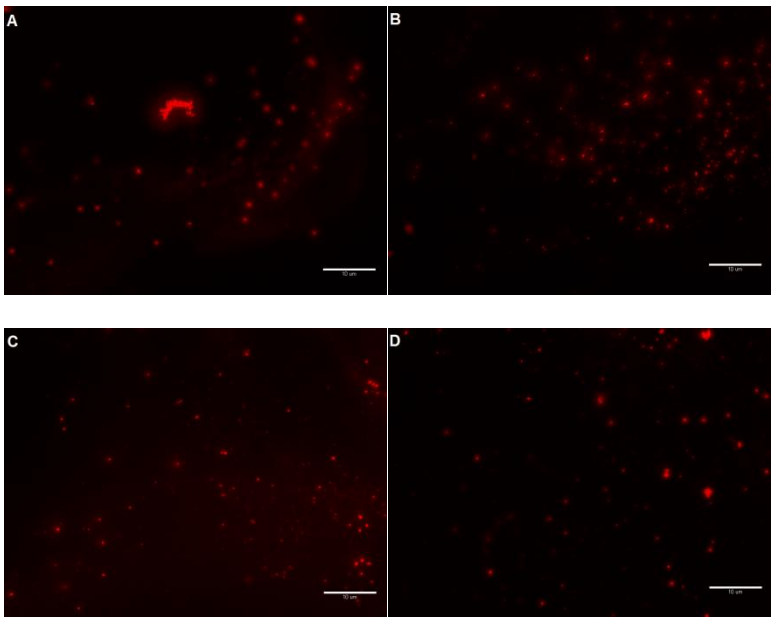

Image F10. Epifluorescence microscopy for Halochelin E with 4 Eq. Fe^{+3}. Magnification at 60 X; scale bars at 10 µm.

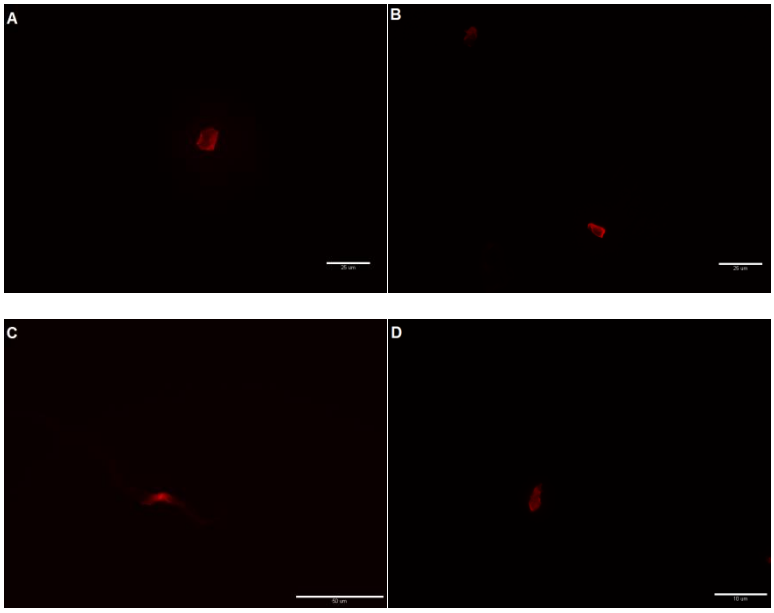

Image F11. Epifluorescence microscopy for Halochelin E 1 Eq. Fe^{+3} controls. Magnification at 20X (A – C) and 60X (D); scale bars at 10 (D), 25 (A and B) and 50 μm (C).

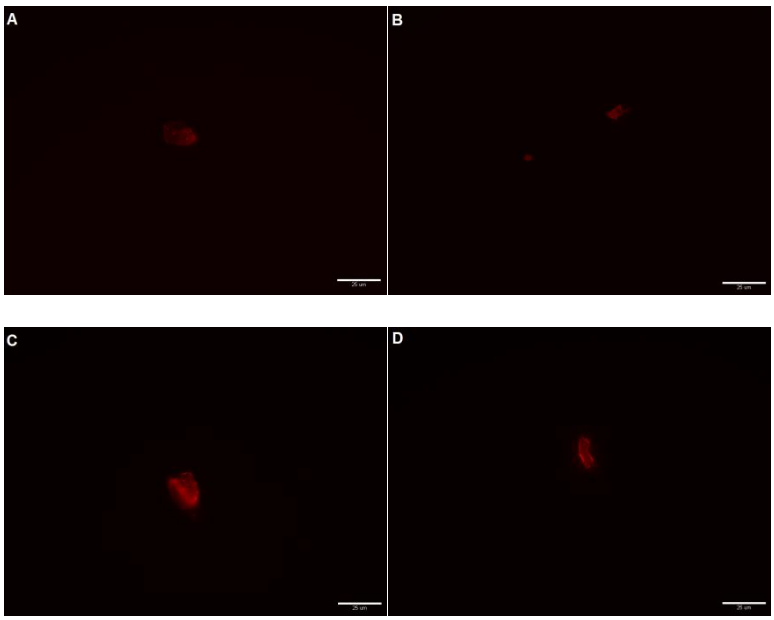

Image F12. Epifluorescence microscopy for Halochelin E 4 Eq. Fe^{+3} controls. Magnification at 20X; scale bars at 25 μm.

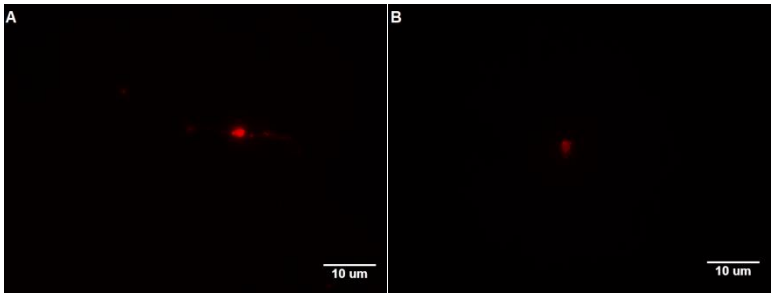

Image F13. Epifluorescence microscopy for Halochelin F without ferric iron. Magnification at 60X; scale bars at 10 μm.

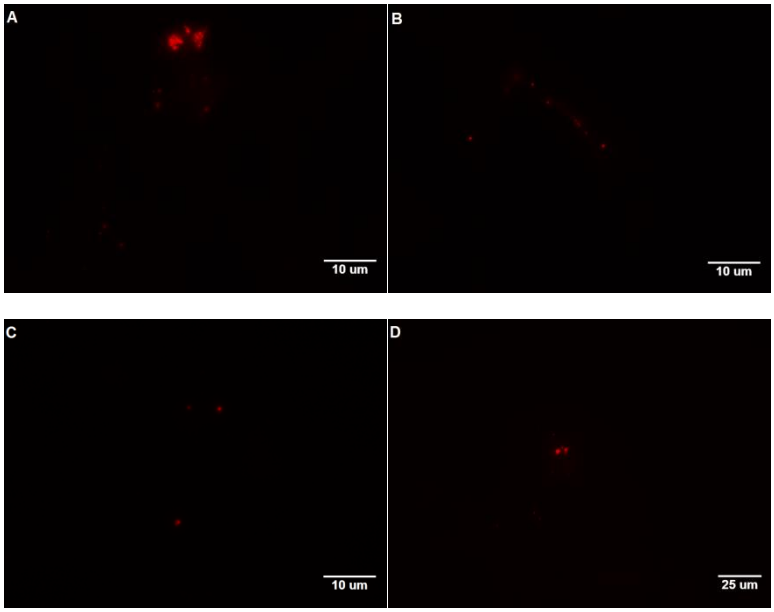

Image F14. Epifluorescence microscopy for Halochelin F with 1 Eq. Fe^{+3}. Magnification at 20X (D) and 60X (A – C); scale bars at 10 (A – C) and 25 μm (D).

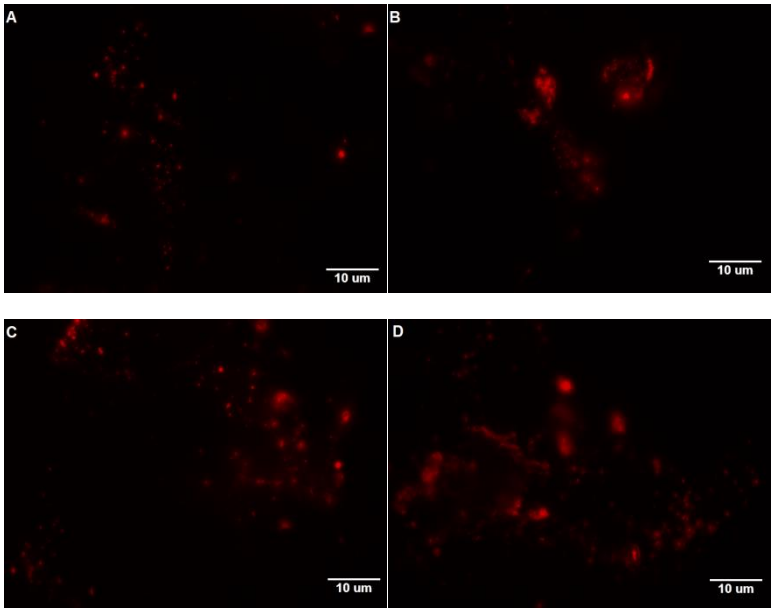

Image F15. Epifluorescence microscopy for Halochelin F with 4 Eq. Fe^{+3}. Magnification at 60X; scale bars at 10 μm.

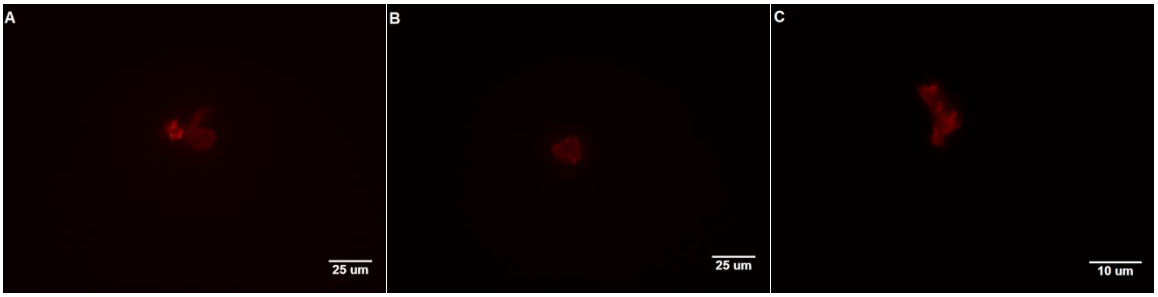

Image F16. Epifluorescence microscopy for Halochelin F 1 Eq. Fe^{+3} controls. Magnification at 20X (A – B) and 60X (C); scale bars at 10 (C) and 25 μm (A and B).

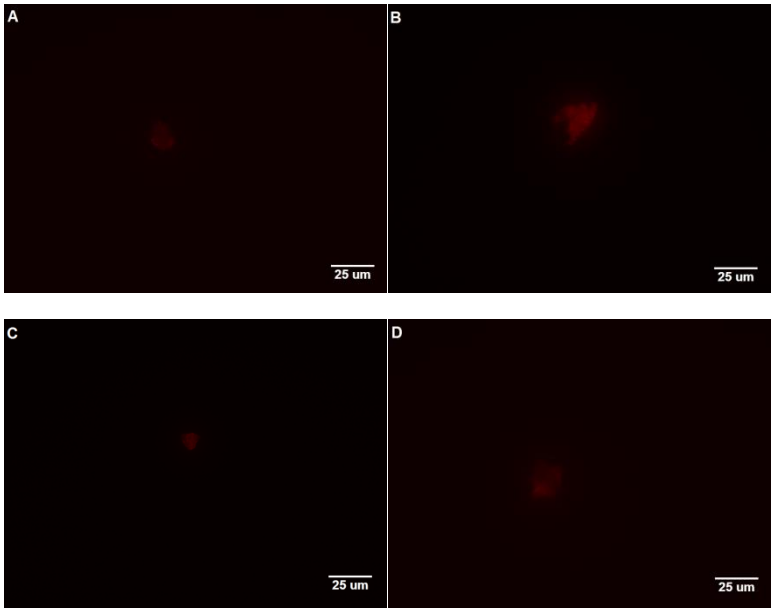

Image F17. Epifluorescence microscopy for Halochelin F 4 Eq. Fe^{+3} controls. Magnification at 20X; scale bars at 25 µm.

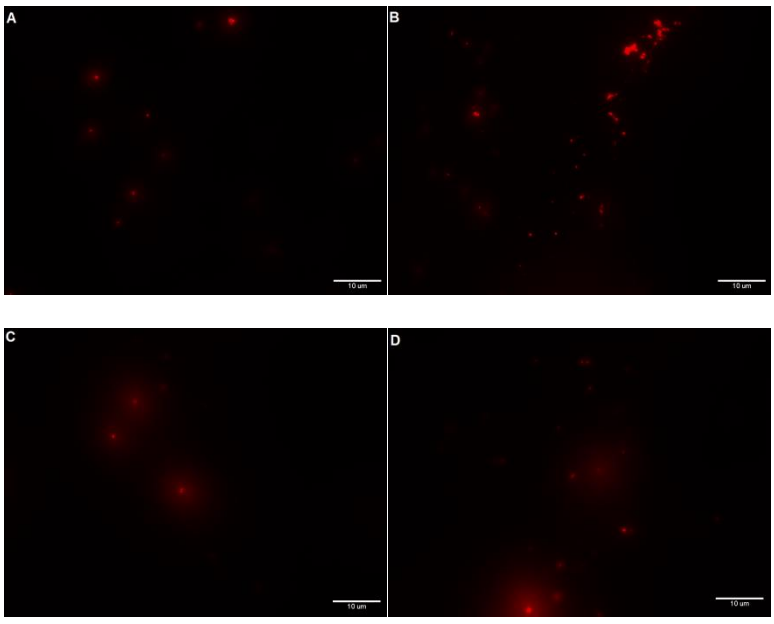

Image F18. Epifluorescence microscopy for Sodachelin C without ferric iron. Magnification at 60X; scale bars at 10 µm.

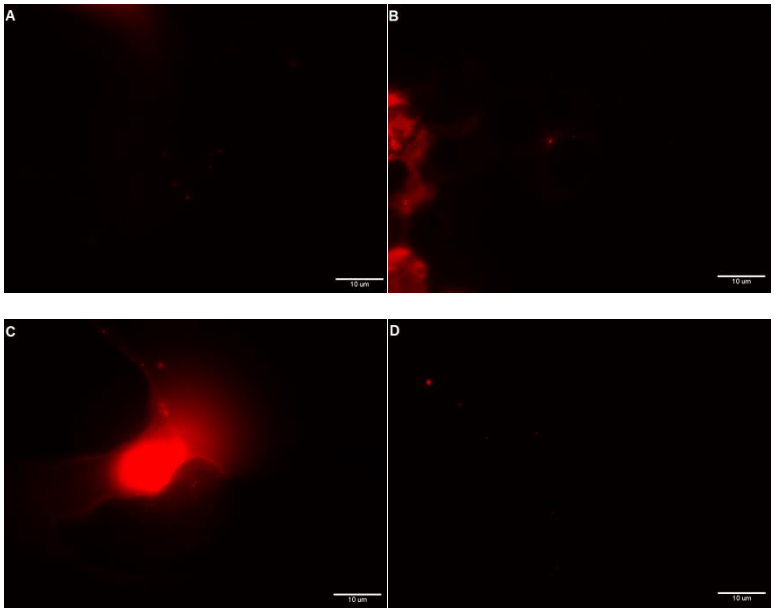

Image F19. Epifluorescence microscopy for Sodachelin C with 1 Eq. Fe^{+3}. Magnification at 60X; scale bars at 10 µm.

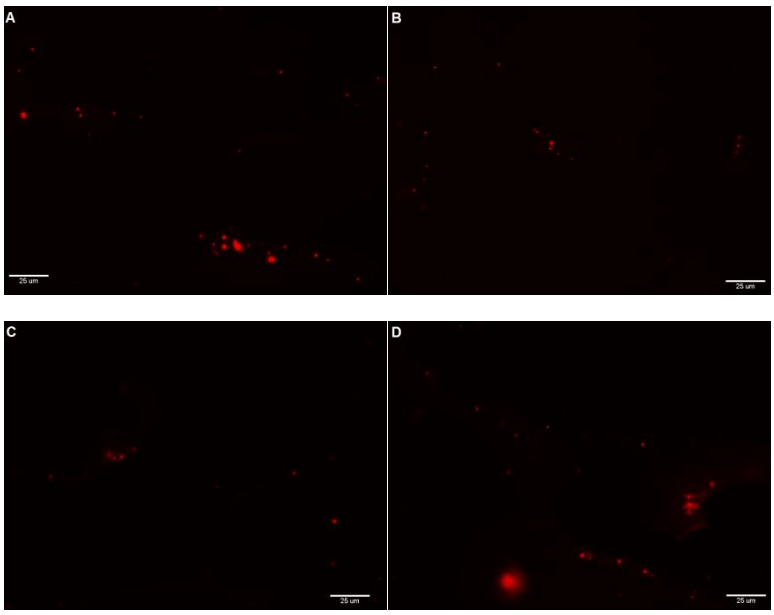

Image F20. Epifluorescence microscopy for Sodachelin C with 4 Eq. Fe^{+3}. Magnification at 20X; scale bars at 25 µm.

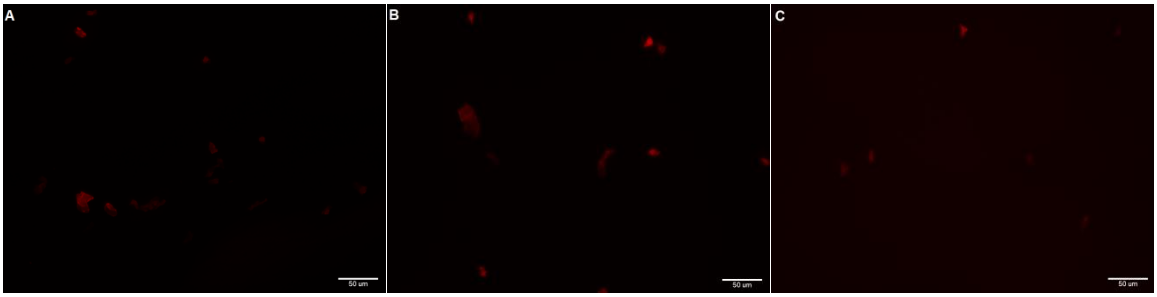

Image F21. Epifluorescence microscopy for Sodachelin C 1 Eq. Fe^{+3} controls. Magnification at 10X; scale bars at 50 µm.

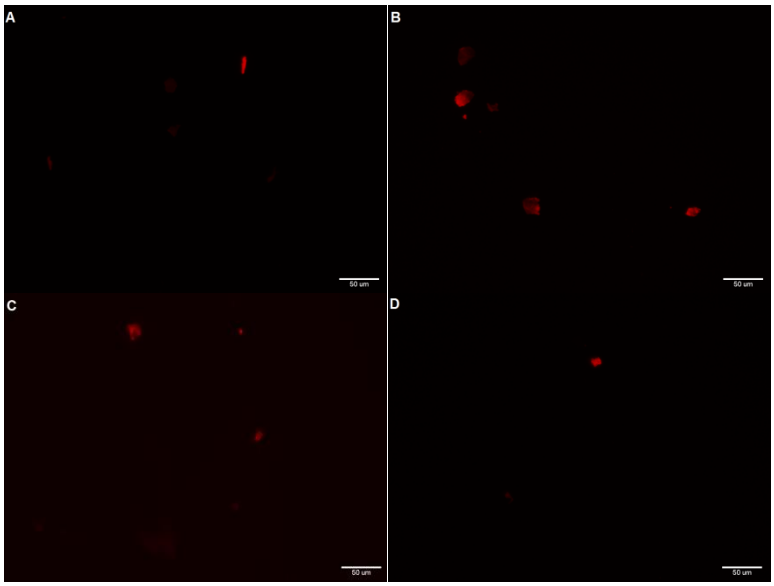

Image F22. Epifluorescence microscopy for Sodachelin C 4 Eq. Fe^{+3} controls. Magnification at 10X; scale bars at 50 µm.

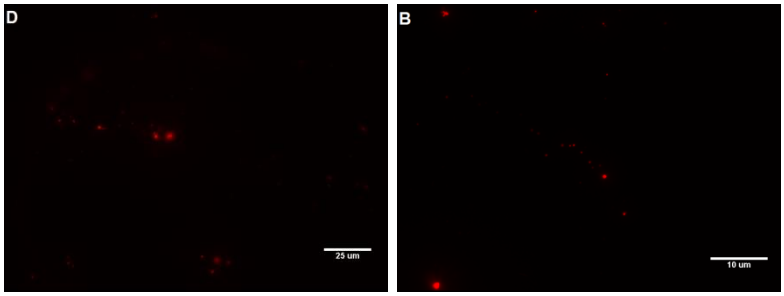

Image F23. Epifluorescence microscopy for Sodachelin D without ferric iron. Magnification at 20X (A) and 60X (B); scale bars at 10 (B) and 25 µm (A).

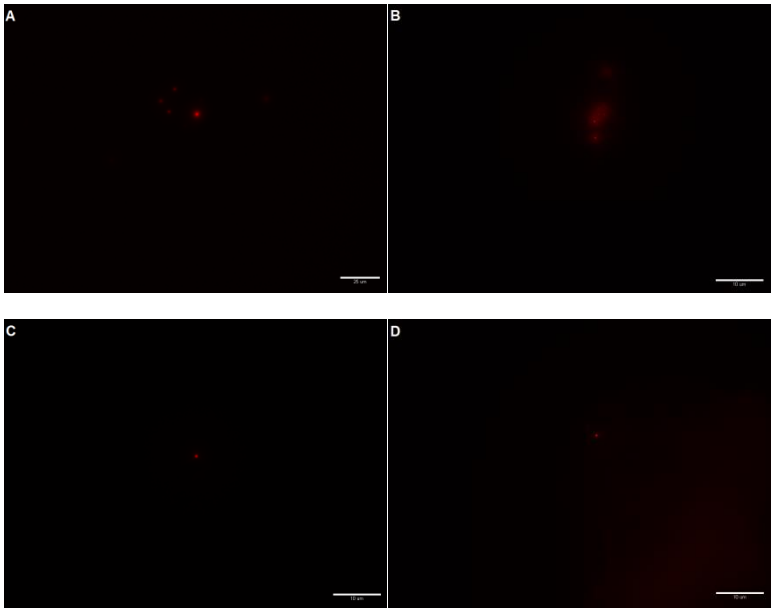

Image F24. Epifluorescence microscopy for Sodachelin D with 1 Eq. Fe^{+3}. Magnification at 20X (A) and 60X (B – C); scale bars at 10 (B – C) and 25 µm (A).

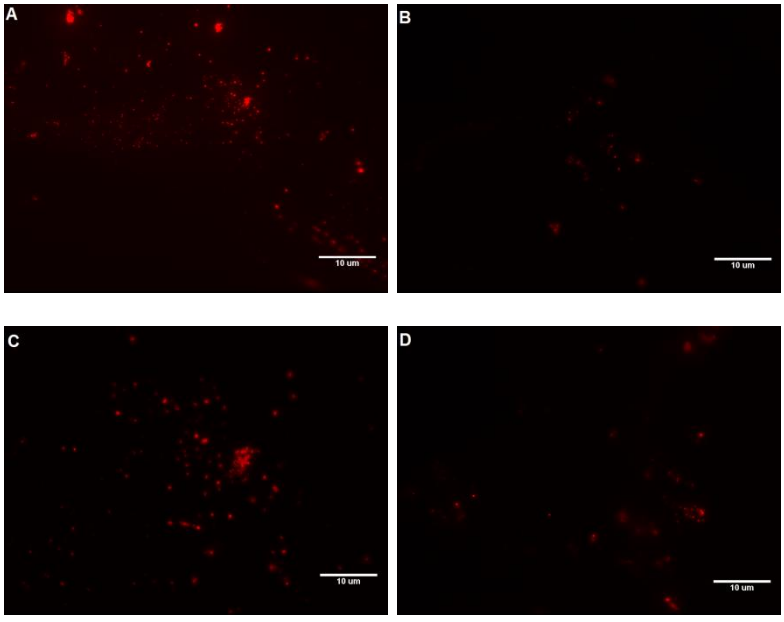

Image F25. Epifluorescence microscopy for Sodachelin D with 4 Eq. Fe^{+3}. Magnification at 60X; scale bars at 10 µm.

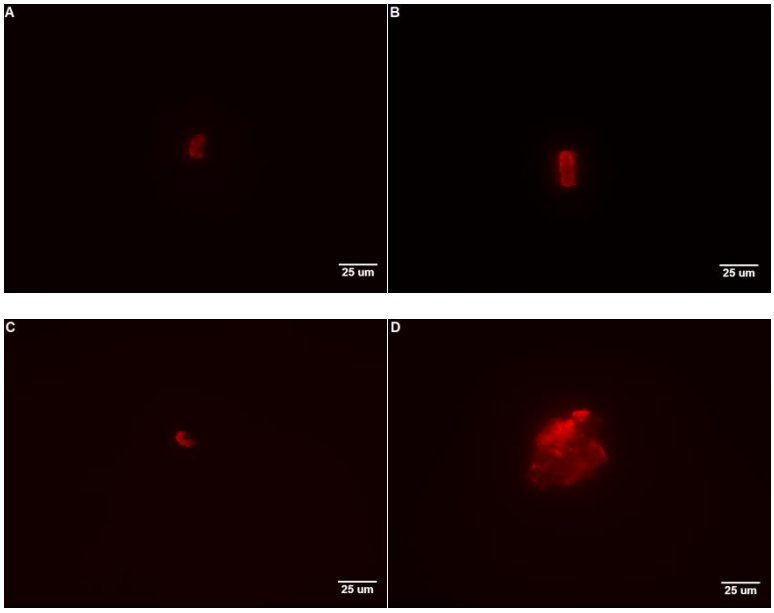

Image F26. Epifluorescence microscopy for Sodachelin D 1 Eq. Fe^{+3} controls. Magnification at 20X; scale bars at 25 µm.

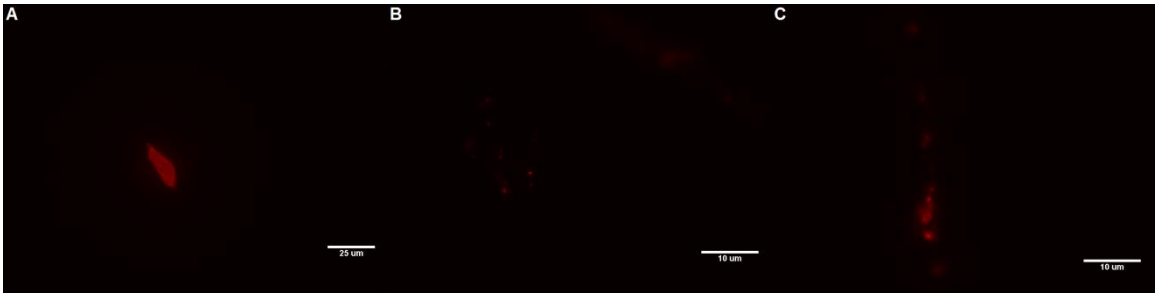

Image F27. Epifluorescence microscopy for Sodachelin D 4 Eq. Fe^{+3} controls. Magnification at 20X (A) and 60X (B and C); scale bars at 10 (B and C) and 25 µm (A).